# DNAPL AND LNAPL DISTRIBUTIONS IN SOILS; EXPERIMENTAL AND MODELING STUDIES

D.S. Durnford, D.B. McWhorter, C.D. Miller, A. Swanson, F. Marinelli, H.L. Trantham

Colorado State University
Fort Collins, CO 80523

October 1997

FINAL REPORT

19980430 111

DTIC QUALITY INSPECTED 3

# REPORT DOCUMENTATION PAGE

Public reporting burden for this collection of information is estimated to average 1 hour per response, including the time for reviewing instructions, searching existing data sources, gathering and maintaining the data needed, and completing and reviewing the collection of information. Send comments regarding this burden estimate or any other aspect of this collection of information, including suggestions for reducing this burden, to Washington Headquarters Services, Directorate for Information Operations and Reports, 1215 Jefferson Davis Highway, Suite 1204, Arlington, VA 22202-4302, and to the Office of Management and Budget, Paperwork Reduction Project (0704-0188), Washington, DC 20503.

| 1. AGENCY USE ONLY (Leave blank) | 2. REPORT DATE<br>Oct. 1997 | 3. REPORT TYPE AND DATES COVERED<br>Final  15 Mar 94-14 Mar 97 |
|---|---|---|

**4. TITLE AND SUBTITLE**

DNAPL AND LNAPL DISTRIBUTIONS IN SOILS:
EXPERIMENTAL AND MODELING STUDIES

**5. FUNDING NUMBERS**

F49620-94-1-0193

**6. AUTHOR(S)**

D.S. Durnford, D.B. McWhorter, F. Marinelli,
C.D. Miller, A.Swanson,

**7. PERFORMING ORGANIZATION NAME(S) AND ADDRESS(ES)**

Chemical and Bioresource Engr.
Colorado State University
Fort Collins, CO 80523

**8. PERFORMING ORGANIZATION REPORT NUMBER**

**9. SPONSORING/MONITORING AGENCY NAME(S) AND ADDRESS(ES)**

Air Force Office of Sponsored Research
110 Duncan Avenue, Suite 115
Bolling AFB, DC 20332-0001

**10. SPONSORING/MONITORING AGENCY REPORT NUMBER**

**11. SUPPLEMENTARY NOTES**

**12a. DISTRIBUTION/AVAILABILITY STATEMENT**

Approved for public release.
distribution unlimited

**12b. DISTRIBUTION CODE**

**13. ABSTRACT (Maximum 200 words)**

This project contributes to our understanding of the intricacies of immiscible fluid behavior in soils contaminated with non aqueous phase liquids (NAPLs). First, one and two-dimensional laboratory experiments conducted to study the distribution and flow of DNAPLs and LNAPLs in homogeneous and layered soils show that seemingly subtle aspects of immiscible fluid behavior can manifest themselves in important large scale effects. For example, it is shown that the equilibrium distribution of an LNAPL lens can only be explained by hysteresis in the capillary pressure-saturation relation. Second, although it is generally recognized that immiscible transport is highly sensitive to soil heterogeneities, current models are not well equipped to characterize their influence on NAPL flow. This report summarizes a unique method for modeling one-dimensional, multiphase flow through porous media. Third, the development of a two-dimensional pore-scale model based on a modified diffusion limited aggregation algorithm is presented. We felt the limitation of a low capillary number imposed by percolation-based models was too stringent for most DNAPLs of interest in contaminant hydrology. The model presented simulates the unstable flow characteristics often exhibited when DNAPLs invade water-saturated soil.

**14. SUBJECT TERMS**

DNAPLS, LNAPLS
Groundwater, NAPLs, water quality, hydrocarbons,
pore scale modeling, heterogeneous, hysteresis

**15. NUMBER OF PAGES**

**16. PRICE CODE**

| 17. SECURITY CLASSIFICATION OF REPORT<br>unclassified | 18. SECURITY CLASSIFICATION OF THIS PAGE<br>unclassified | 19. SECURITY CLASSIFICATION OF ABSTRACT<br>unclassified | 20. LIMITATION OF ABSTRACT<br>UL |
|---|---|---|---|

(Reverse side of this page intentionally blank)

# DNAPL AND LNAPL DISTRIBUTIONS IN SOILS; EXPERIMENTAL AND MODELING STUDIES

D.S. Durnford, D.B. McWhorter, C.D. Miller, A. Swanson, F. Marinelli, H.L. Trantham

Colorado State University
Fort Collins, CO 80523

October 1997

FINAL REPORT

# EXECUTIVE SUMMARY

## DNAPL AND LNAPL DISTRIBUTIONS IN SOILS: EXPERIMENTAL AND MODELING RESULTS

### By

D.S. Durnford, D.B. McWhorter, F. Marinelli, C.D. Miller,
A. Swanson and H. Trantham

The Air Force Office of Scientific Research Program in Environmental Quality supports research that provides a technology base for eliminating potential environmental hazards. The Air Force uses a variety of hazardous materials that can be introduced into the soil environment through spills or leaks. Of interest in this report are the thousands of sites contaminated with fuels or solvents. These fluids are classified as nonaqueous phase liquids (NAPLs) because they have low solubilities in water and their fate and transport in soils are determined by the physics of immiscible fluid flow in porous media. Understanding immiscible fluid flow in porous media, with the goal of characterizing and remediating subsurface sites contaminated with nonaqueous phase liquids, is the focus of this project.

This report summarizes three different components of AFOSR Project No. F49620-94-1-0193. Section II of the report provides examples of seemingly subtle aspects of immiscible fluid behavior that, nonetheless, are manifested in important large-scale effects. Results of one and two-dimensional multiphase laboratory experiments in homogeneous and layered soils are presented. Results show the importance of hysteresis in the capillary pressure-saturation relation. We also identify a non-toxic DNAPL surrogate that can be used in laboratory experiments.

Section III presents a unique method for modeling one-dimensional, multiphase flow through layered media. This is an important problem in contaminant hydrology because of the prevalence of natural layered soil formations and the sensitivity of NAPL flow to small-scale heterogeneities. While it is recognized that NAPL transport is highly sensitive to heterogeneities, currently available models are poorly equipped to accommodate their influence on multiphase flow. To avoid the difficulties found when using most other models, our approach is to reduce the governing nonlinear, partial differential equation in time and space to a second-order, ordinary differential equation by applying finite difference techniques to the time derivative only. While this technique has limited generality, it proved to have significant advantages when modeling one-dimensional, two-phase flow through layered soils. By means of this model, we can gain insight into multiphase, flow processes at a textural interface.

In Section IV, we present details of a two-dimensional, pore-scale model based on a modified diffusion limited aggregation algorithm. One of the most stringent limitations of commonly used percolation models is that they only apply to low capillary number flows. Whereas this restriction is not significant for LNAPLs, we felt it was too limiting for most DNAPLs of interest in contaminant hydrology. DNAPLs are often less viscous than water and exhibit unstable flow characteristics. The stochastic aggregation model developed in this project allows us to more realistically characterize these unstable flow phenomena.

The results of this project will be disseminated in refereed journal publications. To date, the following reports, theses and papers are available:

Miller, C.D. and D. S. Durnford. 1996. An experimental study of immiscible flow through layered sands. In: Reddi, L.K. (Ed.) Non-Aqueous Phase Liquids (NAPLS) in Subsurface Environments: Assessment and Remediation. ASCE, New York, NY. p. 628-638.

Rimmer, A., D. DiCarlo, T. Steenhuis, B. Bierck, D. Durnford and J.-Y. Parlange. 1996. Rapid fluid content measurement method in an oil-water-sand system using synchrotron X-rays. Elsevier Press, The Netherlands. (accepted, in press)

Durnford, D. S. D. B. McWhorter, C. Miller, F. Marinelli and H. Trantham. 1997. Modeling and experimental studies of NAPL distribution and flow in porous media. In: Proceedings of the Joint USAF/US Army Contractors/grantees meeting, Environmental Quality, Panama City, FL.

Marinelli. F. and D. Durnford. 1998. Semianalytical Solution for Unsaturated Flow, submitted to ASCE J. of Irrigation and Drainage. (in revision).

Marinelli, F. and D.S. Durnford. 1996. LNAPL thickness in monitoring wells considering hysteresis and entrapment. Ground Water 34(3):405-414.

Marinelli, F., D.S. Durnford and D.B. McWhorter. Semianalytical solution for two-fluid flow, submitted to J. of Contaminant Hydrology.

Trantham, H. and D.S. Durnford. Stochastic Aggregation Modeling (SAM) of immiscible flow in porous media. submitted to the Journal of Contaminant Hydrology (in revision).

Durnford, D.S. and F. Marinelli. 1995. Distribution of liquid phase hydrocarbons in layered soil. Proceedings, USAF/Army Joint Contractors/Grantees Meeting, Basic Research in Environmental Quality, Subsurface Fate and Transport, Boulder, CO.

Steenhuis, T., J.-Y. Parlange, D. Chandler, A. Rimmer, Z. Cohen, W. Condit, D. Durnford, B. Bierck. 1995. Fingers in oil-water systems. Abstract International Union of Geodesy and Geophysics XXI General Assembly. July 2-14, Boulder CO.


Marinelli, Frederick. 1996. Semi-analytical solutions for one-dimensional flow of immiscible fluids in layered porous media. Ph.D. dissertation. Civil Engineering Dept. Colorado State University, Fort Collins, CO.


Miller, Calvin. 1997. Laboratory investigations of solvents in heterogeneous porous media. M.S. Thesis, Chemical and Bioresource Engr., Colorado State University, Fort Collins, CO.

Swanson, Angela. 1997. Laboratory investigations of hydrocarbon fuels in heterogeneous porous media. M.S. Thesis, Chemical and Bioresource Engr. Colorado State University, Fort Collins, CO.

# TABLE OF CONTENTS

## SECTION I

## SECTION II

# SECTION III

## SECTION IV

## SECTION V

# SECTION I

## SECTION I

## 1.1    INTRODUCTION

Understanding immiscible fluid behavior in porous media, in an effort to characterize and remediate subsurface sites contaminated with nonaqueous-phase liquids (NAPLs), has been the focus of considerable research over the last decade.  This has been approached from many perspectives - from field scale behavior to laboratory studies to analytical and numerical modeling.  Although research has now generally progressed to investigation of remediation technologies and evaluation at the field scale, much has been learned, and remains to be fully appreciated, about the subtle aspects of immiscible fluid behavior.  A better understanding of the small scale intricacies of NAPL behavior can, and has, led to more accurate conceptual models of the subsurface distribution and behavior of these contaminants.  Our research combines experimental laboratory investigations and mathematical modeling to gain insight into the physical phenomena governing the flow and distribution of NAPLs in porous media. Emphasis is placed on the effects of hysteresis in multiphase flow in layered soils.

This report summarizes three different topics in immiscible fluids.  Section II provides examples of seemingly subtle aspects of immiscible fluid behavior.  However, it is shown that this behavior can be manifested as important large scale effects in certain scenarios.  Results of one and two-dimensional multiphase laboratory experiments of transient flow in  layered soils are presented.  This is an important problem in contaminant hydrology both because of the prevalence of natural layered soil formations and because

layers are artificially created by processes such as hydrofracturing, a practice that is increasingly being used in remediation of tight soils. Capillary barriers are another example where accurate simulation of multiphase, transient flow across textural interfaces is important. At a smaller scale, it is generally recognized that NAPL transport is highly sensitive to subsurface heterogeneities (Kueper and Frind, 1991; Pantazidou and Sitar, 1993; Illangasekare, et al., 1995). Chapter 1 in section II summarizes a laboratory experiment conducted in a vertical column with fine and coarse layering. Water was drained and replaced with either oil or air. A dual energy gamma system was used to quantify fluid saturations during transient drainage. The model presented later in Section III was used to simulate this experiment. Several two-dimensional flume experiments are also presented in this section. The objective of these experiments was to determine the lens configuration of an LNAPL or DNAPL lens in equilibrium. Results show the importance of hysteresis in the capillary pressure-saturation relation. We also identify a nontoxic DNAPL surrogate that can be used in laboratory experiments.

Section III presents a unique method for modeling one-dimensional, multiphase flow through layered media. Models that simulate flow of immiscible organic contaminants in groundwater are reviewed by Abriola (1988), Pankow and Cherry (1996) and Mercer et al. (1996). However, as Mercer et al. note "immiscible transport of NAPLs is highly sensitive to subsurface heterogeneities .... and the commonly available models are not well-equipped to accommodate their influence in multiphase flow". To avoid the difficulties inherent in most available models, our approach is to reduce the governing nonlinear, partial differential equation in time and space to a second-order,

ordinary differential equation by applying a finite difference approximation to the time derivative only. Then, for each time step, the resulting equation is solved as an initial boundary problem by the Runge-Kutta method. Using specified or assumed boundary conditions, the shooting method is used in an iterative manner to meet the specific boundary conditions at the other end of the flow regime. This approach differs from traditional finite difference or finite element models in the following ways: (1) a set of equations is solved explicitly and sequentially instead of simultaneously, (2) the spacing between nodes is varied within and between time steps based on accuracy criteria, and (3) the iteration process requires convergence of only one boundary condition value, rather than iterations being performed simultaneously on values associated wit all internal nodes. The second chapter in this section discusses the need for multiphase modeling, rather than Richards' equation, for simulations such as one-dimensional drainage, and the third chapter verifies the model by comparing simulations with laboratory data.

Section IV presents details of a two-dimensional pore scale model based on a modified diffusion limited aggregation algorithm. We also developed, as part of this project, an invasion percolation model to simulate pore scale processes in porous media, and predict macroscopic capillary pressure-saturation relations and relative hydraulic conductivity for strongly water-wetted systems at low capillary numbers. After completion of the percolation model, however, we revised our approach to pore scale modeling. One of the most stringent limitation on models based on percolation is that they are limited to low capillary numbers. Whereas this restriction is not significant for

LNAPLs, we felt it was too limiting for modeling dense non-aqueous phase liquids which exhibit unstable flow.

## 1.2 REFERENCES

Abriola, L.M. 1988. Multiphase flow and transport models for organic chemicals; A review and assessment, EPRI EA-5976, Research Report 2377-5, Palo Alto, CA.

Illangakesare, T., J.L. Ramsey, Jr., K.H. Jensen, M.B. Butts. 1995. Experimental study of movement and distribution of dense organic contaminants in heterogeneous aquifers. J. Contaminant Hydrology 20:1-25.

Kueper, B. and E.O. Frind. 1991. Two-phase flow in heterogeneous porous media, 1. Model development. Water Resources Research 27(6):1049-1057.

Mercer, J.W., Z. Adeel and C.R. Faust. 1996. A review of NAPL modeling approaches for remediation. In: Reddi, L.N. (ed.) Non-aqueous phase liquids (NAPLs) in subsurface environments: Assessment and remediation. ASCE, Washington, DC

Pankow, F. and J.A. Cherry. 1996. Dense chlorinated solvents and other DNAPLs in groundwater. Waterloo Press, Portland, OR

Pantazidou, M. and N. Sitar. Emplacement of non-aqueous phase liquids in the vadose zone, Water Resources Research 29(3):705-722.

## 1.3 ACKNOWLEDGMENTS

# SECTION II

# SECTION II

## Chapter 1

## EXPERIMENTAL STUDY OF ONE-DIMENSIONAL IMMISCIBLE FLUID DRAINAGE

## IN LAYERED SANDS

**Abstract**

Data that characterize transient flow of nonaqueous phase liquids in heterogeneous media are needed for verification of multiphase flow models. This paper summarizes three drainage experiments in layered sands performed specifically to provide such data. The layered system consists of a coarse sand between two finer sands. In all cases, water was the draining fluid. In the first experiment, air at atmospheric pressure was allowed to move freely into and out of the coarse sand layer. In the second experiment, air entry into the coarse layer was only possible through the overlying fine sand. These two experiments illustrated effects of nonwetting phase accessibility. In the third experiment, water was displaced by a light nonaqueous phase liquid. Both the effect of nonwetting phase access to the coarse material and the effect of a non-negligible viscosity were evident in this experiment. The three experiments represent a typical progression in multiphase model development. The layered system results in flow conditions that give many conventional models computational problems due to property discontinuities at layer interfaces.

## 1.1 INTRODUCTION

The scale at which subsurface heterogeneities can be characterized in a field situation is limited. However, a better understanding of how heterogeneities affect the transport and distribution of nonaqueous phase liquids (NAPLs) on a small scale leads to more accurate conceptualizations of site contamination, better interpretations of observed field data, and more realistic models. The conceptual model assumed for the distribution of a contaminant greatly affects the determination of important site characteristics such as rate of mass transfer by diffusion, mobility of a contaminant, the areal extent of contamination, and even the estimation of total mass present. Therefore, understanding small scale intricacies of NAPL transport is relevant to interpretation of field data and design of field scale remediation strategies.

In modeling transient, multiphase flow with conventional finite difference and finite element models, numerical instabilities and mass balance errors can occur if there are saturation discontinuities and/or large pressure gradients (Celia et al., 1990; Ségol, 1994). The problem is particularly acute when a sharp saturation front crosses the interface between two dissimilar soils. Nonetheless, the importance of adequately characterizing layered or otherwise heterogeneous media has been clearly shown in many experimental studies (e.g., Kueper and Frind, 1991; Pantazidou and Sitar, 1993; Illangasekare et al., 1995a, 1995b). The objective of this work was to provide simple laboratory data for model verification of two-phase flow in layered porous media.

## 1.2 MATERIALS AND METHODS

Experiments were conducted in a vertical column packed with fine sand from the bottom of the column to a height of 43 cm, a coarse sand from 43 to 57.5 cm, and fine sand again from 57.5 cm to 80 cm. Three experiments were conducted. In experiment one, water drained through the bottom of the column and was replaced with air that was allowed to freely enter and exit the column through ports at the top of the coarse sand layer. Valves allowing air entry were opened as soon as the water pressure in the coarse layer became less than atmospheric. In the second experiment, the air was again the displacing fluid but free access was not provided into and out of the column through the ports. The only pathway for the air was through the overlying finer layer. In the third experiment, a lighter-than-water nonaqueous phase liquid (LNAPL) was the displacing fluid.

The inside dimensions of the experimental column were 91 cm high, 15.3 cm wide and 5.6 cm thick. The front and back walls were constructed with 0.635 cm-thick glass. The side walls were aluminum. Twelve pressure ports were drilled into one side of the column, two each at six locations along the height of the column. Hydrophilic and hydrophobic pressure tensiometers (Noller, 1992) were installed at each of the six locations and connected to a data acquisition system.

Fluid saturations were measured using a dual-energy gamma attenuation system. Gamma attenuation theory and its application to multiphase flow problems in porous media are well documented in the literature, including discussions of the errors typically observed with gamma attenuation measurements (Eckberg and Sunada, 1984; Schiegg and McBride, 1987; Nofziger and Swartzendruber, 1974; Stroosnijder and DeSwart,

1974; Lenhard et al., 1988, 1991; Lenhard and Parker, 1988; Ferrand et al., 1986, 1989; Illangasekare et al., 1995b; Oostrom et al., 1995). Details of the system used in this study are given by Noller (1992).

The porous media used for this investigation were two different clean sands obtained from Colorado Silica Sand, Inc., Colorado Springs, Colorado. The finer sand is referred to as Colorado Springs Silica Sand (CSSS) #100 and the coarser sand is referred to as CSSS #40-60. Physical and hydraulic properties of the sands are shown in Table 1.1. Both Brooks-Corey (Brooks and Corey, 1966) and van Genuchten (van Genuchten, 1980) parameters were fit to water-air retention data for the two sands and are also given in Table 1.1. (The water retention curves and particle size distributions are included in Appendix A.) The column was packed following the raining method of Rad and Tumay (1985).

Table 1.1. Sand properties.

| | CSSS #100 | CSSS #40-60 |
|---|---|---|
| Mean Grain Diameter, $D_{50}$ (mm) | 0.16 | 0.27 |
| $D_{10}$ (mm) | 0.08 | 0.25 |
| $D_{90}$ (mm) | 0.30 | 0.30 |
| Uniformity Coefficient ($D_{60}/D_{10}$) | 2.18 | 1.12 |
| Brooks-Corey $P_d$ (cm of water) | 41 | 18 |
| Brooks-Corey $\lambda$ | 1.7 | 3.4 |
| van Genuchten n | 4.4 | 6.3 |
| van Genuchten $\alpha$ (cm of water)$^{-1}$ | 0.016 | 0.041 |
| Residual Water Saturation, $S_{wr}$ | 0.08 | 0.05 |
| Avg. Packed Porosity | 0.37 | 0.37 |
| Hydraulic Conductivity (cm s$^{-1}$) | 0.002 | 0.010 |

Distilled water was used as the wetting fluid in the column experiments. The nonwetting fluids were air and a 15:1 ratio by volume of Soltrol 220 and 1-iodododecane, $CH_3(CH_2)_9 I$. Soltrol 220 is a clear, isoparaffinic solvent manufactured by Phillips Petroleum Co., Bartlesville, Oklahoma. The presence of iodide increases the gamma attenuation by the Soltrol and enhances differences in the attenuation coefficients of the water and Soltrol (Lenhard et al., 1988). An organic dye, Sudan IV (Aldrich Chemical Co., Milwaukee, Wisconsin) was added to the Soltrol to allow visual differentiation between the LNAPL and the water phases. Properties of the Soltrol/iododecane/dye mixture are given in Table 1.2. Before each experiment, the soil column was flushed with $CO_2$ and then saturated with distilled water from the bottom at a rate of 3 ml/min. An initial wetting phase saturation of approximately 90% was obtained for all experiments.

Table 1.2. Fluid properties of water and Soltrol/iododecane/dye mixture (at 22°C).

|  | water | LNAPL |
|---|---|---|
| Density (g cm$^{-3}$) | 0.997 | 0.83 |
| Viscosity (centipoise) | 0.95 | 3.65 |
| Surface Tension (dynes cm$^{-1}$) | 70 | 28 |
| Interfacial Tension (dynes cm$^{-1}$) | N/A | 42[a] |
| Gamma Attenuation Coeff. (cm$^2$ g$^{-1}$) |  |  |
| $^{241}$Am | 0.205 | 0.508 |
| $^{137}$Cs | 0.092 | 0.088 |

[a] values decrease from 42 to 35 dynes cm$^{-1}$ with water contact. The model presented later used the initial value 42 dynes cm$^{-1}$.

## 1.3 EXPERIMENTAL PROCEDURES

*Experiment 1: Water drainage with "inviscid air" at atmospheric pressure.* A first step in multiphase model verification is to model an air-water flow problem assuming the air can move freely into and out of the flow domain with the pressure of the air everywhere atmospheric. In experiment 1, this scenario was simulated by providing an air inlet into the coarse layer. This was recently described by Marinelli (1996) as the more accurate view of the air phase in the Richards equation and not the same as assuming the air to be inviscid, i.e., having zero viscosity. The column was initially saturated with distilled water. At time t = 0, the water table was dropped instantaneously from just above the top of the soil to an elevation 10 cm below the bottom of the column. Thus, the boundary conditions for experiment 1 are a water pressure of -10 cm of water at the bottom of the column and atmospheric air pressure at the top of the column. Data were collected over 57 hours.

*Experiment 2: Water drainage with air.* In experiment 2, the initial and boundary conditions of experiment 1 were repeated. However, in this experiment, the air was not provided a free pathway into the middle layer. Air could only access the middle coarse layer through the overlying finer soil. This may be more realistic in a field situation and represents a progression in modeling difficulty. In this case, water at pressures less than atmospheric in the middle coarse layer will not drain until a pathway for the air through the finer overlying soil exists. Data were collected over 34 hours.

*Experiment 3: Water drainage with an LNAPL.* In experiment 3, an LNAPL was the displacing fluid. Again, the column was initially saturated with water, with a small ponded depth of water just above the top of the soil column. Approximately 5 cm

of LNAPL was added on top of the water. At time t = 0, the water table was dropped

instantaneously to an elevation 10 cm below the bottom of the column. The oil table was

maintained at 5 cm above the top of the column. Therefore, the boundary conditions for

this experiment were a water pressure of -10 cm of water at the bottom of the column,

and an oil pressure of 5 cm of oil at the top of the column.

Drainage was allowed to continue until the oil-water interface approached the

bottom of the column, and was stopped by changing the lower boundary pressure to 80

cm of water at time t = 375 minutes. The subsequent reimbibition of water was

monitored for 27 hours.

## 1.4 RESULTS AND DISCUSSION

Fluid saturations and outflow rates of the wetting fluid were recorded and yielded

good information. Pressure data was recorded for the water-air experiments but, due to

equipment failures, only limited pressure data was taken for the water-oil experiment.

Summaries of these data are presented here. The set of outflow and saturation data is

included in Appendix A.

Figure 1.1 shows wetting phase outflow rate versus time for the three

experiments. In both water-air drainage experiments, the coarse sand layer desaturated

while saturations in the upper sand layer were still quite high. The effect of this early

desaturation of the coarse layer is shown by an abrupt decrease in outflow rate in

experiments 1 and 2 between 50 and 80 minutes. When the coarse layer desaturated, the

relative permeability in that layer decreased significantly, retarding drainage of the water

from the overlying finer material. The low relative permeability in the coarse material and consequent reduction in drainage rate illustrate the mechanism behind capillary barriers.
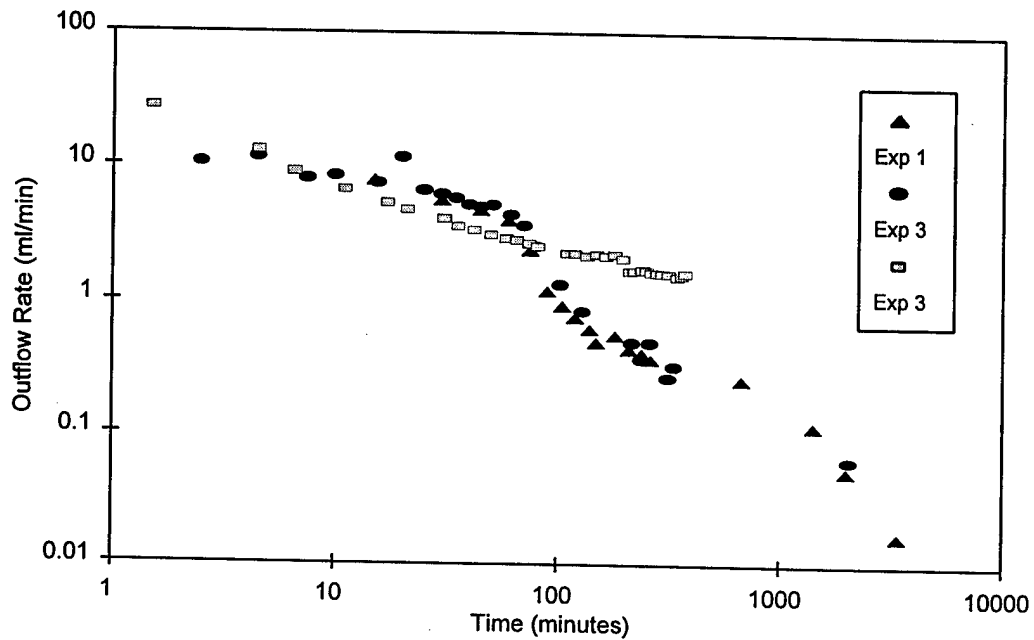


**Figure 1.1 Outflow rate with time for experiments 1, 2, and 3.**

The water pressure in the coarse layer can become less than atmospheric without desaturation of the pores if air entry is not permitted. If the middle layer stays saturated longer, the equivalent overall permeability will be larger for a longer time and a difference should be seen in the column outflow rate. Differences in the drainage rate between experiments 1 and 2 in figure 1.1 are not evident when plotted on the same curve as the water-LNAPL experiment data. This is because the viscosity of the air is about 50 times less than that of water, so when there is even a slight desaturation of the fine layer,

the air flows freely through the surface layer and the middle layer desaturates quickly.

The LNAPL has a viscosity four times larger than water so even when access is available for the nonwetting fluid, the coarse layer doesn't drain as quickly. Therefore, differences between the air and LNAPL nonwetting phases are much more evident in figure 1.1 than differences between the two air experiments. However, differences between experiments 1 and 2 can be seen by comparing saturation profiles and cumulative outflow from these two experiments. Figure 1.2 shows wetting phase saturations at the same time from the two water-air experiments, with higher saturations remaining in experiment 1. Figure 1.3 shows that cumulative outflow in experiment 1 lags behind cumulative outflow in experiment 2. As long as the coarse layer stays saturated, the wetting phase relative permeability in the coarse layer equals the saturated permeability for that layer. Drainage is slowed when the middle layer desaturates and permeability decreases. The cumulative outflow graph also clearly shows a change in slope for each of the water-air experiments. These slopes correspond to the drainage rate before and after the coarse layer desaturated.
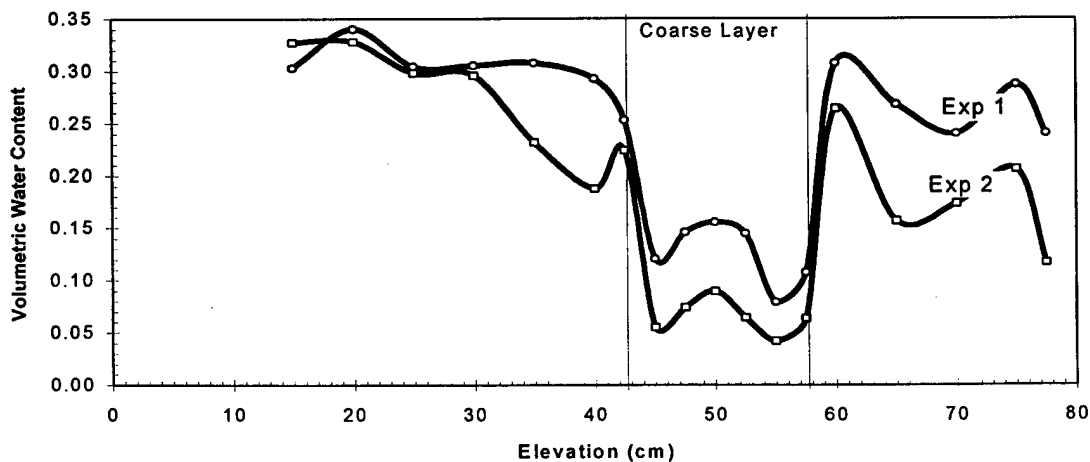


Figure 1.2. Volumetric water content with elevation for air experiments at 3.5 hours.

The water-LNAPL experiment shows effects both of accessibility and of a nonnegligible viscosity of the nonwetting phase. In experiment three, the LNAPL is not provided free access to the middle coarse layer and, in addition, the LNAPL viscosity is about four times larger than the water viscosity. The result is the water-LNAPL front moves from the top of the column downward at a relatively uniform rate. This is shown in figure 1.4. The middle layer cannot desaturate until the LNAPL has both access to the layer through the overlying fine soil and time to move into the coarser layer. The rate that the LNAPL can move through the fine layer to the coarse layer is dependent on the NAPL saturation in the fine layer. If the NAPL saturation is low, i.e., the fine layer has not drained significantly, the permeability of the NAPL in the top layer is small.
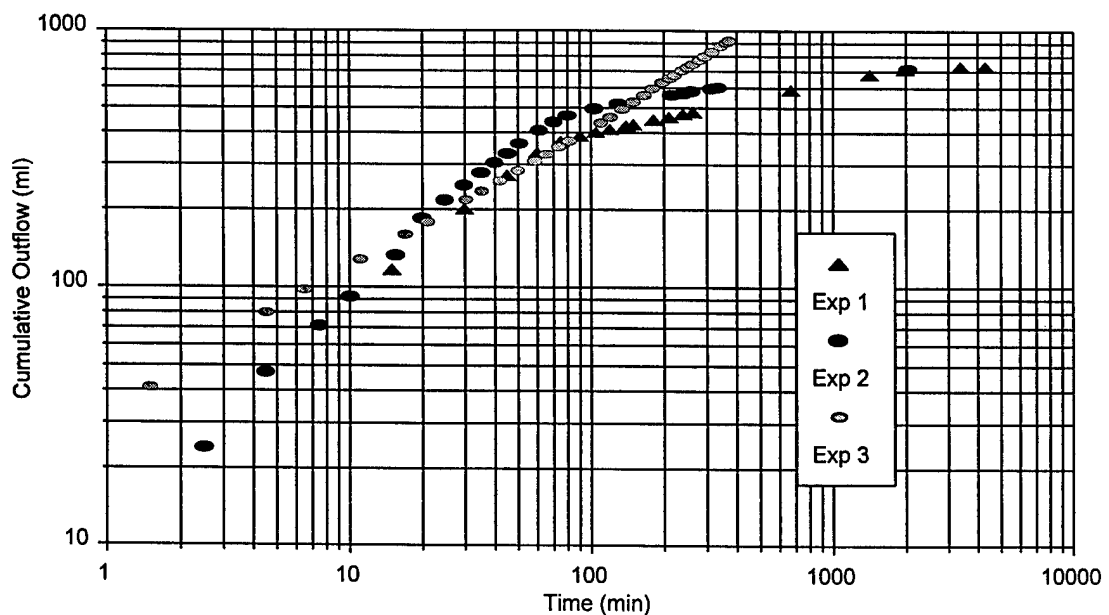
Figure 1.3. Cumulative outflow with time for experiments 1, 2, and 3.
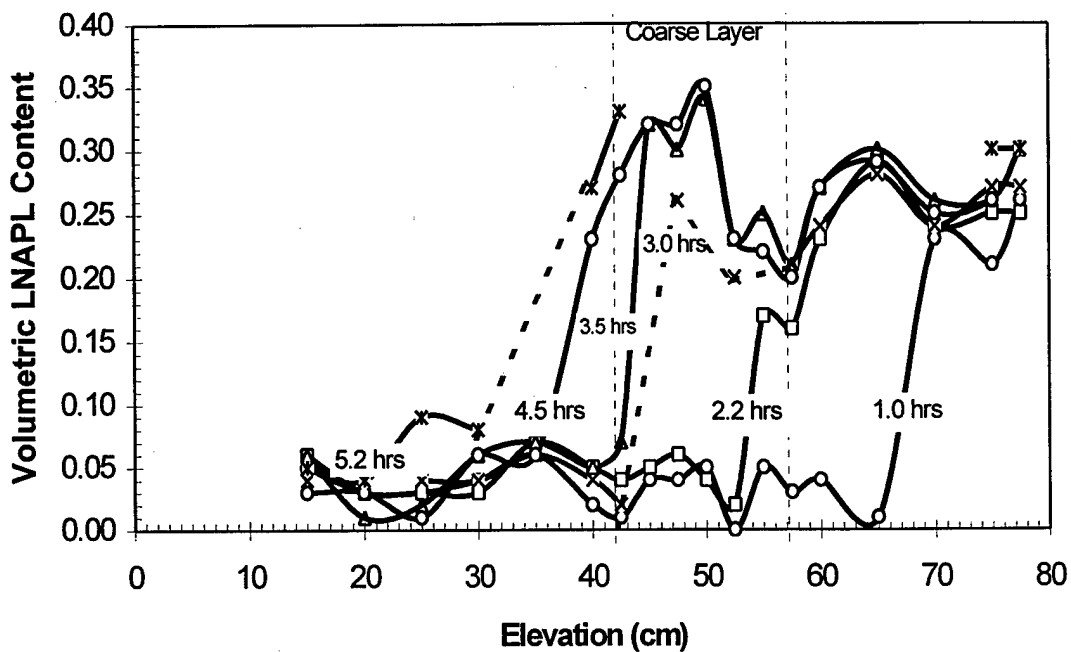
**Figure 1.4. Migration of the LNAPL front.**

There are some subtle features of the figures presented that are worth noting and lend credibility to the gamma data. In figure 1.4, the highest saturation of the LNAPL in the coarse layer is slightly higher than the saturation of the LNAPL in the overlying fine layer. This reflects a higher residual water content in the fine layer. In figure 1.3, there are slight changes in slope noticeable if early data and late data are compared for experiment 3. The higher slope on the cumulative outflow curve would be expected because relatively more of the column being drained at this time is coarse material with higher saturated permeability.

Another interesting feature is an abrupt decrease in outflow rate in experiment 3 at about 200 minutes. This is shown clearly in figure 1.5. From the saturation data (figure 1.4), it can be seen that the abrupt drop in outflow rate corresponds to the time when the water-LNAPL interface moved from the coarse layer into the lower fine layer. This effect is also captured, at least qualitatively, by the numerical modeling of this experiment also shown in figure 1.5. It should be noted that the model shown in figure 1.5 used the parameters presented in tables 1.1 and 1.2 with no calibration for a fit. For more information on the numerical model and a similar experiment the reader is referred to Marinelli (1996). The capillary pressure required for pore drainage is inversely related to pore size by the LaPlace equation of capillarity (Corey, 1994). When the interface moved into the fine layer, the pore size decreased and the capillary pressure had to increase before drainage could continue. Thus, the gradient also decreased, reducing outflow. Since the fluid-fluid front is sharp, the drop in outflow is also abrupt.

At time t = 375 minutes, drainage in experiment 3 was stopped by changing the lower boundary condition to a positive water pressure of 80 cm, i.e., raising the water table to the top of the column. This reversed the gradient and water reimbibed into the column, approaching an equilibrium distribution over the next 24 hours. Figure 1.6 shows saturations at time t = 33 hours. This figure shows high LNAPL contents just below the interface between the coarse and fine layers. This trapping of LNAPL below a finer layer has been observed in field studies (Vroblesky et al., 1995).
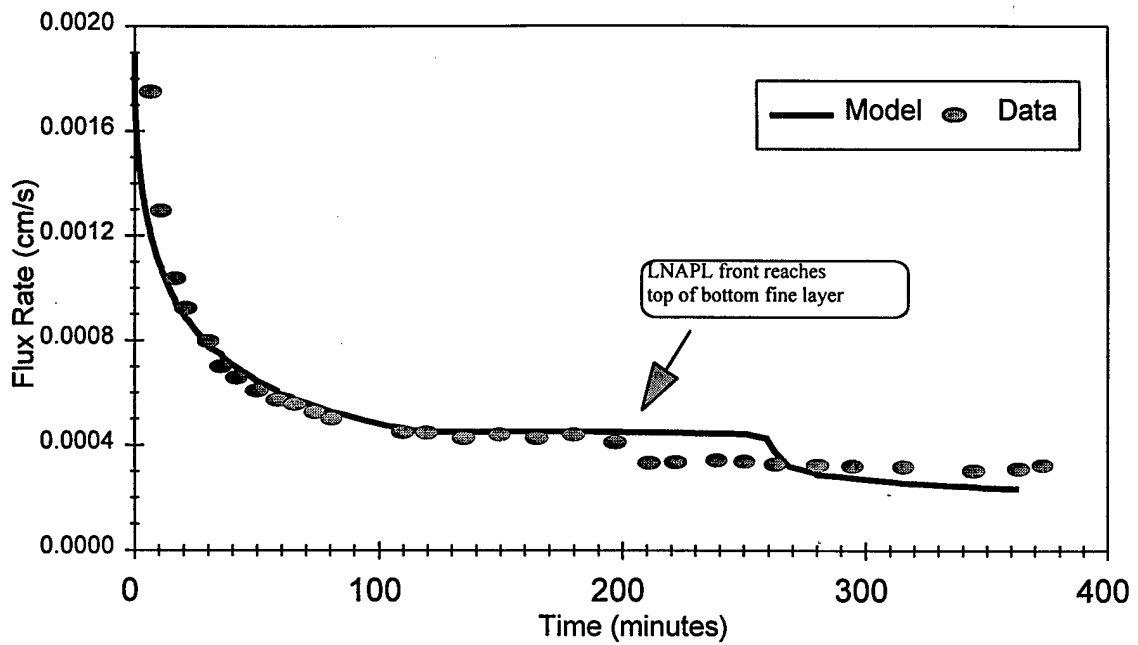
**Figure 1.5. Outflow rate for the LNAPL experiment showing an abrupt decrease at 200 minutes.**
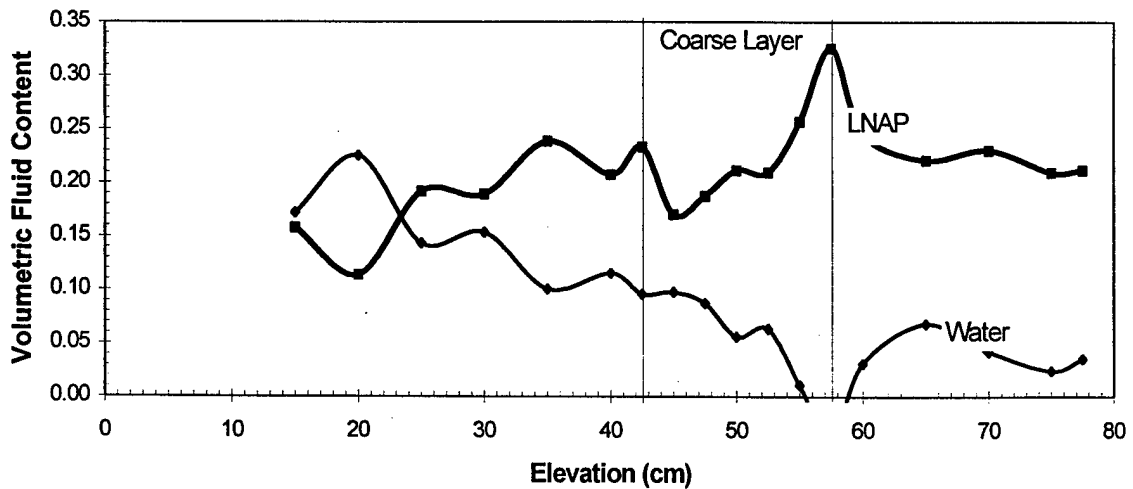


**Figure 1.6. Fluid contents at 33 hours, 27 hours after the water table was returned to the top of the column.**

## 1.5 CONCLUSIONS

The laboratory experiments presented in this paper provide data for drainage of immiscible fluids in layered soils. Soil layering results in discontinuities in saturations and permeabilities, effects that often create numerical difficulties in conventional finite difference and finite element models. The data acquired are sufficiently detailed to be useful for evaluation of two-phase flow models. Effects of soil layering, nonwetting phase access, and differences in those effects for air and LNAPL systems were observed.

## 1.6 REFERENCES

Brooks, R. H. and A. T. Corey. 1966. Properties of porous media affecting flow. *Journal of Irrigation and Drainage Div.*, ASCE, 92(IR2):61-68.

Celia, A. M., E.T. Bouloutas and R.L. Zarba. 1990. A general mass-conservation numerical solution for the unsaturated flow equation. *Water Resources Research.* 26(7):1483-1496.

Corey, A. T. 1994. *Mechanics of Immiscible Fluids in Porous Media.* Water Resources Publications, Littleton, CO, 252 pp.

Eckberg, D.K. and D.K. Sunada. 1984. Nonsteady three-phase immiscible fluid distribution in porous media. *Water Resources Research.* 20:1891-1897.

Ferrand, L.A., P.C.D. Milly, and G.F. Pinder. 1986. Dual-gamma attenuation for the determination of porous medium saturated with respect to three fluids. *Water Resources Research.* 22:1657-1663.

Ferrand, L.A., P.C.D. Milly, and G.F. Pinder. 1989. Experimental determination of three-fluid saturation profiles in porous media. *Journal of Contaminant Hydrology.* 4:373- 395.

Illangasekare, T.H., E.J. Armbruster III and D.N. Yates. 1995a. Nonaqueous-phase fluids in heterogeneous aquifers-experimental study. *Journal of Environmental Engineering.* ASCE. 121(8):571-579.

Illangasekare, T.H., J.L. Ramsey, Jr., K.H. Jensen, M.B. Butts. 1995b. Experimental study of movement and distribution of dense organic contaminants in heterogeneous aquifers. *Journal of Contaminant Hydrology.* 20:1-25.

Kueper, B. H. and E.O. Frind. 1991. Two-phase flow in heterogeneous media. 1. Model development. *Water Resources Research.* 27(6):1049-1057.

Lenhard, R.J., J.H. Dane, J.C. Parker, and J.J. Kaluarachchi. 1988. Measurement and simulation of one-dimensional transient three-phase flow for monotonic liquid drainage. *Water Resources Research.* 24:853-863.

Lenhard, R.J. and J.C. Parker. 1988. Experimental validation of the theory of extending two-phase saturation-pressure relations to three-fluid phase systems for monotonic drainage paths. *Water Resources Research.* 24:373-380.

Lenhard, R.J., J.C. Parker and J.J. Kaluarachchi. 1991. Comparing simulated and experimental hysteretic two-phase transient fluid flow phenomena. *Water Resources Research.* 27:2113-2124.

Marinelli, F. 1996. Semi-analytical solutions for one-dimensional flow of immiscible fluids in layered porous media. Ph.D. dissertation. Colorado State University, Fort Collins, CO. 124 pp.

Nofziger, D.L. and D. Swartzendruber. 1974. Material content of binary physical mixtures as measured with a dual-energy beam of gamma rays. *Journal of Applied Physics.* 45:5443-5449.

Noller, K.L. 1992. Calibration of a dual-beam gamma system to investigate multiphase equilibrium profiles in soil. Master's thesis. Colorado State University, Fort Collins, CO. 163 pp.

Oostrom, M., J.H. Dane, B.C. Missildine and R.J. Lenhard. 1995. Error analysis of dual-energy gamma radiation measurements. *Soil Science.* 160(1):28-42.

Pantazidou, M., and N. Sitar. 1993. Emplacement of nonaqueous-phase liquids in the vadose zone. *Water Resources Research.* 29(3):705-722.

Rad, N.S. and M. T. Tumay. 1985. Factors affecting sand specimen preparation by raining. *Geotechnical Testing Journal.* ASTM. 10(1):31-37.

Scheigg, H.O. and J.F. McBride. 1987. Laboratory setup to study two-dimensional multiphase flow in porous media. *Proceedings of the NWWA/API Conference on Petroleum Hydrocarbons and Organic Chemicals in Ground Water - Prevention, Detection and Restoration,* Houston, Texas. pp. 371-394.

Ségol, G. 1994. *Classic Groundwater Simulations*. Prentice-Hall, Inc., Englewood Cliffs, NJ.

Stroosnijder, L. and J.G. DeSwart. 1974. Column scanning with simultaneous use of Am 241 and Cs 137 gamma radiation. *Soil Science Journal.* 118(2):61-69.

Van Genuchten, M. Th. 1980. A closed-form equation for predicting the hydraulic conductivity of unsaturated soils. *Soil Science Society of America Journal.* 44:892-898.

Vroblesky, D.A., J.F. Robertson and L.D. Rhodes. 1995. Stratigraphic trapping of spilled jet fuel beneath the water table. *Ground Water Monitoring and Remediation.* 15(2):177-183.

Chapter 2

GEOMETRY OF NAPL MOUNDS IN WATER-NAPL SYSTEMS

**Abstract**

Nonaqueous-phase liquids (NAPLs) in the subsurface can be distributed in

mounds or pools of significant size and thickness, at relatively high NAPL saturations. A

depression in a fine textured heterogeneity is not required for this to occur. The

mechanics of immiscible fluids allow lateral stability even on perfectly flat or uniformly

sloped strata. This paper summarizes laboratory experiments performed to illustrate this

behavior and to verify an expression given to estimate the maximum height of a static

NAPL mound. It is shown that this analysis applies both to DNAPLs (denser-than-water

NAPLs) on top of heterogeneities and to air and LNAPLs (lighter-than-water NAPLs)

trapped below the water table beneath heterogeneities. It is also shown that this behavior

cannot be explained without considering the hysteresis in capillary pressure-saturation

relationships. Models not incorporating this hysteresis may result in incorrect

simulations of the migration and distribution of NAPLs in the subsurface.

## 2.1 INTRODUCTION

The behavior of NAPLs in the subsurface has been the subject of much research

in recent years. Groundwater contamination from NAPLs such as gasoline and

chlorinated solvents is a widespread problem. An understanding of the principles

involved with NAPLs in groundwater is necessary for accurate assessment and effective remediation of these sites.

The transport and distribution of NAPLs is strongly affected by subsurface heterogeneities. Although the detail to which subsurface heterogeneities can be characterized in the field is limited, a better understanding of how these heterogeneities affect NAPL distribution should lead to more accurate conceptualizations of site contamination, better interpretations of observed field data, and more realistic models. The conceptual model assumed for the distribution of a free-phase contaminant greatly affects the estimation of important site characteristics such as the rate of mass transfer by diffusion or dissolution, the mobility of the contaminant, and the areal extent of a contaminant.

Pools or mounds of denser-than-water NAPLs (DNAPLs) commonly occur on low permeability lenses or strata in the subsurface. The trapping of lighter-than-water NAPLs (LNAPLs) under lenses below the water table has also been observed with jet fuel (Vroblesky et al., 1995) and with air from air sparging (Lundegard and Anderson, 1996). Depressions in low permeability lenses are not required for NAPL pools of significant size to form, they can form on flat lenses and even in homogeneous material (Keuper et al., 1993). Understanding the behavior and distribution of these pools contributes to the characterization and remediation of the numerous DNAPL contaminated sites.

McWhorter and Kueper (1996) and Kueper et al. (1993) explain how the mechanics involved with NAPL pools can be used to interpret observed DNAPL thicknesses in monitoring wells, and to estimate the thickness and volume of DNAPL

pools. Lundegard and Anderson (1996) discuss air mounding beneath lenses during air sparging. They mention this mounding can lead to complex air flow patterns and can greatly increase lateral groundwater displacement. This exaggerated displacement under heterogeneous conditions casts doubt on its use as an indicator of the air sparging radius-of-influence. They conclude that under heterogeneous conditions, detailed knowledge of site stratigraphy and sediment properties is necessary to predict the flow response of air injection. Accurately estimating the extent of air trapped under lenses could improve these predictions.

The objectives of this study were 1) to predict the maximum thickness of laterally stable NAPL mounds by accounting for hysteresis in the capillary pressure-saturation (Pc-S) relationships, 2) to extend this analysis to LNAPL and air mounds trapped beneath low permeability lenses, and 3) to provide laboratory verification of the predictive equations of this immiscible fluid behavior. It is shown that the phenomena of static NAPL mounds on subsurface heterogeneities cannot be fully explained without considering hysteresis.

## 2.2 CAPILLARY PRESSURE-SATURATION RELATIONSHIPS

In most aquifer materials, NAPLs are nonwetting with respect to water, meaning water has the greater attraction to the matrix. Combined with a non-zero interfacial tension between two immiscible fluids, this enables a pressure difference to be supported in porous media (Corey, 1994). This pressure difference is termed the capillary pressure and is defined as the nonwetting fluid pressure minus the wetting fluid pressure. If the capillary pressure is increased, the nonwetting fluid (the NAPL or air) can displace water

from the matrix. Figure 2.1 shows a typical relationship between capillary pressure and NAPL-water saturation for a volume of porous media.

The nonwetting phase entry pressure of a porous medium refers to the capillary pressure below which little or no desaturation of the water occurs (Corey, 1994). Above this pressure, the water in some pores begins to be displaced by the nonwetting phase, and saturation decreases rapidly along the primary drainage curve, eventually approaching an irreducible or residual level of water saturation. If the capillary pressure is then decreased, the water will begin to reimbibe into the media. However, hysteresis is exhibited in the capillary pressure-saturation (Pc-S) relationship. As the water reimbibes from a residual saturation, the saturation increases along a secondary curve, termed the primary wetting or imbition curve. As the capillary pressure goes to zero, not all the nonwetting fluid is displaced, leaving a trapped or residual nonwetting phase.
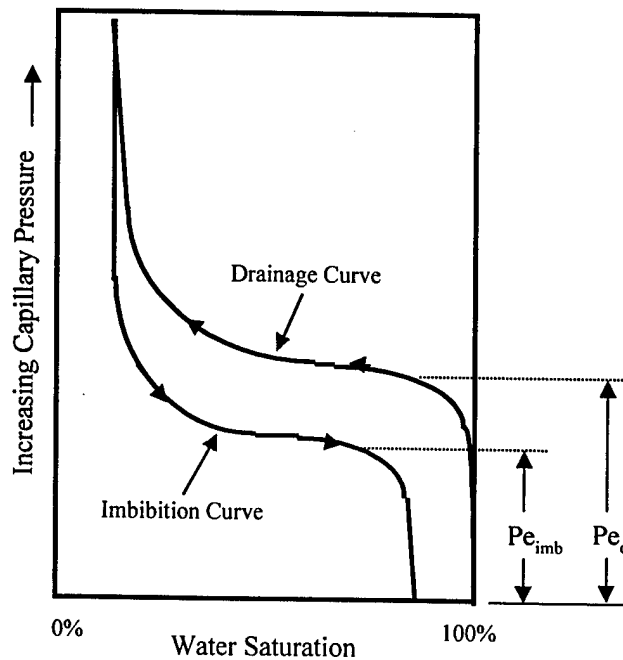


Figure 2.1. A typical relationship between capillary pressure and fluid saturation in a volume of porous media, illustrating the hysteresis exhibited between drainage and imbition curves.

Although much less used and documented in the literature, the imbibition curve of the Pc-S relationship often exhibits an inflection point roughly analogous to entry pressure of the drainage curve (Baker and Hillel, 1990; Liu et al., 1993; Hogarth et al., 1988). Below this point, water saturation changes only slightly with decreasing capillary pressure. Particularly in a uniform sand, it is near this pressure that NAPL saturations dramatically decrease and water saturations increase with decreasing capillary pressures. This inflection point is referred to here as the imbibition entry pressure.

## 2.3 THEORY OF NAPL MOUND FORMATION

DNAPLs that are spilled or leaked into the subsurface move through the vadose zone under the influence of gravity and capillary forces. If sufficient volume is spilled a DNAPL will reach and penetrate the water table. Depending on the volume and rate of the spill, when a DNAPL migrating downward below the water table encounters a fine lens, it can begin to pool, mound up, and spread across the lens. Once the source of the DNAPL spill is exhausted, the mound height will decrease as the DNAPL spreads laterally. However, as asserted by Kueper et al. (1993), a mound will not spread indefinitely, even on a flat lens. The lateral spreading of a NAPL collecting and mounding on even a flat lens will stop when the mound height has decreased to a point where there is no longer sufficient capillary pressure at the advancing edge to overcome the entry pressure of the aquifer material. The maximum thickness of this NAPL mound is dependent on the density difference of the two fluids and the entry pressure of the surrounding matrix. These parameters can lead to significant volumes of NAPL associated with heterogeneities.

Figure 2.2 shows the hydrostatic pressure distribution in a DNAPL mound. Since the DNAPL is denser than water, its pressure increases faster with depth than the water pressure. Therefore, the capillary pressure increases with depth to a maximum at the bottom of the mound. In a similar analysis, Kueper et al. (1993) and McWhorter and Kueper (1996) explain that for the mound to remain stationary, the capillary pressure at the bottom of the mound has to be equal to or less than the entry pressure of the aquitard material upon which it is perched. This is used to estimate the maximum pool thickness before penetration into the aquitard. However, for the point of incipient lateral motion, the capillary pressure at the bottom leading edge of the mound (point 1) is equal to the entry pressure of the surrounding media.
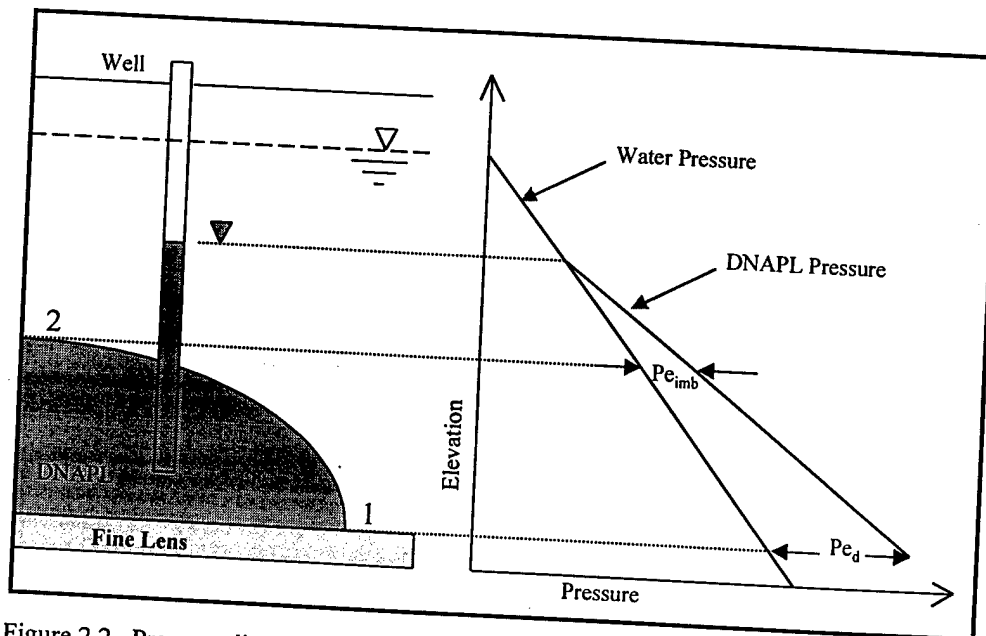


Figure 2.2. Pressure distribution in a static DNAPL mound perched on a fine textured lens in saturated porous media. $Pe_d$ denotes the water drainage entry pressure and $Pe_{imb}$ the water imbibition entry pressure of the media.

From this analysis the capillary pressure at all fluid-fluid interfaces must be less than the nonwetting phase entry pressure of the media except at the bottom of the mound. This would seem to imply that reinvasion of the water would occur and therefore the DNAPL could not exist in mounds. This is resolved by considering the hysteresis in the Pc-S relationships. The top of the DNAPL mound (Point 2 in Figure 2.2) would be receding, i.e., DNAPL draining from the pores. Therefore, the saturations at the top would be given by the secondary Pc-S curve, the water imbibition curve, if we assume the water in the DNAPL invaded zone had decreased close to residual contents. This would allow high DNAPL saturations to remain at low capillary pressures. The upper boundary of the mound, where DNAPL contents rapidly decrease from high to residual saturations, would correspond to the point where the capillary pressure is equal to the imbibition entry pressure of the surrounding media.

This analysis leads to a simple expression for the maximum mound thickness:

$$T_{max} = \frac{Pe_d - Pe_{imb}}{\Delta \rho g} \tag{1}$$

where $Pe_d$ is the water-NAPL drainage entry pressure of the aquifer media, $Pe_{imb}$ is the water-NAPL imbibition entry pressure of the media, $\Delta \rho$ is the density difference between the DNAPL and water, and g is gravity. This is similar to equations given by Kueper et al. (1993) and McWhorter and Kueper (1996) with two differences for this application. First, they use the entry pressure of the underlying material in the expression to give the maximum height before downward DNAPL penetration into the aquitard. Here the entry pressure of the surrounding aquifer material is used to find the smaller height that must be reached for lateral stability.

The second difference in these expressions is the capillary pressure assumed for the top of the mound. Kueper et al. (1993) and McWhorter and Kueper (1996) both discuss the potential water imbibition conditions above a mound, but approximate the capillary pressure as close to zero for the top of a pool height. More specifically, McWhorter and Kueper (1996) state that the upper surface of the *connected* DNAPL lies where the capillary pressure is zero. That is probably the best assumption for media with a wide distribution of pore sizes, where significant connected DNAPL saturations could remain well below the imbibition entry pressure, and/or where the media might not exhibit a distinct imbibition entry pressure. However, in media with a uniform narrow pore size distribution, the upper boundary of high DNAPL saturation can only correspond to the imbibition entry pressure. That is the value that should be used in the expression to estimate the maximum static thickness on a horizontal lens. It will be shown later that using a capillary pressure of zero for the top of the mound, instead of the imbibition entry pressure, could overestimate the thickness by 2.5 times in certain porous media.

The mechanics described above for DNAPL mounds should also apply to static LNAPL or air mounds trapped under low permeability lenses below the water table. Figure 2.3 shows the hydrostatic distribution of pressures for this case. Since LNAPLs are less dense than water, the capillary pressure would increase with elevation to a maximum at the top. Again, the advancing edge at the top of the mound would be at the drainage entry pressure of the media while the bottom receding boundary of LNAPL saturations correspond to pressures on the water imbibiton curve.
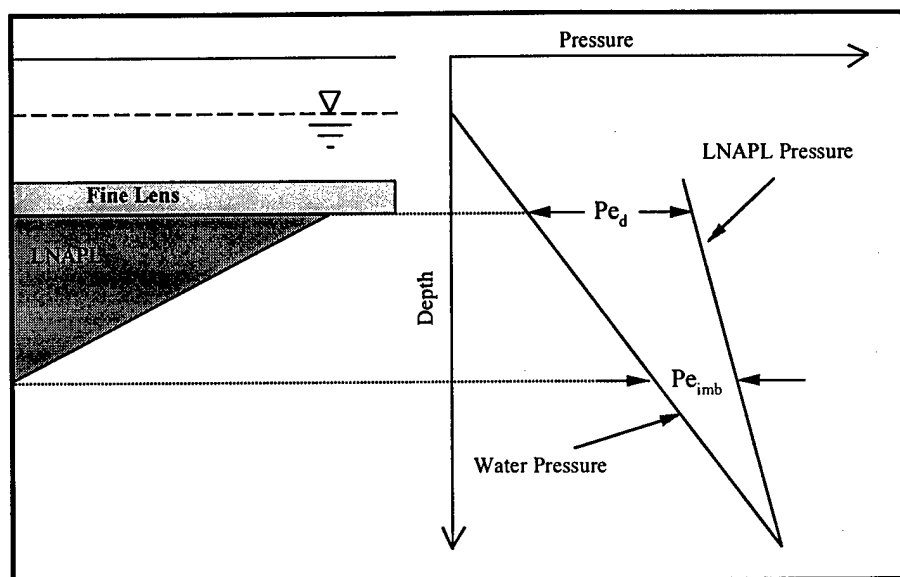
Figure 2.3 Pressure distribution in a static LNAPL mound trapped below the water table beneath a fine textured lens.

Note that this analysis is for a static mound on a hypothetical flat fine soil layer. It does not explain the thickness, and thus the aquitard penetrating head, that could build up during dynamic flow conditions or in a low lying depression. Also, it only predicts a maximum thickness, assuming the NAPL volume and infiltration dynamics were sufficient to reach it. Of course, a flat heterogeneity is not necessary for this analysis. The mechanics also predict the additional thickness supported above and in addition to DNAPL pooled in a depression. Then, this analysis would predict the thickness supported above the highest point of a depression in a fine lens.

It should also be noted that this analysis is for a material with a non-zero entry pressure, i.e., one that exhibits a Brooks-Corey Pc-S relationship (Corey, 1994). Macropores may exist that cannot provide the necessary capillary resistance for a static mound of significant size. A van Genuchten Pc-S relationship (van Genuchten, 1980)

assumes a connected NAPL and some saturation at all capillary pressures. However, even if a van Genuchten porous media permits some flow of the NAPL below the entry pressure, the relative permeability of the NAPL would typically be so low that the difference in mound thickness is insignificant or only manifests itself after a very long time.

This analysis has implications for NAPL remobilization since a mound at a maximum stable thickness would clearly be at the point of incipient motion. First, the entry pressure is directly proportional to the interfacial tension between the two fluids. Therefore, a lowering of the interfacial tension, through surfactant flushing for example, could cause the NAPL to again become mobile. Second, the hydrostatics show that although the maximum mound thickness is independent of its depth below the water table, changes in gradients of water pressure have the potential to remobilize the NAPL mound. Indeed, there have been field cases in which DNAPL that had been static for decades mobilized in significant volumes, entering wells intended only for pumping and treating the aqueous phase. Groundwater pumping in a contaminated zone could cause NAPL migration around a previously perching lens and deeper into the aquifer. The hydrostatics also show a possible benefit of mass removal. Removing NAPL from pools and mounds would likely reduce their potential for remobilization and redistribution.

## 2.4 EXAMPLES OF THE MAXIMUM THICKNESS OF NAPL MOUNDS

The above analysis illustrates the role of hysteresis in the behavior of NAPLs in porous media, and how that behavior enables a mound of significant size to remain static.

For illustration, table 2.1 contains predicted maximum mound thicknesses for various

NAPLs and air in a hypothetical fine and medium sand. For the fine sand, an air-water

drainage entry pressure of 70 cm of water (6860 Pa) and an air-water imbibition entry

pressure of 42 cm of water (4116 Pa) was used. For the medium sand, the drainage and

imbibition air-water entry pressures were assumed to be 20 cm of water (1960 Pa) and 12

cm of water (1176 Pa), respectively. The NAPL-water entry pressures were calculated by

scaling the air-water entry pressures by the ratio of interfacial tension between the two

fluids (Lenhard and Parker, 1987). Imbibition entry pressures are often estimated as one-

half of the drainage entry pressure. However, in the experiments presented later a

$Pe_{imb}/Pe_d$ ratio of 0.6 was measured, and that ratio is used in these examples. Note that

from this ratio it follows that if $Pc = 0$ is assumed for the upper mound boundary instead

of $Pc = Pe_{imb}$, equation (1) would predict a maximum mound thickness 2.5 times greater.

**Table 2.1.** Examples of the maximum thickness of laterally stable NAPL mounds in medium and fine grained sand (air-water entry pressures of 20 and 70 cm of water (1960 and 6860 Pa), respectively).

| Fluid | Density | Interfacial Tension | Thickness in Medium Sand | Thickness in Fine Sand |
|-------|---------|---------------------|--------------------------|------------------------|
| | $(g\ cm^{-3})$ | $(dynes\ cm^{-1})$ | $(cm)$ | $(cm)$ |
| Trichloroethylene | 1.47 | 35 | 8.3 | 29.0 |
| Tetrachloroethylene | 1.63 | 44 | 7.8 | 27.2 |
| 1,1,1-Trichloroethane | 1.35 | 45 | 14.3 | 50.0 |
| 1,2-Dichloroethane | 1.26 | 30 | 12.8 | 44.9 |
| Air | $\approx 0$ | 72 | 8.0 | 28.0 |
| Gasoline | 0.73 | 50 | 20.6 | 72.0 |
| Benzene | 0.87 | 35 | 29.9 | 104.7 |
| Jet Fuel | 0.82 | 50 | 30.9 | 108.0 |
| Creosote | 1.03 | 20 | 74.1 | 259.3 |

## 2.5 LABORATORY VERIFICATION

### Equipment

Laboratory experiments were performed to verify equation (1), and to gain insight into the configuration the mounds would exhibit. Experiments were conducted in two thin glass flumes (one with interior dimensions 105 x 63 x 1 cm and the second with interior dimensions 90 x 110 x 1 cm) in conjunction with a light attenuation system. (Glass et al., 1989; Tidwell and Glass, 1994). Light attenuation measurements take advantage of the fact that the intensity of light transmitted through a thin slab of silica sand is strongly affected by the fluid saturation. The thin flumes were illuminated from behind and images captured using an analog ccd camera with a high accuracy monochrome frame grabber. This method allows fluid content observations to be based on an average over the entire thickness of the experimental cell, reducing the influence of occasionally significant edge effects.

### Materials

Two sizes (20/30 mesh and 30/40 mesh) of Ottawa sand were sieved from U.S. Silica Sand #14 (U.S. Silica Sand, Ottawa, IL) and used in the experiments. Sand 20/30 was used in experiments 1 and 3 and sand 30/40 was used in experiments 2 and 4. The air-water entry pressures for the sands were measured in the same experiment flumes under identical packing conditions by measuring the height of the capillary fringe both at equilibrium drainage and imbibition conditions. These are given in table 2.2 along with

the hydraulic conductivities of the sands.  U.S. Silica Sand #F95 (median grain size 150 μm) was used for the fine confining layer in all experiments.

A perfluorocarbon, product name Performance Fluid™ 5070 (PF-5070, 3M Specialty Chemicals, St. Paul, MN), was used for the DNAPL in experiments 1 and 2.  It was selected since it is a non-toxic fluid with physical properties similar to tetrachloroethylene (described in Chapter 3).  Soltrol® 220 (Phillips Petroleum Co., Bartlesville, OK), a hydrocarbon commonly used in LNAPL experiments, was used in experiments 3 and 4.  The relevant properties of these fluids are given in table 2.3.

Table 2.2.  Sand Properties.

|  | 20/ 30 Sand | 30/40 Sand |
|---|---|---|
| $Pe_d$  (cm of water) | 15.0 | 21.0 |
| $Pe_{imb}$ (cm of water) | 8.9 | 13.0 |
| Hydraulic Conductivity  (cm s$^{-1}$) | 0.10 | 0.06 |

Table 2.3.  Fluid Properties.

|  | PF-5070 | Soltrol 220 |
|---|---|---|
| Density    (g cm$^{-3}$) | 1.73 | 0.79 |
| Viscosity  (centipoise) | 0.95 | 3.65 |
| Interfacial Tension (dynes cm$^{-1}$)[a] | 50.5 | 35.2 |

[a] interfacial tension measured with fluids dyed and at an equilibrium value after contact with water in the experimental flume.  The water surface tension after being in contact with the sand was measured to be approximately 68 dynes cm $^{-1}$.

**Experimental Procedure**

Two DNAPL experiments (1 and 2) were performed where DNAPL was introduced above a low permeability layer from a well.  A schematic of the experiments is shown in figure 2.4.  A 10 cm fine sand layer was placed at the bottom of the flume.

Air dry sand was then slowly "rained" in, simultaneously across the entire flume length, using a rectangular funnel and coarse screens to randomize the motion of the sand grains. This method achieved a very uniform packing with an approximate bulk density of 1.7 g cm$^{-3}$. $CO_2$ was flushed through the flume to displace the air in the pore space in order to attain a high water saturation. The flume was then slowly filled with deionized water dyed with FD&C Red #40 at 0.5 ml per 100 ml of water and FD&C Dyes Yellow #5 and Blue #1 each at 0.05 ml per 100 ml water. The DNAPL used in these experiments, PF-5070, has a very low solvency and cannot be dyed. Therefore, this dye mixture was necessary to minimize light transmission through the water phase to allow observation of the DNAPL mound.
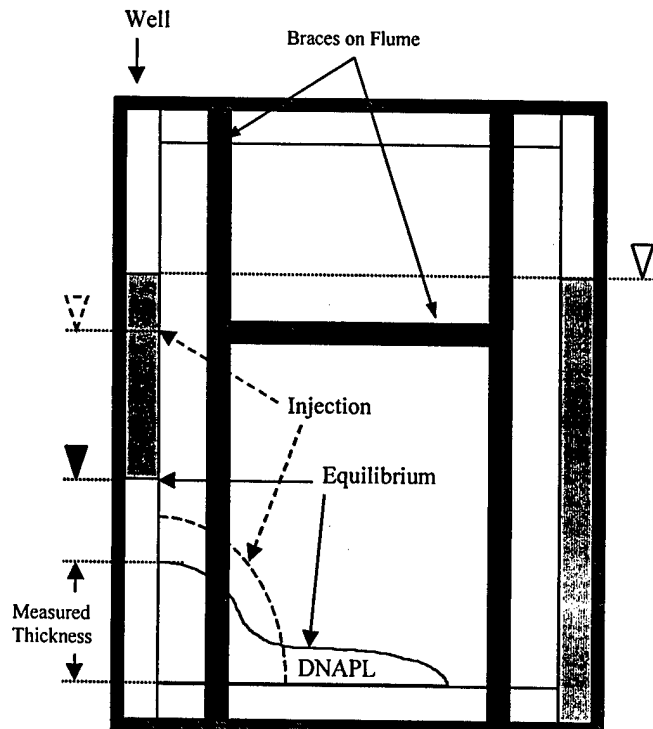


Figure 2.4. Schematic of experiments showing how NAPL was injected through the well and the subsequent redistribution of the NAPL mound.

A well ( 3 x 1 cm rectangular cross section) was located at the left of the flume for DNAPL injection and to monitor the capillary pressure during the experiment. The PF-5070 was injected into the media through the screened well by maintaining a well thickness, and thus a capillary pressure, above the entry pressure of the media. This method allowed a mound height exceeding the predicted maximum thickness to be injected while minimizing lateral spreading across the limited length of the experimental flume. By injecting at a boundary this method also produces a line of symmetry, enabling one half of a larger symmetric mound to be observed in the small cell.

Once a mound of sufficient height was in place, injection was slowed by decreasing the DNAPL head in the well, but still leaving it above the predicted final well thickness to allow it to equilibrate on its own. The capillary pressure and the mound height were then monitored for several days, and in one case for several weeks, to assure that the mound had assumed a stable configuration.

The above procedure was repeated in experiments 3 and 4 with Soltrol 220, dyed with 0.5 % by weight Sudan IV organic dye (Aldrich Chemical Co., Milwaukee, WI). In these experiments, a confining layer was placed across the top of the media. Similar to the procedure in the DNAPL experiment, a slug of the LNAPL was injected into the media along the well and under the confining layer. The capillary pressures and inverted mound height were monitored over several days and exhibited behavior similar to that of the DNAPL experiments.

## 2.6 RESULTS

The measured and predicted maximum mound heights for all experiments are given in table 2.4, along with the equilibrium capillary pressures at the leading edge of the mounds. Figure 2.5 shows this same information on a graph. The values predicted using equation (1) correspond well to the measured values in all experiments. The error between predicted and measured values is well within the measurement error of the input parameters. Figures 2.6 and 2.7 are photographs of the NAPL mounds in experiments 2 and 4 respectively.

The NAPL mounds in these experiments all approached a static equilibrium relatively quickly. Figure 2.8 shows the predicted and measured DNAPL mound height with time along with the approximate capillary pressure at the mound leading edge for experiment 1. Experiment 1 shows an additional DNAPL injection at 50 hours. This was done to assure that the maximum mound thickness had been exceeded. The DNAPL level in the well was used to determine the capillary pressure at the bottom leading edge of the mound. This calculation was made assuming the mound was at equilibrium, i.e., no horizontal pressure gradients. These measurements confirmed that the mound did stop at the oil-water drainage entry pressure of the media. The LNAPL mounds took slightly longer to reach a static equilibrium, due to a higher viscosity and smaller density difference, but exhibited behavior similar to that of the DNAPL experiments. These plots for experiments 2, 3, and 4 are included in Appendix B.

**Table 2.4.** Maximum NAPL mound thickness in laboratory experiments compared to values predicted assuming both the capillary pressure (Pc) at the top of the mound to be equal to zero and to the imbibition entry pressure (Pe$_{imb}$). Also shown is the capillary pressure at the leading edge of the mound compared to the predicted oil-water entry pressure of the media.

| | Predicted using Pc = 0 | Predicted using Pc = Pe$_{imb}$ | Measured |
|---|---|---|---|
| **Mound Thickness** (cm) | | | |
| Exp. 1 | 15.2 | 6.2 | 8.0 |
| Exp. 2 | 21.4 | 8.1 | 7.5 |
| Exp. 3 | 37.0 | 15.0 | 16.5 |
| Exp. 4 | 51.8 | 20.3 | 17.5 |
| **Equil. Cap. Press.** (cm of water) | | | |
| Exp. 1 | | 11.1 | 11.4 |
| Exp. 2 | | 15.6 | 14.3 |
| Exp. 3 | | 7.8 | 8.4 |
| Exp. 4 | | 10.8 | 11.5 |
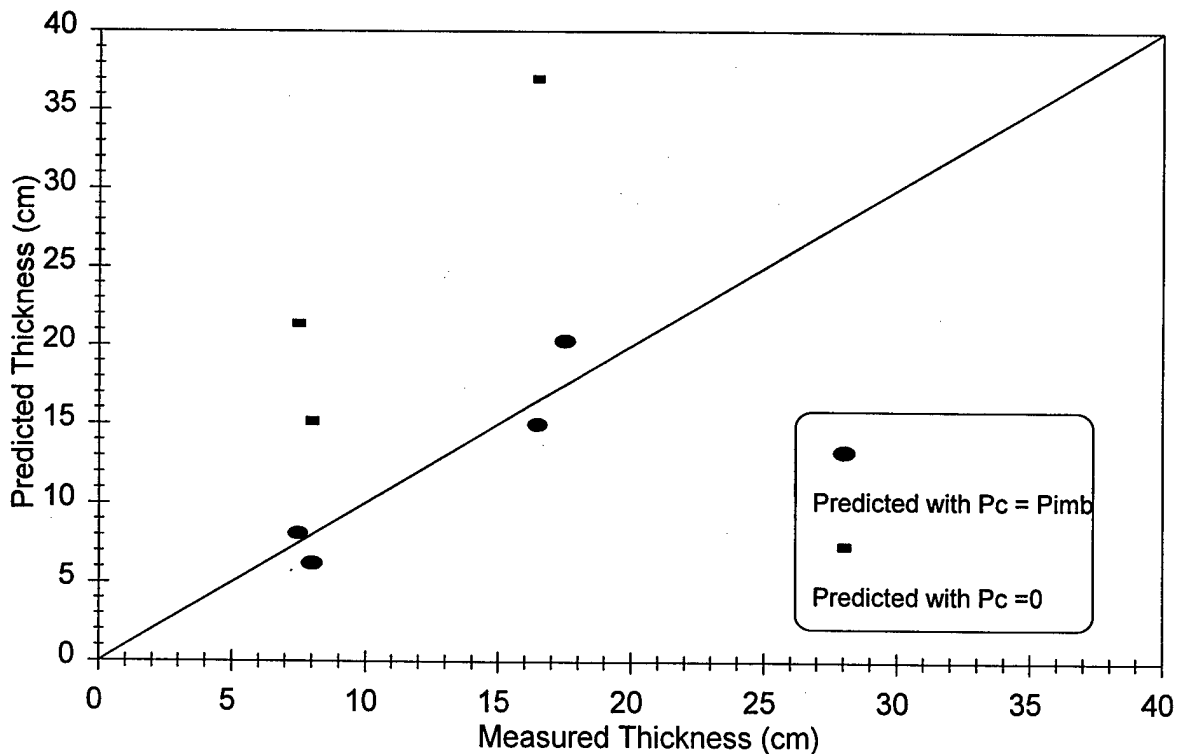


Figure 2.5. Plot comparing measured maximum mound thicknesses with predictions based both on assuming the top of the mound occurs at a capillary pressure equal to zero and equal to the imbibition entry pressure.
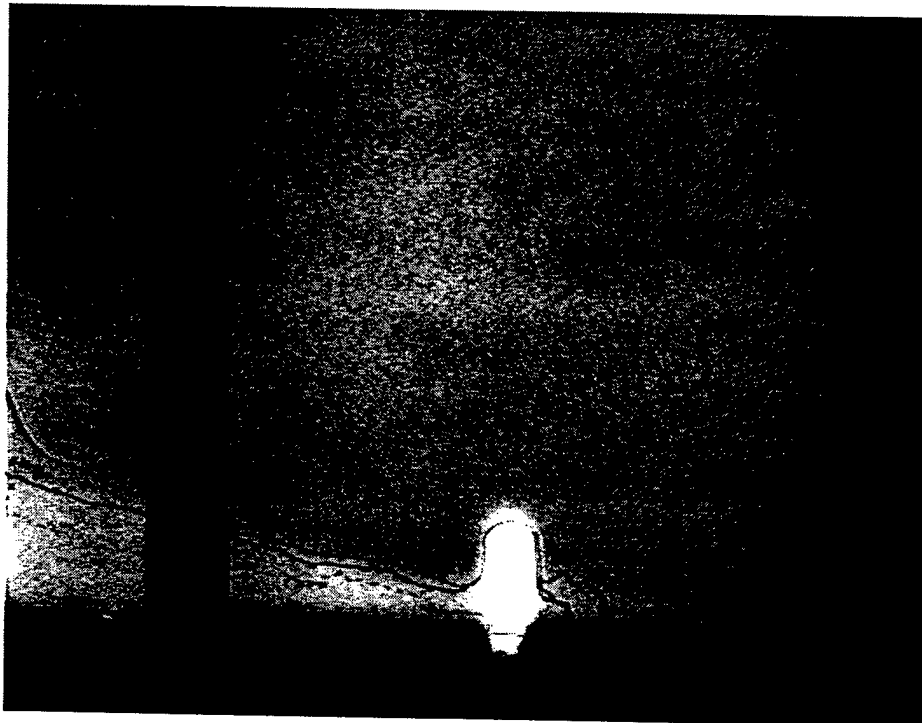
Figure 2.6 Photograph of DNAPL mound (light area at bottom left) in experiment 1 after 5 days.
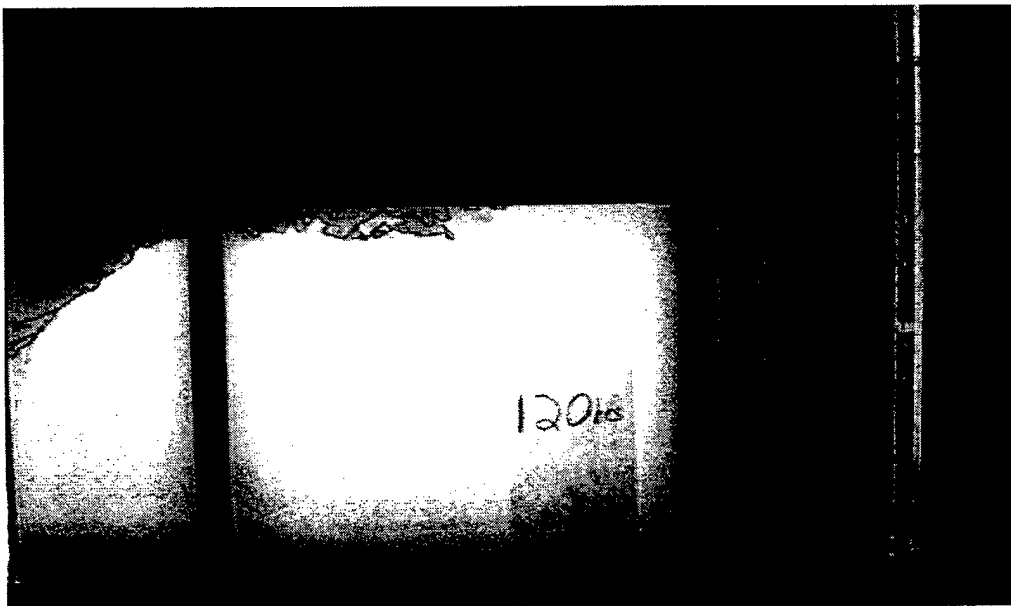
Figure 2.7. Photograph of LNAPL mound (dark area) in experiment 4 after 120 hours.
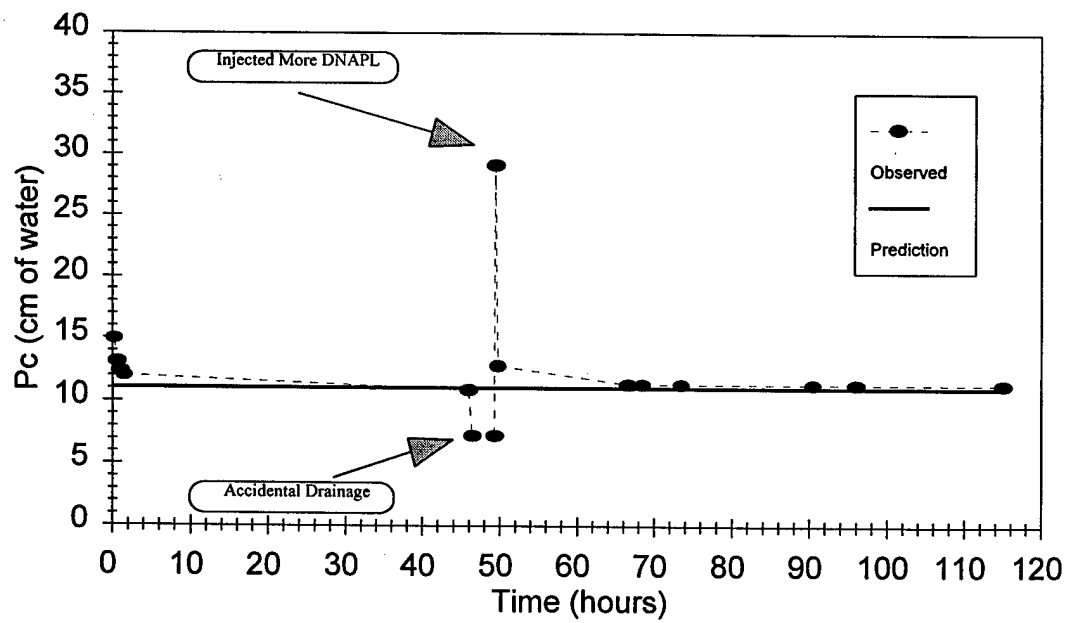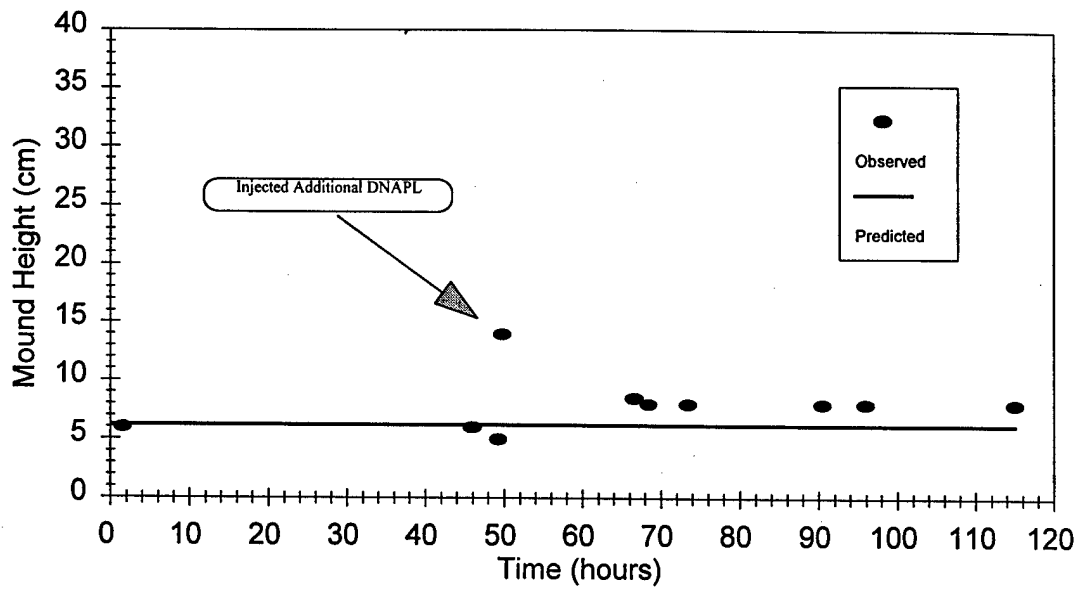
Figure 2.8. Predicted and measured DNAPL mound height with time along with the capillary pressure at the mound leading edge for experiment 1.

Although equilibrium was approached rapidly and a stable mound was created in these experiments, it should be noted that this was not the case in experiments where the sand contained small cracks or heterogeneities of coarse sand. It these cases, the mound still rapidly approached the predicted height, but continued to slowly decrease as the NAPL moved along and filled the crack. If this pathway of low entry pressure led to the opposite well, the media never had the capillary resistance to support a significant pressure, and the mound height continued to diminish as it filled the well. This would also occur in homogeneous media when the advancing mound intersected the opposite well due to having too much volume injected. Once this pathway of NAPL had been established across the media boundary, the NAPL always seemed to be able to flow into the opposite well, even after the mound reached and fell below the entry pressure of the media. One experiment involving air was attempted and also showed these effects. The air did mound under the lens, but easily found or even formed cracks in the sand that allowed its escape. The significance of these effects were dependent mainly on the spill volumes and limited size of the experimental cells. However, they do show that this theory is sensitive to minor heterogeneities, and that the actual static height reached is dependent on the volume of the NAPL spill and the extent of spreading through macroscale pathways.

These effects also highlight that, unlike in these controlled homogeneous experiments, NAPL mounds in the field would have irregular shapes. The mounds did assume similar configurations in all experiments. The maximum thickness of the mound occurred only near the point of injection, with the mound advancing for some distance in

a narrow finger. This shows that using the maximum thickness to estimate the mound volume might have limited use even in homogeneous media.

## 2.7 CONCLUSIONS

Stable mounds of NAPL can form on heterogeneities, with lateral stability existing even on flat or sloped lenses. Fine textured media or small density differences between the NAPL and water can lead to particularly large mounds. This behavior applies both to DNAPL mounds perched on a lens or the bottom of an aquifer and to LNAPLs and air trapped below the water table beneath fine textured lenses.

Modifying previous analyses given for NAPL mounds, it was shown that the upper boundary of the mound (the boundary of high NAPL saturations) in uniform media corresponds more closely to a capillary pressure equal to the imbibition entry pressure of the media than to a capillary pressure of zero. A predictive expression for the maximum thickness of a laterally stable NAPL mound was given and verified with laboratory experiments. This immiscible fluid behavior cannot be explained without considering the hysteresis in capillary pressure-saturation relationships. Models not incorporating hysteresis would likely miss this phenomena and may provide incorrect distributions of NAPLs in the subsurface.

## 2.8 REFERENCES

Baker, R. S. and D. Hillel. 1990. Laboratory tests of a theory of fingering during infiltration into layered soils. *Soil Science Society of America Journal*. 54:20-30.

Corey, A. T. 1994. *Mechanics of immiscible fluids in porous media*. Water Resources Publications, Littleton, CO, 252 pp.

Glass, R.J., T.S. Steenhuis, and J.-Y. Parlange. 1989. Mechanism for finger persistence in homogeneous, unsaturated, porous media: Theory and verification. *Soil Science*. 148(1):60-70.

Hogarth, W. L., J. Hopmans, J. -Y. Parlange, and R. Haverkamp. 1988. Application of a simple soil-water hysteresis model. *Journal of Hydrology*. (98):21-29.

Kueper, B.H., D. Redman, R.B. Star, S. Reitsma, and M. Mah. 1993. A field experiment to study the behavior of tetrachloroethylene below the water table: Spatial distribution of residual and pooled DNAPL. *Ground Water*. 31(5):756-766.

Lenhard, R. J. and J. C. Parker. 1987. Measurement and prediction of saturation-pressure relationships in three phase porous media systems. *Journal of Contaminant Hydrology*. 1:407-424.

Liu, Y., B. R. Bierck, J. S. Selker, T. S. Steenhuis, and J. -Y. Parlange. 1993. High intensity x-ray and tensiometer measurements in rapidly changing preferential flow fields. *Soil Science Society of America Journal*. 57:1188-1192.

Lundegard, P. D. and G. Andersen. 1996. Multiphase numerical simulation of air sparging performance. *Ground Water*. 34(3):451-460.

McWhorter, D. B. and B. H. Kueper. 1996. Mechanics and Mathematics of the Movement of Dense Non-Aqueous Phase Liquids (DNAPLs) in Porous Media. In *Dense Chlorinated Solvents and other DNAPLs in Groundwater*, edited by J. F. Pankow and J.A. Cherry. Waterloo Press. pp. 475-506.

Tidwell, V.C. and R.J. Glass. 1994. X ray and visible light transmission for laboratory measurement of two-dimensional saturation fields in thin-slab systems. *Water Resources Research*. 30(11):2873-2882.

Van Genuchten, M. Th. 1980. A closed-form equation for predicting the hydraulic conductivity of unsaturated soils. *Soil Science Society of America Journal*. 44:892-898.

Vroblesky, D.A., J.F. Robertson and L.D. Rhodes. 1995. Stratigraphic trapping of spilled jet fuel beneath the water table. *Ground Water Monitoring and Remediation.* 15(2):177-183.

Chapter 3

## A NON-TOXIC DNAPL SURROGATE FOR LABORATORY AND FIELD EXPERIMENTS

**Abstract**

Laboratory experiments using dense chlorinated solvents present concerns with health, disposal, and reactivity with laboratory materials. Regulatory restrictions prohibit field experiments with chlorinated solvents. Perfluorocarbons are inert, non-toxic, denser-than-water, nonaqueous phase liquids, most having viscosities less than that of water. The fluid properties of this family of chemicals closely match those of chlorinated solvents. The properties of these compounds relevant to subsurface transport and related research were determined and are presented here. A laboratory spill of a perfluorocarbon into saturated, heterogeneous, porous media was conducted to provide qualitative observation of its behavior and to evaluate its visual detection during an experiment. Their properties show that perfluorocarbons may be suitable surrogate fluids for many laboratory and field investigations into the behavior of dense chlorinated solvents in groundwater.

## 3.1 INTRODUCTION

The widespread use and physical properties of dense chlorinated solvents have made them common and uniquely problematic groundwater contaminants (Pankow et al.,

1996).  Much research is currently conducted into the behavior and remediation of this group of denser-than-water, nonaqueous phase liquids (DNAPLs).  However, chlorinated solvents are toxic, volatile, strong solvents, and regulated hazardous materials.  Therefore, laboratory experiments with them present concerns for human health and safety, reactivity with laboratory materials, and proper disposal.  These factors often complicate or prohibit needed laboratory experiments (Kueper and Gerhard, 1995; Thomson et al., 1992), and consequently, researchers have commonly desired and long sought after a suitable surrogate fluid.  A non-toxic, non-reactive DNAPL would benefit laboratory research.

Since chlorinated solvents are hazardous materials, regulations prohibit field experiments with them (Kueper and Frind, 1991).  Except for a number of notable experiments in the Borden aquifer in Canada (e.g., Poulsen and Kueper, 1992; Kueper et al., 1993) most research has been limited to laboratory experiments, case studies, and numerical simulations.  The ability to conduct field experiments with a non-toxic DNAPL would be a tremendous asset to researchers.

Perfluorocarbons, a non-toxic family of compounds with densities and viscosities very similar to those of dense chlorinated solvents, are identified here for possible use as DNAPL surrogates in laboratory and field experiments.  Their properties most relevant to DNAPL research were determined and are presented.

## 3.2 PERFLUOROCARBONS

The perfluorocarbons investigated here are made by 3M, St. Paul, MN, with the product names of Fluorinert™ liquids and Performance Fluids™. Fluorinert and Performance Fluids are chemically identical compounds, except that the Fluorinert liquids are subjected to higher quality assurance for use in different applications (personal communication, Steve Pignato, 3M Specialty Chemicals Division, St. Paul, MN, 1996).

*Fluid Properties of DNAPLs.* DNAPL flow in the subsurface is governed largely by the fluid properties density, viscosity, and interfacial tension. The high densities and low viscosities of chlorinated solvents allow relatively rapid and extensive downward movement in the subsurface (Pankow et al., 1996). DNAPLs are nonwetting fluids with respect to water for most geologic materials. The interfacial tensions between chlorinated solvents and water are low enough to permit entry into small fractures and pores, but at the same time, high enough that transport is strongly affected by subsurface heterogeneities (Pankow et al., 1996). These properties of chlorinated solvents are closely matched by various perfluorocarbons. Properties of some common DNAPLs are given in table 3.1. Table 3.2 lists these properties for various perfluorocarbons.

**Table 3.1. Properties of common DNAPLs: Trichloroethylene (TCE), Tetrachloroethylene (PCE), and 1,1,1-Trichloroethane (TCA). (from Cohen and Mercer, 1993)**

| | Density (g cm$^{-3}$) | Absolute Viscosity (cP) | Kinematic Viscosity (cSt) | Surface Tension (dynes cm$^{-1}$) | Interfacial Tension (dynes cm$^{-1}$) | Solubility In Water (mg l$^{-1}$) | Vapor Pressure @~25°C (mm Hg) |
|---|---|---|---|---|---|---|---|
| TCE | 1.47 | 0.57 | 0.38 | 29 | 34 | 1100 | 57.9 |
| PCE | 1.63 | 0.93 | 0.57 | 32 | 44 | 150 | 17.8 |
| TCA | 1.35 | 0.91 | 0.67 | 25 | 45 | 757 | 123.0 |

**Table 3.2. Properties of various 3M Fluorinert™ Liquids (FC) and Performance Fluids™**
(from Material Safety and Data Sheets and 3M (1994) unless stated otherwise)

| Product [a] | Density (g cm$^{-3}$) | Absolute Viscosity (cP) | Kinematic Viscosity (cSt) | Surface Tension (dynes cm$^{-1}$) | Interfacial [b] Tension (dynes cm$^{-1}$) | Solubility In Water (mg l$^{-1}$) | Vapor [c] Pressure (mm Hg) |
|---|---|---|---|---|---|---|---|
| FC-75 | 1.80 | 1.40 | 0.77 | 15 | | <10 | 31 |
| FC-87 | 1.63 | 0.65 | 0.40 | 9 | | <10 | 610 |
| FC-72 | 1.68 | 0.67 | 0.40 | 12 | 57 | <10 · | 232 |
| FC-84 | 1.73 | 0.95 | 0.55 | 13 | 58 | <10 | 79 |
| FC-40 | 1.87 | 4.11 | 2.2 | 16 | 52 | <10 | 3 |
| PF-5060[d] | 1.68 | 0.67 | 0.40 | 12 | | <10 | 232 |
| PF-5070[e] | 1.73 | 0.95 | 0.55 | 13 | 56 | <10 | 79 |
| PF-5080[f] | 1.76 | 1.40 | 0.77 | 15 | | <10 | 45 |

[a] Fluorinert Liquids are designated by FC, Performance Fluids by PF.
[b] measured at 18° C using a ring tensiometer (CSC Scientific Company, Fairfax, VA)
[c] at 25° C
[d] same as FC-72.
[e] same as FC-84.
[f] same as FC-75, although values differed slightly between sources.

***Chemical Properties.*** Fluorinert liquids and Performance Fluids are clear, colorless, and odorless. They consist primarily of fluorinated chains of six to eight carbons. Fluorination is complete, so they contain no hydrogen or chlorine, and therefore do not contribute to stratospheric ozone layer damage (3M, 1994). The very strong carbon-fluorine bonds result in these compounds being chemically inert, and extremely stable (Ju et al., 1991). They are non-flammable, and will exert essentially no solvent action on non-fluorinated compounds (3M, 1994). They have very low water solubilities, and are immiscible with most organic compounds as well (Zhu, 1993). One particularly interesting characteristic is that these perfluorocarbons have high oxygen solubilities, on the order of 50 ml of gas per 100 ml of liquid at 1 atm and 25°C (Ju et al., 1991).

***Health and Safety***. The Material Safety and Data Sheet (MSDS) for Performance Fluid 5070 (PF-5070) states that this fluid poses no significant health hazard unless exposed to extreme heat. At high temperatures, some toxic decomposition products can occur. As a "good industrial hygiene practice", the MSDS recommends proper ventilation, but no irritation is expected from moderate inhalation. PF-5070 is listed as non-irritating for dermal and eye exposure, and "practically non-toxic" for oral exposure. PF-5070 poses insignificant toxicity to aquatic organisms, including waste treatment microorganisms.

The medical uses of similar perfluorocarbons give further testimony to their low-toxicity. Their high oxygen solubility, combined with being inert and non-toxic, give rise to applications such as liquid ventilation for human lung disease, artificial blood, and as an oxygen transfer mechanism in bioreactors (Goldfarb, 1992; Leach et al., 1996; Spence, 1995; Ju et al., 1991). Perfluorocarbons also have applications in electronics manufacturing and as alternatives to chlorofluorocarbons in refrigeration.

Permission was obtained from the local wastewater treatment plant for disposal of small quantities in the municipal sewer system (personal communication, David Meyer, City of Fort Collins Wastewater Treatment Plant, 1996). Furthermore, *preliminary* permission was obtained to conduct controlled spills of PF-5070 in field experiments in Colorado (personal communication, Peter Laux, Colorado Department of Public Health and Environment, 1996). Of course, permission would have to be obtained on an individual basis and from the appropriate local agencies for experiments and disposal elsewhere.

*Detection.* As a result of being highly inert, perfluorocarbons cannot be dyed. The common organic dyes Sudan III and Sudan IV (Aldrich Chemical, Milwaukee, WI) as well as Oil Blue N (Aldrich Chemical) and Uvitex-OB (Ciba-Geigy), were all tested. It was determined that no dye will be dissolved in these perfluorocarbons except for a highly toxic dye illegal in the U.S. (personal communication, Steve Pignato, 3M, St. Paul, MN, 1995). Visual detection in the laboratory was accomplished by using dyed water along with a clear Performance Fluid.

The relative dielectric strength of the Performance Fluids (around 1.8) makes them suitable for subsurface monitoring with ground penetrating radar and time domain reflectometry as discussed by Brewster et al. (1995) and Kueper et al. (1993). Also, the absence of perfluorocarbons in the natural environment have made them excellent chemical tracers in applications such as monitoring building airflow and in studies of borehole cross-contamination in groundwater wells (Cheong and Riffat, 1995; Russell, et al., 1989).

*Gamma Attenuation.* Gamma energy attenuation has been used as a laboratory measurement technique in a number of studies of DNAPL flow and distribution in soil (e.g., Ferrand et al., 1986; Illangasekare et al., 1995). By knowing how much a fluid attenuates gamma energy, the fluid saturations in a soil column can be determined. The cesium ($^{137}$Cs) and americium ($^{241}$Am) gamma attenuation coefficients for a few perfluorocarbons were measured and are given in table 3.3 along with the attenuation coefficients for water, trichloroethylene, and 1,1,1-trichloroethane.

**Table 3.3. Gamma Attenuation Coefficients.** $(cm^2\ g^{-1})$

|  | $^{137}Cs$ | $^{241}Am$ |
|---|---|---|
| FC-84 [a] | 0.073 | 0.174 |
| FC-72 | 0.076 | 0.172 |
| 1,1,1 Trichloroethane (TCA) [b] | 0.078 | 0.336 |
| Trichloroethylene (TCE) [c] | 0.070 | 0.367 |
| Water | 0.092 | 0.205 |

[a] FC = Fluorinert liquid, FC-84 same product as PF-5070
[b] from Illangasekare et al., 1995
[c] from Ferrand et al., 1986

*Water Solubility.* Perfluorocarbons have very low solubilities in water (<10 mg/l). This is a limitation for some research applications, such as in monitoring dissolved phase contaminants or where dissolution of a NAPL is under investigation. However, this is an advantage in other applications. For example, the interfacial tension between water and a NAPL often changes with time as the dissolved concentrations equilibrate, often complicating analysis (e.g., Schroth et al., 1995). The interfacial tension between water and various perfluorocarbons was monitored over a period of 7 days using a ring tensiometer (DuNouy Tensiometers, CSC Scientific Company, Inc., Fairfax, VA). The interfacial tension did not change significantly with time, decreasing less than 4%.

*Cost.* The Performance Fluids currently cost about $50 per liter. This compares with about $8 per liter for trichloroethylene (TCE) and about $6 per liter for tetrachloroethylene (PCE). However, the disposal costs for chlorinated solvents can range from $3 per liter to $18 per liter, with little or no disposal costs for perfluorocarbons if sewer disposal is permissible. Also, since the perfluorocarbons are highly inert and have low solubilities of water, contamination of the fluid is not a strong concern, making recovery and reuse possible in the laboratory.

## 3.3 EXPERIMENTAL OBSERVATIONS

A laboratory spill of Performance Fluid 5070 (PF-5070) into a saturated, heterogeneous, sand column was conducted. This was done primarily to evaluate how well the clear DNAPL could be visually detected by dying the water phase instead of the NAPL as is typically done, and also to gain general observations and experience with its use in laboratory experiments. PF-5070 was selected for experimentation since its density and viscosity most closely match that of PCE.

The experiment was conducted in a thin glass flume (1 cm x 63 cm x 107 cm) in conjunction with a light attenuation system similar to that described by Glass et al. (1989) and Tidwell and Glass (1994). The column was packed with a medium sand (median grain diameter, $D_{50}$ = 0.50 mm) containing two very coarse sand lenses ($D_{50}$ = 2.00 mm) and a fine sand lens ($D_{50}$ = 0.15 mm). A schematic of the sand packing is shown in figure 3.1.
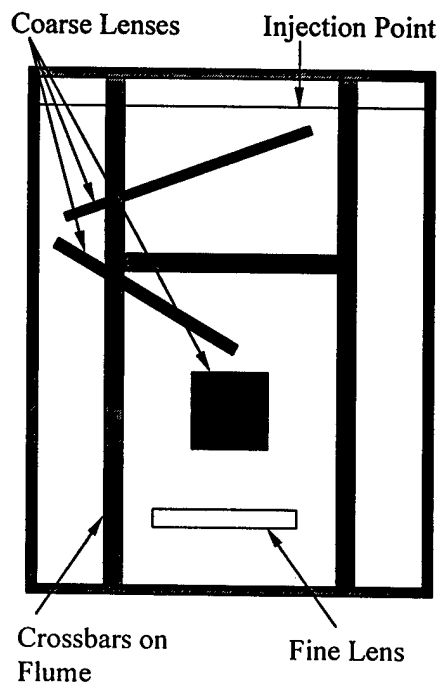


Figure 3.1. Schematic of sand packing for experiment with Performance Fluid 5070.

Light attenuation measurements take advantage of the fact that the intensity of light transmitted through a thin column of silica sand is strongly affected by the fluid saturation. Since both the clear DNAPL and water easily transmit light through the column, the water was dyed with red food color (FD&C Red #40) to a concentration of 0.5 ml per 100 ml water plus green food color (FD&C Dyes Yellow #5 and Blue #1) at 0.05 ml per 100 ml water. The purpose of this mixture was to minimize light transmission through the water phase, and therefore, allow visual DNAPL monitoring. In addition to color photographs, images were captured using an analog ccd camera (Cohu 4910 Series, San Diego, CA) in conjunction with a high accuracy monochrome frame grabber and image analysis software (Data Translation, Inc., Model DT3155 frame grabber and Global Lab Image™ software, Marlboro, MA).

Figure 3.2(a) shows the saturated column before the DNAPL spill. Figures 3.2(b) and 3.3 were taken during the spill. The bright areas in figure 3.2(b) indicate the presence of the clear DNAPL. The red areas are the dyed water. As expected, the perfluorocarbon fluid required some positive capillary pressure to penetrate the saturated zone and then moved easily downward. In the saturated zone, the coarse sand was a preferential flow path and trap to the fluid, while the fine lens acted as a barrier. This is behavior typical of DNAPLs (Illangasekare et al., 1995).

In the coarse material, the presence of the DNAPL was very clear. However, the medium sand had a higher water content, causing a less distinct difference between the light transmitted by the two fluids, and therefore, making DNAPL detection more difficult. Furthermore, some edge effects were observed in the medium sand, i.e.,
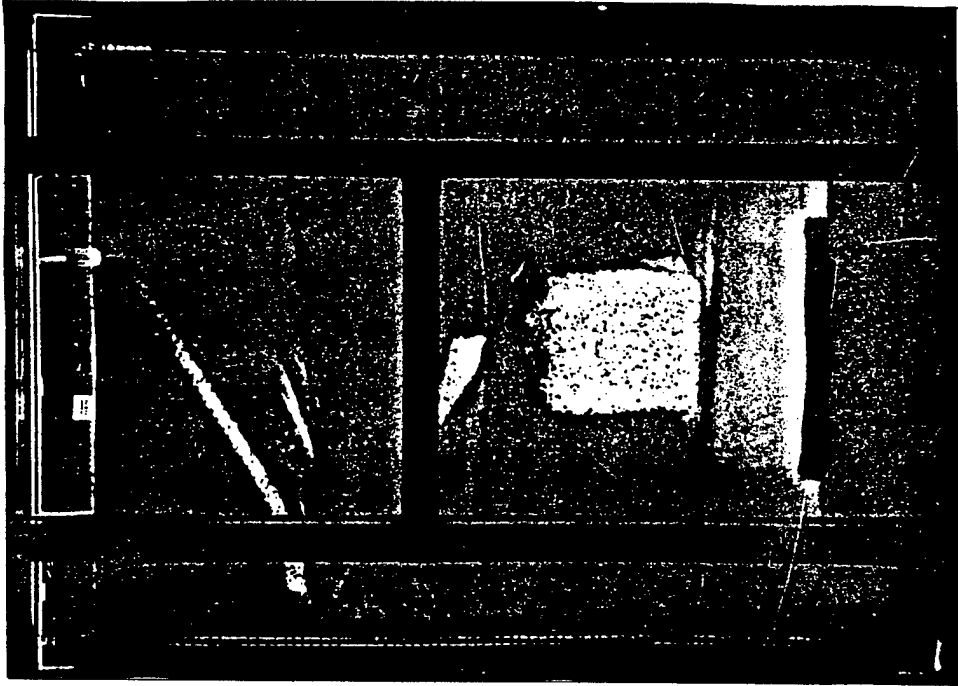
(b)
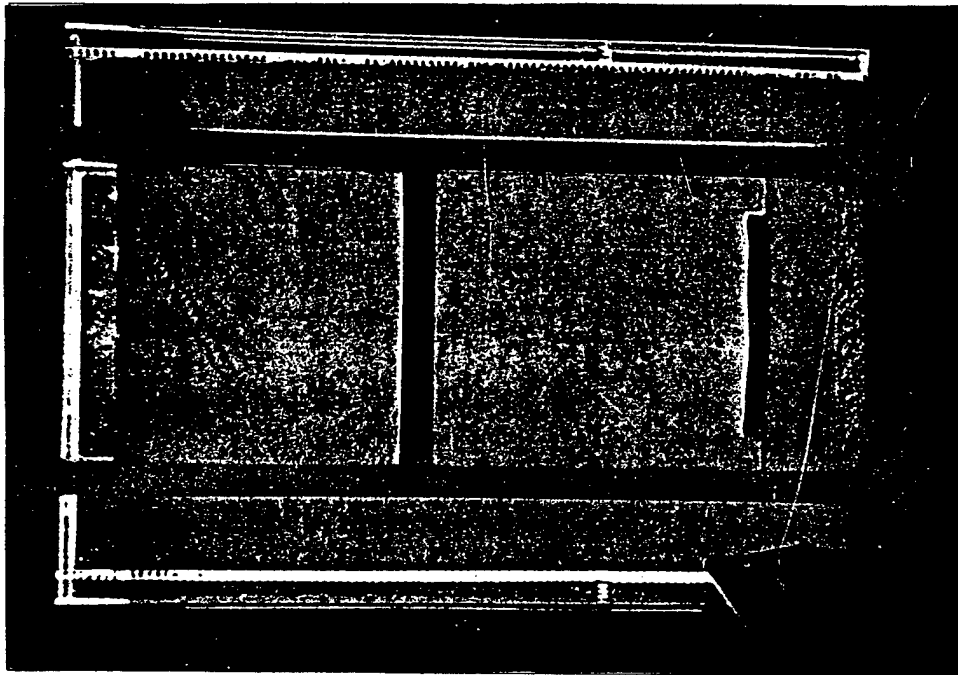
(a)

Figure 3.2. Experimental column before (a) and after (b) the spill of PF-5070. The water is dyed red while the bright areas indicate high DNAPL saturations.

DNAPL preferentially moving along the front and rear glass. One advantage of using a thin column and light attenuation measurements is that it allows observation of the fluid saturations averaged over the column thickness. This does allow more accurate determination of the significance of any edge effects. Although more difficult in this medium sand, DNAPL detection was still possible. Figure 3.3 is a close up taken with the image analysis equipment of the DNAPL in the medium sand as it mounded on and flowed around the fine lens.
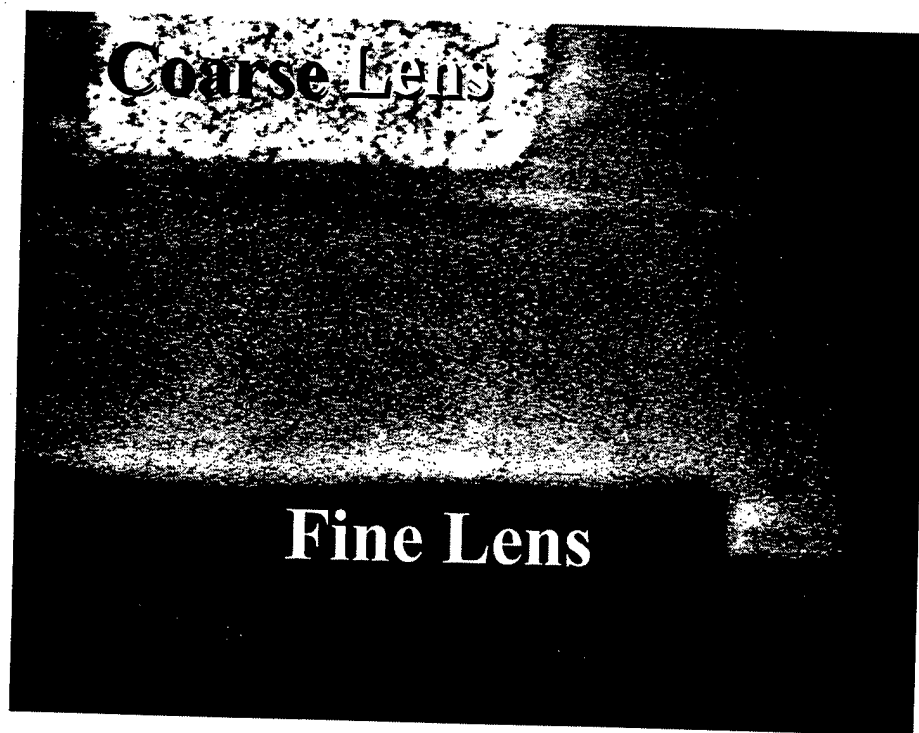


**Figure 3.3.** A close-up view of the laboratory spill, showing the DNAPL presence in the medium sand as it mounded on and flowed around a fine lens.

## 3.4 CONCLUSIONS

A group of non-toxic, inert, dense nonaqueous phase liquids has been identified and investigated as surrogate fluids for chlorinated solvents in laboratory and field experiments. They have fluid properties very similar to those of the dense chlorinated solvents but pose no health hazard and are not regulated hazardous materials. They are not reactive with laboratory materials. Therefore, these perfluorocarbons could be a great asset to laboratory and field research on dense chlorinated solvents in groundwater.

**Note:** An additional fluorocarbon which only recently became commercially available is mentioned in Appendix C along with some ideas for further research on these fluids.)

## 3.5 REFERENCES

3M. 1994. *Fluorinert™ Liquids*. 3M Electronic Products Division, Austin, Texas.

Brewster, M.L., A.P. Annan, J.P. Greenhouse, B.H. Kueper, G.R. Olhoeft, J.D. Redman, and K.A. Sander. 1995. Observed migration of a controlled DNAPL release by geophysical methods. *Ground Water*. 33(6):977-987.

Cheong, K.W., and S.B. Riffat. 1995. A new approach for measuring airflows in buildings using a perfluorocarbon tracer. *Applied Energy*. 51(3):223.

Cohen, R.M., and J.W. Mercer. 1993. *DNAPL Site Evaluation*. CRC Press, Boca Raton, Florida.

Ferrand, L.A., P.C.D. Milly, and G.F. Pinder. 1986. Dual-gamma attenuation for the determination of porous medium saturated with respect to three fluids. *Water Resources Research*. 22(12):1657-1663.

Glass, R.J., T.S. Steenhuis, and J.-Y. Parlange. 1989. Mechanism for finger persistence in homogeneous, unsaturated, porous media: Theory and verification. *Soil Science.* 148(1):60-70.

Goldfarb, B. 1992. Liquid breathing moves from science fiction to science fact. *Medical World News.* January, p. 40.

Illangasekare, T.H., J.L. Ramsey, Jr., K.H. Jensen, and M.B. Butts. 1995. Experimental study of movement and distribution of dense organic contaminants in heterogeneous aquifers. *Journal of Contaminant Hydrology.* 20:1-25.

Ju, L.K., J.F. Lee, and W.B. Armiger. 1991. Enhancing oxygen transfer in bioreactors by perfluorocarbon emulsions. *Biotechnology Progress.* 7:323-329.

Kueper, B.H., and J. I. Gerhard. 1995. Variability of point source infiltration rates for two-phase flow in heterogeneous porous media. *Water Resources Research.* 31(12):2971-2980.

Kueper, B.H., D. Redman, R.B. Star, S. Reitsma, and M. Mah. 1993. A field experiment to study the behavior of tetrachloroethylene below the water table: Spatial distribution of residual and pooled DNAPL. *Ground Water.* 31(5):756-766.

Kuerper, B.H., and E.O Frind. 1991. Two-phase flow in heterogeneous porous media 1. Model Development. *Water Resources Research.* 27(6):1049-1057.

Leach, C.L., J.S. Greenspan, S.D. Rubenstein, T.H. Shaffer, M.R. Wolfson, J.C. Jackson, R. DeLemos, and B.P. Fuhrman. 1996. Partial liquid ventilation with perflubron in premature infants with severe respiratory distress syndrome. *New England Journal of Medicine.* 335(11):761-767.

Pankow, J.F., S. Feenstra, J.A. Cherry, and M.C. Ryan. 1996. Dense Chlorinated Solvents in Groundwater: Background and History of the Problem. In *Dense Chlorinated Solvents and other DNAPLs in Groundwater*, edited by J. F. Pankow and J.A. Cherry, Waterloo Press, pp. 1-52.

Poulsen, M., and B.H. Kueper. 1992. A field experiment to study the behavior of tetrachloroethylene in unsaturated porous media. *Environmental Science and Technology.* 26(5):889-895.

Russell, B.F., J.M. Hubbell, and S.C. Minkin. 1989. Drilling and sampling procedures to minimize borehole cross-contamination. In *Proceedings of the Third National Outdoor Action Conference on Aquifer Restoration, Groundwater Monitoring, and Geophysical Methods*, National Water Well Association, Dublin, Ohio. pp. 81-93

Schroth, M.H., J.D. Istok, S.J. Ahearn, and J.S. Selker. 1995. Geometry and position of light nonaqueous-phase liquid lenses in water-wetted porous media. *Journal of Contaminant Hydrology.* 19:269-287.

Spence R.K. 1995. Perfluorocarbons in the twenty-first century: clinical applications as transfusion alternatives. *Artificial Cells, Blood Substitutes, and Immobilization Biotechnology.* 23(3):367-380.

Thomson, N.R., D.N. Graham, and G.J. Farquar. 1992. One-dimensional immiscible displacement experiments. *Journal of Contaminant Hydrology.* 10:197-223.

Tidwell, V.C. and R.J. Glass. 1994. X ray and visible light transmission for laboratory measurement of two-dimensional saturation fields in thin-slab systems. *Water Resources Research.* 30(11):2873-2882.

Zhu, D.W. 1993. A novel reaction medium: Perfluorocarbon fluids. *Synthesis.* October: 953-954, 1993.

# Chapter 4

# GEOMETRY OF LNAPL MOUNDS IN WATER-NAPL-AIR SYSTEMS

**Abstract**

Light nonaqueous phase liquids (LNAPLs), such as petroleum hydrocarbons, are released to the subsurface environment through spills or leaks from buried storage and transmission facilities. When spillled at or near the land surface, an LNAPL will migrate vertically downward with some lateral spreading, until it reaches a water-saturated zone. If sufficient volume of LNAPL has been spilled, it will form a lens and spread. This paper presents a conceptual model of an LNAPL lens and summarizes laboratory experiments that illustrate the equilibrium distribution of an LNAPL lens at the capillary fringe in a homogeneous sand.

## 4.1 INTRODUCTION

The contamination of soils and aquifers by LNAPLs is a widespread problem. Gasoline leaked from underground storage tanks is an example of an LNAPL that poses potential environmental risks in both the vadose zone and underlying saturated zone. Predicting the movement and distribution of LNAPLs in the subsurface environment is critical to the design of effective mitigation measures for contaminated soils.

Capillary pressure-saturation relationships in a porous medium determine the distribution of immiscible fluids under static conditions and can largely influence the movement of the fluids when the system is not at equilibrium. Capillary pressure is a

function of the physical and chemical properties of the fluids and the porous media, and is defined as:

$$P_c \equiv P_{nw} - P_w = 2\sigma \cos\alpha / r \qquad (4\text{-}1)$$

where $P_c$ is the capillary pressure, $P_{nw}$ is the pressure in the nonwetting phase, $P_w$ is the pressure in the wetting phase, $\sigma$ is the interfacial tension between the fluids in contact; $\alpha$ is the contact angle of the fluid-fluid interface with the porous media, and r is the effective radius of curvature of the interface (Corey, 1994). In a three-phase water-NAPL-air system, it is usually assumed that the water phase is the wetting phase, the NAPL phase is intermediate, and the air phase is the nonwetting phase (Lenhard and Parker, 1987). In the presence of three fluids, two relevant phase interfaces exist: a water-NAPL interface and a NAPL-air interface (van Geel et al., 1994).

Capillary pressure-saturation ($P_c$-S) relationships are hysteretic, i.e. fluid saturations or contents are not unique functions of the capillary pressure. Several studies have shown the importance of hysteresis in multifluid flow in porous media (Lenhard, 1992; van Geel and Sykes, 1994; Essaid et al., 1993; and Buesing and Pantazidou, 1996).

Pantazidou and Sitar (1993) conducted two-dimensional LNAPL infiltration experiments in sands and derived equations to predict the maximum vertical dimension of LNAPL lenses in the vadose zone. In their model, they simplified the actual pore geometry of the sand by assuming that NAPL advance and drainage was dictated by the sizes of pore necks and pore bodies, each of which could be identified with a characteristic diameter. They considered a lens with curved upper and lower boundaries. To compute the vertical dimensions, Pantazidou and Sitar (1993) wrote equations for the balance of

forces acting at three points on the lens boundaries. The midpoint on the upper boundary of the lens was assumed to be an air-NAPL interface. Because NAPL is the wetting fluid with respect to air and drains from the pores, this interface was located in the pore necks.

Governing Forces at:
Point 1) NAPL-Air
Point 2) NAPL-Water
Point 3) NAPL-Air
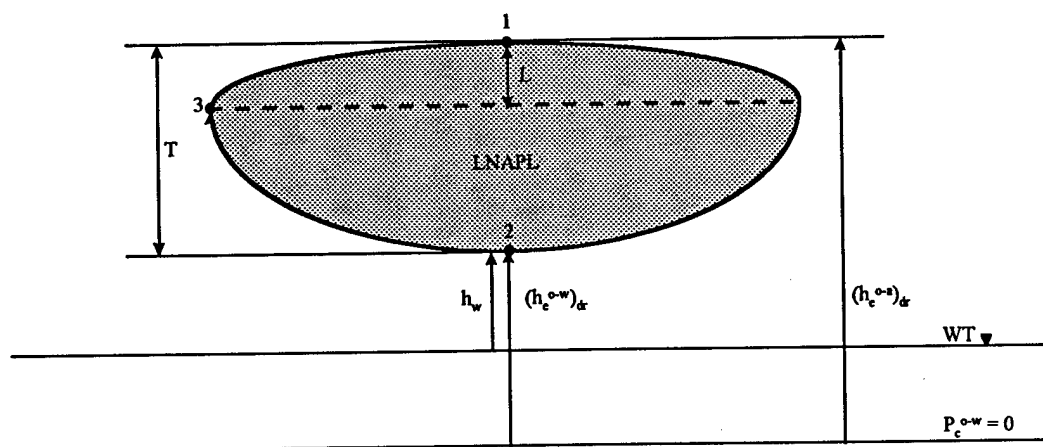


Figure 4-1. Schematic of an LNAPL lens at equilibrium, as presented by Pantazidou and Sitar (1993).

The midpoint on the lens lower boundary was assumed to be governed by a NAPL-water interface. It was assumed water is more wetting with respect to the NAPL and drains from the pores, thus this interface should also be located in the pore necks. The difference in NAPL pressures between points 1 and 2 at equilibrium is given by the static NAPL pressure distribution. Solving for T, Pantazidou and Sitar (1993) derived the equation:

$$T = (1/\rho_o g)[4(\sigma_{ow} + \sigma_{ao})/d_n - \rho_w g h_w] \qquad (4\text{-}2)$$

where T is the maximum vertical thickness of the NAPL lens; and $\rho_o$ is the NAPL density, $\rho_w$ is the water density; $\sigma_{ow}$ and $\sigma_{ao}$ are the interfacial oil-water tension and oil surface tension, respectively, and $h_w$ is the distance between the water table and the bottom of the lens. They assumed the top boundary was oil-air drainage, the bottom boundary was water-oil drainage and the advancing edge of the lens was at the oil-air imbibition entry pressure.

Schroth et al. (1995) extend the theory of Pantazidou and Sitar (1993) by making the assumption that the top of the lens was at the top of the water-air capillary fringe. The pore neck diameter $d_n$ was calculated using the Laplace capillary rise equation:

$$d_n = (4\sigma_{aw})/(\rho_w g h_{cap}) \tag{4-3}$$

where $h_{cap}$ is the capillary fringe height. The height of point 2 above the water table, $h_w$, (Figure 4-1) was expressed as:

$$h_w = h_{cap} - T \tag{4-4}$$

Eq. 4-4 was inserted into Eq. 4-2. The total lens thickness then becomes:

$$T = 1/\rho_o g [4(\sigma_{ao} + \sigma_{ow})/dn - \rho_w g h_{cap} + \rho_w g T] \tag{4-5}$$

Solving Eq. 4-3 for $h_{cap}$ and substituting it into Eq. 4-5 and solving for T gave a fully explicit equation for computing T:

$$T = 4[(\sigma_{aw} - \sigma_{ao} - \sigma_{ow})]/[d_n g(\rho_w - \rho_o)] \tag{4-6}$$

Schroth et al. (1995) also found, in their experiments, that the upper boundary was flat. The results presented by Schroth et al. (1995) did not match predictions well. They attributed the error to the time dependence of the interfacial tension.

In contrast to Pantazidou and Sitar (1993), Abdul (1988) predicted that NAPLs form lenses in the capillary fringe with horizontal upper and curved lower boundaries. He speculated that NAPL would fully penetrate the capillary fringe and at equilibrium form "pancake-shaped" lenses.

In this paper, we incorporate three phase air-NAPL-water relationships in a new analysis and develop a conceptual model of the LNAPL lens during infiltration and at equilibrium. Two-dimensional flume experiments were used to verify the conceptual model.

## 4.2 MATERIALS AND METHODS

The experimental flume (Figure 4-2) was constructed from two sheets of 122 cm x 91cm x 1.27 cm tempered glass placed inside of a steel frame. The glass was separated by a 1-cm thick aluminum spacer, which was sealed to the glass with Silicone® high vacuum grease. Two vertical bars, the height of the column, and a horizontal bar connecting the vertical bars, were used to minimize deflection of the glass during the experiments. Fully screened vertical wells were installed at each end of the flume. A light box was set up behind the flume and used to distinguish the saturated and unsaturated zones. An analog charge couple device (CCD) camera placed in front of the flume recorded the movement of LNAPL over time. A framegrabber converted the LNAPL images to digital format.
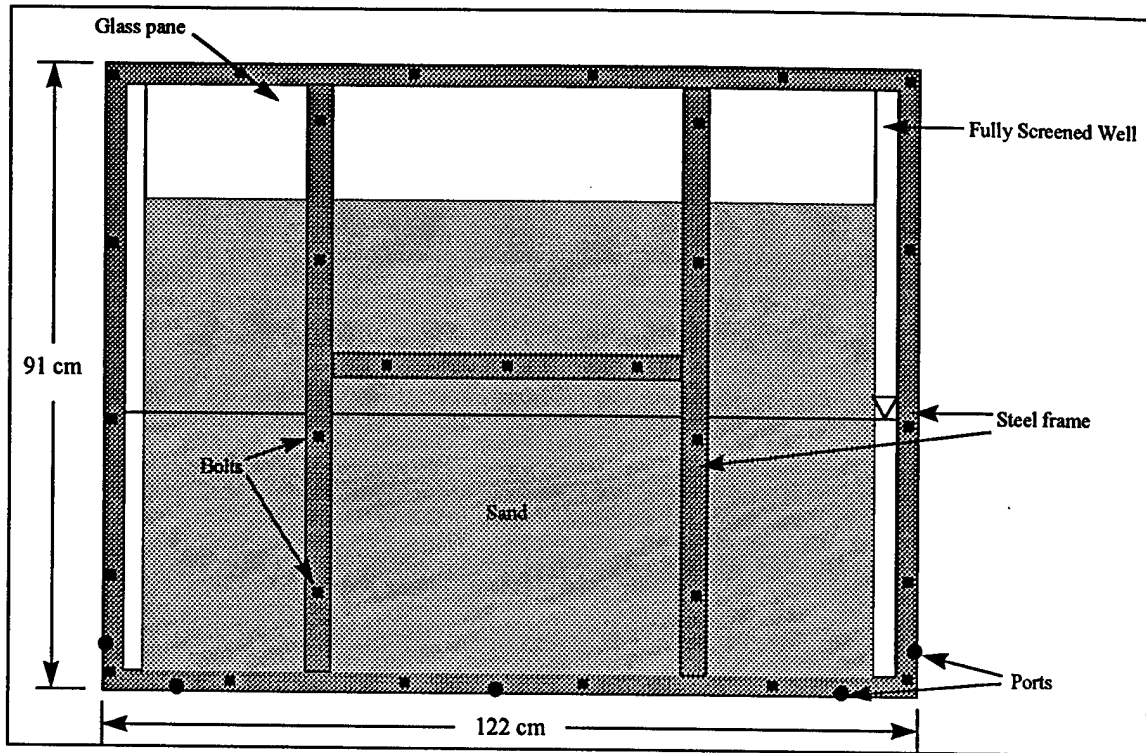
**Figure 4-2. Flume Schematic (not to scale).**

The LNAPL used in the experiments was Soltrol 220® (Phillips Petroleum Co., Bartlesville, OK). Soltrol 220® is a mixture of branched alkanes having low solubility in water (Lenhard, 1992). Its components can be found in a variety of petrochemical products, e.g. diesel fuel (Schroth et al., 1995). To distinguish between water and the LNAPL during the experiments, the LNAPL was dyed by adding 0.01% by weight of Sudan IV® (Aldrich Chemical Company, Milwaukee, WI). Sudan IV® is a fat stain of bright red color and is virtually insoluble in water. The density of the dyed Soltrol 220® was measured in the laboratory as 0.79 gm/cm³. The aqueous phase used was deionized water. The density of the water was assumed to be 1 gm/cm³.

Two sets of fluids pairs were used in the experiments. Interfacial tensions are given in Table 4-1. The values shown were measured with fluids drained from the flume after the experiments. The LNAPL-water interfacial tension before contact with the sand was 44.6 dynes/cm.

**TABLE 4-1.  Values of Parameters.**

| | Fluid Set 1 (Experiments 1-3) | | | Fluid Set 2 (Experiment 4) | |
|---|---|---|---|---|---|
| Parameter | Air-water | LNAPL-water | Air-LNAPL | LNAPL-water | Units |
| $P_{ed}$ | 20580 | 10976 | 8045 | 5457 | dynes/cm$^2$ |
| $P_{ei}^1$ | 13720 | 7317 | 5363 | 3638 | dynes/cm$^2$ |
| $P_{ei}^2$ | 14700 | 7840 | 5746 | 3898 | dynes/cm$^2$ |
| $\sigma^3$ | 66 | 35.2 | 25.8 | 17.5 | dynes/cm |
| $h_{ed}$ | 21 | 11.2 | 8.2 | 5.6 | cm of wetting fluid |
| $h_{ei}^1$ | 14 | 7.5 | 5.5 | 3.7 | cm of wetting fluid |
| $h_{ei}^2$ | 15 | 8.0 | 5.9 | 4 | cm of wetting fluid |

1. Using $h_{ei}^{a-w}$ = 14 cm estimated in flume.
2. Using $h_{ei}^{a-w}$ = 15 cm.
3. ASTM Method

A spreading coefficient $C_{sp}$, is defined as:

$$C_{sp} = \sigma_{aw} - (\sigma_{ao} + \sigma_{ow})  \hspace{2cm} (4\text{-}7)$$

where $\sigma_{aw}$, $\sigma_{ao}$ and $\sigma_{ow}$ are the surface tensions of water and oil and the oil water interfacial tension. If the spreading coefficient is positive, the oil phase will spread as film flow between the air and water phases in the unsaturated zone. The spreading coefficients are 10.3 and 28 for fluid sets 1 and 2, respectively.

Experiments were conducted using F-14 sand (U.S. Silica Sand, Ottawa, Illinois). The particle size distribution was measured in the laboratory (Figure 4-3) by sieving

(ASTM Method 4464). In order to obtain a more homogeneous sand, the F-14 sand was sieved with a U.S. Standard #40 sieve (0.425 mm). Particles less than 0.425 mm and greater than 0.589 mm were discarded.

A 2-cm thick layer of #8-12 (2.362-1.397 mm) mesh silica sand (Colorado Silica Sand Inc., Colorado Springs, Colorado) was placed at the bottom of the flume to facilitate drainage. A "rainer" was used to pack the flume (Rad and Tumey, 1987). The "rainer" consisted of an acrylic hopper that extended across the full width of the flume and packing was conducted by raining continuously to prevent local gradations in particle size. The bulk density of the soil was approximately 1.7 gm/cm$^3$.

The flume was initially flushed with $CO_2$ gas through the bottom ports on both sides (Figure 4-2) to replace the air in the pore space, and then slowly saturated with deionized, deaired water from the bottom. After saturating the sand pack, the water reservoir was lowered to a level of 8.5 cm above the bottom of the flume. The water was allowed to drain for at least 15 hours, resulting in a capillary fringe height ($h_{cd}^{a-w}$) measured visually in the flume of 21 cm $\pm$ 0.5 cm. The capillary fringe was determined visually as the zone above the water table where the effective saturation is very close to 1.0. We use the terms capillary fringe and entry pressure interchangeably. Hence, the entry pressure head on the drainage curve for the sieved sand was 21 cm $\pm$ 0.5 cm ($P_{cd}^{a-w}$ = 20580 dynes/cm$^2$). To obtain the entry pressure head on the imbibition curve, the water level was raised at a steady rate using a peristaltic pump to a level of 40 cm above the bottom of the flume. The water was allowed to imbibe for 17 hours, creating a fringe height of 14 cm $\pm$ 0.5 cm.
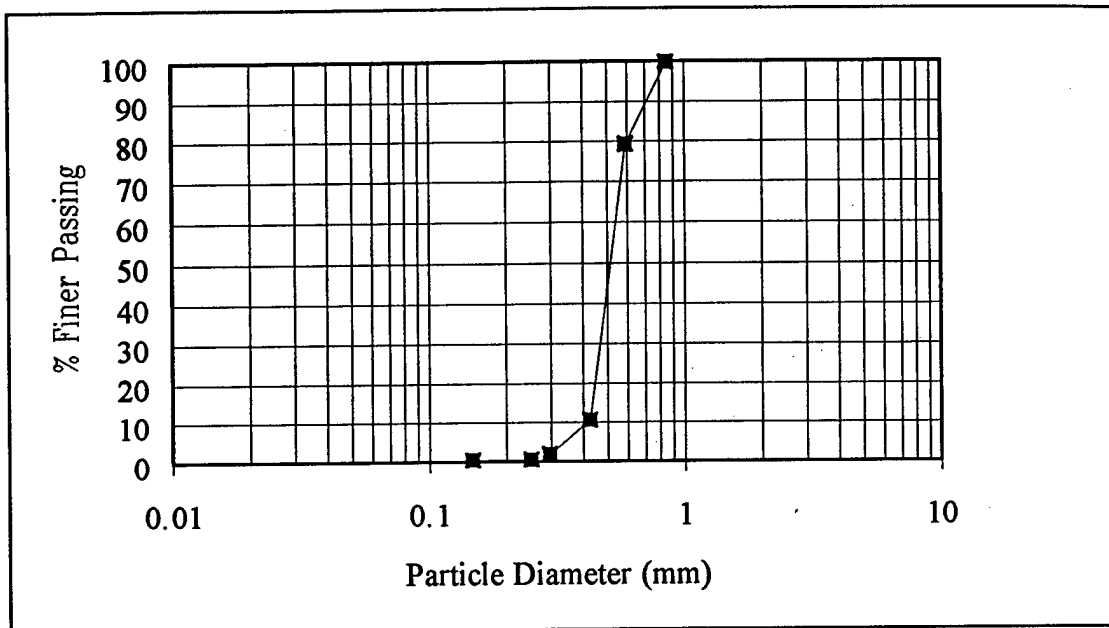
**Figure 4-3. Particle size distribution for F-14 sand.**

## 4.3 CONCEPTUAL MODEL OF AN LNAPL SPILL AND LENS

Figure 4 shows the ccd camera pictures of a spill with fluid set 2. These photos will be used to illustrate the conceptual model. When an LNAPL is spilled near the soil surface, it moves through the unsaturated zone as a result of gravity and pressure gradients, (figure 4-4a). As the LNAPL reaches areas of higher water saturation near the capillary fringe, it spreads horizontally until the capillary forces equilibrate. The capillary pressure at the advancing edge of the lens is the water-oil entry pressure on the drainage curve.

An LNAPL with a positive spreading coefficient spreads horizontally between the water and air phases as a film (Figure 4-4b). The LNAPL continues migrating downward,

on an oil-water drainage curve (Figure 4-4b, point A) until it establishes itself on the top

of a compressed capillary fringe (Figure 4-4c, point B). Over time the LNAPL

"rebounds" upward and shifts to an oil-water imbibition curve at the bottom of the lens

(Figure 4c, point C), as it continues to move laterally on top of the capillary fringe, along

the oil-water drainage curve (Figure 4-4c, point D). A schematic of a lens at equilibrium

and the equilibrium pressure distribution are shown in figure 4-5.



unsaturated zone

saturated zone
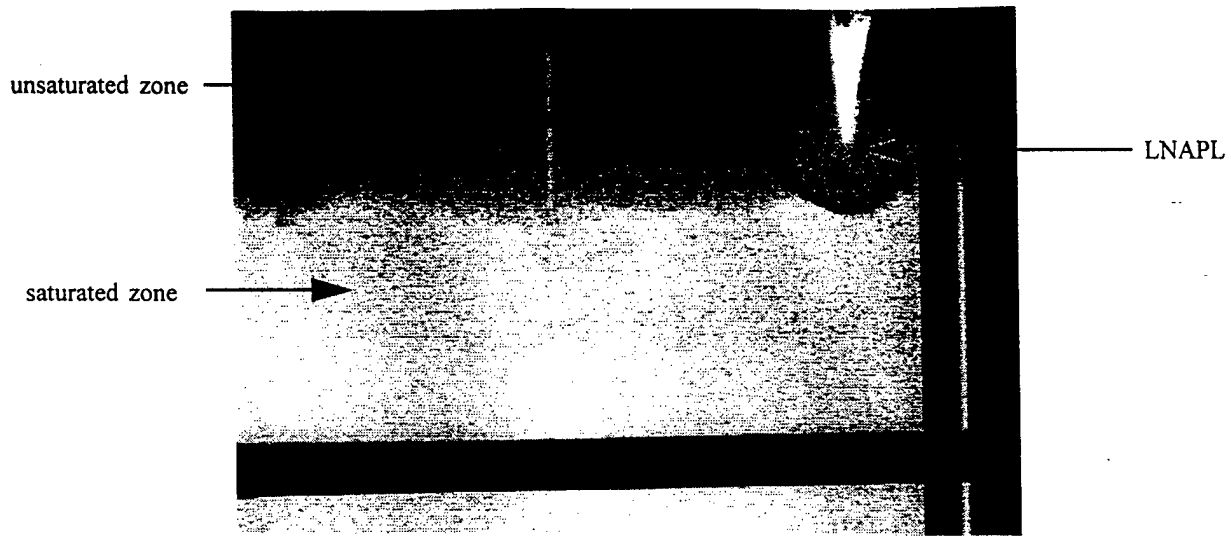
LNAPL

**Figure 4-4a. Injection of LNAPL.**



**Figure 4-4b. LNAPL len at an early time.**
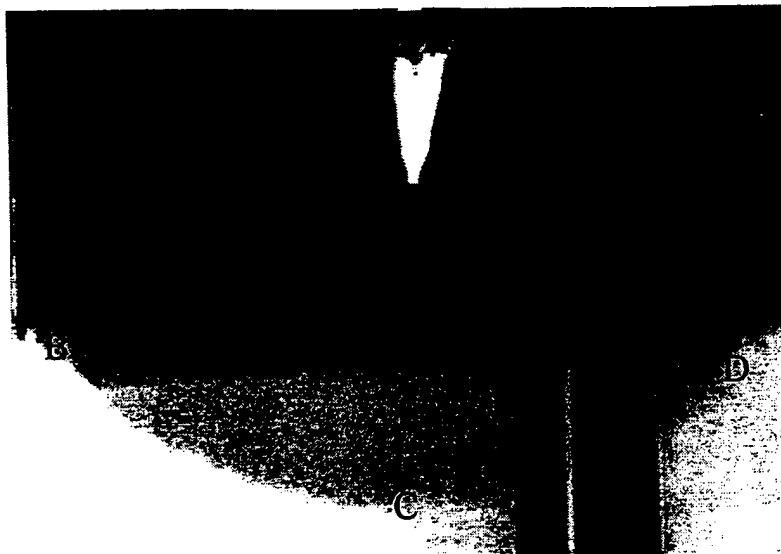
Figure 4-4c. LNAPL lens at equilibrium.



At Point 1: $P_{ed}^{a-o}$
At Point 2: $P_{ei}^{o-w}$
At Point 3: $P_{ed}^{o-w}$
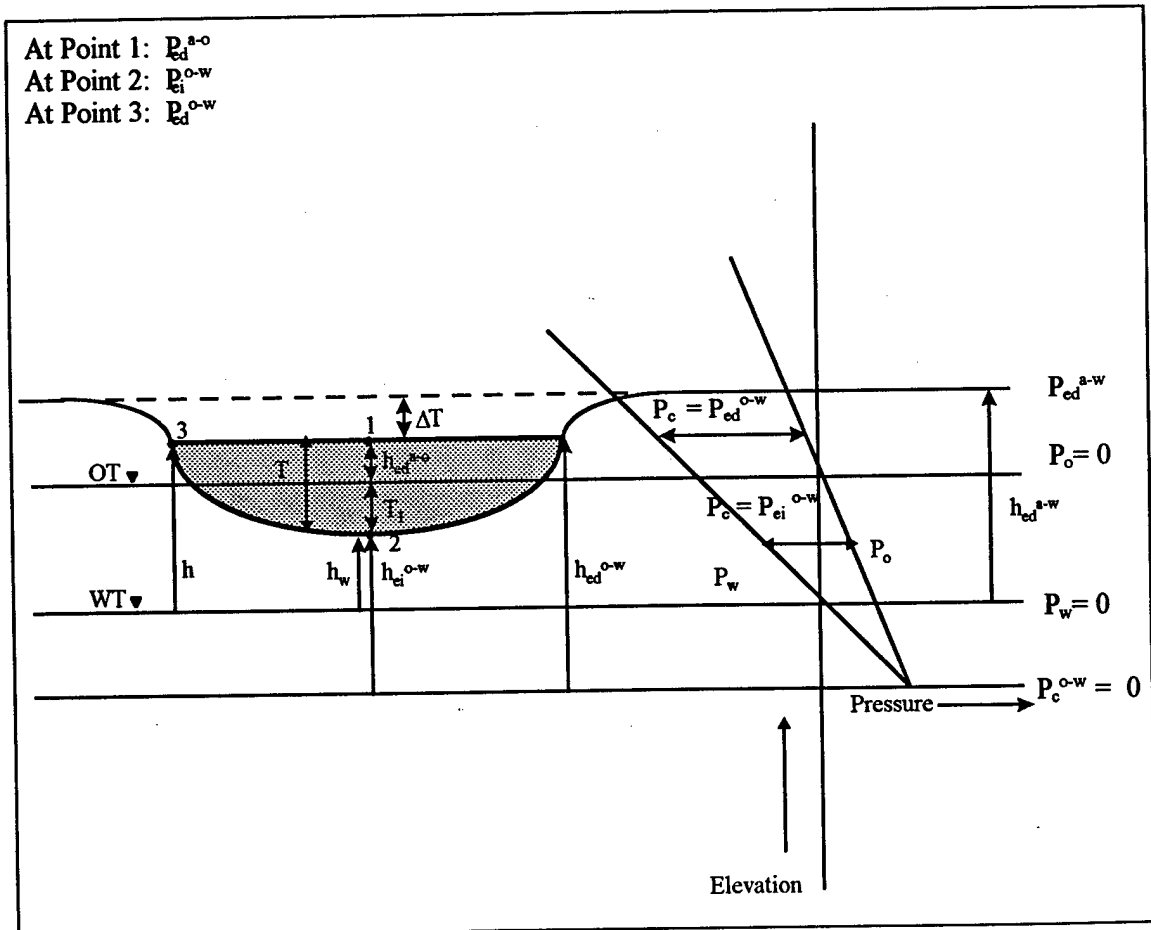
Figure 4-5. Pressure distribution and notation assumed for LNAPL lens.

## 4.4    LABORATORY FLUME EXPERIMENTS

Two-fluid phase experiments were conducted initially to verify the assumption that the advancing edge of the LNAPL lens was at a capillary pressure equal to the drainage entry pressure in an LNAPL-water system. The flume was filled with the sieved sand and saturated with deionized water. The top of the coarse sand was at a height of 60.5 cm above the bottom of the flume. A layer of F-95 (U.S. Silica Sand, Ottawa, Illinois) sand was wet-packed on top of the coarse sand. The fine sand created a boundary along which the LNAPL would advance and eventually reach equilibrium. The water level was kept at the top of the fine layer as it was packed in the flume. The wet packing was used to eliminate any entrapped air at the interface.

Using the scaling relationship as defined by Parker et al. (1987), the entry pressure head for the LNAPL-water drainage curve, $h_{ed}^{o-w}$ was estimated as 11.2 cm water by:

$$h_{ed}^{o-w} = h_{ed}^{a-w} (\beta_{aw}/\beta_{ow}) \tag{4-9}$$

where $\beta_{aw}=1$ and $\beta_{ow}=\sigma_{aw}/\sigma_{ow}$. The entry pressure head for the LNAPL-water imbibition curve, $h_{ei}^{o-w}$, was estimated as 3.7 cm water by:

$$h_{ei}^{o-w} = h_{ei}^{a-w} (\beta_{aw}/\beta_{ow}) \tag{4-11}$$

The maximum thickness predicted in cm of oil was obtained by:

$$T_{max} = h_{ed}^{o-w} - h_{ei}^{o-w} \text{ (in cm of water)}(\rho_w/\Delta\rho) \tag{4-12}$$

which yields 17.7 cm of oil.

The water table was maintained 5 cm above the fine-coarse interface. Once the water table was established, the boundary between the unsaturated and saturated zones was easily distinguished. In order to exceed the maximum predicted thickness, the height of oil in the well was maintained slightly more than 30 cm above the interface or 90 cm

above the bottom of the flume. The LNAPL was injected in the left well using a peristaltic pump. Initially, the LNAPL was injected at 90 ml/min, then the pump was turned on and off periodically to maintain the desired oil level in the well. After injection, the mound height was allowed to decrease until the LNAPL lens came to equilibrium. The maximum height of the mound measured at the well at equilibrium (110 hours) was 17.7 cm, which was the maximum thickness predicted. Figures 4-6 a-h show the computer images taken during the experiment. The computer images show clearly the hysteresis effect at point A. As the LNAPL shifts from an LNAPL-water drainage curve, to an LNAPL-water imbibition curve, the bottom of the lens moves upward. The bottom of the mound moved up, and pivoted around point A as the leading edge advanced (point B). Figure 4-7 shows the difference in oil pressure in the well and water pressure at the elevation of the textural interface, i.e. at the advancing edge of the lens. After about 18 hours, this pressure difference was constant at the entry pressure of LNAPL-water drainage curve.
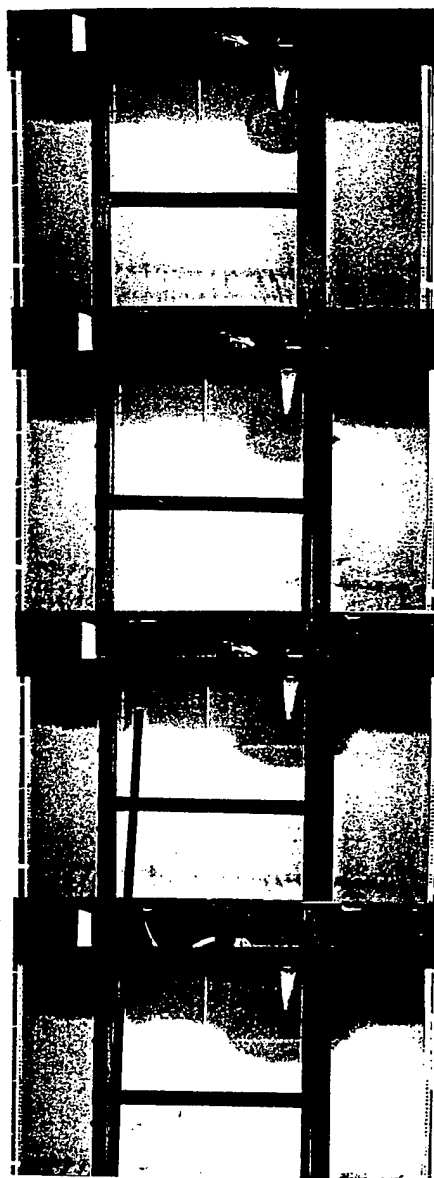
Figure 4-6. Preliminary experiment showing progression of lens in a two-phase system.
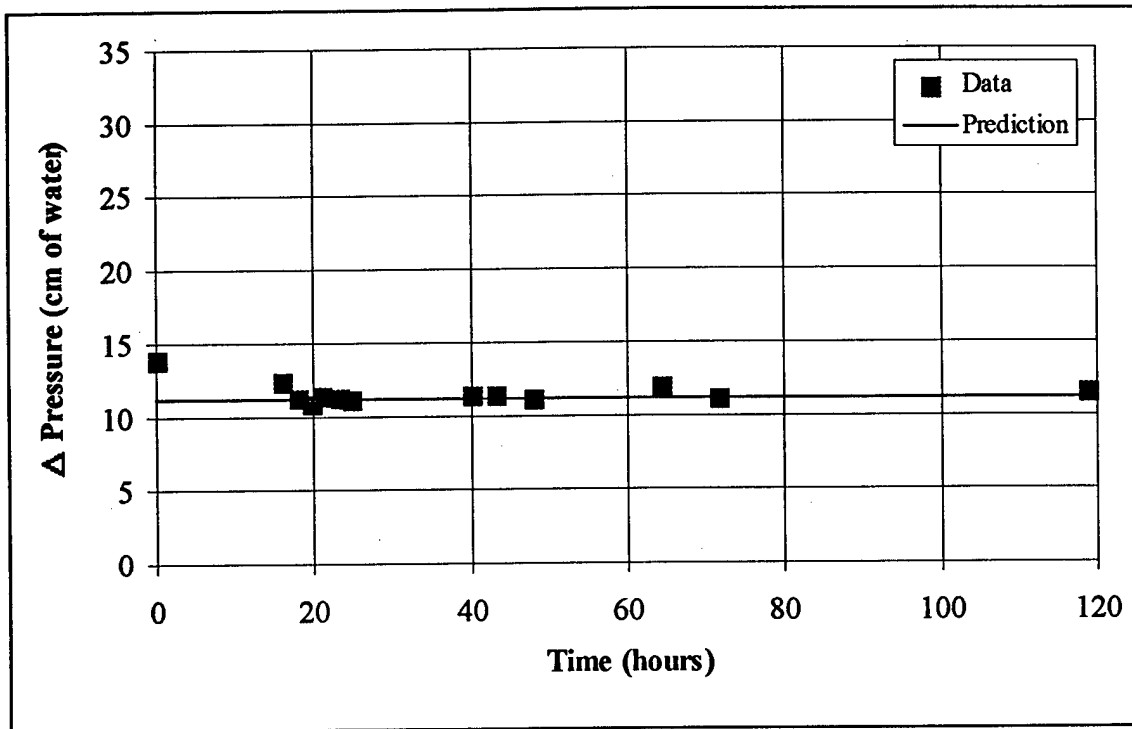
**Figure 4-7. Change in pressure with time.**

Three-fluid phase experiments simulating an LNAPL spill were conducted. The objective of the experiments was to verify the assumptions governing the infiltration and equilibrium position and thickness of the lens. Table 4-2 summarizes the results of the three-phase experiments. Notation was given in figure 4-5.

The flume was dry packed with the sieved sand. After saturating the flume, the water levels in the wells were lowered to 44 cm above the bottom of the flume. The water was allowed to drain for 22 hours, creating a capillary fringe height of 21 cm. A cumulative volume of 165 ml of fluid set 1 was injected approximately 13 cm above the top of the fringe. The injection of the LNAPL occurred over a ten minute period. After

the injection of the LNAPL ceased, the water table height, mound height, and mound length were recorded with time.

The second experiment was conducted to observe the effects of adding less solution than experiment 1. After saturating the flume, the water levels in the wells were lowered to 18.5 cm above the bottom of the flume. The water was allowed to drain for 22 hours, creating a capillary fringe height of 21 cm. A cumulative volume of 100 ml of Solution 1 was injected approximately 6 cm above the top of the fringe (at the top of the sand). The injection of the LNAPL occurred over a five minute period.

After equilibration an additional 50 ml of fluid set 1 was added to the lens. This is referred to as experiment 3. It was assumed that during the infiltration of the additional solution, the lens would spread in the vertical and horizontal directions and then "rebound" upward to its final position. The last experiment measured the final thickness of a lens using fluid set 2. The flume was dry packed with the F-14 sand. The top of the sand was at a height of 90 cm above the bottom of the flume.

Computer images taken during experiments 1 and 3 are shown in figures 4-8 and 4-9. Graphs of lens height with time are shown in figures 4-10, 4-11 and 4-12. Measured and predicted values are given in Table 4-2. The final measured thicknesses were about 15 cm. Depending on whether 14 cm or 15 cm was used as the imbibition entry pressure, the predicted thickness was 17.8 cm and 15.2 cm, respectively. The value for $\Delta T$ at equilibrium was approximately 2 cm which is close to the predicted value of 1.6 cm. Thus, the location of the lens with respect to the top of the capillary fringe can be predicted from the interfacial tensions and soil properties. Note that the sum of $\Delta T + T + h_w$ should be equal to 21 cm.

TABLE 2. Comparison of Measured and Predicted.

| Experiment | Total Soltrol added (ml) | Measured thickness, T (cm) | Predicted 'ΔT[1] (cm) | Measured ΔT (cm) | Predicted $h_w^2$ (cm) | Measured $h_w$ (cm) | Predicted thickness[3], T (cm) | Predicted thickness[4], T (cm) | Predicted $h_{ol}^{a-w\,5}$ (cm) | Measured $h_{ol}^{a-w}$ (cm) |
|---|---|---|---|---|---|---|---|---|---|---|
| 1 | 165 | 15 | 1.6 | 1.9 | 4.4 | 0.3 | 17.8 | 15.2 | 21.2 | 21.0 |
| 2 | 100 | 13 | 1.6 | 2.6 | 6.4 | 6 | 17.8 | 15.2 | 23.2 | 21.0 |
| 3 | 150 | 15 | 1.6 | 1.6 | 4.4 | 5.8 | 17.8 | 15.2 | 21.2 | 21.0 |
| 4 | 50 | 8 | 7 | 6.4 | 6 | 11 | 8.8 | 7.8 | 20.8 | 21.0 |

1. $\Delta T = h_{ol}^{a-w} - h$
2. $h_w = h_{ol}^{a-w} - T - \Delta T$
3. $h_{oi}^{a-w} = 14$ cm
4. $h_{oi}^{a-w} = 15$ cm
5. $h_{ol}^{w-s} = \Delta T + h_w + T$
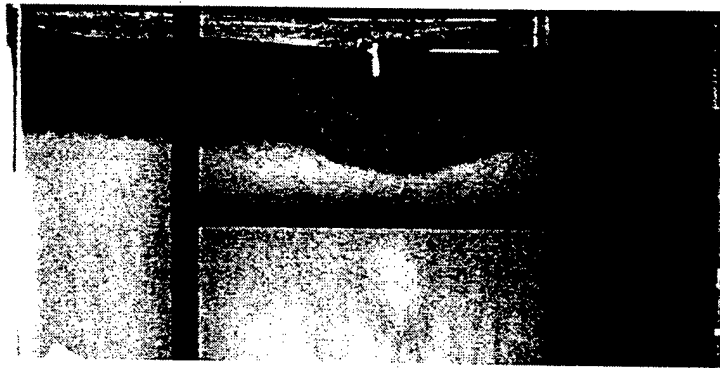
Experiment 1: Injection.
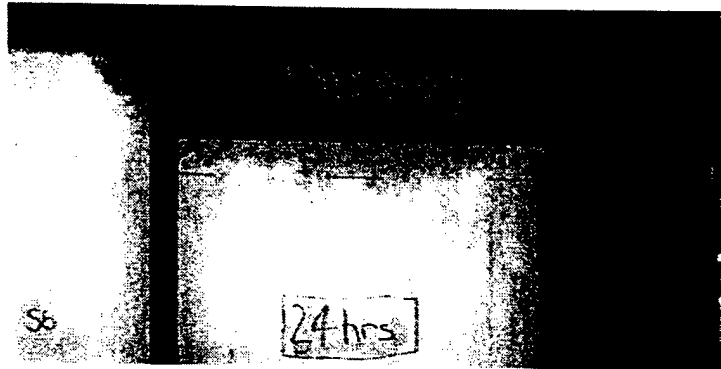


Figure4-8b Experiment 1: 24 hours after injection.



Figure 4-9 Experiment 3: LNAPL mound 2 days after injection.
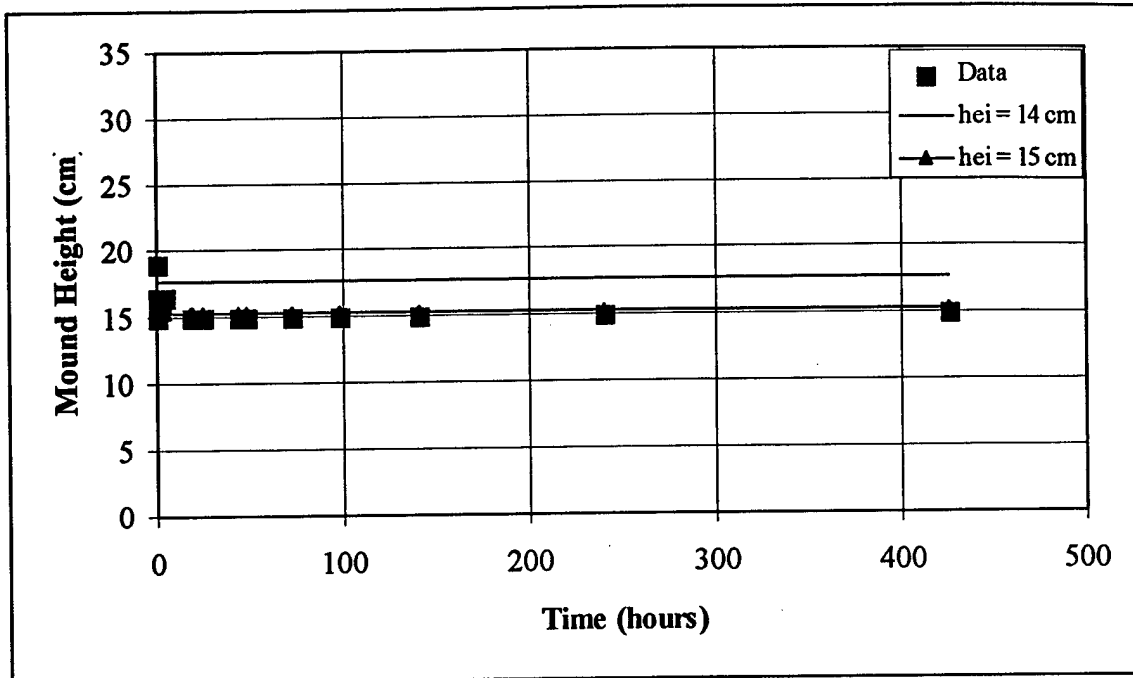
**Figure 4-10. Mound height with time for Experiment 1.**
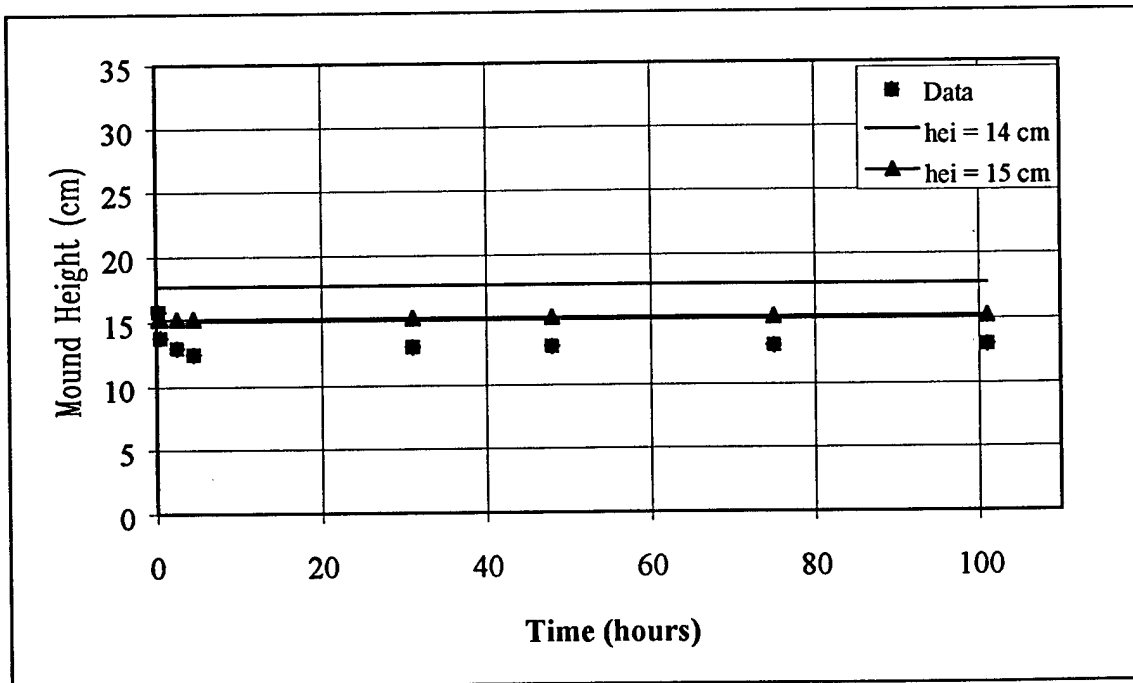


**Figure 4-11. Mound height with time for Experiment 2.**
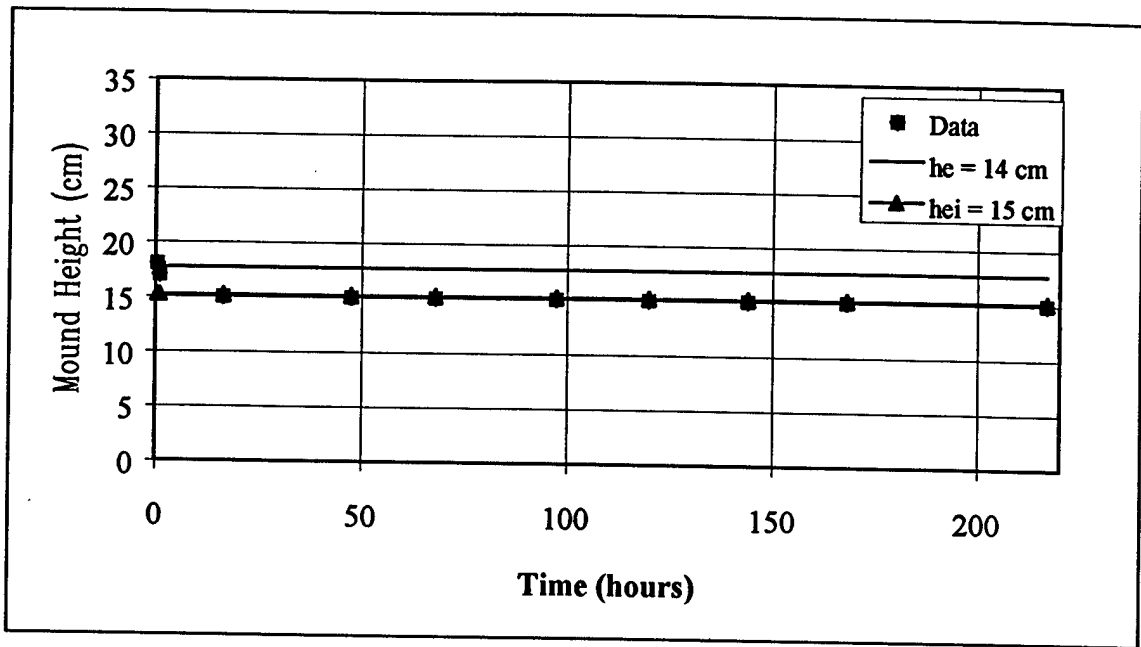
**Figure 4-12. Mound height with time for Experiment 3.**

## 4.5    SUMMARY AND CONCLUSIONS

A conceptual model of LNAPL infiltration and spreading at the capillary fringe was developed and verified with a series of experiments in a two-dimensional flume. Conclusions which can be drawn from this work are

- the top of the lens is not necessarily at the top of the capillary fringe but its location can be calculated from the water-NAPL and NAPL-air interfacial tensions,

- capillary pressures at each point on the water-NAPL boundary are on a different hysteresis loop of the water-NAPL capillary pressure-saturation curve,

- the top of an LNAPL lens is flat and the capillary pressure at each point is at the air entry pressure on the air-NAPL imbibition curve,

- the capillary pressure at the advancing edge of the lens is the entry pressure on the water-NAPL drainage curve

and

- the maximum possible thickness of an LNAPL lens is the difference between the capillary pressure entry head on the oil-water drainage curve and the capillary pressure entry head on the oil-water imbibition curve.

## 4.6    REFERENCES

Abdul, A.S., 1988.  Migration of petroleum products through sandy hydrogeologic systems.  Ground Water Monitoring Review, 8: 73-81.

American Society for Testing and Materials, 1993. American National Standards Annual Book.  Philadelphia, PA.

Buesing, J.L. and Pantazidou, M., 1996. The role of capillary pressure curve selection in modeling LNAPL transport in the vadose zone. L.N. Reddi (Ed.) Nonaqueous Phase Liquids (NAPLS) in the Subsurface Environment: Assessment and Remediation. Proceedings of the specialty conference held in conjunction with the ASCE National Convention, Washington, DC, November 12-14, 1996. ASCE, N.Y., N.Y. pp. 490-501.

Corey, A.T. 1994. *Mechanics of Immiscible Fluids in Porous Media*. Water Resources Publications, Highlands Ranch, CO. pp. 38-50.

Essaid, H.I., Herkelrath, W.N. and Hess, K.M., 1993. Simulation of fluid distribution in porous media. Water Resources Research 29: 1753-1770.

Klute, A., 1987 Methods of Soil Analysis: Part 1 Physical and Mineralogical Methods. Soil Science Society of America, Inc., Madison, Wisconsin.

Lenhard, R.J., 1992. Measurement and modeling of three-phase saturation-pressure hysteresis. Journal of Contaminant Hydrology 9: 243-269.

Pantazidou, M. and Sitar, N., 1993. Emplacement of nonaqueous liquids in the vadose zone. Water Resources Research, 29: 705-722.

Parker, J.C. and Lenhard, R.J., 1987. A model for hysteretic constitutive relations governing multiphase flow, 1. Saturation-pressure relations. Water Resources Research, 23: 2187-2196.

Parker. J.C., Lenhard, R.J., and Kuppusamy, T., 1987. A parametric model for constitutive properties governing multiphase fluid flow in porous media. Water Resources Research, 23: 618-624.

Rad, N. S. and Tumay, M.T., 1987. Factors affecting sand specimen preparation by raining. Geotechnical Testing Journal, GTJODJ, Vol. 10, No. 1, pp. 31-37.

Schroth, M.H., Istok, J.D., Ahearn, S.J., and Selker, J.S., 1995. Geometry and position of light nonaqueous-phase liquid lenses in water-wetted porous media. Journal of Contaminant Hydrology, 19: 269-287.

van Geel, P.J. and Sykes, J.F., 1994a. Laboratory and model simulations of an LNAPL spill in a variably-saturated sand medium. 1. Laboratory experiment and image analysis techniques. Journal of Contaminant Hydrology, 17: 1-25.

van Geel, P.J. and Sykes, J.F., 1994b. Laboratory and model simulations of an LNAPL spill in a variably-saturated sand medium. 2. Comparison of laboratory and model results. Journal of Contaminant Hydrology, 17: 27-53.

# SECTION III

SECTION III

CHAPTER 1

A SEMI-ANALYTICAL SOLUTION FOR ONE-DIMENSIONAL,
TWO-FLUID FLOW IN LAYERED POROUS MEDIA

**Abstract**

A semi-analytical solution is developed for simulating transient, one-dimensional, two-fluid immiscible flow in layered media. The solution uses the Runge-Kutta integration method to solve the governing flow equations and an iterative shooting technique to insure that all boundary conditions are satisfied. This semi-analytical solution extends previous two-fluid solutions to vertical flow, layered media, and finite-length flow regions. Evaluation of two initial-boundary-value problems suggests that the proposed semi-analytical solution can simulate certain physical problems in two-fluid flow without experiencing the types of numerical instabilities commonly associated with traditional finite difference and finite element numerical models. The primary disadvantages of the solution are that it is limited to one-dimensional flow, requires the development of problem-specific iteration schemes for different types of physical problems, and sometimes does not converge smoothly within a time step. Continued development of this semi-analytical technique, however, will likely result in an efficient method for solving many types of one-dimensional, two-fluid flow problems.

## 1.1 INTRODUCTION

Mathematical simulation of two-fluid immiscible flow is of technical interest in many fields of engineering and geology. Practical applications of two-fluid flow theory include agricultural infiltration and drainage in layered soils, migration of nonaqueous

phase contaminants, and extraction of petroleum products. Simulation of two-fluid flow in layered or otherwise heterogeneous porous media has commonly been difficult using traditional finite difference and finite element models. Due to the highly nonlinear governing equations, these modeling approaches can exhibit numerical instabilities and convergence problems, particularly when sharp saturation fronts move across material interfaces.

A semi-analytical solution has been developed for the one-dimensional Richards equation which does not appear subject to the types of stability problems that can affect traditional numerical models. In this chapter, the general solution strategy developed for the Richards equation is extended to the transient, one-dimensional, two-fluid flow equations. Initial-boundary-value problems in two-fluid flow are solved using the Runge-Kutta integration technique in conjunction with the shooting method to satisfy the specified boundary conditions. This approach differs from finite difference and finite element models in the following ways:

- A set of equations is solved explicitly and sequentially, whereas finite difference and finite element formulations generally require simultaneous solution of a set of equations.

- The spacing between nodes is varied within and between time steps based on accuracy criteria. This differs from traditional models which rely on a fixed-in-space numerical mesh.

- The iteration process requires convergence of only one or two boundary condition values, rather than iterations being performed simultaneously on values associated with all internal nodes.

Exact integral solutions for one-dimensional, two-fluid flow have been developed by McWhorter and Sunada (1990). These solutions are limited to horizontal flow problems and assume a semi-infinite, homogenous porous medium. The semi-analytical technique

described in this chapter extends the McWhorter-Sunada solutions to vertical flow, layered systems, and finite-length flow regions. The resulting transient model has been successfully applied to several types of imbibition and drainage problems in homogeneous and layered porous media.

## 1.2    THEORY

Partial differential equations for one-dimensional flow of two immiscible, incompressible fluids have been derived by several authors (e.g., Buckley and Leverett, 1942; McWhorter, 1971; Morel-Seytoux, 1973; Fokas and Yortsos, 1982; Corey, 1994). A discussion of these equations and associated assumptions is provided in McWhorter and Sunada (1990).

Referring to Figure 1-1, the flux equation for two-fluid flow can be written as:

$$q_w = q_t f - \sin(\theta)E - D\frac{\partial S_e}{\partial x} \qquad (1\text{-}1)$$

where the nomenclature is defined in Table 1. In this form, the flux equation is written using effective saturation ($S_e$) as the dependent variable. Effective saturation is a normalized saturation for the wetting fluid defined by:

$$S_e(h_c) = \frac{S_w - S_r}{1 - S_r} \qquad (1\text{-}2)$$

$S_e$ is functionally related to capillary pressure head ($h_c$), which is defined as the difference between the nonwetting and wetting fluid pressure heads:

$$h_c = h_{nw} - h_w \qquad (1\text{-}3)$$
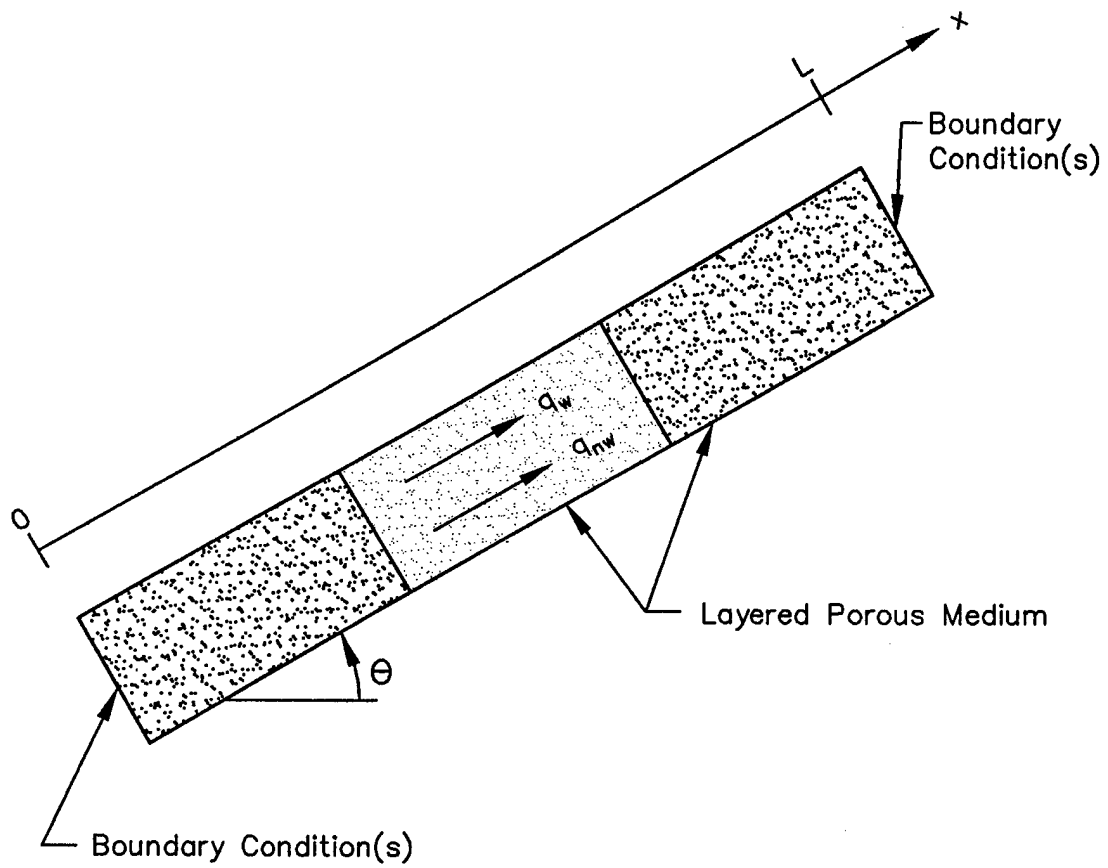
**Figure 1-1. One-Dimensional Flow Domain for the Two-Fluid Solution.**

## Table 1-1. Nomenclature Used for the Two-Fluid Solution.

C      Effective saturation capacity $[L^{-1}]$

D      Hydraulic diffusivity function for two-fluid flow $[L^2 \, T^{-1}]$

E      Gravity-related function for two-fluid flow $[L \, T^{-1}]$

f      Mobility ratio [dimensionless]

g      Acceleration of gravity $[L \, T^{-2}]$

h      Fluid pressure head [L]

$h_c$      Capillary pressure head [L]

$h_d$      Brooks-Corey displacement pressure head [L]

$h_{nw}$      Nonwetting-fluid pressure head [L]

$h_w$      Wetting-fluid pressure head [L]

k      Intrinsic permeability of porous media $[L^2]$

$k_{mw}$      Relative permeability of nonwetting fluid [dimensionless]

$k_{rw}$      Relative permeability of wetting fluid [dimensionless]

$q_{nw}$      Nonwetting fluid flux (Darcy velocity) $[L \, T^{-1}]$

$q_w$      Wetting fluid flux (Darcy velocity) $[L \, T^{-1}]$

$q_t$      Total fluid flux (Darcy velocity) $[L \, T^{-1}]$

P      Fluid pressure $[M \, L^{-1} \, T^{-2}]$

$S_e$      Effective saturation [dimensionless]

$S_e^t$      Effective saturation at time level t (end of last time step) [dimensionless]

$S_e^{t+\Delta t}$      Effective saturation at time level $t+\Delta t$ (end of current time step) [dimensionless]

$S_{nw}$      Volumetric nonwetting-fluid saturation [dimensionless]

$S_o$      Initial effective saturation at t = 0 [dimensionless]

$S_w$      Volumetric wetting-fluid saturation [dimensionless]

$S_r$      Irreducible volumetric saturation [dimensionless]

t      Elapsed time [T]

$\Delta t$      Duration of time step [T]

x      Distance from boundary [L]

$\Delta x$      Distance between two adjacent nodes [L]

θ      Orientation of flow system (angle counterclockwise from horizontal) [degrees or radians]

φ      Total porosity [dimensionless]

**Table 1-1. (continued)**

$\lambda$      Brooks-Corey pore size distribution index [dimensionless]

$\rho_o$      Reference density [M L$^{-3}$]

$\rho_{nw}$      Density of nonwetting fluid [M L$^{-3}$]

$\rho_w$      Density of wetting fluid [M L$^{-3}$]

$\mu_{nw}$      Viscosity of nonwetting fluid [M L$^{-1}$ T$^{-1}$]

$\mu_w$      Viscosity of wetting fluid [M L$^{-1}$ T$^{-1}$]

$S_r$ in equation (2) is the irreducible (minimum) wetting fluid saturation which is approached at very high capillary pressure heads.

In the flux equation, the functions f, D, and E are defined, respectively, as:

$$f(S_e) = \left[ 1 + \frac{k_{mw}(S_e)\ \mu_w}{k_{rw}(S_e)\ \mu_{nw}} \right]^{-1} \tag{1-4}$$

$$D(S_e) = -\left( \frac{k\rho_o g}{\mu_{nw}} \right) \frac{k_{mw}(S_e)\ f(S_e)}{C(S_e)} \tag{1-5}$$

$$E(S_e) = \left( 1 - \frac{\rho_{nw}}{\rho_w} \right) \left( \frac{k\rho_o g}{u_{nw}} \right) k_{mw}(S_e)\ f(S_e) \tag{1-6}$$

where:

$$C(S_e) = \frac{dS_e}{dh_c} \tag{1-7}$$

and $k_{rw}$ and $k_{mw}$ are the relative permeabilities of the wetting and nonwetting fluids, respectively. In equations (1-5) and (1-6), $\rho_o$ is an arbitrary reference density which relates fluid pressures to pressure heads:

$$h = \frac{P}{\rho_o g} \qquad (1\text{-}8)$$

Total volume flux ($q_t$) is defined as the sum of the wetting and nonwetting fluid fluxes:

$$q_t = q_w + q_{nw} \qquad (1\text{-}9)$$

If the porous medium is rigid and contains two incompressible fluids, continuity relationships lead to:

$$\frac{\partial q_t}{\partial x} = 0 \qquad (1\text{-}10)$$

which requires that $q_t(x,t) = q_t(t)$. In other words, at any given time, the total flux is spatially uniform throughout the flow system.

In terms of effective saturation, the differential form of the wetting fluid continuity equation in the x direction is:

$$\frac{\partial q_w}{\partial x} = -\phi(1-S_r)\frac{\partial S_e}{\partial t} \qquad (1\text{-}11)$$

Taking the derivative of (1-1) and combining with (1-11) leads to the governing flow equation for two-fluid flow:

$$\frac{\partial}{\partial x}\left(D\frac{\partial S_e}{\partial x}\right) + \left[\sin(\theta)\left(\frac{dE}{dS_e}\right) - q_t\left(\frac{df}{dS_e}\right)\right]\frac{\partial S_e}{\partial x} = \phi(1-S_r)\frac{\partial S_e}{\partial t} \qquad (1\text{-}12)$$

Note that in order to preserve continuity of the nonwetting fluid, the two-fluid model requires that differential equations (1-10) and (1-12) be solved simultaneously.

## 1.3    BROOKS-COREY RELATIONSHIPS

In equation (1-12), the functional relationships between capillary pressure head, effective saturation, and relative permeabilities are completely arbitrary. In this study, we use equations developed by Brooks and Corey (1964, 1966) to define these constitutive relationships. Effective saturation is related to capillary pressure head as follows:

$$S_e(h_c) = \begin{cases} \left( \dfrac{h_c}{h_d} \right)^{-\lambda} & \text{for } h_c > h_d \\ 1 & \text{for } h_c \leq h_d \end{cases} \tag{1-13}$$

where $\lambda$ is the pore size distribution index for the porous medium and $h_d$ is the displacement pressure for the medium and fluids of interest. Note that during drainage, the capillary pressure head must exceed the displacement pressure head before desaturation ($S_e < 1$) takes place.

Relative permeabilities for the wetting and nonwetting fluids are:

$$k_{rw}(S_e) = S_e^{3+2/\lambda} \tag{1-14}$$

$$k_{rnw}(S_e) = (1 - S_e)^2 \left( 1 - S_e^{1+2/\lambda} \right) \tag{1-15}$$

Note that Corey (1994) presents some modifications to the above equation for $k_{rnw}$ which are not utilized in this chapter. The function C is given by:

$$C(S_e) = -\frac{\lambda}{h_d} S_e^{1+1/\lambda} \tag{1-16}$$

All other functions used in this chapter can be derived by algebraic manipulation and/or differentiation of the above equations.

## 1.4 NUMERICAL APPROACH

### 1.4.1 Approximation of the Two-Fluid Flow Equation

For conditions where $S_e < 1$, we approximate the time derivative in (1-12) using a finite difference approach:

$$\frac{d}{dx}\left(D\frac{dS_e}{dx}\right) + \left[\sin(\theta)\left(\frac{dE}{dS_e}\right) - q_t\left(\frac{df}{dS_e}\right)\right]\frac{dS_e}{dx} = \phi(1-S_r)\left(\frac{S_e^{t+\Delta t} - S_e^{t}}{\Delta t}\right) \quad (1\text{-}17)$$

where $\Delta t$ is the duration of the current time step, and $S_e^{t}$, $S_e^{t+\Delta t}$ are the effective saturations at x occurring at the beginning and end of the time step, respectively. Since time (t) is no longer an independent variable, we express the left-hand side of (1-17) in terms of ordinary derivatives. Applying the chain rule to the left-hand side and algebraic manipulation leads to:

$$\frac{d^2 S_e^{t+\Delta t}}{dx^2} = \left[-\frac{\left(\frac{dD}{dS_e}\right)}{D}\right]\left(\frac{dS_e^{t+\Delta t}}{dx}\right)^2 + \left[\frac{q_t\left(\frac{df}{dS_e}\right) - \sin(\theta)\left(\frac{dE}{dS_e}\right)}{D}\right]\frac{dS_e^{t+\Delta t}}{dx} + \dots$$

$$\dots \left[\frac{\phi(1-S_r)}{\Delta t\, D}\right]S_e^{t+\Delta t} + \left[-\frac{\phi(1-S_r)}{\Delta t\, D}S_e^{t}(x)\right] \quad (1\text{-}18)$$

Note that in the above equation, the dependent variable $S_e$ and its space derivatives are evaluated at time level $t+\Delta t$ (i.e., at the end of the current time step), which implies a fully backward-in-time numerical scheme. Furthermore, the value $S_e^{t}(x)$ is known *a priori* from the results of the last time step. Adopting the notation, $S_e = S_e^{t+\Delta t}$, equation (1-18) has the general form:

$$S_e'' = F(S_e, S_e', q_t, x) = f_1 \cdot (S_e')^2 + f_2 \cdot S_e' + f_3 \cdot S_e + f_4 \quad (1\text{-}19)$$

where $f_1$ and $f_3$ are functions of $S_e$, $f_2$ is a function of $S_e$ and $q_t$, and $f_4$ is a function of $S_e$ and x. For each time step, this second-order ordinary differential equation is integrated to determine both $S_e(x)$ and $S_e'(x)$ using the fifth-order Runge-Kutta algorithms presented in Press *et al.* (1992). These algorithms contain an adaptive stepsize control, which modifies the distance between nodes ($\Delta x$) based on user-specified accuracy criteria. Since the node coordinates change each time the solution is evaluated, values of $S_e^t(x)$ must be interpolated from results of the previous time step. This is performed using the cubic spline interpolation algorithm presented in Press *et al.* (1992).

Calculations proceed node-by-node beginning at x = 0. Evaluation at a node only requires information determined from previous nodes within the sequence. As a result, the numerical scheme is explicit and requires only the sequential solution of independent equations. Once the values $S_e(x_i)$ and $S_e'(x_i)$ are obtained for a node located at coordinate $x_i$, the capillary pressure head at that node is computed based on equation (1-13):

$$h_c(x_i) = h_d [S_e(x_i)]^{-1/\lambda} \qquad (1\text{-}20)$$

and the wetting fluid flux at the node is computed directly from equation (1):

$$q_w(x_i) = q_t f[S_e(x_i)] - \sin(\theta) E[S_e(x_i)] - D[S_e(x_i)] S_e'(x_i) \qquad (1\text{-}21)$$

The wetting fluid pressure head at the node is computed using a finite difference approximation to the Darcy equation:

$$h_w(x_i) = h_w(x_{i-1}) - \frac{\Delta x \, \mu_w}{2k\rho_o g}\left\{\frac{q_w(x_{i-1})}{k_{rw}[S_e(x_{i-1})]} + \frac{q_w(x_i)}{k_{rw}[S_e(x_i)]}\right\} - \frac{\Delta x \, \rho_w \sin(\theta)}{\rho_o} \qquad (1\text{-}22)$$

where $\Delta x$ is the distance between nodes $x_{i-1}$ and $x_i$. Nonwetting fluid pressure head is computed from the definition of capillary pressure in equation (1-3):

$$h_{nw}(x_i) = h_c(x_i) + h_w(x_i) \tag{1-23}$$

By equation (1-2), the wetting fluid saturation is given by:

$$S_w(x_i) = S_r + (1 - S_r) S_e(x_i) \tag{1-24}$$

and based on continuity, the nonwetting fluid saturation is:

$$S_{nw}(x_i) = 1 - S_w(x_i) \tag{1-25}$$

### 1.4.2 Saturated Conditions

If the porous medium is saturated between two adjacent nodes, $S_e = 1$, $k_{rw} = 1$, and $q_w$ has the same value at both nodes. Equation (1-22) therefore simplifies to:

$$h_w(x_i) = h_w(x_{i-1}) - \Delta x \left[ \frac{q_w(x_{i-1}) \mu_w}{k \rho_o g} + \frac{\rho_w \sin(\theta)}{\rho_o} \right] \tag{1-26}$$

In saturated media, the nonwetting fluid does not exist as continuous (mobile) fluid and thus, its pressure head does not have physical relevance with regard to fluid flow.

### 1.4.3 Material Interfaces

Referring to Figure 1-2, at the interface between two materials, there can be a discontinuity in effective saturation, but pressure heads and fluxes must be

Interface

Material (A)

$q_t{}^A \left\{ \begin{array}{l} q_{nw}{}^A \longrightarrow \\ \\ q_w{}^A \longrightarrow \end{array} \right.$

$\left. \begin{array}{l} \longrightarrow q_{nw}{}^B \\ \\ \longrightarrow q_w{}^B \end{array} \right\} q_t{}^B$

$h_c{}^A \left\{ \begin{array}{l} h_{nw}{}^A \\ \\ h_w{}^A \end{array} \right.$

$\left. \begin{array}{l} h_{nw}{}^B \\ \\ h_w{}^B \end{array} \right\} h_c{}^B$
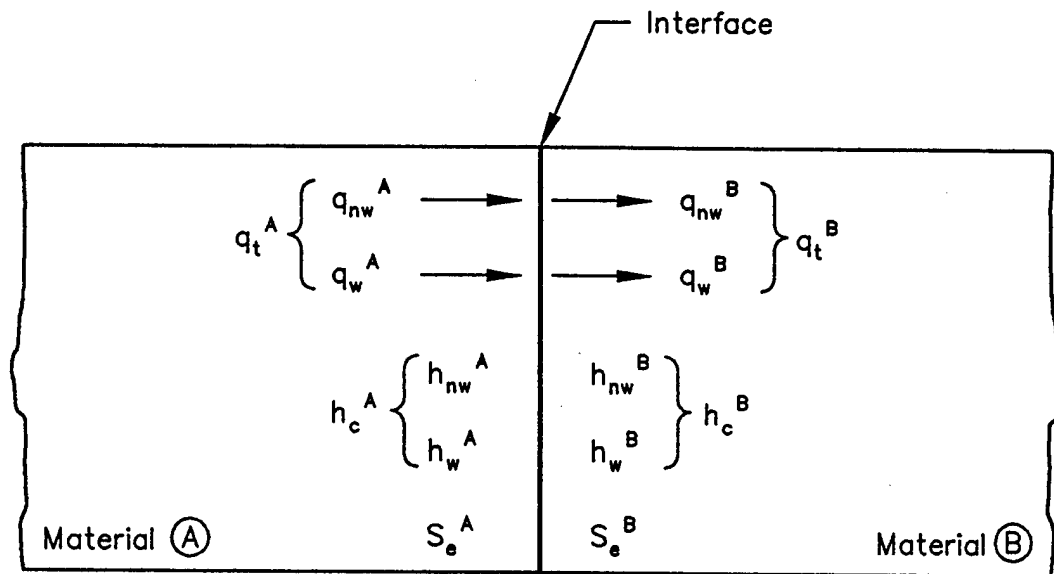
$S_e{}^A$ $S_e{}^B$

Material (B)

Flux Continutiy $\left\{ \begin{array}{l} q_{nw}{}^A = q_{nw}{}^B \\ \\ q_w{}^A = q_w{}^B \end{array} \right\} q_t{}^A = q_t{}^B$

Pressure Continuity $\left\{ \begin{array}{l} h_{nw}{}^A = h_{nw}{}^B \\ \\ h_w{}^A = h_w{}^B \end{array} \right\} h_c{}^A = h_c{}^B$

Saturation Discontinuity $\qquad S_e{}^A \neq S_e{}^B$

**Figure 1-2.** **Numerical Formulation Across a Material Interface for the Two-Fluid Solution.**

continuous across the interface. Using the Brooks-Corey relationships and taking advantage of capillary pressure head continuity:

$$
S_e^B = \begin{cases} \left( \dfrac{h_c^A}{h_d^B} \right)^{-\lambda^B} & \text{for} \quad h_c^A > h_d^B \\[3ex] 1 & \text{for} \quad h_c^A \le h_d^B \end{cases} \tag{1-27}
$$

where the superscript A indicates the capillary pressure head computed in material A *at the interface*, the result of previous calculations, and B indicates capillary properties associated with material B. Note that the above equation is applied only when evaluating the first node (boundary) of a new material layer.

If the magnitude of the nonwetting fluid flux ($q_{nw}$) is greater than zero, flux continuity can be maintained across an interface only if the effective saturation is less than unity on both sides of the interface. When the Runge-Kutta solution is extended across an interface, there can exist a situation where the magnitude of the nonwetting fluid flux is significant, but equation (1-27) computes $S_e^B$ equal to one. This occurs when the capillary pressure in material A is less than the displacement pressure for material B. In this case, the algorithm artificially increases the nonwetting fluid pressure on the B side of the interface so that effective saturation ($S_e^B$) is reduced to 0.999, which is equivalent to raising the capillary pressure to just slightly above the displacement pressure in material B. This procedure allows nonwetting fluid flux continuity to be maintained, but creates a step-change in the nonwetting fluid pressure head and capillary pressure head across the interface. Laboratory experiments have indicated that when a nonwetting fluid exits the outflow face of a porous material, there is a tendency for the wetting fluid saturation to approach unity at the face (Perkins, 1957; McWhorter, 1971; Davis, 1990). For steady flow simulations, Corey (1994) recommends that capillary pressure head at the outflow face be specified as

approximately equal to the displacement pressure head of the porous medium. For material interfaces *within* a flow region, we follow this recommendation by setting the capillary pressure head in the upstream material to just above its displacement pressure head.

### 1.4.4 Boundary Conditions

A characteristic of the numerical formulation is that the solution is constructed explicitly, beginning at $x = 0$ and then proceeding node-by-node across the flow region. To begin the calculations, an input value of $\Delta t$ and boundary conditions at $x = 0$ must be provided. These boundary conditions are $q_w(0,t)$, $S_e(0,t)$, and $q_t(t)$. Note that effective saturation is uniquely defined by specifying either the capillary pressure head or the pressure heads of both fluids. These values can be used in place of effective saturation as a boundary condition. Also, for incompressible fluids, the total fluid flux at time t is a constant for all values of x. When using the Runge Kutta method, it is not known in advance what values of $q_w$, $q_{nw}$, or $S_e$ will be computed at the opposite $(x = L)$ boundary of the system. If boundary conditions are *specified* at $x = L$, an iterative procedure, commonly referred to as the shooting method (Press *et al.*, 1992; Acton, 1990; Keller, 1968), is used to satisfy those conditions. For example, suppose that the prescribed boundary conditions for the problem are $q_t(t)$, $S_e(0,t)$, and $S_e(L,t)$ as shown on Figure 1-3. In this case, we input $\Delta t$, $q_t(t)$, the prescribed value of $S_e(0,t)$, and a *trial* value of $q_w(0,t)$. Then $q_w(0,t)$ is varied in a trial-and-error manner until the computed $S_e$ at the opposite end of the flow system corresponds to the prescribed $x = L$ boundary condition. Depending on the problem under consideration, different combinations of boundary conditions at $x = 0$ can be evaluated using the shooting method to satisfy a prescribed boundary condition at $x = L$.

$$q_t(x,t) = q_t(t)$$

$S_e (0,t)$

Flow Domain

$S_e (L,t)$

$q_w (0,t)$

$q_w (L,t)$

$h_w$

1

3

2

4

$S_e (0,t)$

$S_e (L,t)$

0                                                                L

x
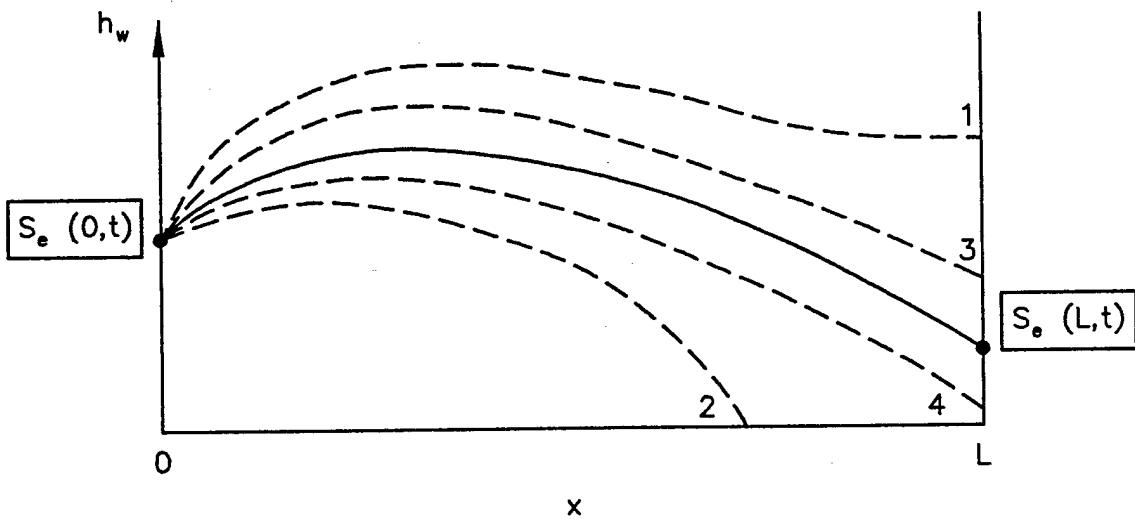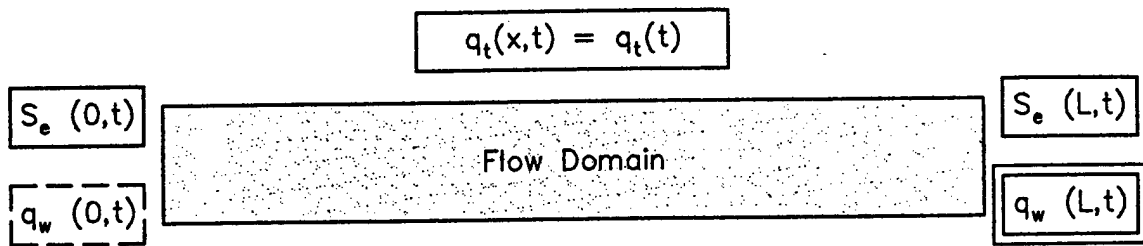
Prescribed Boundary Condition

Trial Value

Computed Value

- - - -  Trial Solution

————  True (Converged) Solution

**Figure 1-3.  Shooting Method Used for the Two-Fluid Solution.**

## 1.5 EXAMPLE SIMULATIONS

### 1.5.1 Example 3A - Horizontal, Two-Direction Displacement of a Nonwetting Fluid

This example considers the displacement of a nonwetting fluid by injection of wetting fluid at one end of a horizontal, finite-length soil column. A description of this initial-boundary-value problem is shown on Figure 1-4 and input parameters are summarized in Table 1-2. Initially, the homogeneous medium-grained sand column contains two fluids under no-flow conditions. The initial pressure heads are zero for the wetting fluid and 32.32 cm for the nonwetting fluid. At the corresponding capillary pressure head of 32.32 cm, the initial effective saturation $(S_o)$ is 0.10 and the volumetric wetting fluid saturation is 0.19 throughout the column. At time zero, the wetting fluid pressure head at x = 0 increases instantaneously from zero to 16.16 cm, which is equivalent to instantaneously raising the saturation from 0.19 to 0.82 at the left side of the column. The increase in wetting fluid pressure and saturation at x = 0 causes the wetting fluid to imbibe into the column which results in displacement of the nonwetting fluid. In general, the displaced nonwetting fluid will exit the column as counter-current flow at x = 0 *and* unidirectional flow at x = L; in other words, the nonwetting fluid displacement process is two-directional. The relative magnitudes of nonwetting fluid outflows at each end of the column depends on the position of the saturation front over time and the pressure heads maintained at x = 0 and x = L.

For this type of physical problem, a two-step iteration procedure is used for each time step. First, the bisect method (Kreyszig, 1988) is used to iterate on $q_w(0,t)$, based on a trial input value of the total fluid flux $[q_t(t)]$. Prior to the saturation front reaching the x = L boundary, these iterations are performed until $S_e(x^*) = S_o$ and $S_e'(x^*) = 0$ at some coordinate $x^* < L$. After the saturation front reaches the x = L boundary, the iterations are performed until $S_e(L) = S_o$. When either of the above conditions are met, the wetting fluid pressure head is computed at x = L and compared with the prescribed
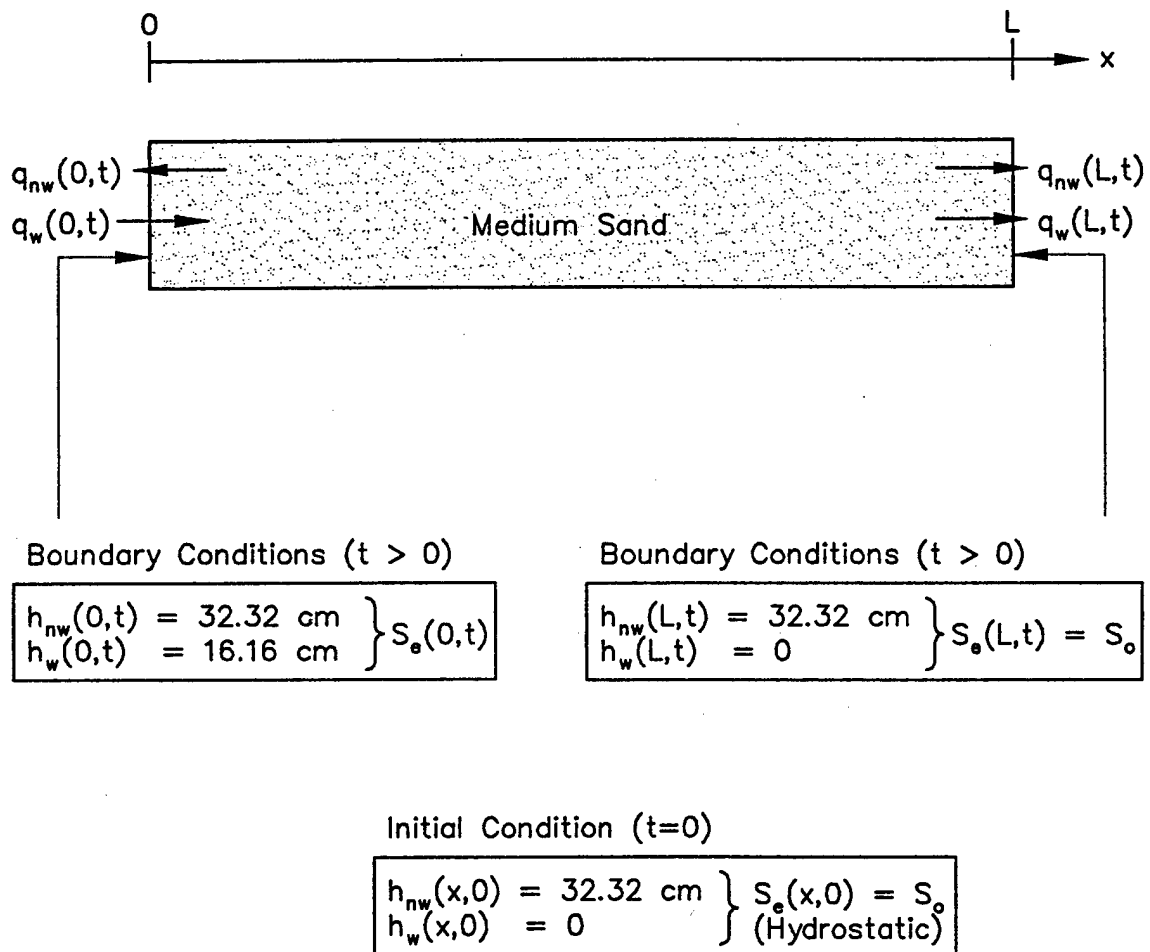
Figure 1-4.    Example 3A - Horizontal, Two-Direction Displacement of a
Nonwetting Fluid Solved by the Two-Fluid Solution.

**Table 1-2.**    **Parameters Used in Example Simulations Based on the Two-Fluid Solution.**

| | | | |
|---|---|---|---|
| $\rho_{nw}$ | 0.8 | $g\ cm^{-3}$ | |
| $\rho_w$ | 1 | $g\ cm^{-3}$ | (water) |
| $\rho_o$ | 1 | $g\ cm^{-3}$ | (water) |
| $g$ | 980 | $cm\ s^{-2}$ | |
| $\mu_{nw}$ | 0.005 | $g\ cm^{-1}\ s^{-1}$ | |
| $\mu_w$ | 0.01 | $g\ cm^{-1}\ s^{-1}$ | |
| $\theta$ | 0 | degrees | (Example 3A) |
| | 90 | degrees | (Example 3B) |

| | Coarse Sand | | Medium Sand | |
|---|---|---|---|---|
| $k$ | $10^{-6}$ | $cm^2$ | $10^{-7}$ | $cm^2$ |
| $\lambda$ | 4 | | 3 | |
| $h_d$ | 10 | cm | 15 | cm |
| $S_r$ | 0.05 | | 0.1 | |
| $\phi$ | 0.35 | | 0.35 | |

boundary condition $h_w(L,t)$. Based on the difference between the computed and prescribed wetting fluid pressures, the trial value of $q_t(t)$ is adjusted and the iteration process repeated. Convergence for the time step is achieved when the computed wetting fluid pressure head at $x = L$ corresponds to the prescribed boundary condition. Using the secant method (Kreyszig, 1988), convergence is usually achieved with three to six adjustments of the $q_t$ value.

Progression of the saturation front into the column is shown on Figure 1-5. Prior to the front reaching the $x = L$ boundary, the saturation profiles have a characteristic shape which is similar to that of nonwetting fluid displacements in a semi-infinite column (McWhorter and Sunada, 1990). At large times, after the front has reached the $x = L$

boundary, the saturation profile takes on the characteristic shape for steady-state flow, in this case with the nonwetting fluid flux is close to zero. Figure 1-6 shows saturation and pressure head profiles existing at an elapsed time of 10,500 seconds. Of interest is the nonwetting fluid pressure head distribution (Figure 1-6b). Although the same nonwetting fluid pressure head is prescribed at both ends of the column, an increased pressure head develops inside the column. This creates a flow divide at $x = 18.4$ cm. Left of the divide, the nonwetting fluid moves toward the $x = 0$ side of the column (counter-current to the wetting fluid flux) and right of the divide, nonwetting fluid flow is toward the $x = L$ boundary (same direction as the wetting fluid flux).

The magnitude of fluid fluxes at the boundaries of the column are shown on Figure 1-7. At early times, fluxes occurring at $x = L$ are relatively small and wetting fluid inflow at $x = 0$ is approximately equal to the nonwetting fluid outflow. Therefore, essentially full counter-current flow occurs at this early stage of the displacement process. At an elapsed time of about $7 \times 10^4$ seconds, the nonwetting fluid outflow at $x = 0$ is relatively small and wetting fluid inflow at $x = 0$ and nonwetting fluid outflow at $x = L$ are approximately equal. This indicates that displacement process is nearly unidirectional throughout the column.

As the saturation front reaches the $x = L$ boundary, there is a rapid increase in the wetting fluid outflow and at large times, a steady-state condition is reached where the wetting fluid inflow at $x = 0$ is approximately equal to its outflow at $x = L$. Because the nonwetting fluid pressure heads are the same at both ends of the column, the nonwetting fluid flux should tend towards zero throughout the column as steady-state is approached. On Figure 1-7, this is clearly shown for the nonwetting fluid outflow at $x = L$. At large time, the nonwetting fluid outflow at $x = 0$ is shown to reach a steady-state flux of about two orders of magnitude lower than the wetting fluid fluxes. This computed nonzero outflow rate appears to be a numerical artifact related to the overall accuracy of the semi-analytical solution.
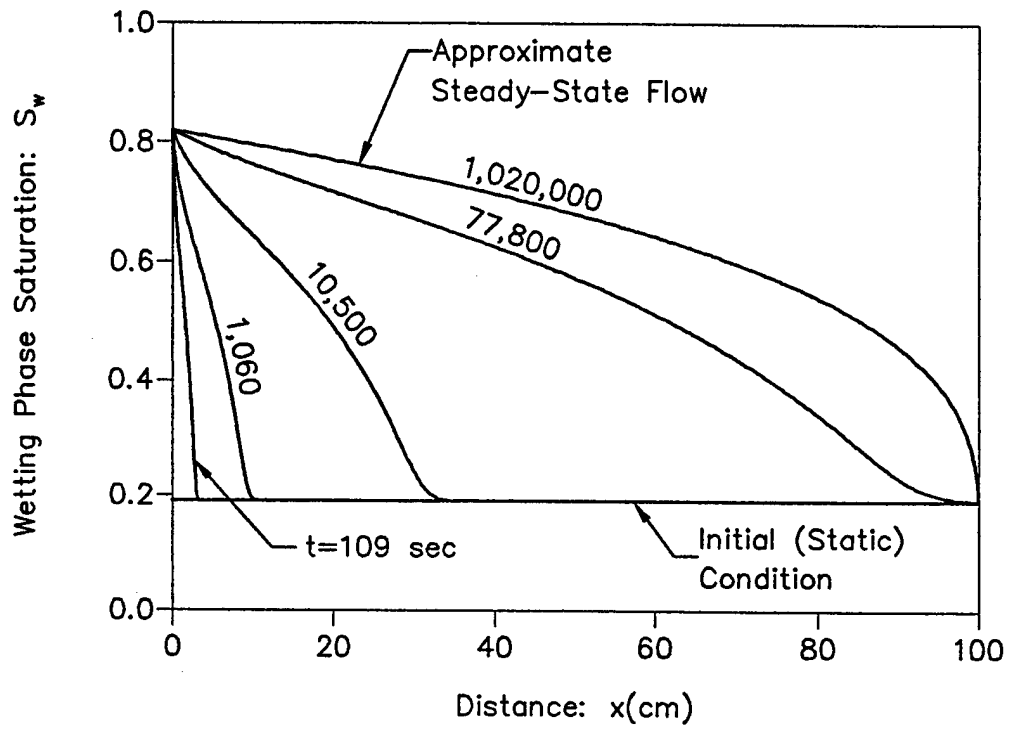
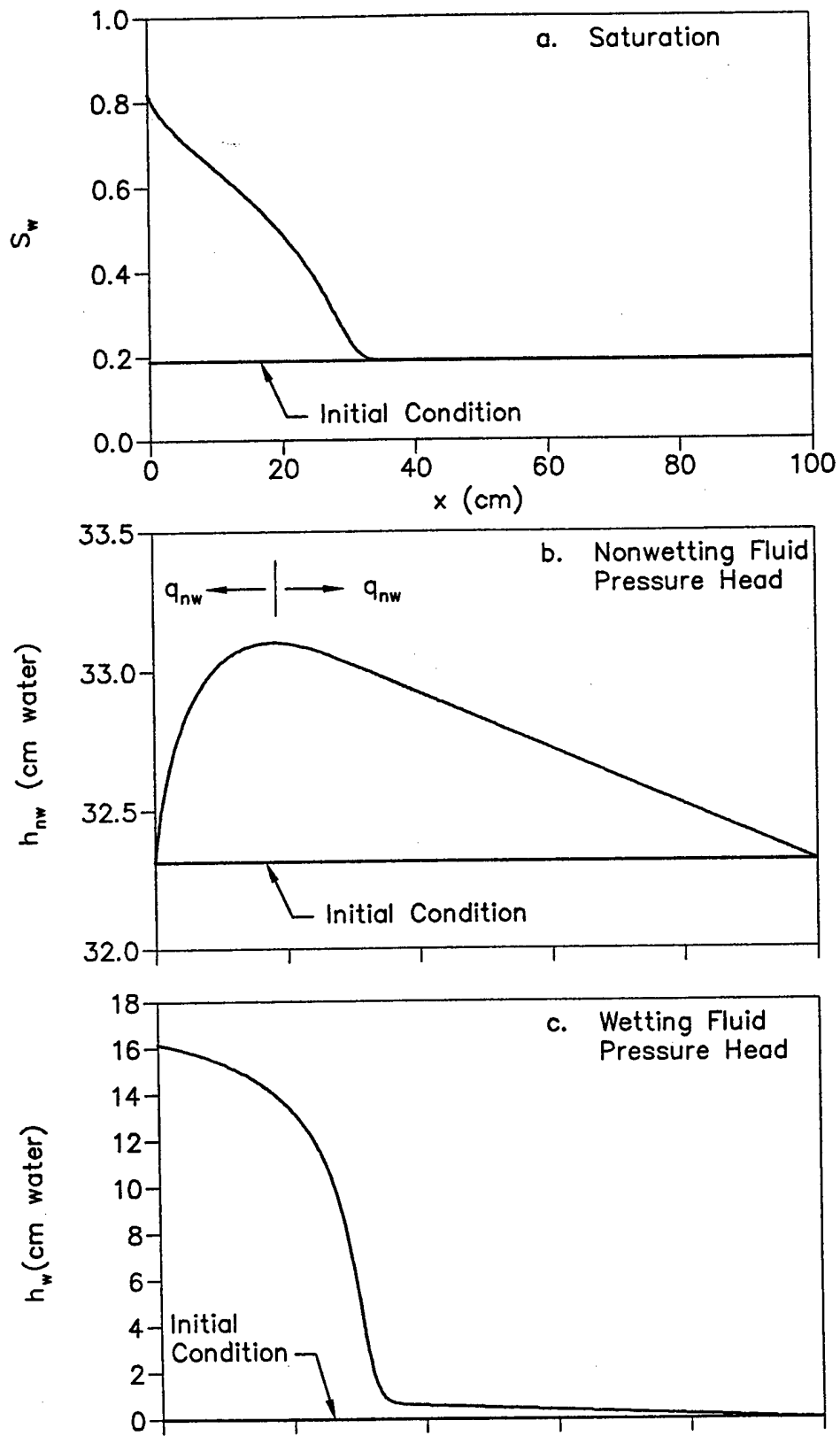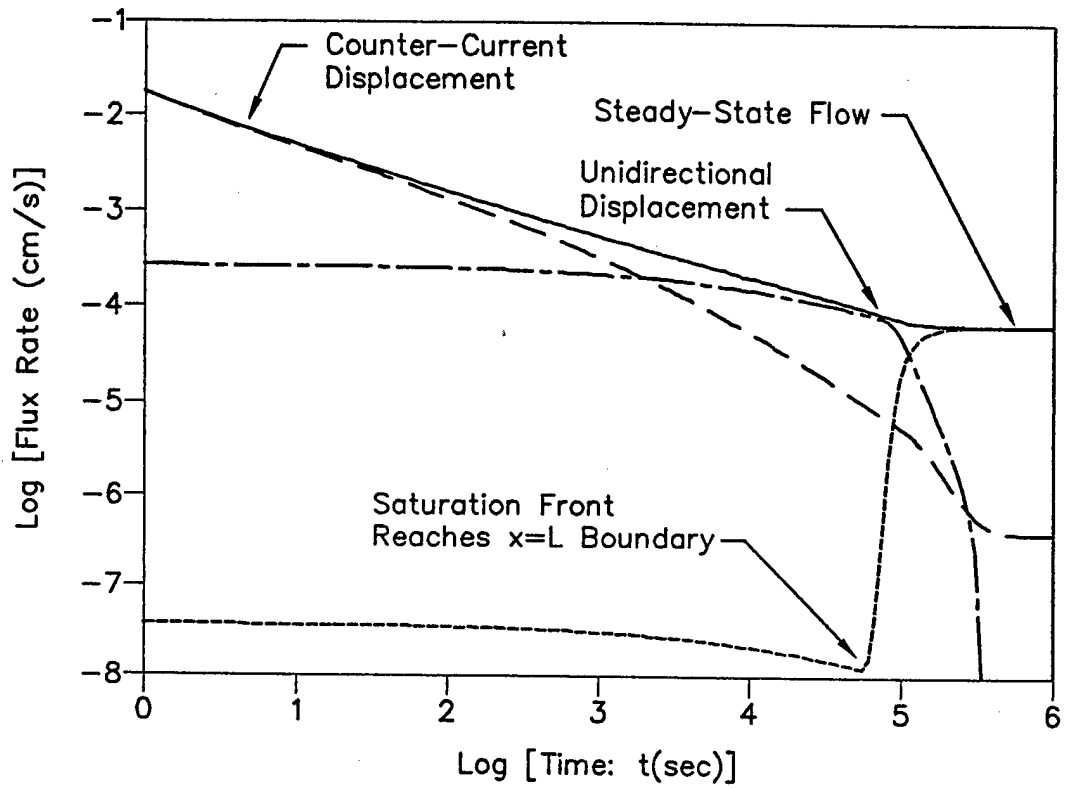**Figure 1-5. Example 3A - Saturation Profiles.**

**Figure 1-6.** Example 3A - Saturation and Pressure Head Profiles.
t = 10,500 seconds

Figure 1-7. Example 3A - Wetting and Nonwetting Fluid Fluxes.

## 1.5.2 Example 3B - Vertical Migration of LNAPL in a Layered Soil

This example considers the downward migration of a light nonaqueous phase liquid (LNAPL), through a layered soil, in response to a lowering of the water table. This constitutes a drainage problem where the wetting fluid (water) is displaced by the nonwetting fluid (LNAPL). The physical problem for the simulation is shown on Figure 1-8 and input parameters are summarized in Table 1-2. The flow domain consists of a three-layer system with a zone of coarse sand situated between two layers of medium sand. Initially, the system is fully saturated with the water-table located at the top of the soil profile. For static conditions, this results in a water pressure head of 100 cm at the base of the profile. At time zero, the water pressure head at the base of the profile is instantaneously lowered from 100 to 67 cm, and a shallow ponding condition for the LNAPL is imposed at the top of the profile. Since the fluids and porous media are assumed to be incompressible, the water pressure head at the top of the profile decreases at time zero and the associated capillary pressure head becomes greater than displacement pressure head. As a consequence, water drains at the top of the soil profile and is displaced by downward moving LNAPL. The displaced water exits the system as outflow at the bottom of the profile.

For this type simulation, a two-step iteration procedure is used for each time step. We define a desaturation point ($x^*$) such that the effective saturation ($S_e$) is equal to 1 for all $x \leq x^*$ and is less than 1 for $x > x^*$. The first step is to input a trial value of $q_w(0,t)$ and then iterate on the $x^*$ value. For $x < x^*$, the system is fully saturated, $q_w = q_t = $ constant, and the water pressure head ($h_w$) distribution is computed using the saturated form of Darcy's law. At $x = x^*$, the following conditions exist: $S_e = 1$, $S_e' \rightarrow (-\infty)$, and $q_t = q_w(0,t)$. These conditions are used as the starting point for the Runge-Kutta method to compute the saturation distribution within the $x > x^*$ region. Using the bisect method, iterations are performed on the $x^*$ value until
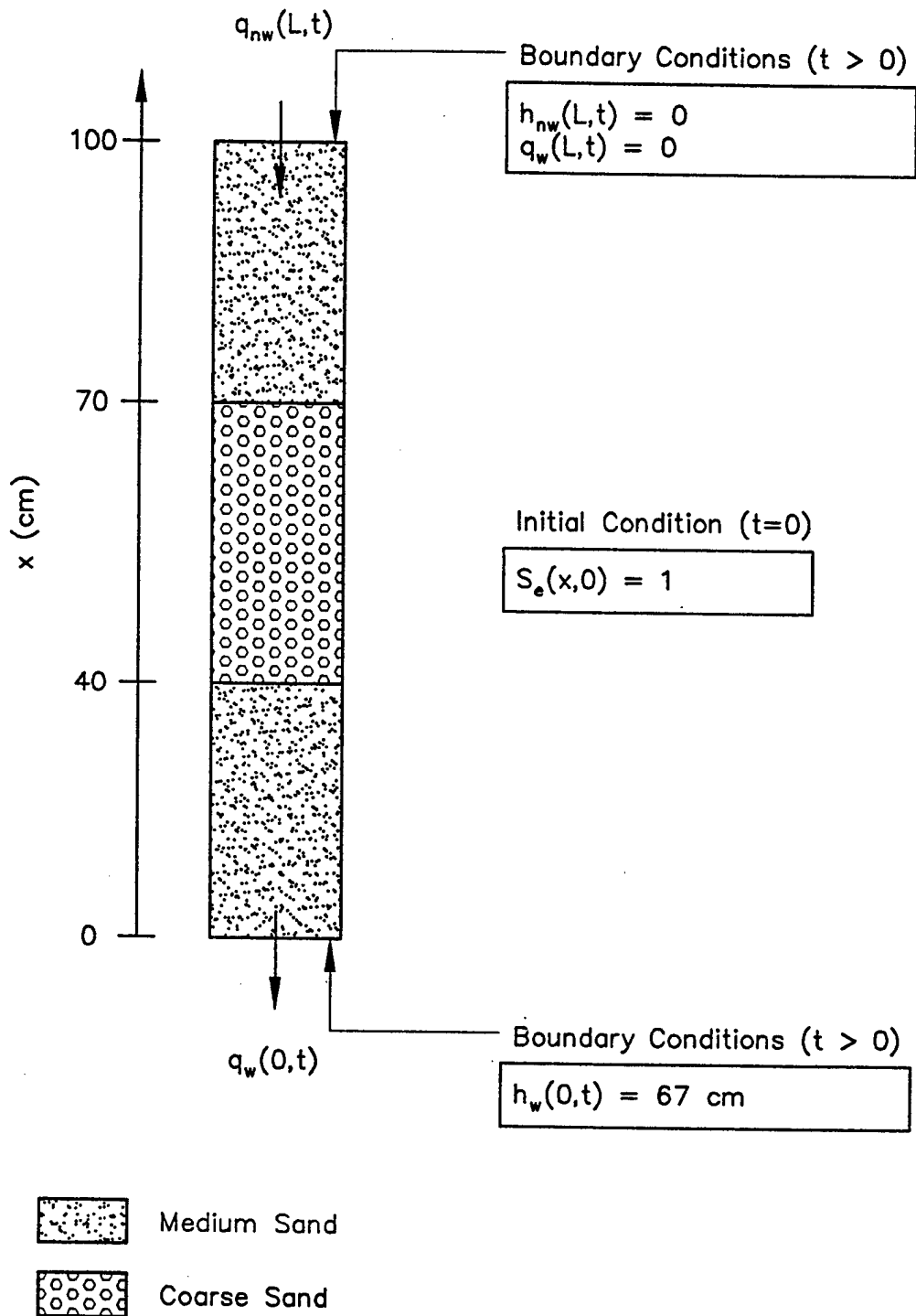
Figure 1-8.   Example 3B - Downward Migration of LNAPL in a Layered Soil
Solved by the Two-Fluid Solution.

$q_w(L,t)$ is computed to be approximately equal to zero, thus satisfying the prescribed no-water-flow boundary condition at the top of the profile. The next step is to compute the nonwetting fluid pressure head at the top of the profile [$h_{nw}(L,t)$]. To satisfy the shallow ponding condition for LNAPL, this value should be zero. If this value is significantly different than zero, the $q_w(0,t)$ input value is adjusted and iterations are once again performed on $x^*$. Using the secant method, the $q_w(0,t)$ input value typically requires three to six adjustments to satisfy the prescribed $h_{nw}(L,t)$ boundary condition. Under certain conditions, the desaturation point may exist at a material interface and the effective saturation at the interface falls below one. In this case, $x^*$ is fixed at the interface coordinate and iterations are performed on $S_e$ rather than $x^*$.

The progression of saturation profiles over time is shown on Figure 1-9. At early times (Figure 1-9a), LNAPL has migrated downward only in the upper medium sand layer and the desaturation point ($x^*$) is located at $x = 85$ cm. At a time of 4,040 seconds, the saturation front reaches the first interface and exhibits a saturation discontinuity as shown on Figure 1-9b. The wetting fluid saturation is nearly equal to one just above the interface and is significantly less than one below the interface. As time progresses (Figures 1-9c and 1-9d), the saturation profile is relatively stable in the upper layer and most desaturation occurs in the middle coarse sand layer. Note that at 12,040 seconds (Figure 1-9d), the bottom of the upper layer is just beginning to desaturate, but the saturation discontinuity across the interface remains. Also, a saturation discontinuity has developed across the interface between the middle and lower layers. At 14,190 seconds (Figure 1-9e), the middle coarse sand layer is mostly desaturated, the front has moved past the second interface, and continued desaturation occurs at the bottom of the upper layer. With increased time (Figures 1-9f and 1-9g), slow desaturation takes place primarily in the upper and lower layers. At infinite time (Figure 1-9h), the desaturation process ceases and a new static condition is established. At this stage, there is no further LNAPL migration and all fluxes are zero.
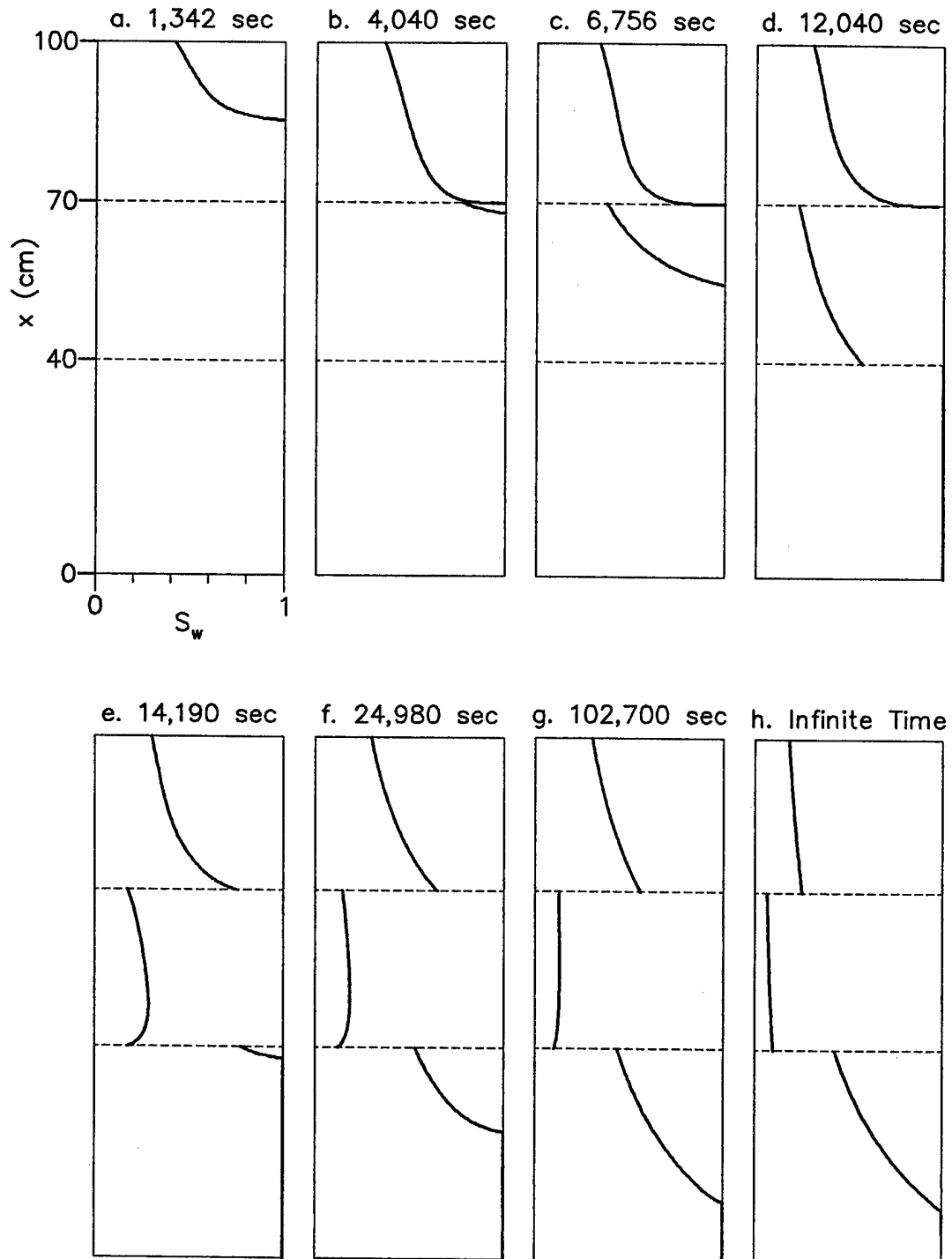
**Figure 1-9. Example 3B - Saturation Profiles.**

The variation in the total fluid flux ($q_t$) over time is shown on Figure 1-10. For this problem, the magnitude of the total fluid flux is equal to the LNAPL inflow rate at the top of the soil profile and the water outflow rate at the bottom of the profile. After the saturation front reaches the first interface (about 4,000 seconds) there is a temporary increase in the total fluid flux, which is presumably caused by the relatively rapid initial desaturation of the middle coarse sand layer. Between about 4,000 and 12,000 seconds, the flux decreases gradually as the middle layer continues to desaturate. At about 12,000 seconds, the front interacts with the second interface and there is a sharp decrease in the total fluid flux. At large times, the middle layer is almost completely desaturated and very slow desaturation takes place in the upper and lower layers. As a consequence, the flux decreases to small values.

## 1.6    DISCUSSION

The Runge-Kutta and shooting methods employed in this solution do not exhibit the types of stability problems commonly associated with traditional finite difference and finite element numerical models. We have not experienced any stability problems when a saturation front crosses a material interface, even if large discontinuities exist in both $S_e$ and $S_e'$ at the interface. The proposed solution method seems capable of efficiently solving certain types of two-fluid flow problems that have been difficult to simulate with traditional models.

There are occasions, however, when convergence within a time step is not easily achieved using this solution technique. Adjustment of accuracy parameters and/or the time step size nearly always achieves convergence, but this can be something of a trial-and-error process. We have intentionally designed the current computer code with minimum automation capabilities in selecting or adjusting these numerical parameters. It is our expectation that alternative solution methods, improved

Note: $q_t(t) = q_w(0,t) = q_{nw}(L,t)$

Front Reaches First Interface

Front Interacts with Second Interface

Middle Layer Mostly Desaturated

Approaching
Static Condition
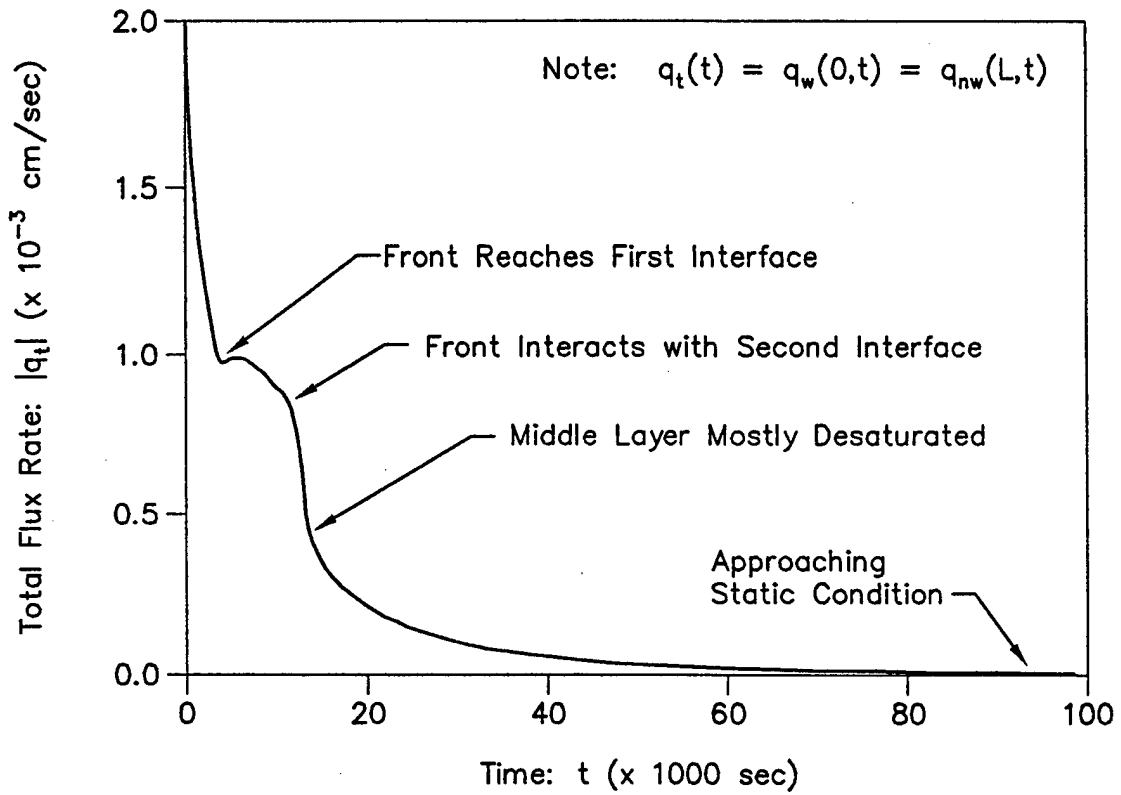
Figure 1-10. Example 3B - Total Volume Flux.

programming, and increased numerical precision, will greatly enhance the convergence characteristics of this solution method.

One significant limitation of this solution is that problem-specific iteration schemes must be designed for different types of physical problems, and sometimes the iteration scheme itself must change during the course of a simulation. Development of efficient iteration strategies can be time consuming and usually requires some physical understanding and intuition of the physical problem under consideration.

## 1.7 CONCLUSIONS

The semi-analytical solution presented in this chapter appears to be a promising technique for solving certain types of one-dimensional problems in two-fluid flow. Our goal in this chapter has been to present the basic solution strategy and show that it is capable of solving problems of practical interest in two-fluid flow. The method is particularly well suited for simulating flow in layered media and does not exhibit the types of stability problems that can occur in traditional finite difference and finite element numerical models. The primary disadvantages of the proposed solution are that it is limited to one-dimensional flow, requires the development of problem-specific iteration schemes for different types of physical problems, and sometimes does not converge smoothly within a time step. Continued development of this semi-analytical technique, however, will likely result in an efficient method for solving many types of one-dimensional, two-fluid flow problems.

## 1.8 REFERENCES

Acton, F.S. 1990. *Numerical Methods That Work; 1990 Corrected Addition.* Mathematical Association of America, Washington, D.C.

Brooks, R.H. and A.T. Corey. 1964. Hydraulic properties of porous media. Colorado State University Hydrologic Paper No. 3, Fort Collins, CO.

Brooks, R.H. and A.T. Corey. 1966. Properties of porous media affecting fluid flow. *Proc. Irrigation and Drainage Division*, American Society of Civil Engineers, 92(IR2), pp. 61-87.

Buckley, S.E. and M.C. Leverett. 1942. Mechanism of fluid displacement in sands. *Trans. American Institute of Mining, Metallogical, and Petroleum Engineers*, 146, pp. 107-116.

Corey, A.T. 1994. *Mechanics of Immiscible Fluids in Porous Media*. Water Resources Publications, Highlands Ranch, CO.

Davis, E.L. 1990. *New Laboratory Method for Determining Relative Permeability*. Ph.D. Dissertation, Colorado State University, Fort Collins.

Fokas, A.S. and Y.C. Yortsos. 1982. On the exactly solvable equation $S_t = [(\beta S + \gamma)^{-2} S_x]_x + \alpha(\beta S + \gamma)^{-2} S_x$ occurring in two-phase flow in porous media. *SIAM Journal of Applied Mathematics*, 42(2), pp. 318-332.

Keller, H.B. 1968. *Numerical Methods for Two-Point Boundary-Value Problems*. Blaisdell Publishing, Waltham, MA.

Kreyszig, E. 1988. *Advanced Engineering Mathematics, Sixth Edition*. John Wiley & Sons, Inc.

McWhorter, D.B. 1971. Infiltration affected by flow of air. Hydrology Paper No. 49, Colorado State University, Fort Collins, CO.

McWhorter, D.B. and D.K. Sunada. 1990. Exact integral solutions for two-phase flow. *Water Resources Research*, 26(3), pp 399-413.

Morel-Seytoux, H.J. 1973. Two-phase flows in porous media. In *Advances in Hydroscience*, 9, R.J.M. DeWiest, editor, Academic Press, San Diego, CA.

Perkins, Jr. F.M. 1957. An investigation of the role of capillary forces in laboratory water floods. *Trans. AIME*, 210, pp. 409-413.

Press, W.H., S.A. Teukolsky, W.T. Vetterling and B.P. Flannery. 1992. *Numerical Recipes in Fortran, the Art of Scientific Computing, Second Edition*, Cambridge University Press.

CHAPTER 2

# COMPARISON OF THE RICHARDS EQUATION AND TWO-FLUID FLOW EQUATIONS FOR DRAINAGE WITH LIMITED AIR ACCESS

**Abstract**

Analysis of drainage in air-water systems has traditionally been based on solutions to the Richards equation. Utilizing analytical models for two-fluid flow with zero and finite air viscosities, the assumptions of the Richards model are critically evaluated for the case where air access into the porous medium is restricted. It is shown that for certain types of drainage problems, the Richards model does not provide for accurate simulation of drainage behavior, particularly in layered soils with real air viscosity. Furthermore, there is a class of drainage problems for which the Richards equation does not allow a theoretical solution to be obtained. In these cases, rigorous simulation of the drainage process can only be performed by considering the two-fluid (air-water) dynamics of the system. Because the Richards equation assumes that no air pressure gradients exist within the system, it could be interpreted to contain an implicit assumption of zero air viscosity. This conceptualization is inaccurate and potentially misleading, because the Richards equation is not recovered from the two-fluid flow equations in the limit of zero air viscosity. It is more appropriate to view the Richards equation as an *unlimited air access* model, where air is *supplied* to the system at zero pressure head.

## 2.1  INTRODUCTION

Mathematical simulation of water drainage, under partially saturated conditions, is of practical interest in agricultural and geotechnical engineering. During the drainage process, any decrease in water saturation must be accompanied by movement of air

into the system to occupy pore space previously containing water. Drainage analyses using analytical equations or numerical models have traditionally been based on solutions to the Richards equation (Richards, 1931; Jury et al., 1991). Two basic assumptions in the Richards equation are (1) the air pressure is spatially uniform and (2) air is freely accessible to all points within the flow system regardless of the saturation distribution. Some investigators (Corey, 1994; Dullien, 1992) have considered the Richards equation to be applicable to systems in which air offers no resistance to flow, which could be interpreted to imply that the air viscosity is effectively equal to zero. At face value, this interpretation may seem reasonable because air viscosity is only about 2 percent of the viscosity of water. Furthermore, at zero viscosity, air movement can take place with no pressure gradient, which is consistent with the uniform air pressure assumption.

Technical interest in the simultaneous flow of immiscible fluids has led to the development of analytical solutions and numerical models which can be used to analyze two-fluid (air-water) flow in porous media. These mathematical models can explicitly account for viscous air flow and are not limited by the uniform air pressure assumption used in the Richards equation. In addition, simulations can be performed that consider limitations on the access of air into the medium. With the ability to simulate two-fluid flow in homogeneous and layered systems, it is of interest to evaluate the applicability of the Richards equation for simulating practical problems of drainage in air-water systems.

Our treatment of drainage gives full consideration to the simultaneous bulk flow of air and water. The potential effects of air flow on the drainage of water have not been systematically investigated. Most studies of simultaneous air-water flow have focused on the infiltration problem (McWhorter, 1971; Morel-Seytoux, 1969, 1973). An approximate analysis of column drainage as a two-fluid problem is presented in Morel-Seytoux (1975).

In this chapter, the assumptions of the Richards equation are critically evaluated considering two-fluid flow theory. Attention is focused on details of the flux equations associated with the Richards and two-fluid flow models. In addition, we develop and compare a third analysis approach, termed the *zero-viscosity model*, which is derived from the two-fluid equations in the limit as the air viscosity goes to zero. Of particular interest is the applicability of the various models to drainage problems in layered soils. To evaluate initial-boundary-value problems for both the Richards equation and the two-fluid flow equations, use is made of the semi-analytical solutions developed in Chapters 2 and 3 of this dissertation.

## 2.2 FAILURE OF THE RICHARDS EQUATION TO SIMULATE A SIMPLE DRAINAGE PROBLEM

This evaluation has been prompted by the fact that the Richards formulation is apparently unable to provide a theoretical solution to certain types of air-water drainage problems. An example of such a problem is presented in this section. Referring to Figure 2-1, consider vertical drainage in a laboratory soil column having impermeable walls. Initially, the column is fully saturated and hydrostatic, with the phreatic (zero water pressure) surface located at the top of the soil. At time zero, the valve is opened and water discharges to the atmosphere at the end of a drainage pipe. Laboratory experience indicates that under these conditions, air will spontaneously invade the top of the column and displace the water which drains out the bottom. With time, a desaturation front will migrate downward from the top of the column. Because the sides and base of the column are sealed, and the lower portion of the soil is saturated, there is no air access to the bottom of the column. Thus, no desaturation can occur at the base of the soil until such time that the desaturation front has migrated downward to this level.

Shown on Figure 2-1 is a saturation profile at some time after initiation of the drainage process. We define an incipient desaturation point, which is located at coordinate x*. The column is fully saturated below the desaturation point and partially saturated above the point.

In the region above and including the desaturation point, the Richards flux equation, presented in Chapter 2, can be written for vertical flow as:

$$|q_w| = K \, k_{rw}(S_w) \left( 1 - \frac{1}{C_w(S_w)} \frac{\partial S_w}{\partial x} \right) \quad \text{for } S_w \leq 1 \tag{2-1}$$

where $|q_w|$ is the magnitude of the (downward) water flux, K is the saturated hydraulic conductivity of the porous medium, $k_{rw}$ is the relative water permeability, and saturation capacity is defined as:

$$C_w(S_w) = \frac{dS_w}{dh_c} \tag{2-2}$$

At the desaturation point ($S_w = 1$), the relative water permeability is equal to unity and equation (2) becomes:

$$|q_w*| = K \left( 1 - \frac{1}{C_w(1)} \frac{\partial S_w}{\partial x} \right) \quad \text{at } x = x* \tag{2-3}$$

Saturation capacity always has a negative value and the saturation profile on Figure 2-1 shows that at x*, the derivative of $S_w$ must be either zero or a negative value. With these considerations, it must be concluded that for the Richards model:

$$|q_w*|_{max} = K \qquad \text{Richards Model} \tag{2-4}$$
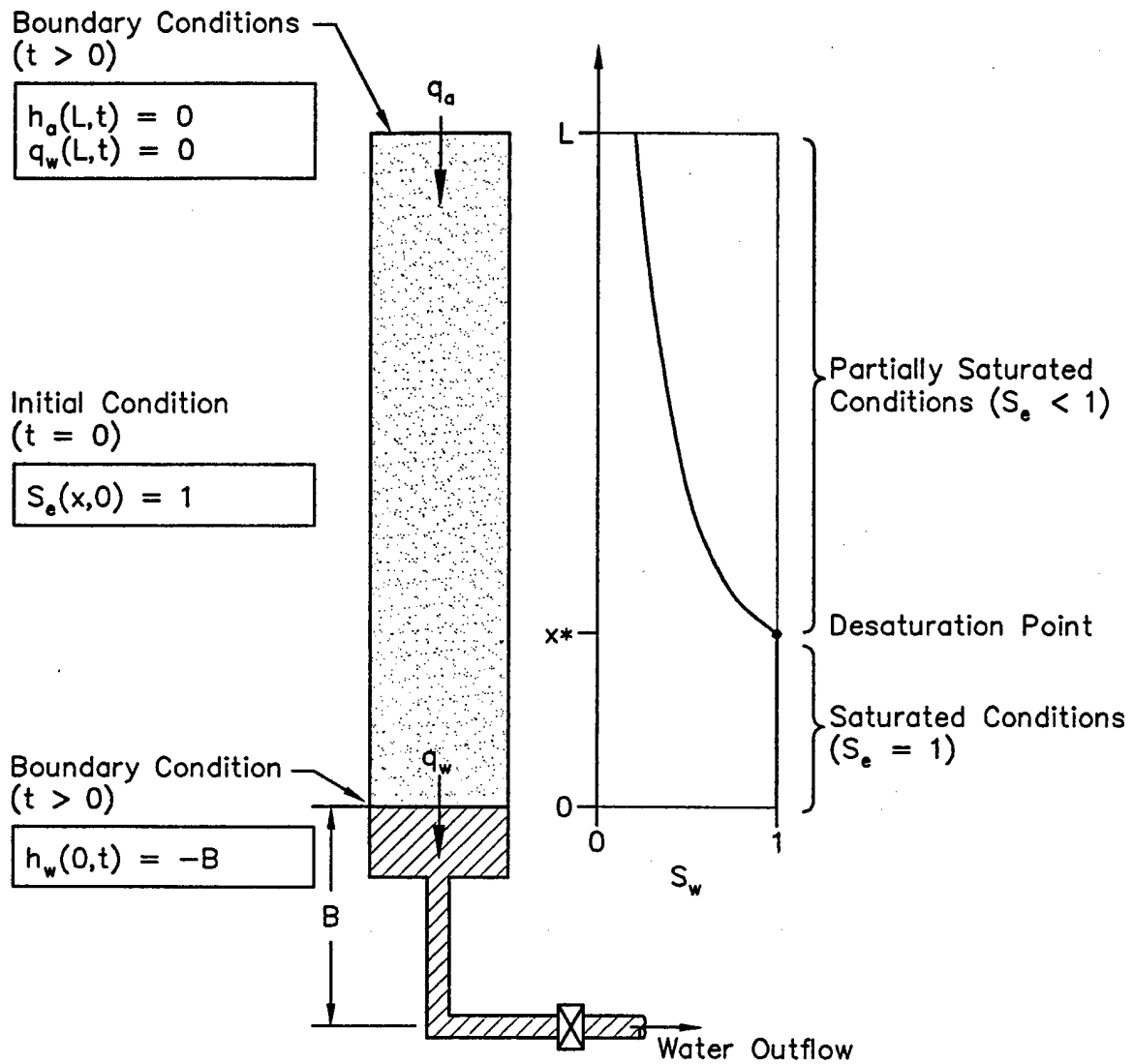
**Figure 2-1. Vertical Drainage in a Homegeneous Soil Column.**

Boundary Conditions
(t > 0)

$h_a(L,t) = 0$
$q_w(L,t) = 0$

$q_a$

L

Partially Saturated
Conditions ($S_e < 1$)

Initial Condition
(t = 0)

$S_e(x,0) = 1$

x*

Desaturation Point

Saturated Conditions
($S_e = 1$)

Boundary Condition
(t > 0)

$h_w(0,t) = -B$

$q_w$

B

0

0                    1

$S_w$

Water Outflow

This equation indicates that at the desaturation point, the maximum water flux that can be computed using the Richards flux equation is equal to the saturated hydraulic conductivity of the material containing the desaturation point.

Capillary pressure head ($h_c$) is defined as the difference between the air and water pressure heads. At the desaturation point, the water saturation is equal to unity and the Brooks-Corey (1964, 1966) saturation relationships require that the capillary pressure head be equal to the displacement pressure head ($h_d$). Using the traditional Richards assumption that the air pressure head is everywhere equal to zero, the capillary pressure head becomes equal to the negative of the water pressure head ($h_w$). The above considerations lead to:

$$h_w = -h_d \quad \text{at} \quad x = x* \tag{2-5}$$

Because the column is saturated for $x \leq x*$, the water flux at the desaturation point can be computed alternatively using the saturated form of Darcy's law. Considering that the water pressure head is equal to $-h_d$ at $x = x*$ and $-B$ at $x = 0$, the water flux in the saturated portion of the column, including the desaturation point, is:

$$|q_w*| = K \left[ \frac{B - h_d}{x*} + 1 \right] \qquad \text{Darcy's Law} \tag{2-6}$$

The dimension B is equal to the magnitude of the water pressure (suction) head at the base of the soil. It is observed from the above equation that if the dimension B is greater than the value of the displacement pressure head ($h_d$), Darcy's law gives a water flux at $x = x*$ which is larger than the value that can be theoretically computed by the Richards flux equation at the same point. From a physical standpoint, the elevation of the discharge pipe is completely arbitrary. Thus, for the case where $B > h_d$, the physical problem shown on Figure 2-1 cannot be solved using the Richards formulation.

For this situation, the Richards equation simply does not apply because it is not capable of maintaining flux continuity at the desaturation point when $B \succ h_d$. Under these conditions, the magnitude of the water flux at the desaturation point exceeds the saturated hydraulic conductivity. If the Richards flux equation (3) is solved for the saturation derivative $(\partial S_w / \partial x)$, it will predict that the derivative is positive and greater than zero at the desaturation point. This leads to a contradiction because it would erroneously indicate that there is no desaturation *directly above the desaturation point.*

## 2.3    GOVERNING EQUATIONS FOR ONE-DIMENSIONAL FLOW

To systematically evaluate the above failure of the Richards equation, we present three mathematical models which can be used to evaluate air-water drainage. The governing equations for these models are discussed below.

### 2.3.1    General Relationships

The mathematical nomenclature used in this chapter is summarized in Table 2-1. We write the governing differential equations using effective saturation $(S_e)$ as the dependent variable. Effective saturation is a normalized water saturation defined by:

$$S_e(h_c) = \frac{S_w - S_r}{1 - S_r} \tag{2-7}$$

where $S_w$ is the volumetric water saturation. $S_e$ is functionally related to capillary pressure head $(h_c)$, which is defined as the difference between the air and water pressure heads:

$$h_c = h_a - h_w \tag{2-8}$$

## Table 2-1. Nomenclature Used in Chapter 2.

| | |
|---|---|
| c | Effective saturation capacity $[L^{-1}]$ |
| $c_w$ | Water saturation capacity $[L^{-1}]$ |
| D | Hydraulic diffusivity function used in two-fluid model $[L^2 T^{-1}]$ |
| $D_R$ | Hydraulic diffusivity function used in the Richards model $[L^2 T^{-1}]$ |
| $D_V$ | Hydraulic diffusivity function used in zero-viscosity model $[L^2 T^{-1}]$ |
| E | Gravity-related function used in two-fluid model $[L\ T^{-1}]$ |
| $E_R$ | Gravity-related function used in the Richards model $[L\ T^{-1}]$ |
| $E_V$ | Gravity-related function used in zero-viscosity model $[L\ T^{-1}]$ |
| f | Mobility function used in two-fluid model [dimensionless] |
| $f_V$ | Mobility function used in zero-viscosity model [dimensionless] |
| g | Acceleration of gravity $[L\ T^{-2}]$ |
| h | Fluid pressure head $[L]$ |
| $h_a$ | Air pressure head $[L]$ |
| $h_c$ | Capillary pressure head $[L]$ |
| $h_d$ | Brooks-Corey displacement pressure head $[L]$ |
| $h_w$ | Water pressure head $[L]$ |
| K | Saturated hydraulic conductivity $[L\ T^{-1}]$ |
| k | Intrinsic permeability of porous media $[L^2]$ |
| $k_{ra}$ | Relative air permeability [dimensionless] |
| $k_{rw}$ | Relative water permeability [dimensionless] |
| $q_a$ | Air flux (Darcy velocity) $[L\ T^{-1}]$ |
| $q_t$ | Total volume flux (Darcy velocity) $[L\ T^{-1}]$ |
| $q_w$ | Water flux (Darcy velocity) $[L\ T^{-1}]$ |
| $q_w^*$ | Water flux at desaturation point $[L\ T^{-1}]$ |
| $S_a$ | Volumetric air saturation [dimensionless] |
| $S_e$ | Effective saturation [dimensionless] |
| $S_r$ | Irreducible volumetric saturation [dimensionless] |
| $S_w$ | Volumetric water saturation [dimensionless] |
| t | Elapsed time $[T]$ |
| x | Distance coordinate $[L]$ |
| $x^*$ | Coordinate at desaturation point $[L]$ |

**Table 2-1. (continued)**

$\phi$      Total porosity [dimensionless]

$\lambda$      Brooks-Corey pore size distribution index [dimensionless]

$\rho_w$      Water density [$M\,L^{-3}$]

$\mu_a$      Air viscosity [$M\,L^{-1}\,T^{-1}$]

$\mu_w$      Water viscosity [$M\,L^{-1}\,T^{-1}$]

In this chapter, all pressure heads are expressed in terms of the equivalent height of water in a manometer. $S_r$ is the irreducible (minimum) water saturation which is approached at very high capillary pressure heads. Since the system contains only two fluids, the volumetric air saturation given by:

$$S_a = 1 - S_w \qquad (2\text{-}9)$$

In terms of effective saturation, the differential form of the water continuity equation in the x direction is:

$$\frac{\partial q_w}{\partial x} = -\phi(1-S_r)\frac{\partial S_e}{\partial t} \qquad (2\text{-}10)$$

### 2.3.2 Brooks-Corey Relationships

The functional relationships between capillary pressure head, effective saturation, and relative permeabilities are completely arbitrary. In this study, we use equations developed by Brooks and Corey (1964, 1966) to define these constitutive relationships. Effective saturation is related to capillary pressure head as follows:

$$S_e(h_c) = \begin{cases} \left(\dfrac{h_c}{h_d}\right)^{-\lambda} & \text{for } h_c > h_d \\ 1 & \text{for } h_c \leq h_d \end{cases} \tag{2-11}$$

where $\lambda$ is the pore size distribution index and $h_d$ is the air-water displacement pressure for the medium of interest. Note that during drainage, the capillary pressure head must exceed the displacement pressure head before desaturation ($S_e < 1$) takes place.

Relative permeabilities for water and air are defined, respectively, as:

$$k_{rw}(S_e) = S_e^{3+2/\lambda} \tag{2-12}$$

$$k_{ra}(S_e) = (1-S_e)^2 \left(1 - S_e^{1+2/\lambda}\right) \tag{2-13}$$

Note that in Corey (1994), certain modifications are presented for equation (13) which are not considered in this chapter. Effective water saturation capacity is given by:

$$C(S_e) = \frac{dS_e}{dh_c} = -\frac{\lambda}{h_d} S_e^{1+1/\lambda} \tag{2-14}$$

Note that the value of $C(S_e)$ is always negative. All other functions used in this chapter can be derived by algebraic manipulation and/or differentiation of the above equations.

### 2.3.3 Two-Fluid Flow Model

Referring to Figure 2-2a, the flux equation for vertical two-fluid flow can be written as:

$$q_w = q_t f - E - D\frac{\partial S_e}{\partial x} \tag{2-15a}$$

where the functions f, D, and E are defined, respectively, as:

$$f(S_e) = \left[ 1 + \frac{k_{ra}(S_e)\ \mu_w}{k_{rw}(S_e)\ \mu_a} \right]^{-1} \qquad (2\text{-}15b)$$

$$D(S_e) = - \left( \frac{k\rho_w g}{\mu_a} \right) \frac{k_{ra}(S_e)\ f(S_e)}{C(S_e)} \qquad (2\text{-}15c)$$

$$E(S_e) = \left( \frac{k\rho_w g}{\mu_a} \right) k_{ra}(S_e)\ f(S_e) \qquad (2\text{-}15d)$$

Taking the derivative of (2-15) and combining with (2-10) leads to the first partial differential equation (PDE) for two-fluid flow:

$$\frac{\partial}{\partial x}\left( D\frac{\partial S_e}{\partial x} \right) + \left[ \left( \frac{dE}{dS_e} \right) - q_t\left( \frac{df}{dS_e} \right) \right]\frac{\partial S_e}{\partial x} = \phi(1 - S_r)\frac{\partial S_e}{\partial t} \qquad (2\text{-}16)$$

Total volume flux ($q_t$) is defined as the sum of the water and air fluxes:

$$q_t = q_w + q_a \qquad (2\text{-}17)$$

If the porous medium is rigid and contains two incompressible fluids, continuity relationships lead to the second PDE for two-fluid flow:

$$\frac{\partial q_t}{\partial x} = 0 \qquad (2\text{-}18)$$

which requires that $q_t(x,t) = q_t(t)$. In other words, at any given time, the total flux is spatially uniform throughout the flow system. For many physical problems of air-water flow, the assumption of an incompressible air phase is not reasonable. For drainage problems, however, we consider this assumption to be acceptable as a first-order approximation. Note that the two-fluid model requires that the two PDE's in (16) and (18) be solved simultaneously.
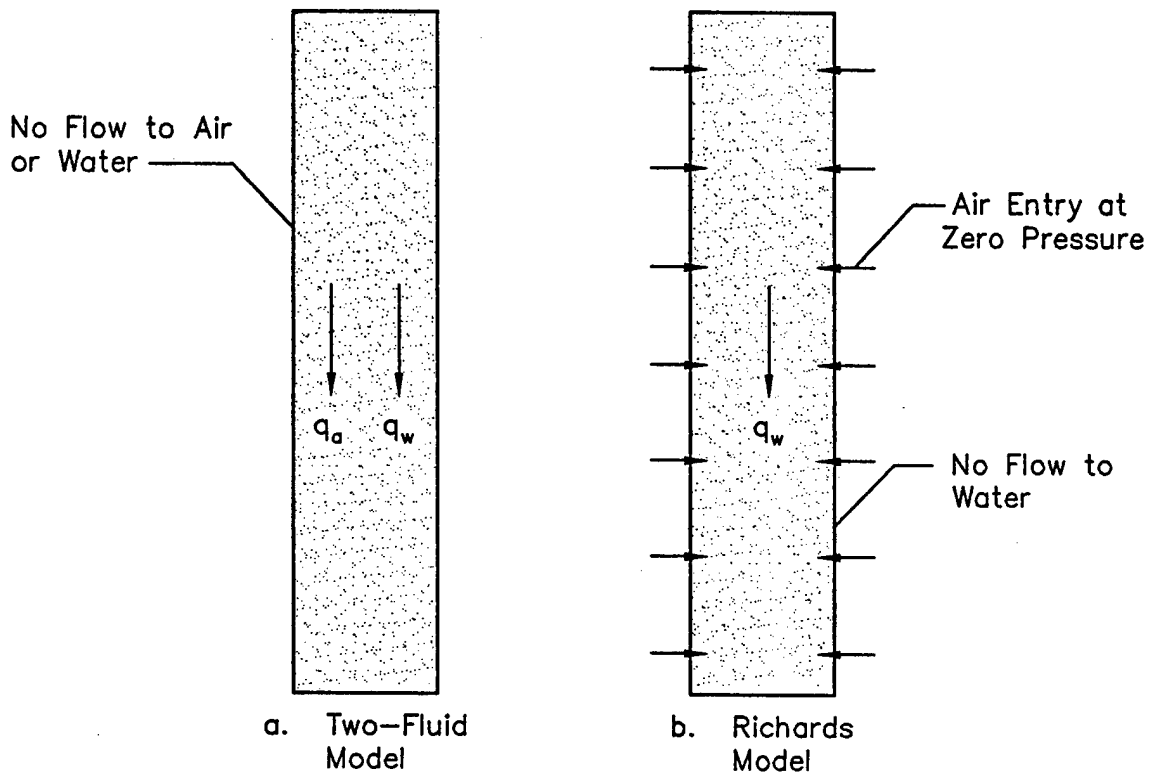
No Flow to Air
or Water

$q_a$   $q_w$

a.   Two—Fluid
     Model

Air Entry at
Zero Pressure

$q_w$

No Flow to
Water

b.   Richards
     Model

Figure 2-2. One-Dimensional Drainage Flow Models.

### 2.3.4 Richards Model

Referring to Figure 2-2b, the Richards flux equation for partially saturated water flow can be written as:

$$q_w = - E_R - D_R \frac{\partial S_e}{\partial x} \qquad (2\text{-}19a)$$

where the functions $D_R$ and $E_R$ are defined, respectively as:

$$D_R(S_e) = - \frac{k \rho_w g}{\mu_w} \frac{k_{rw}(S_e)}{C(S_e)} \qquad (2\text{-}19b)$$

$$E_R(S_e) = \frac{k \rho_w g}{\mu_w} k_{rw}(S_e) \qquad (2\text{-}19c)$$

Taking the derivative of (2-19) and combining with (2-10) leads to the following PDE:

$$\frac{\partial}{\partial x}\left( D_R \frac{\partial S_e}{\partial x} \right) + \left( \frac{dE_R}{dS_e} \right) \frac{\partial S_e}{\partial x} = \phi(1 - S_r)\frac{\partial S_e}{\partial t} \qquad (2\text{-}20)$$

This is an alternate form of the Richards equation (Richards, 1931; Jury *et al.*, 1991) using effective saturation ($S_e$) as the dependent variable.

Assuming that air exists everywhere at atmospheric pressure, the air pressure head is zero and by equation (2-8):

$$h_c = -h_w \qquad (2\text{-}21)$$

### 2.3.5 Zero-Viscosity Model

Equations for the zero-viscosity model are derived by evaluating the two-fluid flow equations in the limit as the air viscosity ( $\mu_a$ ) goes to zero (McWhorter and Marinelli, 1996). Evaluating this limit for equations 2-15b through 2-15d, we obtain:

$$f_v(S_e) = \lim(\mu_a \to 0) \left[ f(S_e) \right] = \begin{cases} 0 & \text{for} \ \ S_e < 1 \\ 1 & \text{for} \ \ S_e = 1 \end{cases} \tag{2-22b}$$

$$D_v(S_e) = \lim(\mu_a \to 0) \left[ D(S_e) \right] = \begin{cases} -\dfrac{k\rho_w g}{\mu_w} \dfrac{k_{rw}(S_e)}{C(S_e)} & \text{for} \ \ S_e < 1 \\ 0 & \text{for} \ \ S_e = 1 \end{cases} \tag{2-22c}$$

$$E_v(S_e) = \lim(\mu_a \to 0) \left[ E(S_e) \right] = \begin{cases} \dfrac{k\rho_w g}{\mu_w} k_{rw}(S_e) & \text{for} \ \ S_e < 1 \\ 0 & \text{for} \ \ S_e = 1 \end{cases} \tag{2-22d}$$

In each case, a discontinuity exists between values associated with $S_e = 1$ and values for $S_e \to 1$. Because $k_{ra}(1) = 0$, the two-fluid flow equations indicate that the above values given for $S_e = 1$ apply for *any* air viscosity. Furthermore, the equations for $S_e < 1$ in (2-22c) and (2-22d) are identical to those defining $D_R$ and $E_R$ in the Richards flux equation (equation 2-19). With these considerations, the flux equation for the zero-viscosity model is written as:

$$q_w = \begin{cases} -E_R - D_R \dfrac{\partial S_e}{\partial x} & \text{for} \ \ S_e < 1 \\ q_t & \text{for} \ \ S_e = 1 \end{cases} \tag{2-22a}$$

and the PDE's for the zero-viscosity model are:

$$\left\{ \begin{array}{ll} \dfrac{\partial}{\partial x}\left(D_R \dfrac{\partial S_e}{\partial x}\right) + \left(\dfrac{dE_R}{dS_e}\right)\dfrac{\partial S_e}{\partial x} = \phi(1-S_r)\dfrac{\partial S_e}{\partial t} \quad \underline{\text{and}} \quad \dfrac{\partial q_t}{\partial x} = 0 \quad \text{for} \quad S_e < 1 \\[4mm] \hspace{8cm} \dfrac{\partial q_t}{\partial x} = 0 \hspace{2.5cm} \text{for} \quad S_e = 1 \end{array} \right.$$

(2-23)

For $S_e < 1$, the zero-viscosity model requires that two differential equations be solved simultaneously. Note that equation (2-23) allows for the possibility of a saturation discontinuity at $S_e = 1$.

### 2.3.6 Discussion

Since the Richards equation is sometimes interpreted to imply that the air viscosity is zero, one might expect the Richards and zero-viscosity models to be equivalent. Inspection of the flux equations and PDE's for both models (equations 2-19, 2-20, 2-22, and 2-23) indicate that the models are not identical. Thus, the traditional Richards formulation for partially saturated flow is not, strictly speaking, recovered from the two-fluid flow formulation in the limit of zero air viscosity.

Insight into the differences between the three models can be gained by evaluating equation 2-22b for the function $f(S_e)$ at different water-air viscosity ratios $(\mu_w/\mu_a)$. On Figure 2-3, the function is plotted for the typical water-air viscosity ratio of 55.6 and for larger values (i.e., for relatively smaller air viscosities). Note that $f(1) = 1$ for any viscosity ratio. This feature is reasonable, because at full saturation, there is no air flow since $k_{ra}(1) = 0$ and water flux must therefore be equal to the total fluid flux. In the limit, as the viscosity ratio goes to infinity (air viscosity goes to zero), $f(1)$ remains equal to unity, but a discontinuity develops because f is equal to zero for all effective saturations less than one. This is the zero-viscosity model definition of the function f as described by equation (2-22b). In the Richards model, the function f is treated as equal
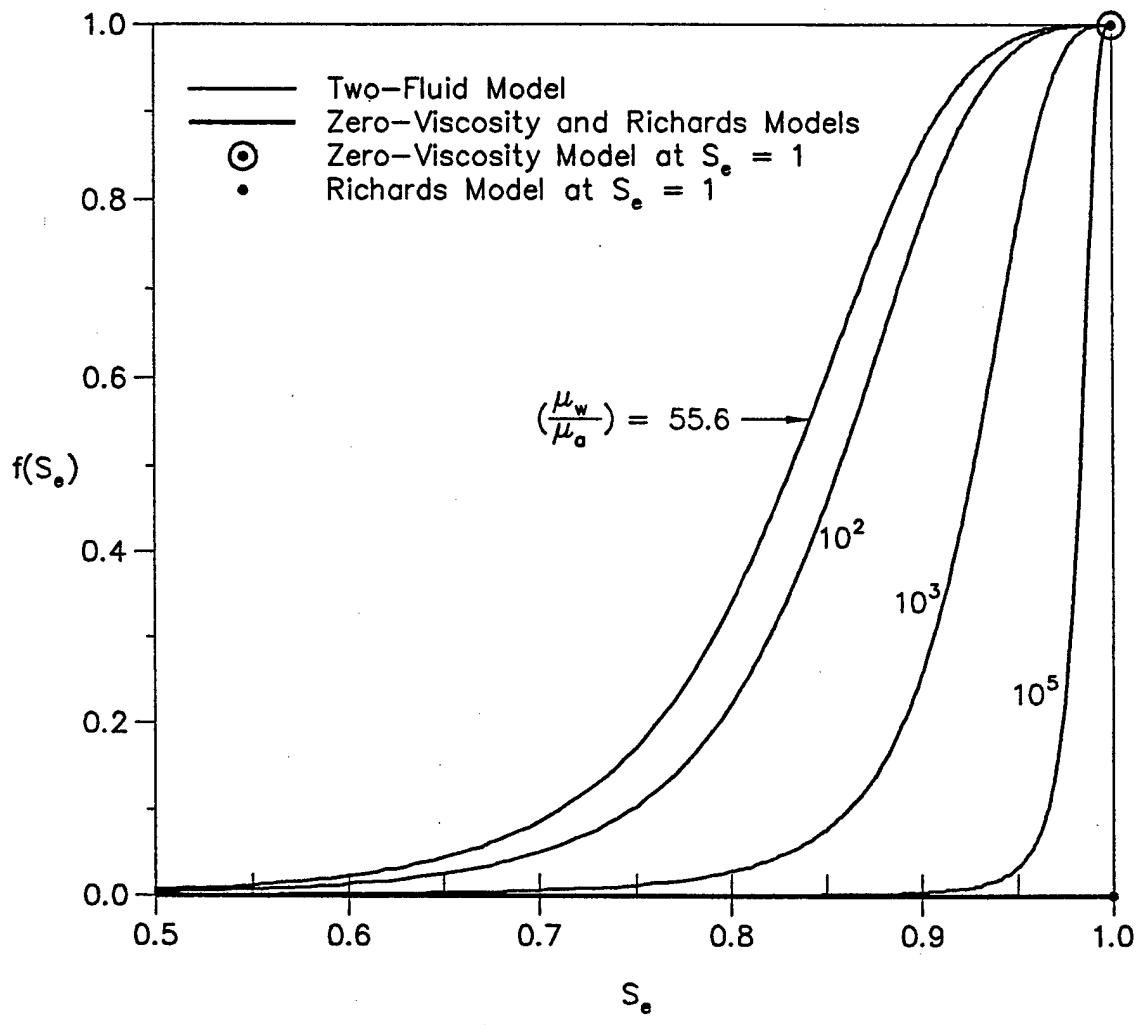
III - 45

Figure 2-3. Function $f(S_e)$  For $\lambda = 2$.

to zero for *all* effective saturations, which is why the function does not appear in the Richards equations.

Inspection of flux equation (2-15a) indicates that for general two-fluid flow, knowledge of the total fluid flux ($q_t$) is required in order to preserve fluid continuity. As the viscosity ratio goes to infinity, equation (2-22a) for the zero-viscosity model shows that knowledge of the total fluid flux is needed to preserve fluid continuity at $S_e = 1$. In the Richards equations, knowledge of the total fluid flux is lost, because the flow dynamics of air is not considered.

Figures 2-4 and 2-5 are plots of the dimensionless forms of the diffusivity [$D(S_e)$] and gravity [$E(S_e)$] functions for different values of the water-air viscosity ratio. It is observed that $D(1) = 0$ and $E(1) = 0$ for all viscosity ratios. These values are retained in the limit as the viscosity ratio goes to infinity, which represents the zero-viscosity model. In this case, each function exhibits a discontinuity between the associated values for $S_e \rightarrow 1$ and $S_e = 1$. For $S_e < 1$, the diffusivity and gravity functions for the Richards model are identical to those of the zero-viscosity model. At $S_e = 1$, however, the Richards functions are continuous and do not exhibit the discontinuities associated with the zero-viscosity model.

## 2.4  VERTICAL DRAINAGE IN A HOMOGENEOUS SOIL

To further investigate the failure of the Richards equation and the overall effect of air viscosity on water drainage, we apply the two-fluid and Richards models to the physical problem shown on Figure 2-1. Due to the discontinuities in functions associated with the zero-viscosity model, it cannot be applied directly. However, the effect of reduced air viscosity can be investigated by examining the behavior of the two-fluid model as the air viscosity is progressively decreased to very small values. Simulations are performed for the case where $B < h_d$, which can be evaluated using the Richards model, and for $B > h_d$ which is not solvable by the Richards model.
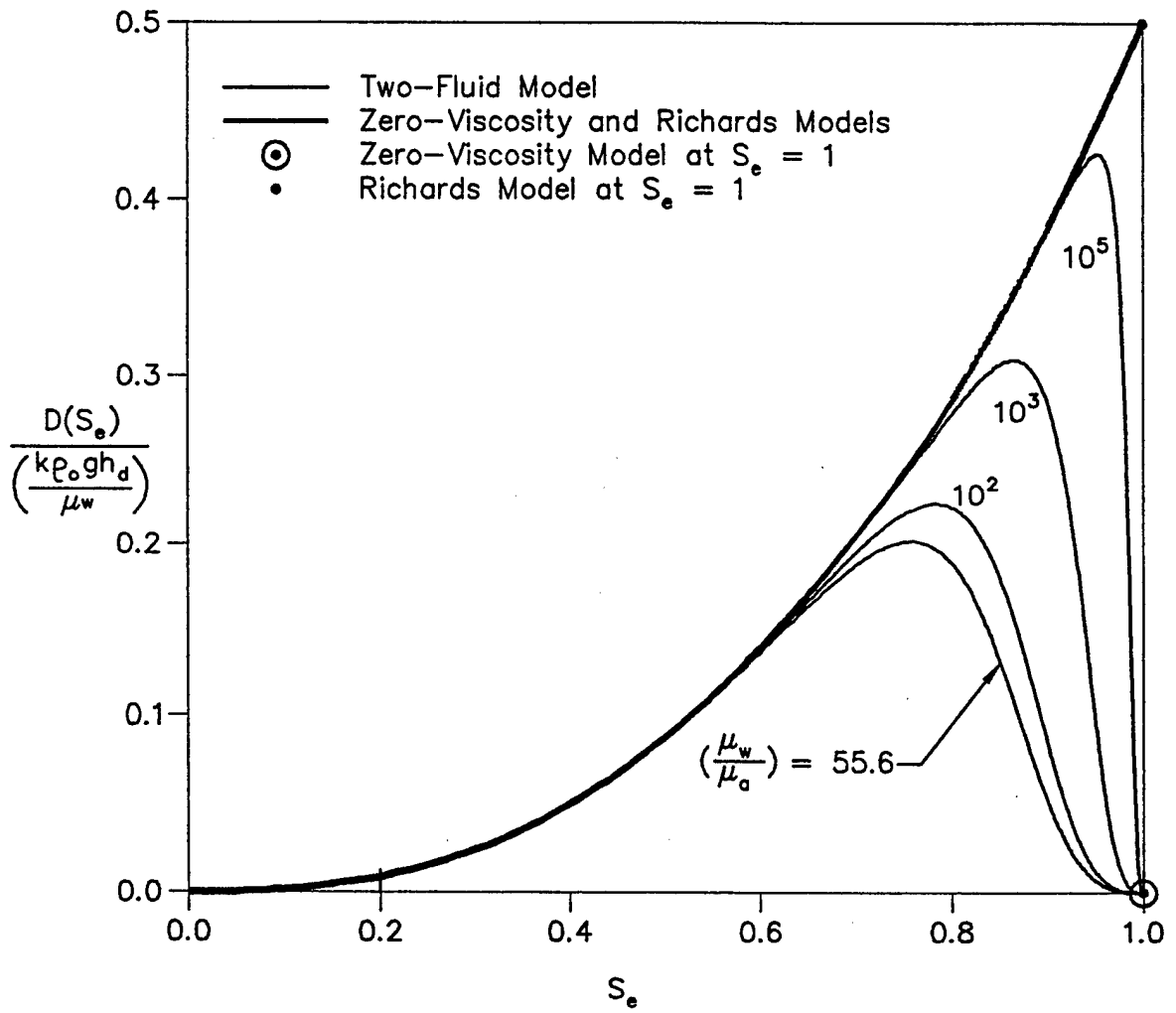
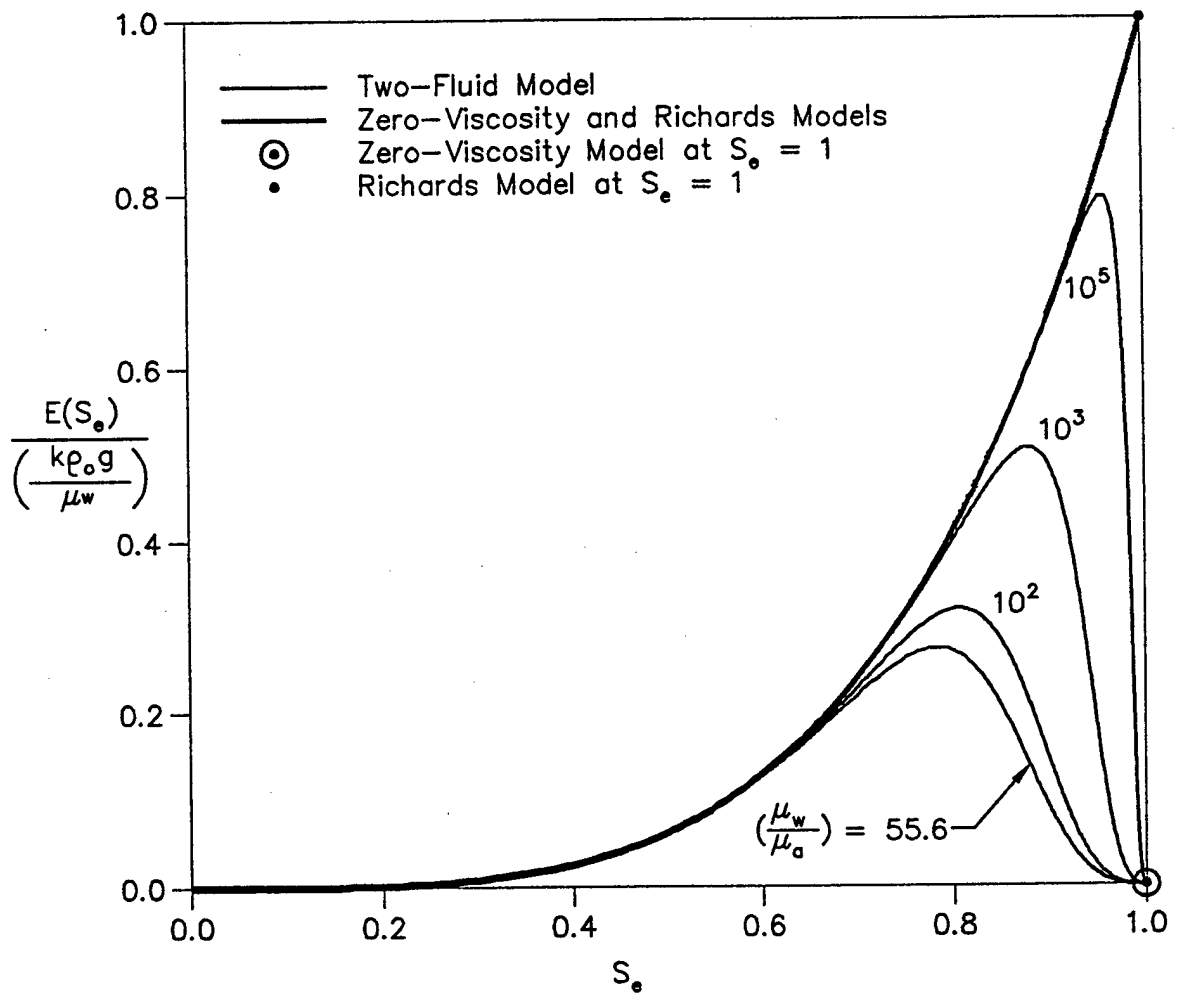**Figure 2-4. Dimensionless Diffusivity Function for λ = 2 and $h_d$ = 15 cm (water).**

**Figure 2-5. Dimensionless Gravity Function for λ = 2.**

The initial-boundary-value problem described on Figure 2-1 can be simulated for both the two-fluid and Richards models using semi-analytical solutions described in Chapter 1 of this report. This problem is described as vertical, one-dimensional, unidirectional displacement of a wetting fluid (water) by a nonwetting fluid (air) in a homogeneous soil. Note that if (1) the fluids and porous medium are assumed to be incompressible, (2) the bottom of the column is fully saturated, and (3) there is no water flow at the top of the column, the following relationship holds for one-dimensional, unidirectional displacement:

$$q_t(t) = q_a(L,t) = q_w(x*,t,) = q_w(0,t) \qquad (2\text{-}24)$$

From a physical standpoint, this equation implies that the sides of the column are impermeable and that air access into the system only takes place at the top of the column.

First, we consider drainage in a 100 cm column, composed of medium-grained sand, where water pressure head at the base is maintained at zero [$h_w(0,t)$ = B = 0]. The soil and fluid properties used in this simulation are summarized in Table 2-2. Based on solutions to the two-fluid model, Figure 2-6a shows computed saturation profiles at an elapsed time of 98 seconds for the typical water-air viscosity ratio of 55.6 and for higher values (lower air viscosities). For the typical viscosity ratio, the extent of air invasion is from the top of the column down to the desaturation point located at $x*$ = 92.2 cm. As the viscosity ratio becomes larger, the extent of air invasion increases. For viscosity ratios of $10^6$ and larger, the saturation distribution does not change and we therefore consider this profile to approach the behavior of the zero-viscosity model. As discussed in the previous section, the parameter B for this example is sufficiently small that evaluation by the Richards model is theoretically possible. As shown on Figure 2-6a, the saturation profile

**Table 2-2.  Parameters Used in Chapter 2.**

| | | | |
|---|---|---|---|
| $\rho_w$ | 1 | g cm$^{-3}$ | |
| $\mu_w$ | 0.01 | g cm$^{-1}$ s$^{-1}$ | |
| $\mu_a$ | 0.00018 | g cm$^{-1}$ s$^{-1}$ | (lower values used in some simulations) |
| g | 980 | cm s$^{-2}$ | |

| | Medium Sand | | Fine Sand | |
|---|---|---|---|---|
| k | 10$^{-7}$ | cm$^2$ | 10$^{-8}$ | cm$^2$ |
| $\lambda$ | 3 | | 1.5 | |
| $h_d$ | 15 | cm | 30 | cm |
| $S_r$ | 0.1 | | 0.2 | |
| $\phi$ | 0.35 | | 0.35 | |

**a. Saturation**     **b. Air Pressure Head**
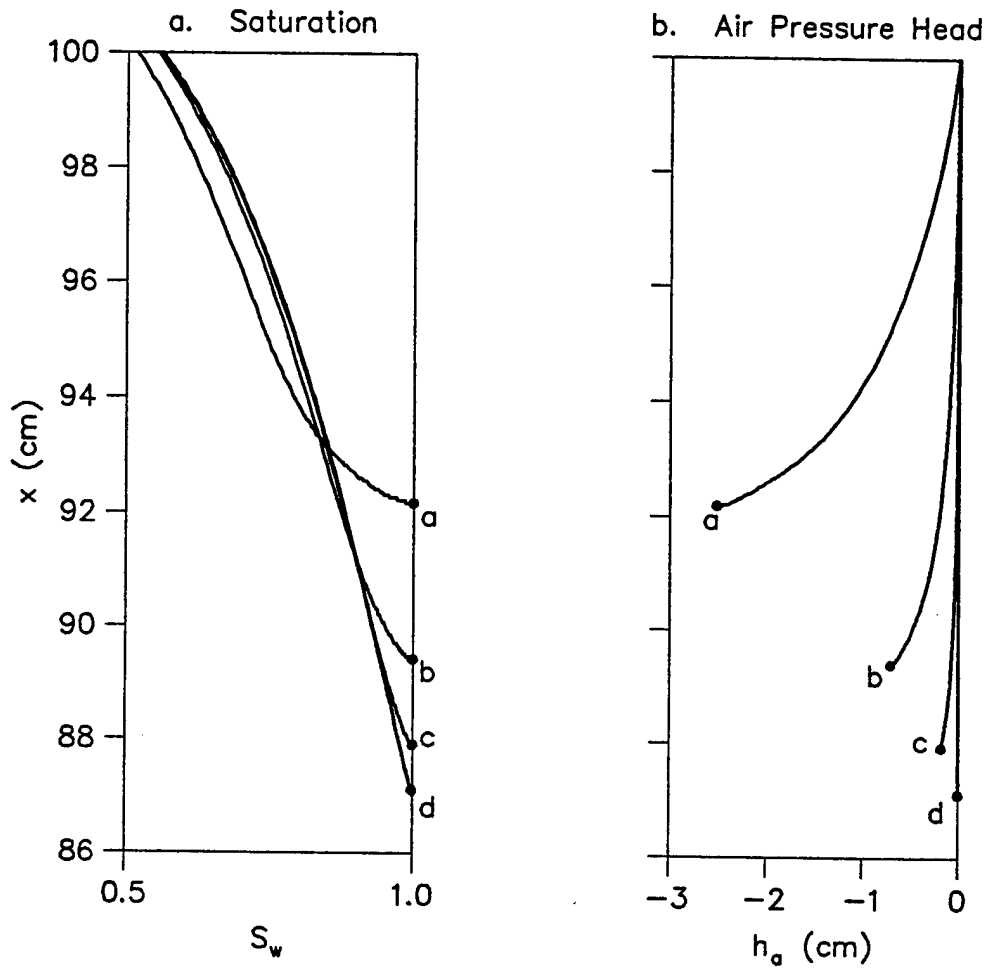
EXPLANATION

•   Desaturation Point

a    $\mu_w/\mu_a$ = 55.6

b         = $10^3$
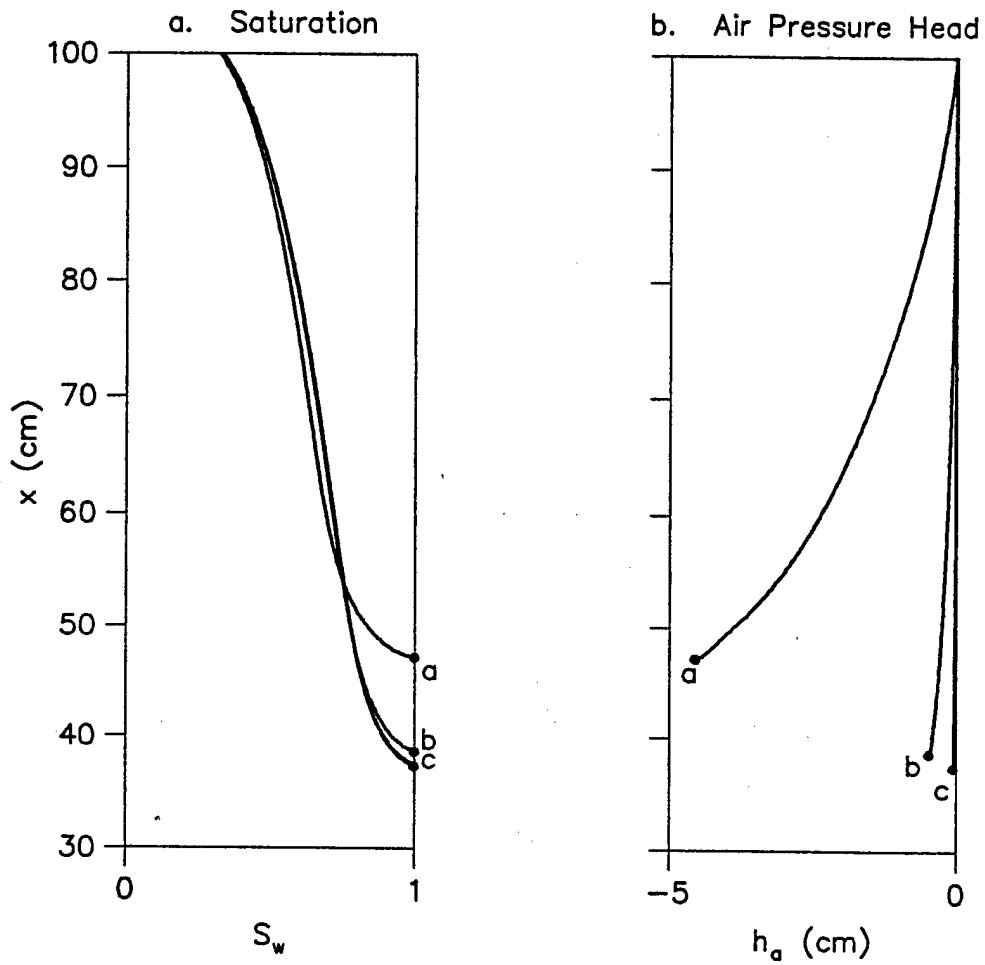
c         = $10^4$

d         = $\geq 10^6$; Richards Model

**Figure 2-6. Drainage in a Homogeneous Soil.**

$h_w(0,t) > - h_d$ ; t = 98 seconds

determined by solution of the Richards equations is identical to that predicted by the two-fluid model at low air viscosity. Note, however, that the shape of saturation profile for the typical viscosity ratio is substantially different from predictions based on the Richards model and the two-fluid model with low air viscosity.

Figure 2-6b shows computed air pressure head distributions associated with the saturation profiles on Figure 2-6a. For the typical viscosity ratio of 55.6, significant negative pressure heads are predicted to develop, reaching magnitudes of about 2.6 cm in vicinity of the desaturation point. As expected, when the viscosity ratio increases, the air pressure heads become closer to zero throughout the zone of air invasion. For viscosity ratios greater than $10^6$, considered for this example to approach zero-viscosity behavior, the air pressure heads are essentially equal to zero throughout the zone of air invasion. Since the Richards model assumes zero air pressure, Figure 2-6b once again indicates that the predictions of the two-fluid model at low air viscosity approach those based on the Richards equation. However, results of the two-fluid analyses indicate that the assumption of low air viscosity is not necessarily valid for real air-water systems.

Figures 2-7a and 2-7b show saturation and air pressure head distributions at an elapsed time of 1057 seconds after initiation of drainage. For the typical water-air viscosity ratio of 55.6, air invasion extends from the top of the column down to $x^* = 47.2$ cm. The characteristics of these plots are similar to those shown on Figure 2-6, with the exception that (1) the extent of air invasion is greater, (2) for typical air viscosity, the magnitude of air pressure head is greater (more negative) at the desaturation point, and (3) the two-fluid model approaches the Richards model at a smaller viscosity ratio of about $10^4$. For this example, Figure 2-7 indicates that as the drainage process proceeds, the effects of air viscosity remain significant both on the shape of the saturation profile and the distribution of air pressures within the zone of air invasion.
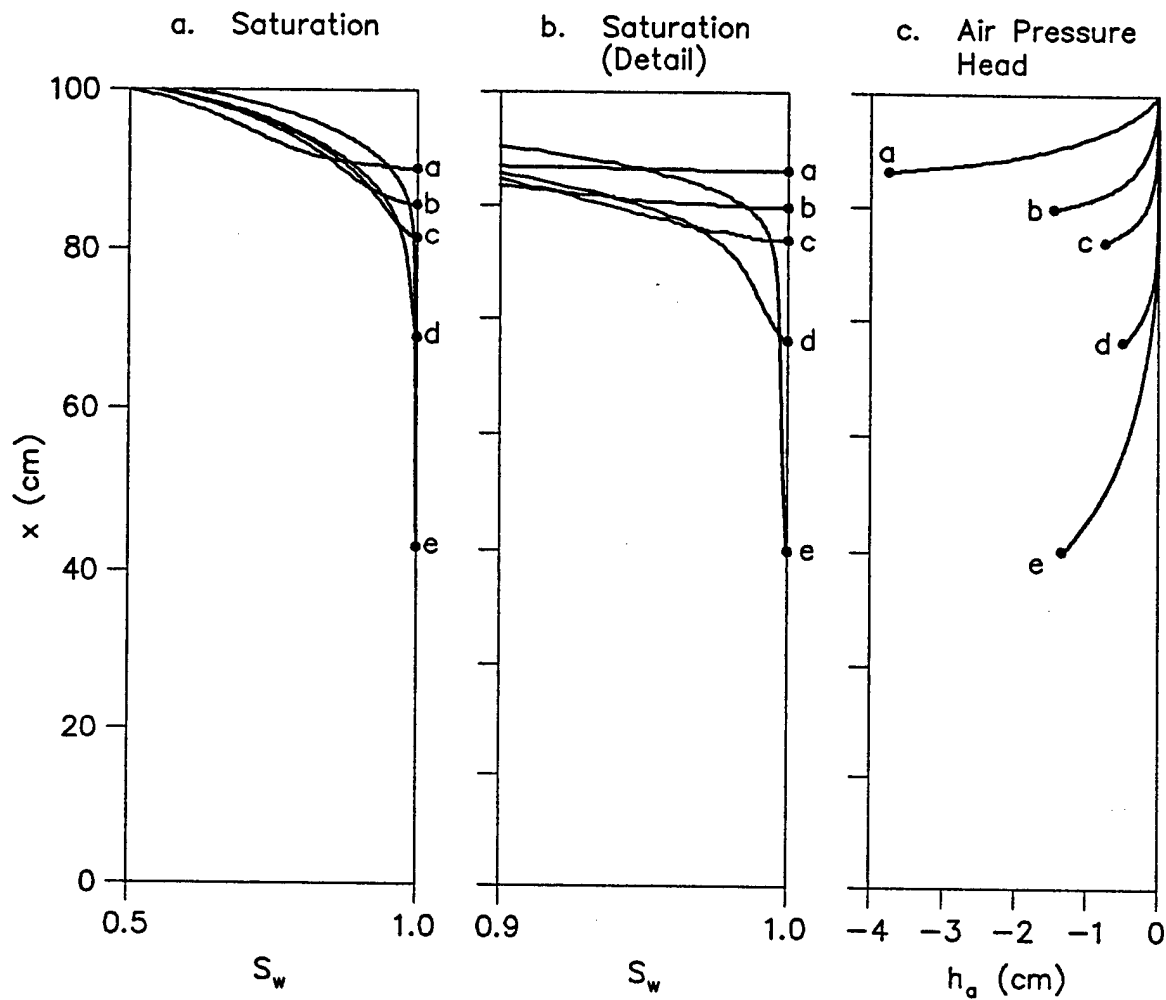
**Figure 2-7. Drainage in a Homogeneous Soil.**

$h_w(0,t) > -h_d$ ; $t = 1057$ seconds

We now consider simulation of drainage in the same soil column where water pressure head at the base [$h_w(0,t)$] is maintained at -20 cm. Since this value is smaller than -$h_d$, the magnitude of the water flux will exceed the saturated hydraulic conductivity (K) and the Richards model cannot be used to simulate this physical system. Saturation profiles at an elapsed time of 98 seconds (Figure 2-8a and 2-8b) show an interesting feature for this case where the water flux is greater than the saturated hydraulic conductivity of the soil [ $|q_w*|$ = $|q_w(0,t)|$ > K]. As the viscosity ratio increases, the extent of air invasion becomes greater and a long zone with very high water saturations (low air saturations) extends progressively farther into the medium. Note that the saturation profile for the viscosity ratio of $10^8$ is actually plotted at a time of 64 seconds, because at 98 seconds it is predicted that the zone of air invasion would extend all the way to the base of the column. Figure 2-8 illustrates that for relatively high water drainage rates, desaturation in a true air-water system is grossly different from what would be predicted by a system with very low air viscosity.

Consider further, the associated air pressure head distributions shown on Figure 2-8c. As with the previous example, significantly negative air pressure heads are predicted for the typical viscosity ratio of 55.6, and the magnitudes of the pressure heads decrease as the ratio is initially increased above this value. However, at a very large viscosity ratio of $10^8$ (very small air viscosity), the magnitude of air pressure heads are predicted to *increase*. This seemingly counter-intuitive result can be explained as follows. Substituting equation (8) into (11) and taking the derivative of the air pressure head with respect to x gives:

$$\frac{dh_a}{dx} = \frac{dh_w}{dx} - \left[\frac{h_d}{\lambda} S_e^{-(1+1/\lambda)}\right] \frac{dS_e}{dx} \qquad (2\text{-}25)$$

**a. Saturation**

**b. Saturation (Detail)**

**c. Air Pressure Head**

$S_w$

$S_w$

$h_a$ (cm)

$x$ (cm)

EXPLANATION

• Desaturation Point

a  $\mu_w/\mu_a = 55.6$  $t = 98$ seconds

b        $= 10^3$      $= 98$ seconds

c        $= 10^4$      $= 98$ seconds

d        $= 10^6$      $= 98$ seconds

e        $= 10^8$      $= 64$ seconds

**Figure 2-8. Drainage in a Homogeneous Soil.**

$$h_w(0,t) < -h_d$$

As discussed previously, at very large viscosity ratios, the lower portion of the soil column develops a long, partially saturated zone where $S_e \rightarrow 1$, which implies that $dS_e/dx \rightarrow 0$. Inspection of equation (2-25) would therefore indicate that within this zone:

$$\frac{dh_a}{dx} \approx \frac{dh_w}{dx} \tag{2-26}$$

Simulation results for the $10^8$ viscosity ratio, indicate that in the lower portion of the saturation profile, that is from the desaturation point at 43.1 cm up to 50 cm, the air pressure gradient is within 2 percent of the water pressure gradient. As the viscosity ratio approaches infinity, we expect that the two derivatives would become identically equal.

Finally, for the physical problem shown on Figure 2-1, we consider direct application of the Richards model with *no qualifications regarding air access* into the flow system. As stated previously, a basic assumption of the Richards model is that air is freely accessible to all portions of the flow system, regardless of the saturation distribution. For the lower boundary condition; $h_w(0,t) > -h_d$, it is shown on Figures 2-6 and 2-7 that the Richards model gives identical results to the two-fluid model at low air viscosity. For this boundary condition, if the access of low-viscosity air is limited to the top of the soil column, there appears to be essentially free air access to all portions of the column undergoing desaturation, and the two models predict the same drainage behavior. However, if the lower boundary condition is $h_w(0,t) < -h_d$, the two models are not equivalent as shown diagrammatically on Figure 2-9. Because the Richards model assumes that the air pressure head is zero, this boundary condition requires that substantial desaturation occurs immediately at the base of the column. As shown on Figure 2-9a, the Richards model predicts simultaneous desaturation at both the top and bottom of the column, with the central portion remaining saturated. Obviously, this
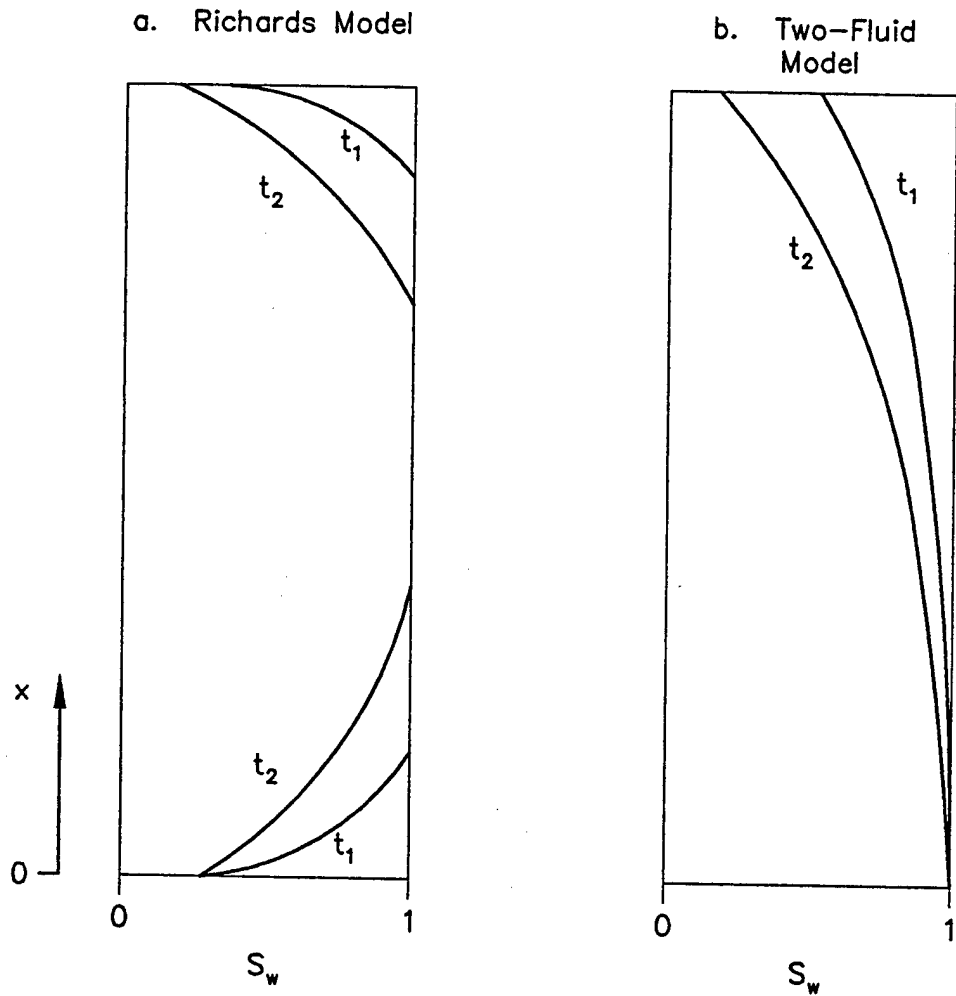
**Figure 2-9.** Diagramatic Comparison of the Richards Model and the Two-Fluid Model at Low Air Viscosity.

$$h_w(0,t) < -h_d$$

situation could only occur if air inlets are provided along the sides of the column, which would violate the physical problem as originally stated. For low air viscosity, Figure 2-9b shows desaturation along the entire length of the column, but with saturation approaching 1 at the base. This is equivalent to capillary pressure head ($h_c$) being approximately equal to the displacement pressure head ($h_d$) at base of the column, which for the stated water pressure boundary condition, requires that the air pressure head is less than zero. As shown on Figure 2-8, under these conditions, a low air viscosity simulation can predict air pressure variations within the flow system even though the air viscosity is very small.

## 2.5    VERTICAL DRAINAGE IN A LAYERED SOIL

At face value, the physical problem described on Figure 2-1 may seem somewhat artificial because of the negative water pressure head condition imposed at the base of the soil. However, it can be shown that for many practical drainage problems in layered soils, the conditions shown on Figure 2-1 can occur within individual layers. This is particularly true within a fine-grained layer that overlies a coarser, more permeable layer. Consider the layered-soil drainage problem described on Figure 2-10 for the case of real air viscosity. The properties of the two sands that comprise the column are summarized in Table 2-2. Initially, the column is fully saturated and hydrostatic, with the water-table (zero water pressure head) surface located at the top of the soil column. At time zero, the water table is instantaneously lowered to the bottom of the column.

Based on the two-fluid semi-analytical solution developed in Chapter 1, computed saturation and pressure head distributions are shown on Figure 2-11 at an elapsed time of 3,360 seconds, prior to arrival of the desaturation front at the interface between the two sands. Of particular interest is that significantly negative air pressure heads develop within the zone of partial saturation and that no desaturation has

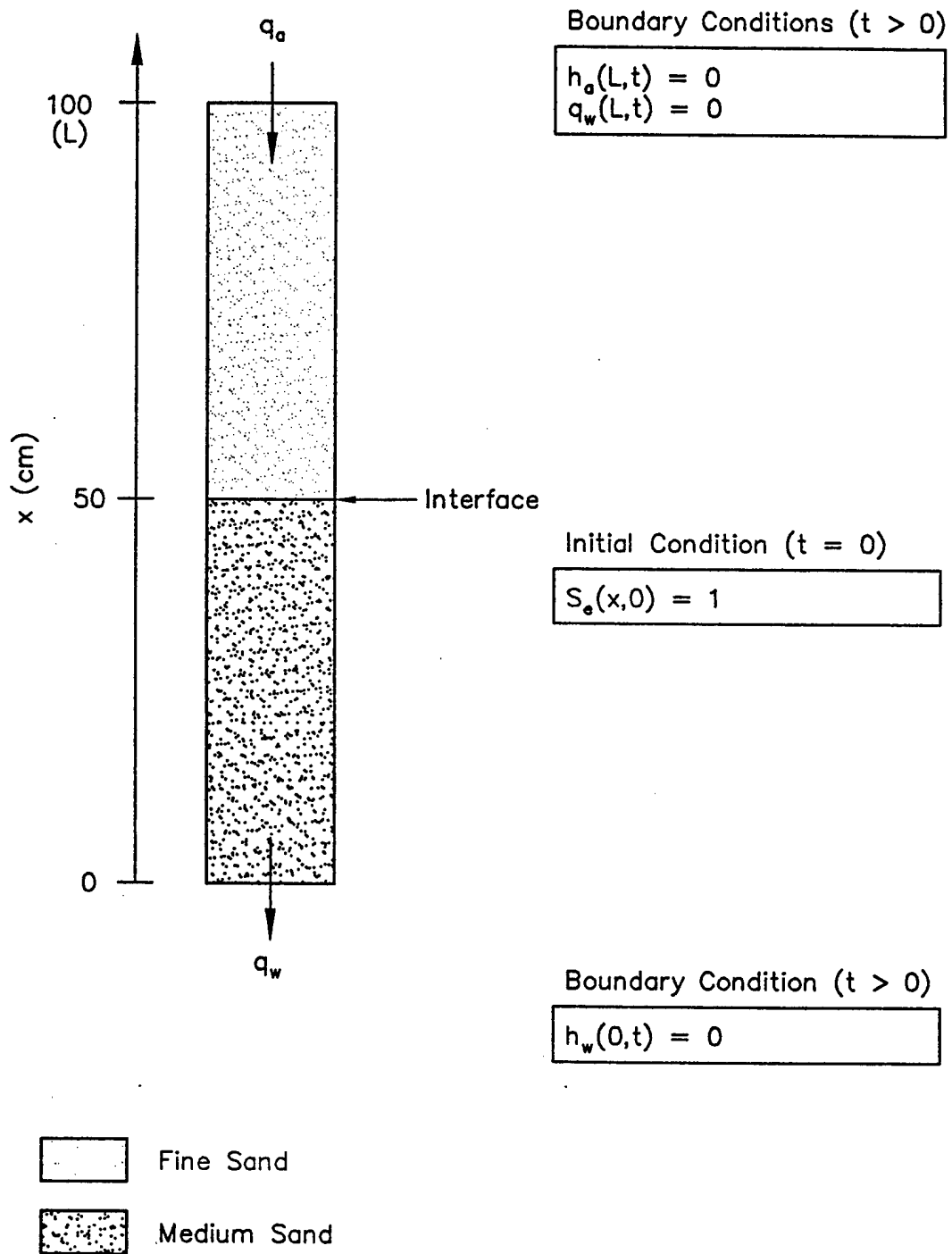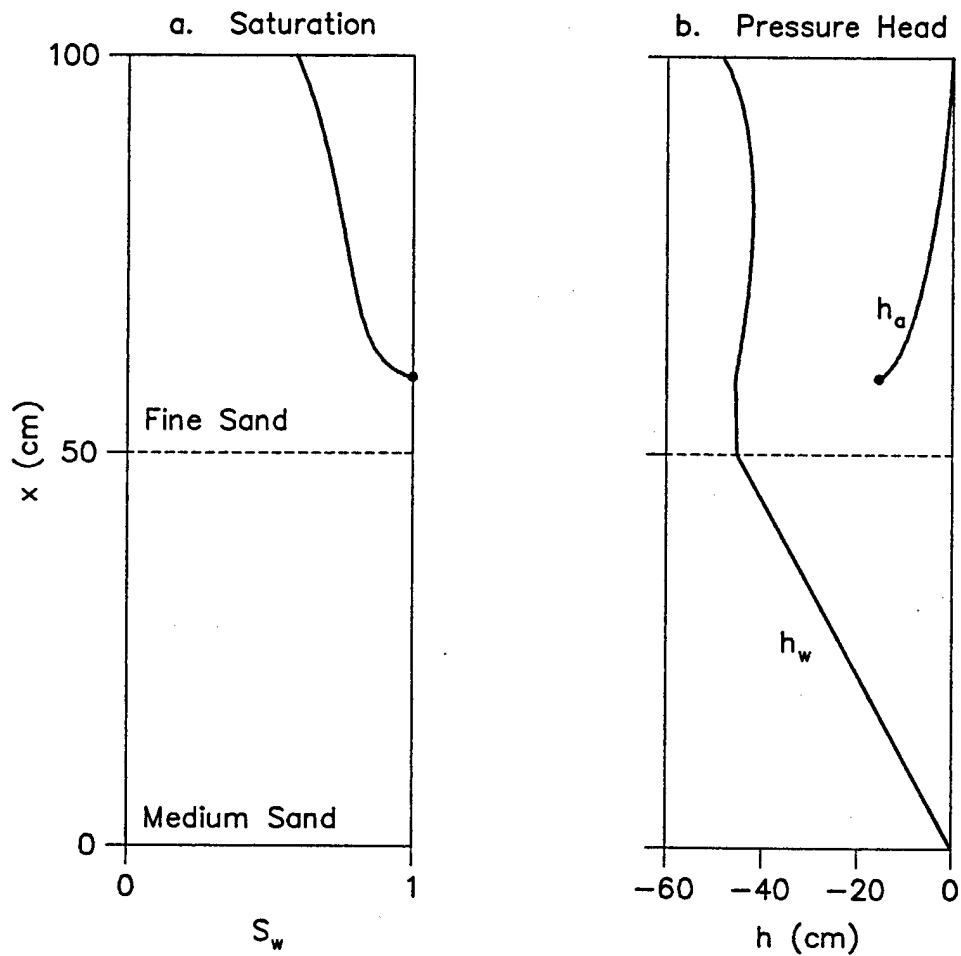**Figure 2-10. Vertical Drainage in a Layered Soil Column.**

**a. Saturation**

**b. Pressure Head**

Fine Sand

Medium Sand

$S_w$

$h$ (cm)

$x$ (cm)

$h_a$

$h_w$

EXPLANATION

● Desaturation Point

**Figure 2-11. Drainage in a Layered Soil. t = 3360 seconds**

occurred in the lower layer. Because the water pressure head at the base of the upper (fine sand) layer is less than the negative of the displacement pressure for this material, $|q_w*| > K_w$ at the desaturation point and the Richards formulation cannot be applied to this drainage problem. This occurs even though the water pressure head at the base of the column is equal to zero. Note further that water pressure heads in the underlying medium sand near the interface are well below the value at which desaturation would occur if air access were permitted through the column walls. If the condition of no lateral access were relaxed, the Richards model could be applied and it would predict that the lower sand would have long since desaturated. However, this would be a departure from the problem statement and the Richards formulation cannot be applied to the problem as posed.

Upon arrival of the desaturation front at the material interface, the lower layer begins to drain. Figure 2-12 shows results of the two-fluid simulation at an elapsed time of 6,470 seconds. Note that significantly negative air pressures persist in both layers. The existence of negative air pressure heads throughout the system implies that for a given saturation (given capillary pressure head), the water pressure head is less than that which would occur if air were present at zero pressure head. The more negative water pressure head has the effect of decreasing the magnitude of the drainage rate, relative to the rate which would occur assuming zero air pressure.

Predicted drainage rates from the layered soil are shown on Figure 2-13. When the desaturation front first arrives at the interface, at an elapsed time of about 4,600 seconds, there occurs a transient increase in the magnitude of the drainage rate. This is caused by the sudden accessibility of air to the lower layer, resulting in rapid desaturation below the interface. This rapid desaturation is manifested as an increase in the magnitude of the drainage rate. As drainage proceeds, the magnitude once again declines and eventually approaches zero as a new static condition is approached. This
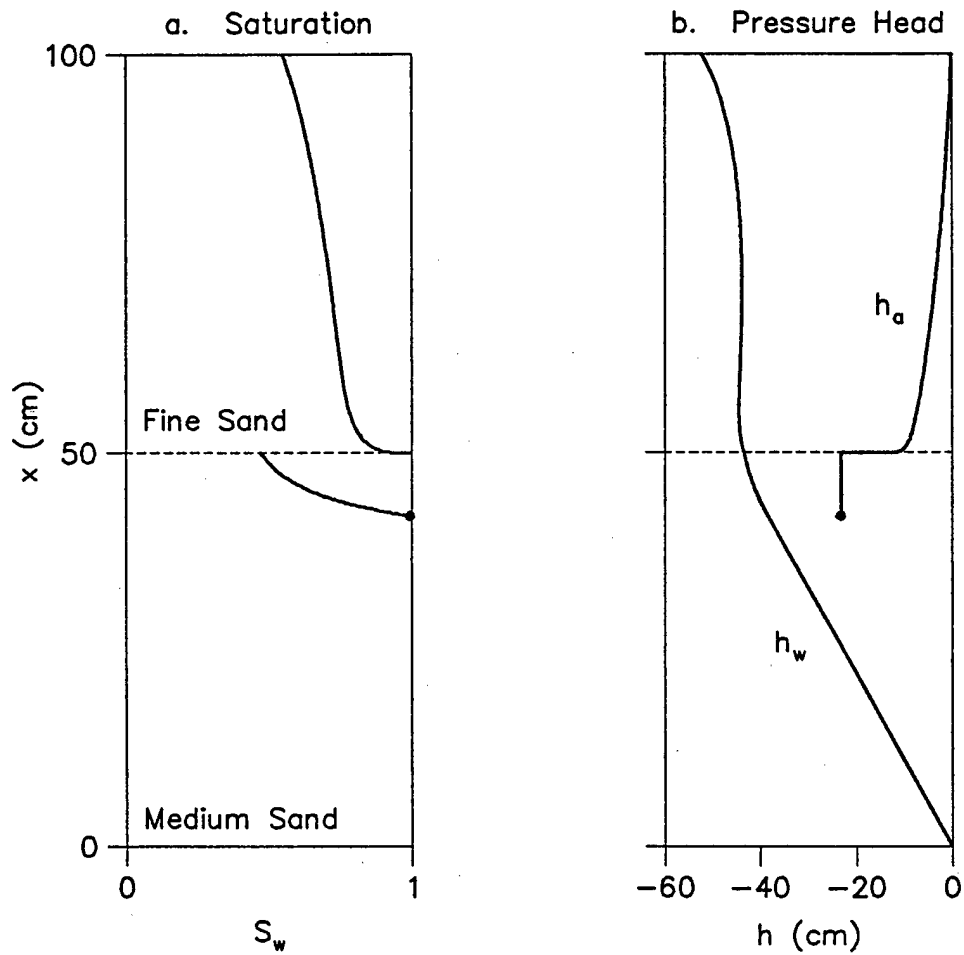
Figure 2-12. Drainage in a Layered Soil. t = 6470 seconds

Figure 2-13. Total Volume Flux for Drainage in a Layered Soil.
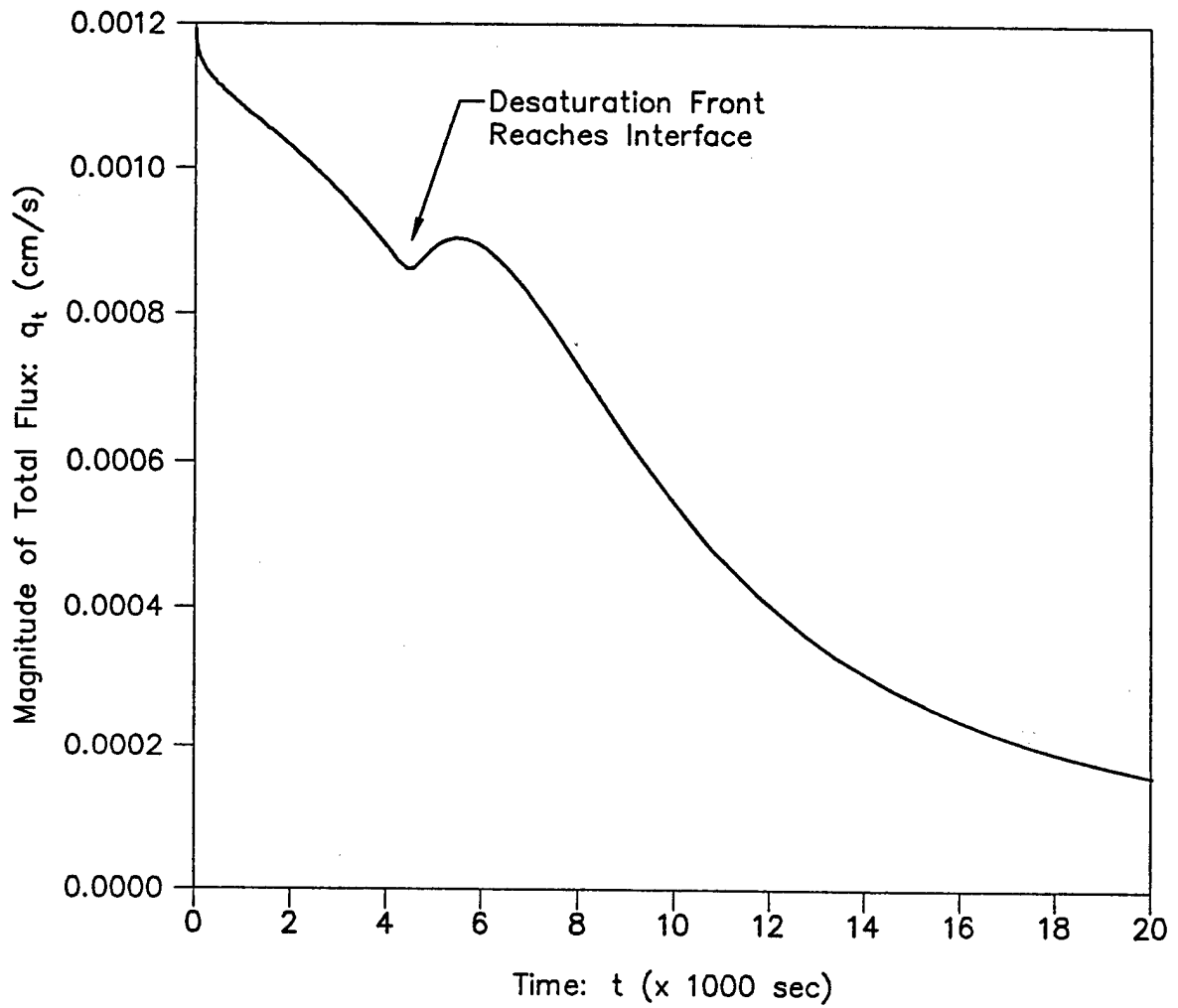
Note:

Total Flux $[q_t(t)]$ = Air (Inflow) Flux at Top of Column $[q_a(L,t)]$

= Water (Outflow) Flux at Bottom of Column $[q_w(0,t)]$

drainage behavior can only be explained by considering two-fluid flow with finite air viscosity.

This simulation clearly shows that for drainage in a layered soil column with limited access of viscous air, the drainage behavior predicted by two-fluid flow theory is grossly different than what would be predicted if one assumes either zero air viscosity or the ability of air to freely access the system laterally. For the case of viscous air with limited access, the drainage rates are lower and the sequence of desaturation from layer to layer is different. The Richards model provides a theoretical solution to this problem *only* if the condition of no lateral air access is relaxed.

## 2.6   CONCLUSIONS

From the standpoint of practical application, the most significant conclusion to be drawn from this study is that the hydraulics of air flow can have a significant impact on the nature of vertical water drainage. The effects of air flow appear to be more pronounced when its access to the porous medium is restricted and when the drainage process occurs in layered or otherwise heterogeneous materials. When air flow is important, rigorous analysis of the drainage process can only be performed by considering two-fluid (air-water) flow, with air possessing a finite viscosity. In general, the effects of viscous air and limited air access is to reduce the rate of drainage and change the sequence by which individual layers desaturate. It can be shown that for many types of drainage problems, air pressure within the flow system is reduced to values which are significantly less than atmospheric.

The Richards equation has traditionally formed the basis for analysis of drainage in air-water systems. When air access is limited, the Richards model can lead to inaccurate simulations of drainage behavior, particularly in layered soils. Saturation distributions and drainage rates predicted by the Richards model can be significantly different from the real behavior of field soils and laboratory test columns. For a certain

class of drainage problems with limited air access, the Richards model does not allow a theoretical solution to be obtained.

Finally, because of the uniform air pressure assumption used to derive the Richards flux equation, the Richards model could be interpreted to contain an implicit assumption of zero air viscosity. In our opinion, it is inaccurate and potentially misleading to interpret the Richards formulation as describing a zero-air-viscosity flow system. It is more accurate to view Richards equation as an *unlimited air access* model, where air is *supplied* to the system at zero pressure head. There are many types of drainage problems where the Richards model will provide similar results as a zero-air-viscosity flow model. However, for certain drainage problems, the Richards model does not predict the drainage behavior that would occur in a true zero-air-viscosity system.

## 2.7    REFERENCES

Brooks, R.H. and A.T. Corey. 1964. Hydraulic properties of porous media. Colorado State University Hydrology Paper No. 3, Fort Collins, CO, 27 pp.

Brooks, R.H. and A.T. Corey. 1966. Properties of porous media affecting fluid flow. *Proc. Irrigation and Drainage Division*, American Society of Civil Engineers, 92(IR2), pp. 61-87.

Corey, A.T. 1994. *Mechanics of Immiscible Fluids in Porous Media*. Water Resources Publications, Highlands Ranch, CO, 252 p.

Dullien, F.A.L. 1992. *Porous Media Fluid Transport and Pore Structure, Second Edition*. Academic Press, Inc.

Jury, W.A., W.R. Gardner and W.H. Gardner. 1991. *Soil Physics, Fifth Edition*. John Wiley & Sons, Inc.

McWhorter, D.B. 1971. Infiltration affected by flow of air. Hydrology Paper No. 49, Colorado State University, Fort Collins, CO.

McWhorter, D.B. and F. Marinelli. 1996. Theory of soil-water Flow. Manuscript in preparation.

Morel-Seytoux, H.J. 1975. Drainage rates from a vertical column. *Hydrological Science Bulletin*, XX(2), pp. 249-255.

Morel-Seytoux, H.J. 1973. Two-phase flows in porous media. In *Advances in Hydroscience*, 9, RJM. DeWiest, editor, Academic Press.

Morel-Seytoux, H.J. 1969. Flow of immiscible liquids in porous media. Chapter 11 in *Flow Through Porous Media*, R.J.M. DeWiest editor, Academic Press.

Richards, L.A. 1931. Capillary conduction of liquids through porous mediums. *Physics*, 1, pp. 318-333.

CHAPTER 3


PERFORMANCE AND SIMULATION OF AN LNAPL-WATER
DRAINAGE EXPERIMENT IN LAYERED SOIL


**Abstract**

A new semi-analytical solution for one-dimensional, two-fluid flow is used to simulate an experiment involving the drainage of LNAPL and water in a laboratory column containing layered sands. Input parameters used in the model are based on independent laboratory measurements of the fluid/soil properties, with only a slight adjustment in the hydraulic conductivity of one of the sands. The fit between model predictions and measured drainage rates is surprisingly good, considering the overall uncertainty in the input parameters and the fact that the model is not extensively calibrated. This study suggests that the semi-analytical solution adequately models two-fluid drainage in layered soils, without experiencing the types of stability problems that can adversely affect the performance of traditional finite difference and finite element numerical models.


**3.1    INTRODUCTION**

The presence of Light Nonaqueous Phase Liquids (LNAPLs) in the subsurface represents a source of ground-water contamination at many hazardous waste sites including oil refineries, heavy manufacturing facilities, petroleum tank farms, and gasoline service stations. Generally distributed near the water table, mobile LNAPL can migrate vertically when the water-table elevation changes. Field observations have indicated that if the water table drops below its previous range of fluctuation, LNAPL may temporarily or permanently disappear from monitoring wells. This situation commonly occurs at field sites after initiation of a ground water pump-and-treat system,

which can lower the water table over a broad area. In Marinelli and Durnford (1996), it is proposed that the above observation can be explained by the process of slow downward migration of LNAPL above the (falling) water table. It is further considered that the LNAPL migration process may be relatively slower and exhibit complex behaviors when it takes place in layered or otherwise heterogeneous soils.

Simulation of vertical, one-dimensional, drainage of LNAPL and water in layered soils has been difficult using traditional finite difference and finite element numerical models. Due to the highly nonlinear governing equations, these modeling approaches can exhibit numerical instabilities and convergence problems, particularly when sharp saturation fronts move across material interfaces. Analytical solutions for immiscible flow developed by McWhorter and Sunada (1990) are not applicable to vertical flow problems and do not explicitly consider layered materials. In Chapter 1, a semi-analytical solution is described for simulating vertical, one-dimensional, two-fluid flow in layered media. The two-fluid semi-analytical solution has been successfully applied to layered materials, without experiencing the types of stability problems that can adversely affect the performance of traditional numerical models.

This chapter describes a simple laboratory drainage experiment where water, in the absence of air, is displaced by LNAPL in a layered soil. The experiment considers the downward migration of LNAPL, below a shallow ponding condition, due to a rapid lowering of the water table. The experimental setup is such that the only fluids in the system are LNAPL (nonwetting fluid) and water (wetting fluid). The observed behavior of this drainage experiment is compared with the simulated results of the two-fluid semi-analytical solution. Independently measured properties of the fluids and porous materials are used as input to the semi-analytical solution. In order for the comparison to be objective, the

mathematical solution is *not* extensively calibrated in an attempt to force a match between the simulation results and laboratory data.

## 3.2 LABORATORY EXPERIMENT

The laboratory setup used for the LNAPL-water drainage experiment is shown on Figure 3-1. From bottom to top, the laboratory column was packed with 40 cm of 100-mesh silica sand, 30 cm of 40-60-mesh silica sand, and 30 cm of 100-mesh silica sand, all manufactured by Colorado Silica Sands, Inc., Colorado Springs, Colorado. The sands were placed by gravity raining using equipment and procedures described in Rad and Tumay (1987). After sand placement, the column was vacuum saturated with de-aired water and left overnight so that any remaining air would dissolve into the water phase. The ball valve was then opened and water was drained from the column until the free water surface was just above the perforated plate. A Marriott siphon containing Soltrol 220 was installed at the top of the column. Soltrol 220 (Phillips Petroleum Company, Bartlesville, Oklahoma) is a very stable LNAPL that is immiscible with water and maintains its fluid properties when in contact with water. The Marriott was positioned so that a Soltrol pond about 5 cm deep was maintained at the top of the column.

At the beginning of the experiment, the ball valve was opened allowing water to discharge from the bottom of the column which caused the LNAPL-water interface at the top of the column to approach the upper surface of the sand. Zero time was specified when the interface reached the top of the upper sand layer. LNAPL flowing into the top of the sand column displaced water which was draining downward and discharging from the base of the column. A graduate cylinder was used to measure the volumes of water discharging from the base of the column. Water drainage was monitored at ten minute intervals for approximately 12 hours.
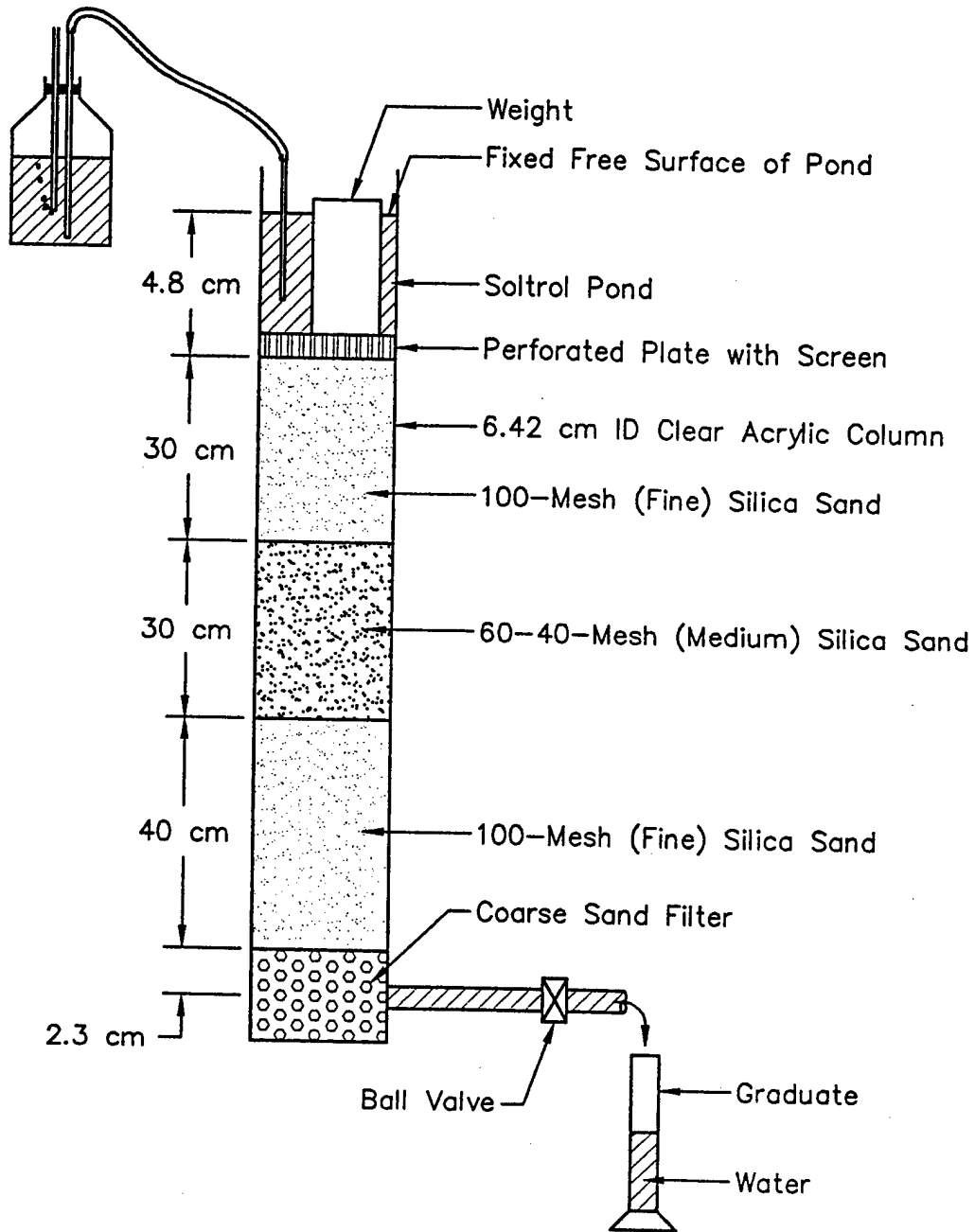
**Figure 3-1. Laboratory Setup for the LNAPL-Water Drainage Experiment.**

Water discharge volumes, measured at periodic time intervals, were used to computed the water discharge flow rate as a function of time. Water drainage flux (darcy velocity) was computed as this flow rate divided by the internal cross-sectional area of the column. Assuming that the fluids and porous medium are incompressible, the water flux at the base of the column should be approximately equal to the LNAPL flux at the top of the column. Water drainage flux over time is shown graphically on Figure 3-2. Of interest is the decreasing water flux during the first 10,000 seconds, the uniform and slowly decreasing flux between 10,000 and 34,000 seconds, and the sharp decrease in flux observed at about 34,500 seconds.

## 3.3    FLUID AND SOIL PROPERTIES

Properties of the fluids and soils used in this experiment have been measured by Miller and Durnford (1996) and are summarized in Table 3-1a,b. Dry bulk densities of the sand layers in the experimental column (Table 3-1c) were determined by weighing the column before and after the placement of each layer. The average porosity of the sand layers was calculated based column weights before and after saturation.

## 3.4    MATHEMATICAL SIMULATION OF THE EXPERIMENT

The governing flow equations for one-dimensional, incompressible, two-fluid flow are discussed in detail in Chapter 1. The initial condition and boundary conditions describing the laboratory experiment are shown on Figure 3-3. Initially the layered column is completely saturated with water. The boundary conditions at the top of the column are (1) no-flow of water and (2) a nonwetting fluid (LNAPL) pressure head is equal to 3.98 cm (water). The latter condition is equivalent to a Soltrol pond height of 4.8 cm above the top of the sand. At the base of the column, the boundary condition is a water pressure head equal to -2.3 cm, which is the elevation difference between the discharge pipe and the base of the fine sand. It is assumed that there are no head
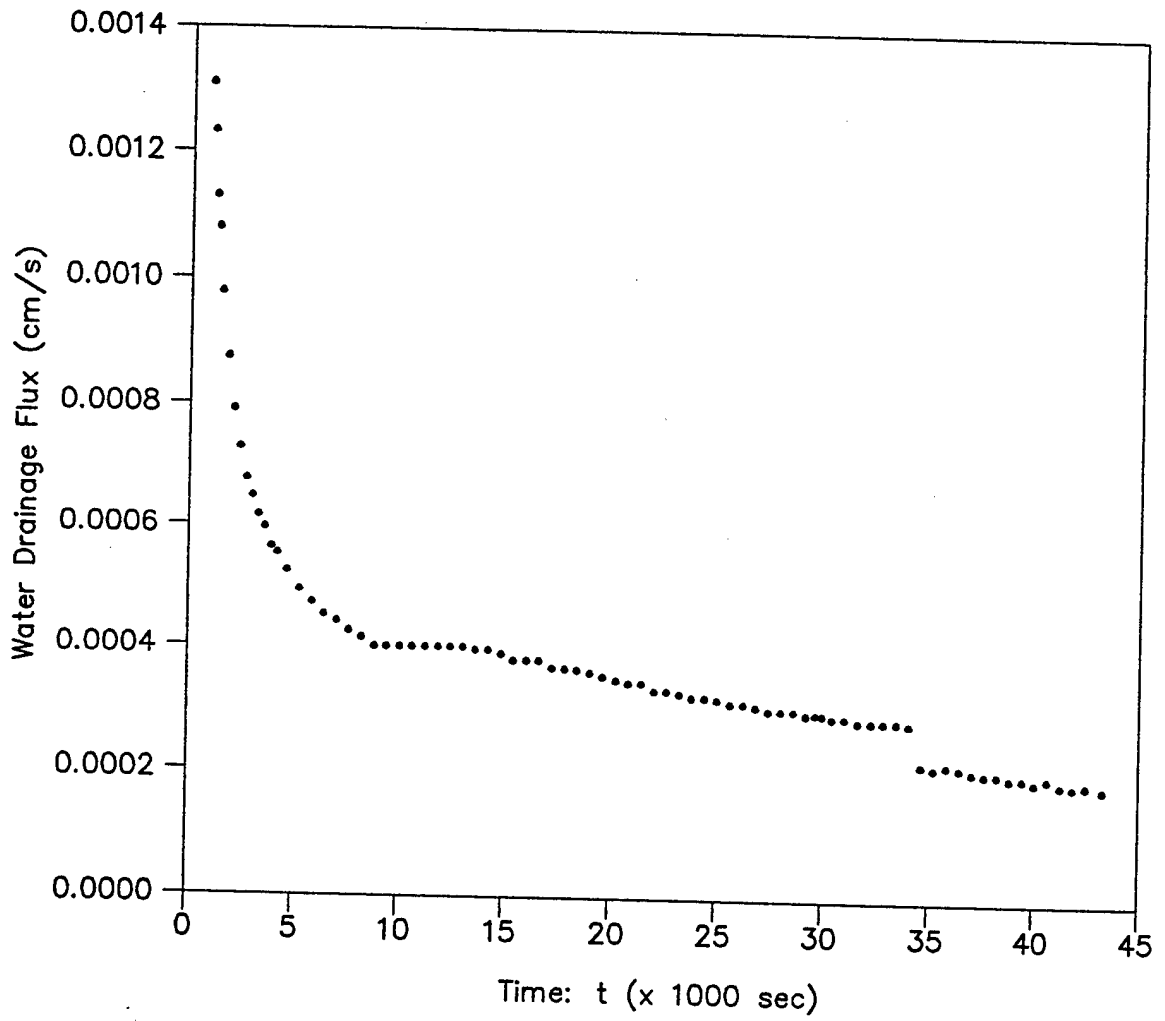
**Figure 3-2. Drainage Experiment - Measured Drainage Flux.**

**Table 3-1. Properties of Fluids and Soils Used in the Drainage Experiment.**

**a. Fluids (a)**

| | Units | Water | Soltrol 220 |
|---|---|---|---|
| Density (b) | $(g\ cm^{-3})$ | 1.00 | 0.83 |
| Viscosity (b) | $(g\ cm^{-1}\ s^{-1})$ | 0.0095 | 0.0365 |
| Surface Tension | $(dyne\ cm^{-1})$ | 70 | 28 |
| Interfacial Tension | $(dyne\ cm^{-1})$ | N/A | 42 |

**b. Soils (a)**

**Sand**

| | Units | Fine Sand | Medium |
|---|---|---|---|
| Description | | 100-Mesh | 40-60-Mesh |
| Mean Grain Diameter, $d_{50}$ | (mm) | 0.16 | 0.27 |
| $d_{10}$ | (mm) | 0.08 | 0.25 |
| $d_{90}$ | (mm) | 0.30 | 0.30 |
| Uniformity Coefficient ($d_{60}/d_{10}$) | | 2.18 | 1.12 |
| Brooks-Corey Air-Water Displacement Pressure Head | (cm water) | 41 | 18 |
| Brooks-Corey Pore Size Distribution Index (b) | | 1.7 | 3.4 |
| Irreducible Saturation (b) | | 0.08 | 0.05 |
| Average Packed Porosity | | 0.37 | 0.37 |
| Saturated Hydraulic Conductivity (b,c) | $(cm\ s^{-1})$ | 0.0020 | 0.010 |

**c. Soils (Experimental Column)**

**Sand**

| | Units | Fine Sand | Medium |
|---|---|---|---|
| Dry Bulk Density | $(g\ cm^{-3})$ | 1.62 | 1.67 |
| Porosity (Average for Both Sands) | | 0.36 | |

**Notes:**

(a)     Values reported in Miller and Durnford (1996)

(b)     Input values for the simulations.

(c)     Second simulation used hydraulic conductivity of 0.0018 cm/s for fine sand.
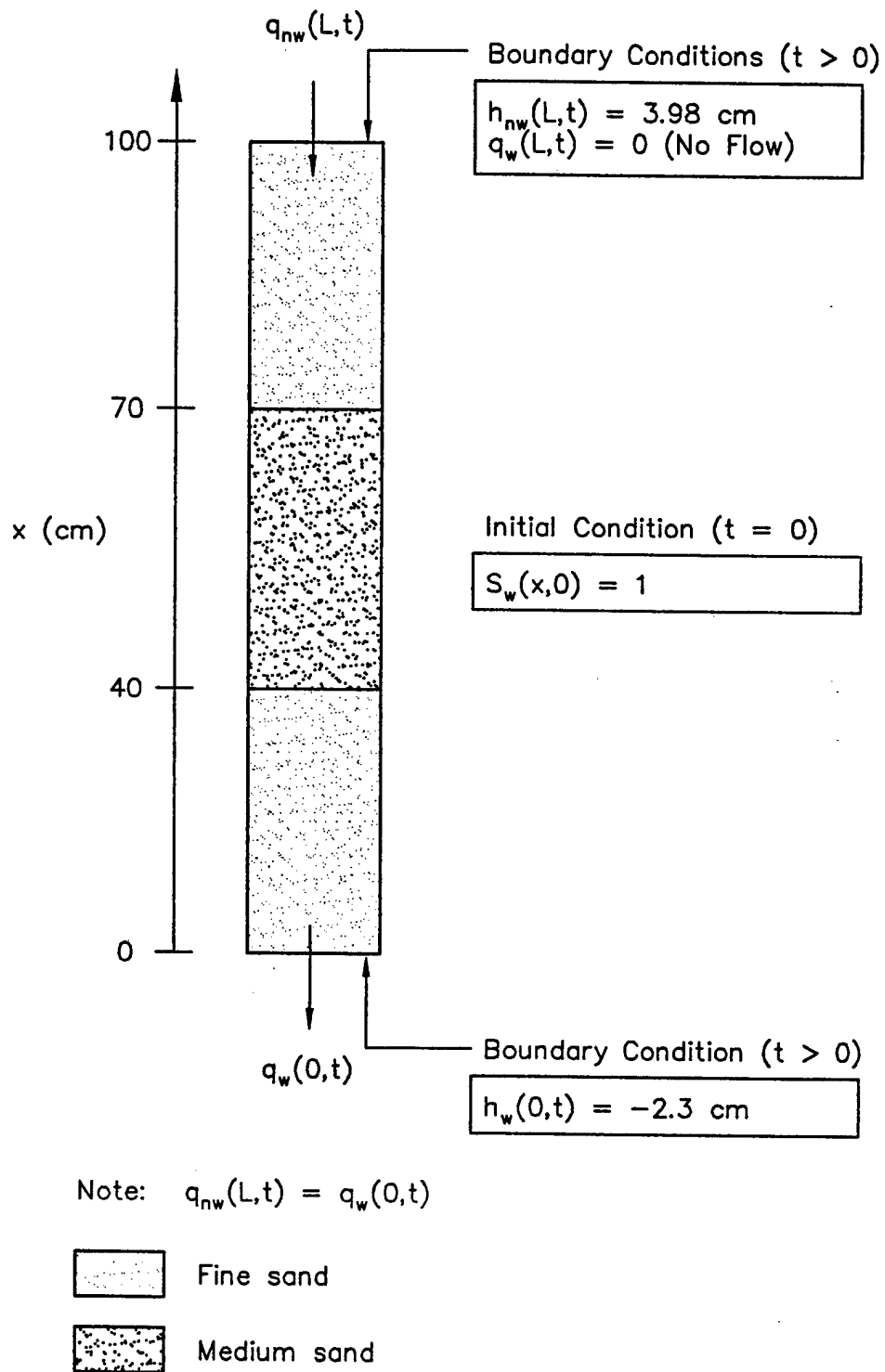
**Figure 3-3.** Initial-Boundary-Value Problem for Simulation of the Drainage Experiment.

losses in the coarse sand filter below the fine sand. The above initial-boundary-value problem is solved using the semi-analytical technique described in Chapter 1.

Equations relating capillary pressure, fluid saturation, and relative permeabilities are based on the Brooks and Corey (1964, 1966) parametric model. For this physical problem, the wetting fluid (water) is always under drainage conditions. Therefore, the capillary pressure - saturation relationships are assumed to be nonhysteretic and to follow main drainage paths. Table 3-1 provides air-water displacement pressure heads for the sands used in the column. For this simulation, we require an estimate of the LNAPL-water displacement pressures. These estimates are obtained by scaling the air-water displacement pressures as follows:

$$h_d^{lw} = h_d^{aw} \left( \frac{\sigma^{lw}}{\sigma^{aw}} \right) \tag{3-1}$$

where $h_d^{lw}$ and $h_d^{aw}$ are the displacement pressure heads for LNAPL-water and air-water systems, respectively, $\sigma^{lw}$ is the LNAPL-water interfacial tension, and $\sigma^{aw}$ is the air-water surface tension. For the Brooks-Corey saturation model, this procedure is equivalent to the scaling approach described by Parker et al. (1987), although they apply this procedure only to the van Genuchten (1980) parametric model. Based on equation (3-1), the LNAPL-water displacement pressure heads are computed to be 10.8 and 24.6 cm (water) for the medium and fine sands, respectively.

Based on the two-fluid semi-analytical solution, the laboratory experiment has been simulated using the above LNAPL-water displacement pressures and other input parameters identified in Table 3-1. On Figure 3-4, simulated water drainage rates from two modeling runs are compared with actual drainage rates measured during the laboratory experiment. The first simulation is based on the initial best-estimate hydraulic conductivity of 0.002 cm/s for the fine sand.
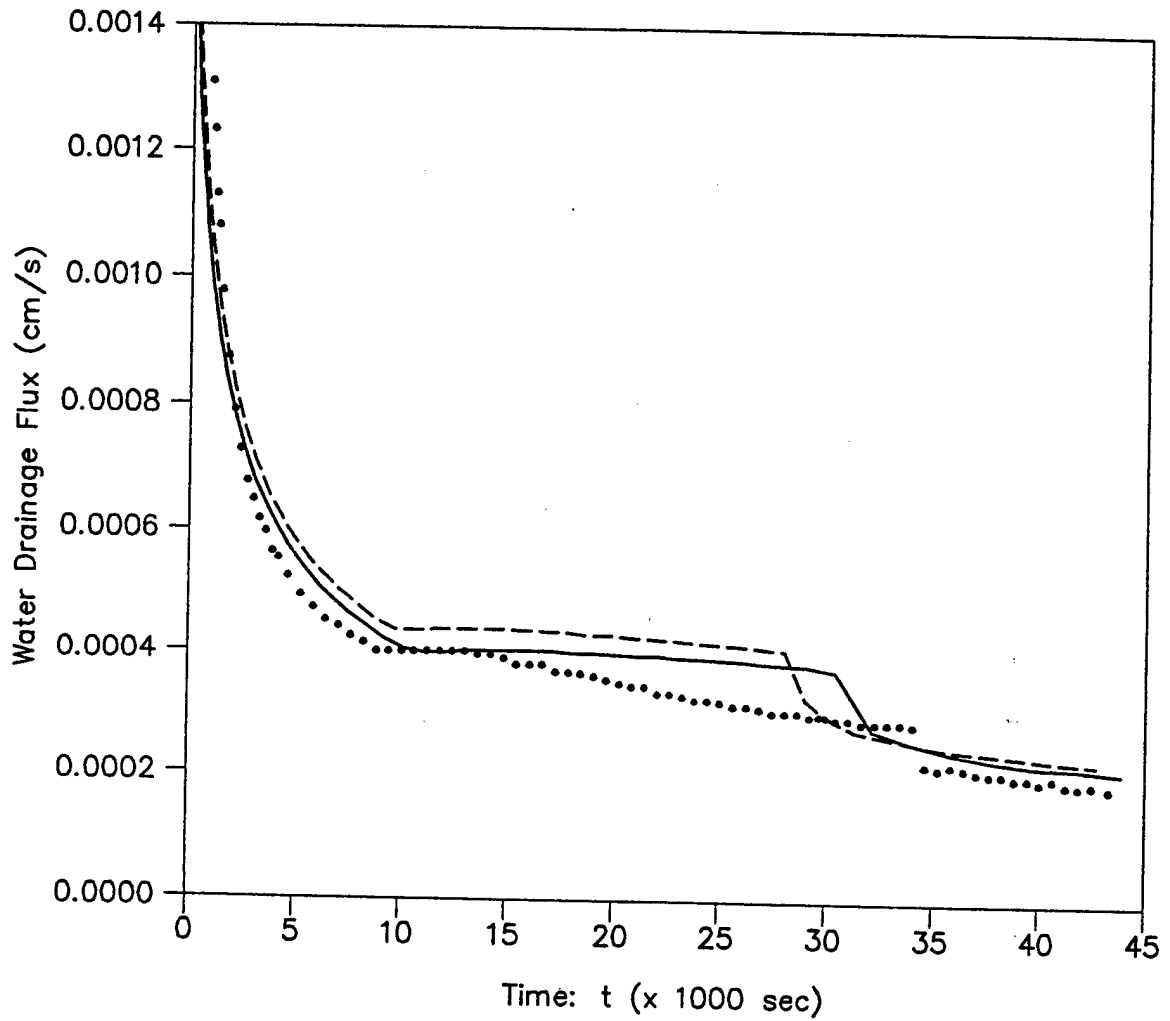
**Figure 3-4. Comparison of Predicted and Measured Drainage Flux.**

It is observed that the predicted fluxes are consistently higher than the measured fluxes. The second modeling run is based on a reduced hydraulic conductivity of 0.0018 cm/s for the fine sand. This decrease in conductivity of approximately 8 percent is considered to be within the uncertainty range associated with the laboratory permeameter test used by Miller and Durnford (1996) to measure the conductivity of the fine sand. The slightly lower conductivity may be reasonable because the packed porosity of the experimental column (36 percent) was less than the packed permeameter porosity (37 percent). The second simulation gives lower fluxes and provides a better fit to the measured data.

Based on the second model simulation, Figure 3-5 shows predicted saturation profiles at different times during the drainage process. At a time of 3,300 seconds (Figure 3-5a), the desaturation front is in the uppermost fine sand layer, Figure 3-5b shows the profile at 11,570 seconds, just after the desaturation front has encountered the first material interface. Note that a saturation discontinuity exists across the interface and that the saturation approaches one at the base of the upper fine sand layer. At 20,570 seconds (Figure 3-5c), the desaturation front has moved downward into the middle medium sand layer. The saturation discontinuity remains at the first interface. On Figure 3-5d, at 32,970 seconds, the desaturation front has just moved past the second interface. Saturation discontinuities are shown to exists at both interfaces and the saturation remains close to unity at the base of the upper layer. In addition, the middle layer is mostly desaturated. Finally, at 44,970 seconds, the desaturation front is predicted to move well into the lower fine sand layer. The saturation discontinuities remain at both interfaces. However, some desaturation is shown to occur at the base of the upper layer.

## 3.5    DISCUSSION

The comparison of simulated results and laboratory data on Figure 3-5 shows that the semi-analytical solution seems to capture the qualitative behavior of the laboratory experiment. The general shapes of the curves are similar, including the sharp reduction in water flux which is predicted to occur when the desaturation front migrates into the lower layer. In general, the semi-analytical solution predicts higher fluxes compared to those measured during the laboratory experiment.

The second simulation provides a better fit to the laboratory data. These simulated results are very close to the laboratory measurements during the first 14,000 seconds. After 14,000 seconds, the simulation shows fluxes that decrease very slowly, while the laboratory experiment indicates more rapidly decreasing fluxes. The abrupt decrease in flux is predicted by the model to occur at about 31,000 seconds, while the observed decrease occurs at about 34,500 seconds. The higher simulated fluxes appear to have the effect of decreasing the time for the middle medium sand layer to desaturate compared to the experimental data. As a result, the model predicts that the saturation front reaches the second interface sooner than what apparently occurred during the experiment. At late times, the simulated drainage fluxes are similar to, but slightly higher than, the laboratory fluxes.

Note that the second simulation is based on *independently* measured fluid and soil properties, with only a slight adjustment in the assumed hydraulic conductivity of the fine sand. As a consequence, this simulation does not represent an extensive calibration effort to force a match between simulation results and measured laboratory data. Considering the overall uncertainty of the fluid/soil properties, the predictions of the semi-analytical solution are surprisingly good.
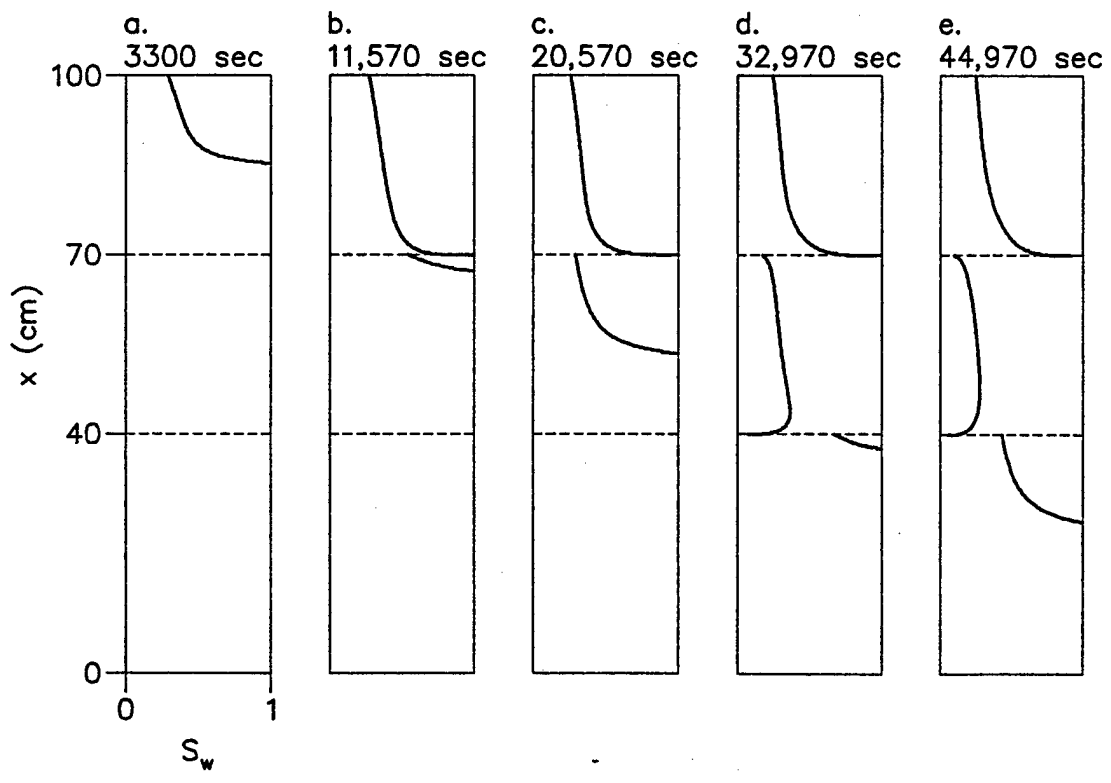
**Figure 3-5. Drainage Experiment - Predicted Saturation Profiles.**

## 3.6    CONCLUSIONS

This study provides evidence that the semi-analytical solution for two-fluid flow adequately models the important physical processes controlling LNAPL-water drainage in layered soils.  The fit between model predictions and measured laboratory data is quite good, considering that the input values are uncertain and that the model was not extensively calibrated.  The semi-analytical solution achieves this level of performance without experiencing the types of stability problems that can adversely affect the performance of traditional finite difference and finite element numerical models.  This study suggests that the semi-analytical solution developed in Chapter 1 may be a promising technique for modeling the one-dimensional flow of immiscible fluids in layered porous media.

## 3.7    REFERENCES

Brooks, R.H. and A.T. Corey. 1964. Hydraulic properties of porous media. Colorado State University Hydrologic Paper No. 3, Fort Collins, CO.

Brooks, R.H. and A.T. Corey. 1966. Properties of porous media affecting fluid flow. *Proc. Irrigation and Drainage Division*, American Society of Civil Engineers, 92(IR2), pp. 61-87.

Marinelli, F. and D.S. Durnford. 1996. LNAPL thickness in monitoring wells considering hysteresis and entrapment. *Ground Water*, 34(3), pp. 405-414.

McWhorter, D.B. and D.K. Sunada. 1990. Exact integral solutions for two-phase flow. *Water Resources Research*, 26(3), pp. 399-413.

Miller, C.D. and D.S. Durnford. 1996. Experimental study of one-dimensional immiscible fluid drainage in layered sands. Proc. 1996 ASCE Special Symposium: Nonaqueous Phase Liquids in the Subsurface Environment: Assessment and Remediation, Washington D.C., November 12-14, 1996.

Parker, J.C. R.J. Lenhard and T. Kuppusamy. 1987. A parametric model for constitutive properties governing multiphase flow in porous media. *Water Resources Research*, 23(4), pp 618-624.

Rad, N.S. and M.T. Tumay. 1987. Factors affecting sand specimen preparation by raining. *Geotechnical Testing Journal*, GTJODJ, 10(1), pp. 31-37.

van Genuchten, M.T. 1980. A closed-form equation for predicting the hydraulic conductivity of unsaturated soils. *Soil Science Society of America Journal*, 44, pp. 892-898.

# SECTION IV

# SECTION IV

## Chapter 1

## Stochastic Aggregation Model (SAM) for NAPL-water displacement in porous media

## Abstract

Characterization of NAPL distribution in the subsurface is a necessary part of

managing environmental risks posed by NAPLs. Modeling NAPL-water displacement

processes at the pore-scale can lead to greater insight and understanding of lateral

spreading, the extent of vertical penetration, and the final fluid distributions of NAPL in

aquifers. A stochastic aggregation model (SAM), based on diffusion limited aggregation

(DLA), has been developed that can predict the configuration of the front produced when

a NAPL displaces water at the pore-scale in a homogeneous porous medium. The model

takes into account the essential properties governing front stability: NAPL-water

viscosity differences, NAPL-water density differences, intrinsic permeability of the

porous media, flow rate, and the inclination angle of the porous media from the

horizontal. These properties are the independent variables for the transition number,

which is derived from two-phase flow equations and uses a macroscopic non-

dimensionalization. The transition number serves as the model's input.

Using the continuum approach to determine fluid-fluid displacements at the pore-

scale is computationally prohibitive and involves many assumptions. Our approach

utilizes the stochastic nature of the DLA algorithm, while including fluid properties,

generalized porous media properties and macroscopic flow rates. Due to the simplicity of

the algorithm, this modeling technique can very quickly produce realistic NAPL-water configurations and allows for a Monte Carlo approach to be utilized.

The model simulations in this paper show front configurations for common NAPLs (1,2 dichloroethane, 1,2 dibromoethane, gasoline, and mineral oil) which range from fingered to stable and can be compared via their fractal dimension. The simulations show the NAPL-water displacement front configuration as it is influenced by the competition between capillary, viscous, and gravitational forces at the pore-scale.

## 1.1 INTRODUCTION

Dense Non-Aqueous Phase Liquids (DNAPLs) are liquids with higher specific gravities than that of water. Their use has been widespread since World War II. Most DNAPLs are solvents, but there are also some liquids used in chemical manufacturing, organic synthesis, and mineral separation that are classified as DNAPLs. Much of the contamination caused by DNAPLs has been the result of leaking underground storage tanks and various other spills caused by the electronic, instrument manufacturing and aerospace industries (Pankow, et al. 1996). While their designation as non-aqueous implies immiscibility with water, DNAPLs can cause significant contamination. The absolute solubilities with water are low for most DNAPLs, but their solubility to maximum contaminant level (MCL) ratios are often high.

Light Non-Aqueous Phase Liquids (LNAPLs) are liquids with a specific gravity less than that of water. Most LNAPLs are associated with the production, refining, and distribution of petroleum products. When LNAPLs are released at the surface they tend to migrate downward through the unsaturated zone to the water table. If large gradients

are present, they may penetrate the water table. Petroleum LNAPLs are relatively biodegradable, but their constituents such as benzene, toluene, ethyl benzene, and xylene can cause widespread contamination (Bedient, 1994).

Managing the environmental risks posed by NAPLs and improving technologies used to clean up contaminated areas depends largely on understanding and predicting the migration of NAPLs. Successful NAPL remediation depends on determining the presence and configuration of the NAPL phase. In the range of possible flow regimes and fluid properties, NAPL displacement of water in porous media can produce fronts which are stable, highly fingered or anything in between. The movement of the front is determined by the competition between viscous, capillary, and gravity forces at the pore level. By understanding the movement of the NAPL at the pore-scale we can gain insight into the distribution of NAPLs in the subsurface. Specifically, site characterization and the level of detail needed for field sampling, estimation of the potential groundwater contamination, and retention capacities can be better determined.

Modeling the NAPL distribution as it displaces water at the pore level, given the characteristics of the NAPL and release conditions, was the focus of this research. Instead of using the continuum approach, a stochastic modeling technique was chosen which utilizes basic instability criteria for two fluids. The advantage of this technique is the speed with which the algorithm can produce simulations. The following objectives were determined to be important in creating a model that could be useful for practical applications.

1. The model should be a computationally simple pore-scale model.

2. The model should be applicable over a wide range of fluid properties and flow conditions.

3. The model should have macroscopic input parameters

Our stochastic aggregation model (SAM) is a variant of Witten and Sander's (1983) Diffusion Limited Aggregation (DLA) model. DLA has been used to model such unstable processes as dielectric breakdown (Niemeyer, et al. 1984; Wiesmann and Zeller, 1986), diffusion-controlled polymerization (Kaufman et al., 1986), chemical dissolution processes (Daccord, 1986), solute leaching (Flury and Fluhler, 1995), viscous fingering (Maloy, et al., 1985; Chen and Wilkinson, 1985), fluid-fluid displacement in Hele Shaw cells (Kadanoff, 1985; Liang, 1986); and fluid-fluid flow in porous media (Paterson, 1984; Lenormand, 1987; Kiriakidis, et al., 1991; Fernandez, et al., 1991). The input to the model is the transition number, T, which is a linear combination of the macroscopic bond and capillary numbers. It is equivalent to the instability criteria of Saffman and Taylor (1958) and Chouke, et al. (1959). The transition number accounts for disparities in the viscosities and densities of the two fluids, and its use as the input to the modified DLA algorithm, SAM, is unique.

## 1.2 BACKGROUND

### 1.2.1. Stochastic Modeling Techniques

Lenormand, et al. (1988) performed micromodel experiments and showed that dramatically different front configurations occur during fluid-fluid displacement in porous media that can be modeled by different stochastic techniques. The domains of the

stochastic modeling techniques are shown in the phase diagram in Figure 1 (Lenormand, 1987). The phase diagram is applicable to displacement of the wetting fluid by the non-wetting fluid without gravity forces. The three domains labeled as DLA, IP, and Plug Flow correspond to displacement of a viscous fluid by a nonviscous fluid, capillary displacement, and displacement of a nonviscous fluid by a viscous fluid, respectively. Plug flow is modeled by a technique called anti-DLA. The areas between these pure domains are governed by a combination of the applicable forces. The limits of these domains are determined by an evaluation of the capillary pressure at the interface between the two fluids and use only the mobility ratio (M) and the microscopic capillary number (Ca) as parameters. The mobility ratio, M, is defined as the ratio of the dynamic viscosity of the displacing fluid to the dynamic viscosity of the displaced fluid:

$$M = \frac{\mu_2}{\mu_1} \tag{1-1}$$

The microscopic capillary number, Ca is defined as the ratio between the viscous forces and the capillary forces (Lake, 1989):

$$Ca = \frac{q\mu}{\sigma \cos\theta} \tag{1-2}$$

where q is the microscopic volumetric flux, $\mu$ is the dynamic viscosity, $\sigma$ is the interfacial tension between the two fluids, and $\theta$ is the contact angle.

Continuum models are considered by Lenormand (1987), to be in the domain labeled stable flow. When immiscible fluid-fluid displacement is not stable, the phase diagram offers modeling techniques for the pure regimes of capillary and viscous fingering and the limits for these pure regimes. To model fluid-fluid displacements
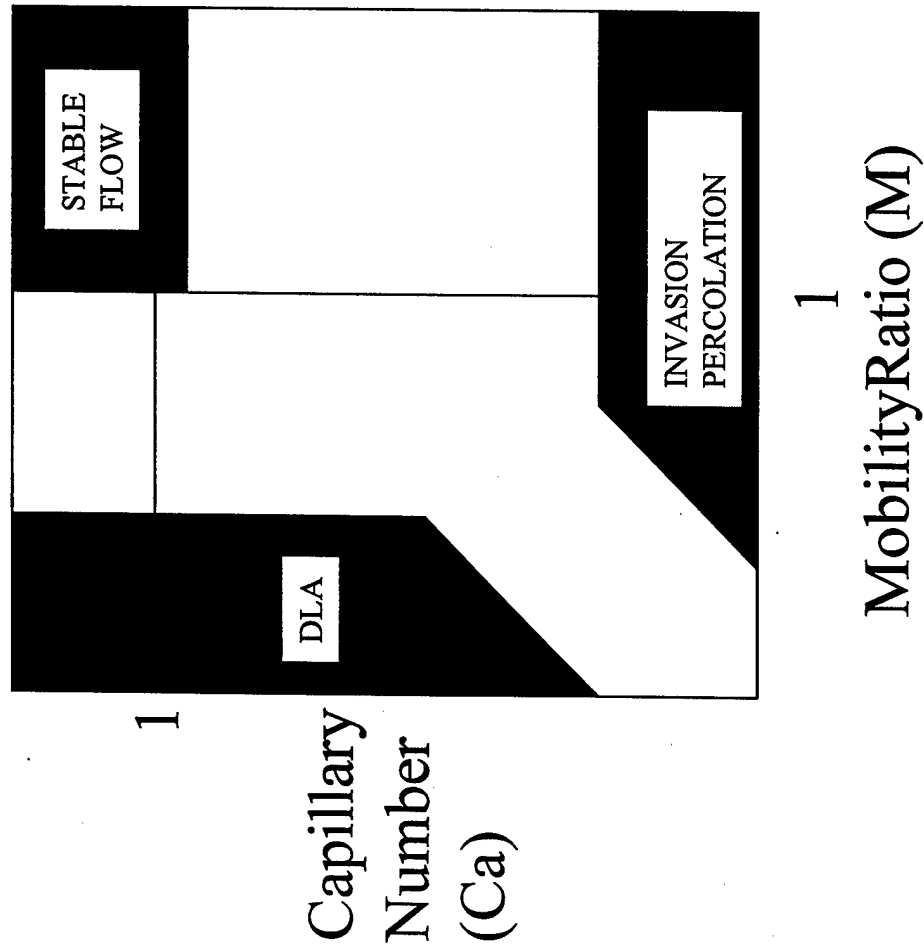
Figure 1. Lenormand's (1987) phase diagram for immiscible fluid-fluid displacement in the absence of gravity. The stochastic modeling techniques corresponding to the regimes for which their use is suggested is shown with varying microscopic capillary number and mobility ratio.

between these regimes, the combined forces acting to stabilize or destabilize the front must be considered. The effects of gravity are also important (Wilkinson, 1984; Birovljev, et al., 1991) and should be included in determining the NAPL-water front configuration.

We will consider the modeling techniques of IP and DLA before discussing how to combine the viscous and capillary effects as well as incorporate gravity forces into the current model, SAM.

Percolation modeling (Broadbent and Hammersley, 1957) takes place on a lattice of specified geometry and as such is designated as a network model. Fatt (1956) was the first to use network models for investigation of porous media. The application of percolation modeling to immiscible fluid-fluid displacement requires two assumptions. The first is that the interface moves as a series of discrete jumps by individual menisci. Surface tension effects purely determine these jumps. The second assumption maintains that the porous media is connected, and in some way random (Wilkinson, 1984). In standard percolation modeling, the probability that a lattice site will be filled is equal to the ratio of the number of sites currently occupied to the total number of sites. For immiscible fluid-fluid displacement, each lattice site has a value assigned to it that is representative of the pore size. When the algorithm begins (for drainage of the wetting fluid) all of the sites with a value greater than some r* will drain; where r* is related to the capillary pressure in the system (Wilkinson, 1984). This technique is limited by its implication that the occupation of one lattice site is independent of the occupation of its neighbor. The result is a lattice with many unconnected clusters where the invading fluid has displaced the defending fluid. In invasion percolation (IP), the method is the similar.

The difference is that for a given capillary pressure, only the lattice sites on the interface between the two fluids may be invaded and regions where the wetting fluid is surrounded by the non-wetting fluid remain trapped (Wilkinson and Willemsen, 1983). This results in a continuous cluster instead of many disconnected ones. IP models have been utilized to investigate hysteresis, boundary effects, ganglia and blob structure, and the effects of contact angle on capillary pressure saturation curves (Chatzis and Dullian, 1985; Li, et al., 1986; Wardlaw, et al., 1987; Jerauld and Salter, 1990; Tsakiroglou and Payatakes, 1990; Ferrand and Celia, 1992; Soll and Celia, 1993; Lowry and Miller, 1995). Berkowitz and Balberg (1993) present a good overview of percolation modeling as it is applied to groundwater hydrology. IP models are only valid for flow dominated by capillary forces, i.e. where the Young-Laplace equation governs the movement of the interface (Dullien, 1992). An example of an aggregate produced by IP is shown in Figure 2.
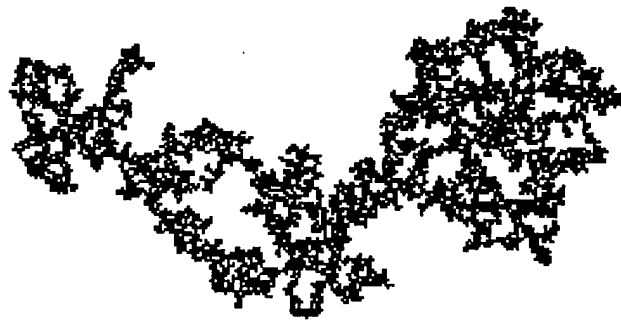


Figure 2. An aggregate produced by invasion
percolation with trapping (Meakin, 1991)

*1.2.2 DLA Modeling*

Aggregate growth by irreversible particle collection is a common phenomenon in nature (Sander, 1984). The displacement of one fluid by another in porous media can be represented by particle aggregation where the growing aggregate represents the invading fluid and the space surrounding the aggregate represents the defending fluid. Several modeling techniques can be used for particle aggregation. These include IP modeling (Wilkinson and Willemsen, 1983), Eden modeling (Sander 1984), ballistic aggregation (Sander, 1984), and DLA (Witten and Sander, 1983). IP modeling was discussed in the previous section, and has can be applied to immiscible fluid displacements dominated by capillary forces. To be able to model fluid-fluid displacements where any combination of viscous, capillary, or gravity forces can govern the stability of the interface, we must take a look at the other aggregate modeling options. Neither Eden modeling nor ballistic aggregation can describe the growth instabilities which are characteristic of many processes including fluid-fluid displacement with unfavorable mobility ratios (Sander, 1986). DLA models, however, produce aggregates resulting from unstable phenomenon using a stochastic process. Following Witten and Sander (1983), numerous other researchers have expanded on both the modeling technique and the applications for the model (Meakin and Deutch, 1986; Meakin, 1986; and Jullien, et al., 1984). Meakin (1988) provides a thorough review of DLA as a model for kinetic growth phenomena.

Diffusion-limited aggregation is an algorithm whereby an initial "seed" particle is placed in the center of a grid. One at a time, particles are released from a random position on the boundary. The particles move from location to location on the grid by taking one-unit steps in a randomly chosen direction. When the particle reaches a

location adjacent to a particle which is part of the aggregate, the walking particle becomes part of the aggregate, and another particle is released. . A DLA aggregate is shown in Figure 3. Qualitatively, the aggregates that are formed in this manner appear disordered with no length scale. This is a result of the "screening" effect of the branches (Sander, 1986). As the aggregate grows, it becomes more and more difficult for a particle to traverse the narrow areas between the branches without coming in contact with and thereby becoming part of the aggregate. Consequently, more particles will come in contact with the aggregate at the ends of the branches.
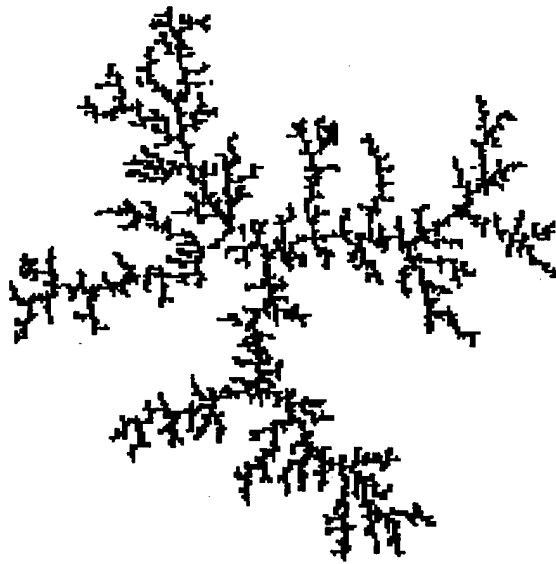


Figure 3. An aggregate produced by Witten and Sander's (1983) original diffusion limited aggregation algorithm.

The probability distribution of the random walkers, $u(r,t)$, obeys the following equation in the continuum limit (Sander, 1986):

$$\frac{\partial u}{\partial t} = D\nabla^2 u \qquad (1\text{-}3)$$

where r is a distance from the aggregate, t is time, and D is a diffusion constant. The boundary conditions are: $u$ equals a constant as r goes to infinity, and $u = 0$ on the aggregate surface. For a steady flux of walkers from a source that is far away from the aggregate surface, the equation can be reduced to the Laplace equation (Sander, 1986):

$$\nabla^2 u = 0 \qquad (1\text{-}4)$$

### 1.2.3 Variations on DLA

There have been many publications that have explored the effects of specific variations on the original DLA algorithm. The authors of this paper have employed some of these in the exploration of the adaptation of DLA to fluid-fluid displacement in porous media with varying flow rates and fluid properties.

To shorten the time it takes walkers to reach the aggregate from very far away, Meakin (1988) allowed particles to take larger steps if they were at a large distance from the occupied sites. This improved the efficiency of the algorithm and allowed the aggregates to be constructed faster while maintaining the same general morphology.

Jullien, et al. (1984) were the first to use a seed line instead of a seed particle. In lieu of sending walkers from a random point on a boundary circle, they sent walkers from a randomly chosen location on a finite width, semi-infinite "ribbon" towards a finite line of seed particles. This adaptation produces aggregate formations that are similar to flow paths made by a non-wetting fluid displacing water in a Hele-Shaw cell. A DLA simulation using a line seed is shown in Figure 4.

The third variation that we will present is the sticking probability. When a two-dimensional circular object is related to its mass by the second power of the radius we

call that object compact. If a two-dimensional circular object such as a DLA aggregate is irregular, we can take the radius of gyration to determine the mass density for that object in two dimensions. If a number between one and two relates the radius of gyration and the mass, we say that the object is fractal (Ferer, et al., 1995). The number relating the radius of gyration and the mass is termed the fractal dimension, D, and can be computed by several different techniques.
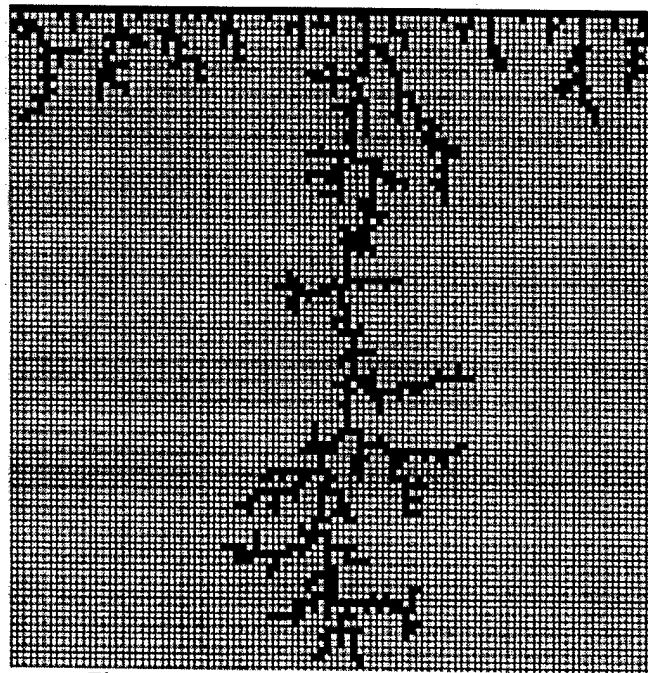


Figure 4. A DLA simulation from a line seed

This notion of the area covered by an object in two dimensions can be thought of as a two dimensional density of the object. We can alter the density of the aggregates created in a DLA simulation by changing the sticking probability. The sticking probability is the probability that a random walker that steps onto a location adjacent to an occupied location will "stick" and become part of the aggregate. The sticking probability essentially determines how susceptible the interface of the aggregate is to

rearrangements. When the sticking probability is unity, we observe classic DLA

formations. As the sticking probability is reduced, the aggregate becomes more compact

which results in a thickening of the aggregate's branches. In the limit as the sticking

probability goes to zero, the aggregate will qualitatively approach a stable front in the

analogy of fluid-fluid displacement in porous media. It was found in the current study

that this transition from fractal to compact configurations follows a power law

relationship.


### 1.2.4 Applications of DLA

The use of DLA to model unstable processes which have similar universal

properties has been investigated (Sander, 1986). These include diffusion-controlled

polymerization (Kaufman et al., 1986), chemical dissolution processes (Daccord, 1986),

dielectric breakdown (Niemeyer et al., 1984; Meakin, 1986), solute leaching (Flury and

Fluhler, 1995), viscous fingering (Maloy et al., 1985; Chen and Wilkinson, 1985), and

fluid-fluid displacement in Hele Shaw cells (Kadanoff, 1985; Liang, 1986). In its first

application to fluid-fluid flow in porous media, Paterson (1984) proposed a mathematical

analogy between flow in porous media and DLA. The macroscopic flow through porous

media is governed by Darcy's law:

$$q = \frac{-k}{\mu}(\nabla p - \rho g \nabla z) \tag{1-5}$$

For an incompressible fluid, the divergence of the flux, q, is zero and in the absence of

gravity we have the Laplace equation for the pressure in the more viscous fluid:

$$\nabla^2 p = 0 \qquad\qquad (1\text{-}6)$$

According to Paterson (1984), this equation is analogous to Equation (1-14) when the

pressure drop in the invading, less viscous fluid is zero. Chen and Wilkinson (1985)

agreed with this analogy and hypothesized that the randomness of a statistically

homogeneous porous media on the pore-scale was modeled by the stochastic nature of the

random walk. The authors who have previously performed experiments to determine if

the Laplace analogy between DLA and flow through porous media is correct use

Equation (1-6) as the basis of the relationship between the DLA model and the fluid-fluid

displacement in porous media (Paterson, 1984; Chen and Wilkinson, 1985; Maloy, et al.,

1985; Lenormand, 1987; Fernandez, et al., 1991; Kiriakidis, et al., 1991).

The history of using DLA to model fluid-fluid displacement began with

comparing Hele-Shaw experiments to DLA simulations. By applying the fluid

incompressibility condition to the flow equation for a viscous fluid being displaced in a

Hele-Shaw cell, Equation (1-5) is obtained. Kadanoff (1985) and Liang (1986) were the

first to use DLA to model air displacing water in a Hele-Shaw cell. Both Kadanoff

(1985) and Liang (1986) modified the original DLA algorithm to include surface tension

effects. This essentially made the fingers look more rounded and less dendritic at the

ends. Nittmann, et al. (1985) and Daccord, et al. (1986) carried out radial Hele-Shaw

experiments with water displacing a high viscosity, non-Newtonian polymer and

compared the resulting fluid configurations to simulations from an original DLA model.

Their simulations very closely match their experimental results and they concluded that

DLA quantitatively modeled the experimental fluid-fluid configuration as measured by

the fractal dimension of each. It was later postulated by Maloy, et al. (1985) that the

DLA algorithm without variations had successfully modeled the radial Hele-Shaw fluid-fluid displacements of Nittmann, et al. (1985) because the required randomness was due to viscosity fluctuations in the more viscous, non-Newtonian fluid. Sherwood (1987) used the mathematical analogy to DLA (the Laplace equation for pressure) to obtain front configurations for the motion of a fluid through porous media. The examples generated by his model are remarkably similar to the examples generated by a DLA algorithm.

Maloy, et al. (1985), Lenormand (1988), Fernandez, et al. (1991), and Kiriakidis, et al. (1991) have all explored the use of DLA modeling for fluid-fluid displacement in porous media using Paterson's original analogy.

Maloy, et al. (1985) conducted experiments whereby epoxy was displaced by air in a radial, two-dimensional porous medium. The resulting finger structures are tree-like and have the same fractal dimension as aggregates produced by DLA. In their determination, when the flow rate is high (more dominant viscous forces), the interface advances on the pore level by selecting the most favorable pore. They (Maloy, et al., 1985) conclude that DLA more appropriately models this behavior because the aggregate growth is controlled by both the Laplace equation and the discrete random advance on the pore level. In IP modeling, the movement is only governed by the pore or pore throat size, and the pressure gradient is neglected.

Lenormand (1988), as presented earlier, suggested the use of different stochastic models with differing front configurations, and gave limits for these models in terms of the microscopic capillary number and mobility ratio. Using the limits calculated by Lenormand (1988), Kiriakidis, et al. (1991) formulated an equation for the sticking probability for yet another variation on DLA consisting of two types of random walkers:

wetting and non-wetting. Gravity was not considered. The model simulations generated by Kiriakidis, et al. (1991) showed that DLA could be used to produce front configurations ranging from fingered to stable. These simulations appear to be qualitatively representative of fluid-fluid displacement in porous media. However, the fluid properties associated with the simulations are not representative of common fluids. The model simulations were generated for water being displaced by non-wetting fluids with dynamic viscosities of 7.6e-5 cp and 13 cp. With the exception of PCB's, the majority of dynamic viscosities for NAPLs lie in the range of 0.3 cp to 8 cp (Mercer and Cohen, 1990).

Fernandez, et al. (1991) used a DLA model with a releasing probability (converse of a sticking probability) to show that there is a crossover between DLA and IP as the releasing probability increases. This is equivalent to saying the NAPL-water front, as modeled by DLA, becomes more stable as the sticking probability decreases. The correlation between the releasing probability and the physics of the fluid-fluid displacement does not include gravity and is related to microscopic properties.

The previous work devoted to the application of DLA to fluid-fluid displacement in porous media has shown that DLA simulations can be produced which are both qualitatively and quantitatively (via comparison of the fractal dimension) similar to experimental fluid-fluid displacements. In addition, the sticking probability was identified by both Kiriakidis (1991) and Fernandez (1991) to be the parameter by which the movement of the interface can be related to the DLA model.

### 1.2.5 Macroscopic Dimensionless Numbers

Macroscopic dimensionless numbers were utilized as model input for SAM. Hilfer and Øren (1996) re-examined the multiphase flow equations and looked at the definition of non-dimensional variables for the microscale and macroscale. When using dimensional analysis for the Navier Stokes equation, the normalized pressure field is traditionally defined as:

$$p = \frac{\mu_w q l}{k} \hat{p} \qquad (1\text{-}7)$$

where the hat indicates the normalized pressure. This definition neglects the potential dependence on saturation history, and bases macroscopic pressures on macroscopic viscous pressure effects. Hilfer and Øren have instead normalized the macroscopic capillary pressure by the displacement pressure from the capillary pressure-saturation curve. The displacement pressure is the pressure that corresponds to the inflection point on the characteristic curve. By using this normalization, the saturation history may be accounted for as the displacement pressure on the drainage or imbibition curve. The resulting macroscopic capillary number, $\overline{Ca}$, is defined as:

$$\overline{Ca} = \frac{\mu \, q l}{k p_d} \qquad (1\text{-}8)$$

where q is a macroscopic flux for the phase of interest, l is a macroscopic length, and k is the intrinsic permeability. Using this analysis, the macroscopic gravity number and gravillary number may also be defined. The gravity number is the ratio of viscous forces to gravity forces and is defined as:

$$\overline{Gr} = \frac{\mu \, ql}{\rho \, gk} \qquad (1\text{-}9)$$

The gravillary number is the ratio of gravity forces to capillary forces. The gravillary number is the familiar bond number (Lake, 1989) when the difference in densities is used. The gravillary number is defined as:

$$\overline{Gl} = \frac{\rho \, gl}{p_d} \qquad (1\text{-}10)$$

## 1.3 THE STOCHASTIC AGGREGATION MODEL (SAM) AND THE TRANSITION NUMBER

SAM is a modified DLA model that makes use of some of the variations mentioned in the background section to model front configurations in fluid-fluid displacements. Specifically, our algorithm models the displacement of water by DNAPLs which are both more and less viscous than water, and LNAPLs which are both more and less viscous than water. In addition, we look at the flow of these fluids under the conditions of increasing flow rates and in a gravity field. The front configurations produced under these conditions range from viscous fingers, to percolation clusters, to stable fronts. The parameters of the model are macroscopic dimensionless numbers and fluid properties.

Our model uses Jullien's (1984) approach of using a seed line where the particle walks from a point on the grid far from the seed, in a region of finite width. A seed line in our case represents a line source of NAPL. We can also use a single seed particle in the middle of the top row of the grid to emulate a NAPL point source. To decrease the

time it takes for a particle to walk to the vicinity of the aggregate, we used Meakin's (1988) approach of allowing the walker to take larger steps when further from the aggregate. If the particle wanders more than seven rows past the furthest occupied space, the particle is removed and another one is released. The final variation incorporated into SAM is the sticking probability. The sticking probability is the only input into the model and its relationship to the transition number will be discussed in the following section.

For the simulations presented here, a square network of 10,000 elements was used. Each element represents a single pore. The pore size may be approximated via the Kozeny-Carmen equation (Dullien, 1992) given the value for intrinsic permeability used in the transition number. For a network of this size, one simulation runs in 0.5 to 4 minutes on an IBM RS6000 depending on the sticking probability.

When the simulation starts, particles are released from a random location opposite the seed point or line. The particle then has an equal probability of moving up, down, right, or left. If the particle encounters the sides of the network, it "bounces off" and continues walking. When the particle reaches a location adjacent to an occupied location, it is incorporated into the aggregate with a probability equal to the sticking probability, and a new particle is released. The simulations presented here were stopped when the bottom of the grid was reached, instead of prescribing a specific number of particles to form an aggregate. Utilizing continuity in the model is currently being studied. Standard IMSL routines (Visual Numerics, Inc., 1984) were used for random number generation.

### 1.3.1 The Transition Number

The transition number, as a sticking probability, is the only input into SAM. In the application of DLA to electrostatics, Niemeyer, et al. (1984) and Wiesmann and Zeller (1986) determined that the gradient of the relevant potential is proportionally related to the sticking probability. In the case of fluid-fluid displacement, we hypothesize that the capillary pressure is the potential that we are interested in. The gradient of the capillary pressure is determined by combining the definition of capillary pressure with Darcy's law written for each phase. The resulting equation for the capillary pressure gradient is equivalent to the equation for stability proposed by Saffman and Taylor (1958) and Chouke, et al. (1959). The interaction of the capillary, viscous, and gravity forces at the interface determines the degree to which the front is stable or fingered as the NAPL displaces the water.

The capillary pressure, $p_c$, is defined as the difference between the pressure in the NAPL phase and the pressure in the water phase:

$$p_c \equiv p_N - p_w \qquad (1\text{-}11)$$

For a two-phase immiscible system, Darcy's law can be written for each phase:

$$q_w = \frac{-kk_{rw}}{\mu_w}(\nabla p_w - \rho_w g \nabla z) \qquad (1\text{-}12)$$

$$q_N = \frac{-kk_{rN}}{\mu_N}(\nabla p_N - \rho_N g \nabla z) \qquad (1\text{-}13)$$

where w denotes water, N denotes NAPL, and q is the volumetric flux (positive in the direction of gravity). If we differentiate (11) and substitute in (12) and (13), we have the equation for the capillary pressure gradient.

$$\nabla p_c = \frac{1}{k}(\frac{q_w \mu_w}{k_{rw}} - \frac{q_N \mu_N}{k_{rN}}) + \Delta \rho g \sin \alpha \qquad (1\text{-}14)$$

where $\Delta \rho = \rho_N - \rho_w$, and $\alpha$ is the angle of the flow from the horizontal.

The capillary pressure gradient is then non-dimensionalized using the same definitions for non-dimensional variables as Hilfer and Øren (1996). These variables are:

$$\nabla = \frac{\hat{\nabla}}{l} \qquad (1\text{-}15)$$

$$p = p_d \hat{p} \qquad (1\text{-}16)$$

The result of non-dimensionalizing the capillary pressure gradient results in Equation (1-17):

$$\hat{\nabla}\hat{p}_c = \frac{q_w \mu_w l}{k_w p_d} - \frac{q_N \mu_N l}{k_N p_d} + \frac{\Delta \rho g l \sin \alpha}{p_d} \qquad (1\text{-}17)$$

Using the previous definitions for the macroscopic capillary and bond numbers, Equation (1-17) can be written as:

$$\hat{\nabla}\hat{p}_c = \overline{Ca}_w - \overline{Ca}_N + \overline{Bo} \qquad (1\text{-}18)$$

Morrow and Songkran (1981) and Dawson and Roberts (1997) have proposed similar linear combinations of the capillary and bond numbers. Morrow and Songkran (1981) explored the effect of viscous and buoyancy forces on the entrapment of LNAPLs in porous media. They found that the amount of entrapped NAPL could be correlated by a linear combination of the microscopic capillary and bond numbers. Dawson and

Roberts (1997), used an approach similar to that presented here to determine residual DNAPL saturations, but non-dimensionalized the capillary pressure with the Leverett (1941) function:

$$\nabla p_c = \frac{\gamma_{Nw} \cos\theta}{k/\phi} \hat{\nabla}\hat{p}_c \qquad (1\text{-}19)$$

In their analysis, the NAPL is assumed be immobile.

The scaled capillary pressure gradient in Equation (1-18) is termed the transition number. The first two terms of the transition number, $T_1$, compares the macroscopic capillary numbers for the wetting and non-wetting phases and therefore captures the combined effect of the viscous and capillary forces. The second term in the transition number, $T_2$, is the macroscopic bond number and includes the effects of gravity forces due to the density difference between the NAPL and water. The sum of these components is termed the transition number as it compares the relative importance of the forces as they transition between viscous dominated, capillary dominated, and gravity dominated. The transition number is thus defined as:

$$T = \left(\overline{Ca_w} - \overline{Ca_N}\right) + \overline{Bo} \qquad (1\text{-}20)$$

The macroscopic capillary number has been previously defined. $\overline{Bo}$ is the macroscopic bond number (macroscopic gravity number with the density difference included).

The first term of the equation is positive for NAPLs that are less viscous than water and negative for NAPLs that are more viscous than water. The second term is positive for DNAPLs and negative for LNAPLs, assuming the NAPL is displacing water from the top. By summing these components, the relative importance of all three forces

is taken into account. Positive values of the transition number correspond to some degree of viscous fingering, and negative numbers indicate a stabilizing of the front. As T approaches zero, the front configuration resembles a percolation cluster.

### 1.3.2 The Transition Number as Model Input

The transition number is the only parameter needed for the model's input, and is based on macroscopic flow conditions and basic fluid properties. It is proposed that the transition number determines the front stability in the same way that the sticking probability changes the cluster density in a SAM simulation. This supposition is based on the work of Fernandez (1991) and Kiriakidis (1991), but has been defined differently and has been extended to include buoyancy forces in this work. As percolation clusters lie quantitatively (in terms of the fractal dimension) and qualitatively between a fingered front and a stable front, they are correlated to a transition number of 0. The transition number is then mapped onto the range of 0 to 1, to facilitate its use in the model as a sticking probability, Ps.

In order to map the ranges of T and Ps, it was necessary to know the point at which the model generated percolation clusters. Percolation clusters are characterized by a fractal dimension of D=91/48 (1.89), (Berkowitz and Balberg, 1993; Meakin, 1991; Oxaal, et al., 1987). The box counting or sandbox method (Meakin, 1985; Daccord, et al. 1986), was used to determine the fractal dimension of the clusters generated by the model. In this method, a square of lattice sites, LxL, is formed around each occupied site. The number of occupied sites within this square is counted, N(L). This is done for different square sizes and a log-log plot of N(L) vs. L is generated. A straight line on this

plot indicates that the cluster is fractal with a fractal dimension equal to the slope of the line. The sticking probability for the model which generated a percolation cluster with D=1.89 was mapped to a zero value for the transition number. This sticking probability was determined to be Ps=0.03, as the sticking probability changes as a power law with the with cluster density. Linear interpolation was then used to relate the transition number to the sticking probability over its range.

## 1.4    RESULTS AND DISCUSSION

Model simulations were carried out for NAPLs with varying densities and viscosities. The angle of inclination of the plane from the horizontal was 90 degrees and 15 degrees. At each angle of inclination, two flow rates were used to show the effect of the changing capillary and bond numbers. The NAPLs used were 1,2 dichloroethane (DCA), 1,2 dibromoethane (EDB), gasoline, and mineral oil. The first two are DNAPLs with DCA being less viscous than water and EDB being more viscous than water. The last two are LNAPLs with gasoline being less viscous than water and mineral oil being more viscous than water.

The fluid properties for each NAPL were taken from Mercer and Cohen (1990) and are listed in Table 1. In Table 2 the transition number as well as its components, the corresponding sticking probability and the fractal dimension are listed for each NAPL at two different flow rates, and two different angles of inclination from the horizontal. Figures 5 to 8 show the model simulations corresponding to the cases in Table 2. In each case, the simulation was stopped when the finger or cluster reached the bottom of the grid. Thus even though two simulations are at the same volumetric flux rate, they may

Table 1
NAPL properties

| NAPL | Density (g/cm$^3$) | Viscosity (cP) |
|---|---|---|
| 1,2 Dichloroethane | 1.26 | 0.887 |
| 1,2 Dibromoethane | 2.17 | 1.49 |
| Gasoline | 0.728 | 0.650 |
| Mineral Oil | 0.822 | 29.0 |

Table 2
Transition Number Calculations

| D | Flux (cm/s) | Angle of Inclination | $T_1$ | $T_2$ | T | Ps |
|---|---|---|---|---|---|---|
| 1,2 Dichloroethane 1.67 | 0.0076 | 90° | 0.0297 | 0.3185 | 0.3482 | 0.3678 |
| 1.81 | | 15° | 0.0297 | 0.0824 | 0.1121 | 0.1388 |
| 1.62 | 0.034 | 90° | 0.1331 | 0.3185 | 0.4516 | 0.4681 |
| 1.72 | | 15° | 0.1331 | 0.0824 | 0.2155 | 0.2391 |
| 1,2 Dibromoethane 1.63 | 0.0076 | 90° | -0.1291 | 1.4316 | 1.3025 | 0.6617 |
| 1.76 | | 15° | -0.1291 | 0.3705 | 0.2414 | 0.1471 |
| 1.69 | 0.034 | 90° | -0.5774 | 1.4316 | 0.8542 | 0.4443 |
| 1.94 | | 15° | -0.5774 | 0.3705 | -0.2069 | 0.0238 |
| Gasoline 1.95 | 0.0076 | 90° | 0.0922 | -0.3332 | -0.2410 | 0.0228 |
| 1.94 | | 15° | 0.0922 | -0.0862 | 0.0060 | 0.0358 |
| 1.89 | 0.034 | 90° | 0.4124 | -0.3332 | 0.0792 | 0.1068 |
| 1.68 | | 15° | 0.4124 | -0.0862 | 0.3262 | 0.3464 |
| Mineral Oil 1.92 | 0.0076 | 90° | -7.375 | -0.2181 | -7.593 | 0.0235 |
| 1.94 | | 15° | -7.375 | -0.0564 | -7.431 | 0.0236 |
| 2.01* | 0.034 | 90° | -32.991 | -0.2181 | -33.209 | 0.00153 |
| 2.01* | | 15° | -32.991 | -0.0564 | -33.047 | 0.00167 |

* D>2 is a result of the box counting method used to calculate the fractal dimension.

not be representative of the NAPL configuration at the same time. Work is currently being performed in which different times for the same flow rate are used to show how the front progresses.

These simulations show the model's ability to use one input parameter, the transition number, to generate an approximate NAPL front configuration. Instability of the NAPL is shown in the pictures, as they range from thin fingers, to fingers with thicker branches, to masses where nearly all of the water has been displaced. The configuration is approximate because, due to random number generation, the configuration for a given transition number may look somewhat different in each simulation.

The fractal dimension, D, was used to compare the relative density of the simulations and is included in the tables for each case. For 1,2 dichloroethane (Figure 5), the NAPL configuration becomes more stable, thicker branches in this case, as the flow rate is decreased and the angle of inclination is decreased. The fractal dimension ranges from D=1.62 for the least stable case at 90° and q=0.034 cm/s to D=1.81 for the most stable case of 15° and q=0.0076 cm/s. A flat front, where NAPL displaces nearly all of the water, would have a fractal dimension approaching D=2. The values for the two terms in the transition number are positive for each scenario. This indicates that higher flow rates (higher capillary number difference) and a higher angle from the horizontal (higher bond number) both contribute to the instability of a DNAPL with a viscosity lower than that of water. The transition number becomes smaller as the flow rate and angle from the horizontal are reduced, but both terms remain positive.

For 1,2 dibromoethane (Figure 6), the least stable case occurs when the flow rate is 0.0076 cm/s and the angle of inclination is at a maximum. The most stable case shown

here results when the flow is increased, but the angle is decreased. Here, the fractal dimensions have a larger range spanning from D=1.63 to D=1.94. When evaluating the transition number components, we see this time that the viscous and gravity forces are in opposition due to the relative viscosity of EDB to water. For larger flow rates, the first term in the transition number becomes more negative indicating that for a DNAPL with a viscosity greater than that of water, higher flow rates will contribute to the fronts stability. For larger angles of inclination, the second term in the transition number becomes greater indicating more unstable flow. For this NAPL, the forces oppose each other.

The third NAPL, gasoline (Figure 7), shows a trend opposite that of EDB. Because gasoline is less viscous than water, it becomes increasingly unstable as the flow rate is increased. Stability is increased in this case by increasing the angle of inclination due to the negative density difference between the two fluids. A crossover between inherently stable and inherently unstable front configurations can occur when the terms of the transition number add to zero. This is approached when q=0.0076 cm/s and the angle from the horizontal is 15°.

In the final case, mineral oil (Figure 8) is used to show the front configuration for a NAPL which is less dense but more viscous than water. For this scenario, both terms in the transition number are negative regardless of the changing flow rate and angle from the horizontal. The fractal dimensions of the simulations range from D=1.92 to D=2.01. With a viscosity 29 times greater than that of water, the first term of the transition number dominates the displacement behavior and the differences due to the angle of inclination are small. A fractal dimension greater than two is a consequence of the inaccuracy of the

box counting method used to calculate the fractal dimension. Specifically, when the cluster reaches the sides of the grid, the box counting method does not account for the filled grid spaces at the very edge of the cluster.

The simulations for each NAPL show approximate configurations for NAPL-water displacement in a porous medium. This configuration is a result of evaluating the viscous, gravity and capillary forces at the pore level. The simulations presented here do not show a residual saturation, but rather a percentage of pore space in which the NAPL displaced the water. Using this information, retention capacity values and subsequent penetration depths can be determined more accurately. Future work for this model includes the incorporation of simple heterogenieties, and the calculation of retention capacities.
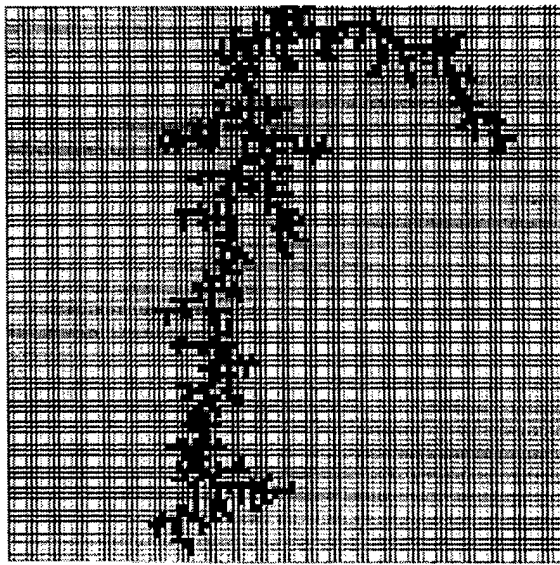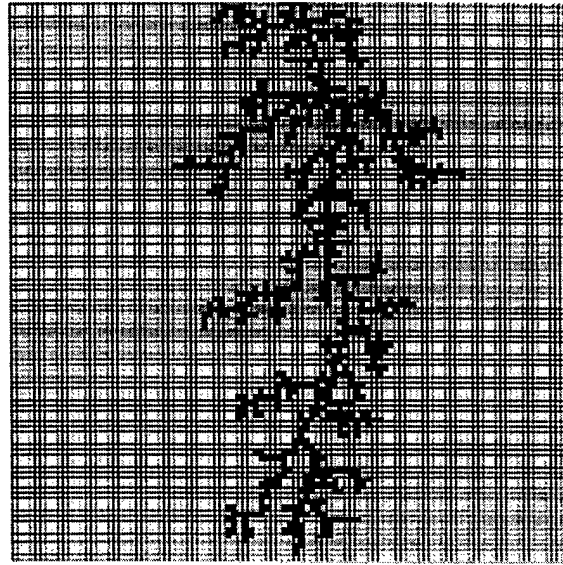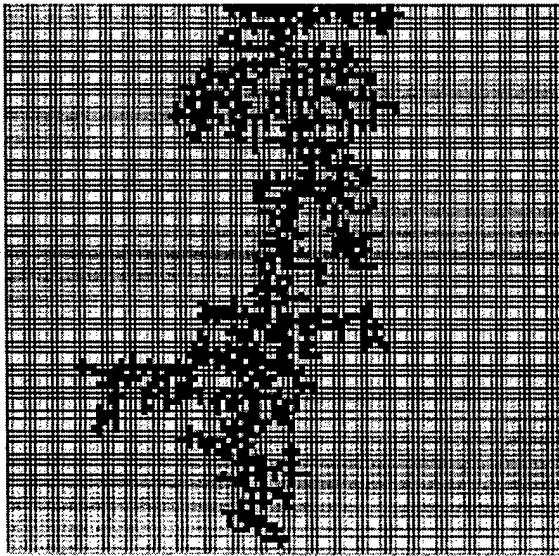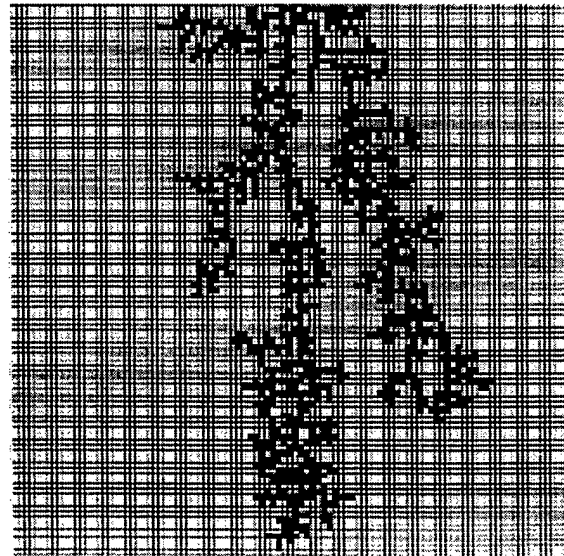
Figure 5. The displacement of water by 1,2 Dichloroethane at different flow rates and different angles of inclination from the horizontal: (a) q=0.0076 cm/s, $\alpha$=90°, (b) q=0.034 cm/s, $\alpha$=90°, (c) q=0.0076 cm/s, $\alpha$=15°, (d) q=0.034 cm/s, $\alpha$=15°.
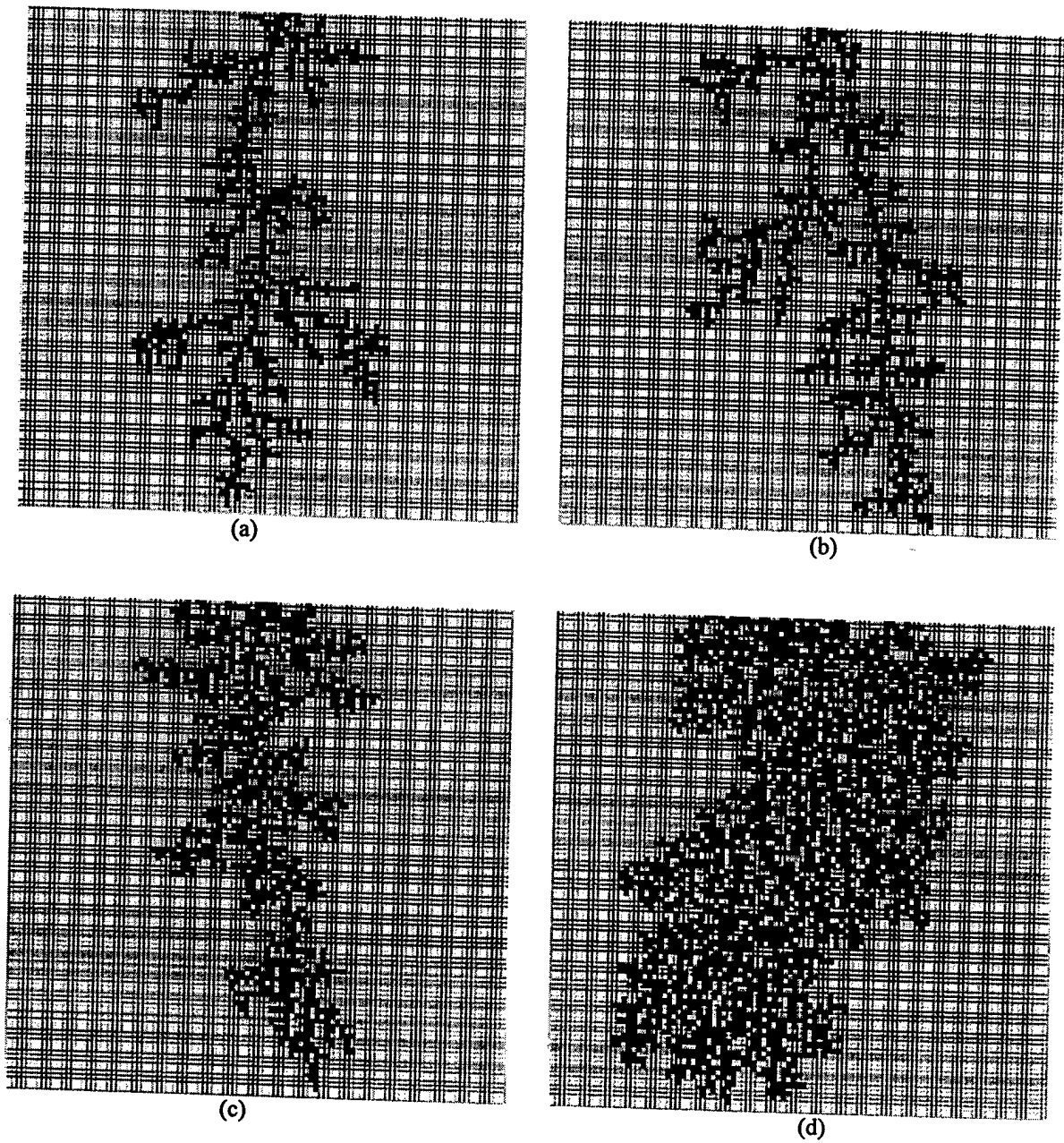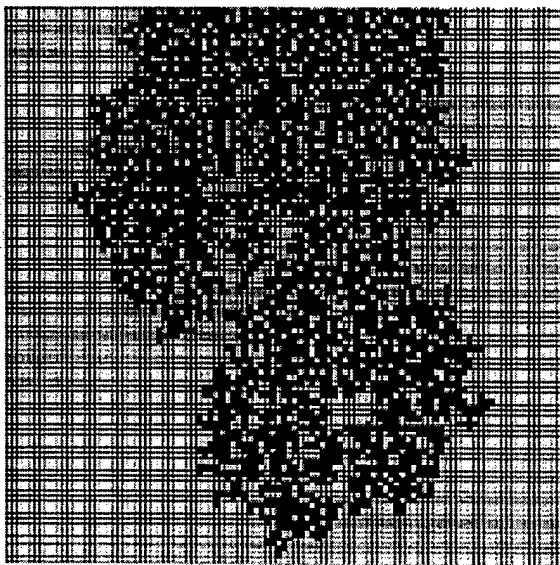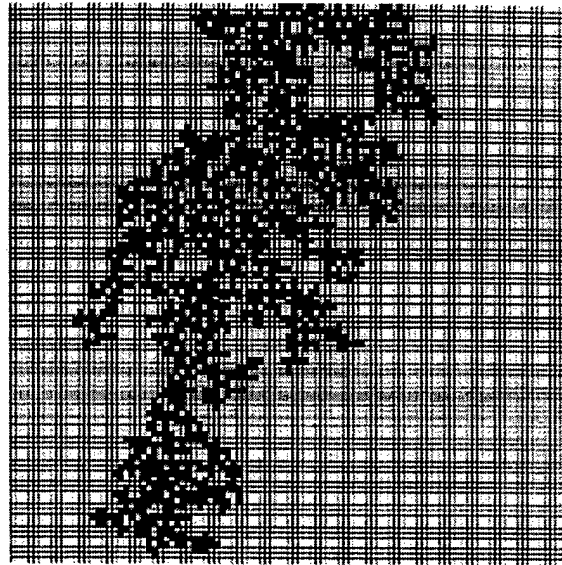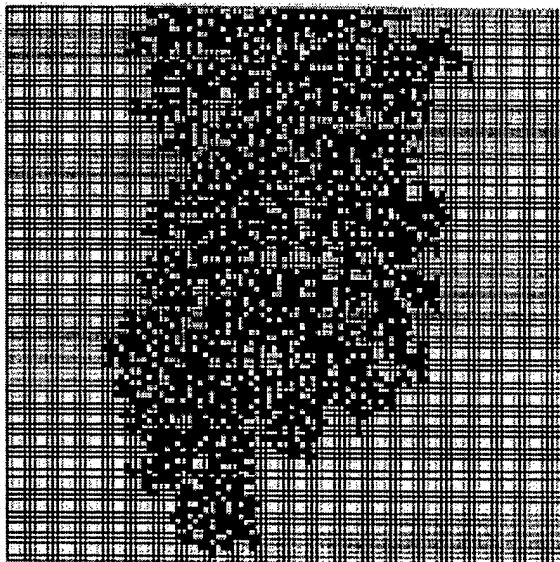
Figure 6. The displacement of water by 1,2 Dibromoethane at different flow rates and different angles of inclination from the horizontal: (a) q=0.0076 cm/s, α=90°, (b) q=0.034 cm/s, α=90°, (c) q=0.0076 cm/s, α=15°, (d) q=0.034 cm/s, α=15°.

Figure 7. The displacement of water by gasoline at different flow rates and different angles of inclination from the horizontal: (a) q=0.0076 cm/s, α=90°, (b) q=0.034 cm/s, α=90°, (c) q=0.0076 cm/s, α=15°, (d) q=0.034 cm/s, α=15°.
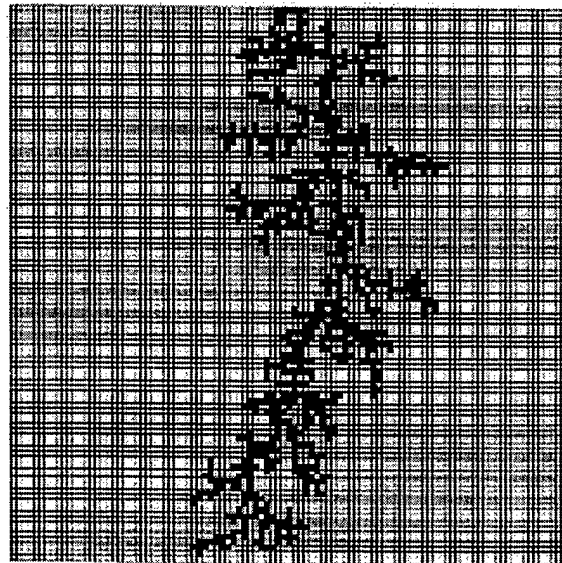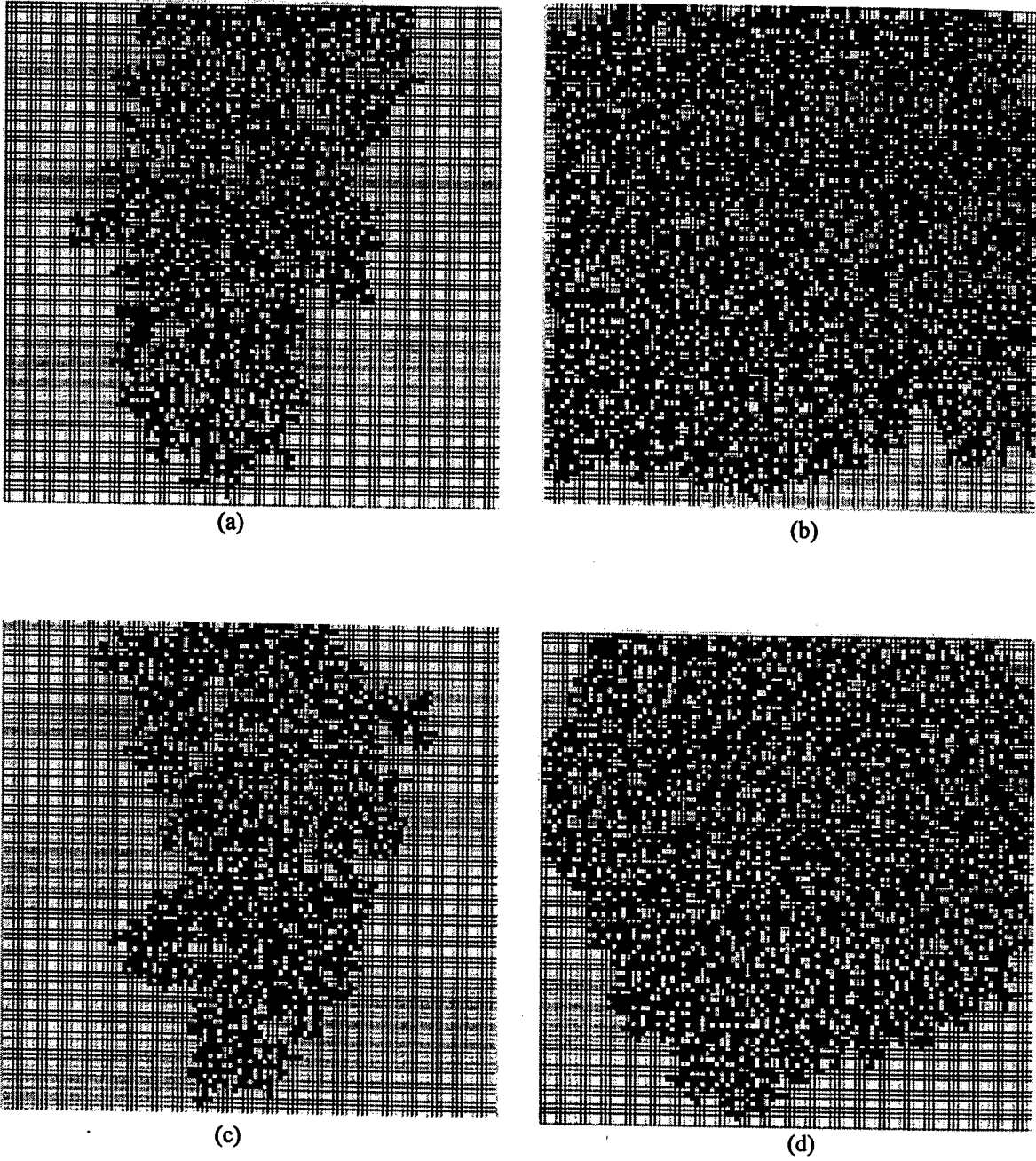
Figure 8.  The displacement of water by mineral oil at different flow rates and different angles of inclination from the horizontal: (a) q=0.0076 cm/s, α=90°, (b) q=0.034 cm/s, α=90°, (c) q=0.0076 cm/s, α=15°, (d) q=0.034 cm/s, α=15°.

## 1.5 CONCLUSIONS

A modeling technique for describing the front configuration for NAPLs displacing water in saturated porous media is presented. The stochastic aggregation model (SAM) is a modified diffusion limited aggregation model that can quickly provide two-dimensional representations.

Capillary, viscous and gravity forces act concurrently to stabilize or destabilize the front when a NAPL displaces water. A transition number has been derived that determines the interplay of these forces, and is a scaled linear combination of the macroscopic capillary and bond numbers. The use of a transition number as the model input is unique in that it includes gravity as well as the fluid's viscosity and density differences and allows the model to create simulations ranging from highly fingered to stable displacements. Easily measured or estimated macroscopic parameters are used to calculate the transition number, thereby contributing to the ease of use and broad application of the model.

In this study, we presented model simulations for four different NAPLs: two LNAPLs, with one less and one more viscous than water, and two DNAPLs, with one less and one more viscous than water. The effects of different flow rates and different inclinations from the horizontal were investigated for each NAPL. Fractal dimensions were calculated and used to compare model results. The simulations accurately show that:

• for a DNAPL which is less viscous than water, as both the NAPL flow rate and the angle from the horizontal is increased the front becomes less stable;

•for a DNAPL which is more viscous than water, as the NAPL flow rate increases the front becomes more stable, but as the angle from the horizontal increases the front becomes less stable;

•for a LNAPL which is less viscous than water, as the NAPL flow rate increases the front becomes less stable, but as the angle from the horizontal increases the front becomes more stable;

•for a LNAPL which is more viscous than water, as both the NAPL flow rate and the angle of inclination is increased the front becomes more stable.


## 1.6    REFERENCES

Bedient, P. B., Rife, H. S. and Newell, C. J., 1994. Ground Water Contamination: Transport and Remediation. Prentice Hall PTR, Englewood Cliffs, NJ.

Berkowitz, B. and Balberg, I., 1993. Percolation theory and its application of groundwater hydrology. Water Resour. Res., 29(4): 775-794.

Birovljev, A., Furuberg, L., Feder, J., Jossang, T., Maloy, K. J. and Aharony, A., 1991. Gravity invasion percolation in two dimensions: experiment and simulation. Phys. Rev. Lett., 67(5): 584-587.

Broadbent, S. R. and Hammersley, J. M., 1957. Percolation processes, crystals and mazes. Proc. Cambridge Philos. Soc., 53: 629-641.

Chatzis, I. and Dullien, F. A. L., 1985. The modeling of mercury porosimetry and the relative permeability of mercury in sandstones using percolation theory. Int. Chem. Eng., 25: 47-66.

Chen, J.-D. and Wilkinson, D., 1985. Pore-scale viscous fingering in porous media. Phys. Rev. Lett., 55: 1892-1895.

Chouke, R. L., Van Meurs, P., and ver der Poel, C., 1959. The instability of slow immiscible, viscous liquid-liquid displacements in porous media. Trans. A. I. M. E., 216: 188-194.

Daccord, G., Nittmann, J. and Stanley, H. E., 1986. Radial viscous fingers and diffusion-limited aggregation: fractal dimension and growth sites. Phys. Rev. Lett., 56: 336-339.

Dawson, H. E. and Roberts, P. V., 1997. Influence of viscous, gravitational, and capillary forces on DNAPL saturation. Ground Water, 35(2): 261-269.

Dullien, F. A. L., 1992. Porous Media: Fluid Transport and Pore Structure. Academic, San Diego, CA.

Fatt, I., 1956. The network model of porous media, I, Capillary pressure characteristics. Trans. AIME Pet. Dev., 207: 144-159.

Ferer, M., Sams, W. N., Geisbrecht, R. A. and Smith, D. H., 1995. Fractal nature of viscous fingering in two-dimensional pore level models. AICHE Journal, 41(4): 749-763.

Fernandez, J. F., Rangel, R. and Rivero, J., 1991. Crossover length from invasion percolation to diffusion-limited aggregation in porous media. Phys. Rev. Lett., 67: 2958-2961.

Ferrand, L. A. and Celia, M. A., 1992. The effect of heterogeneity on the drainage capillary pressure saturation. Water Resour. Res., 28(3): 859-870.

Flury, M. and Fluhler, H., 1995. Modeling solute leaching in soils by diffusion-limited aggregation: Basic concepts and application to conservative solutes. Water Resources Research, 31(10): 2443-2452.

Hilfer, R. and Øren, P. E., 1996. Dimensional analysis of pore scale and field scale immiscible displacement. Transport in Porous Media, 22: 53-72.

Jerauld, G. R., and Salter, S. J., 1990. The effect of pore-structure on hysteresis in relative permeability and capillary pressure: Pore-level modeling. Transport in Porous Media, 5(2): 103-151.

Jullien, R., Kolb, M. and Botet, R., 1984. Diffusion limited aggregation with directed and anisotropic diffusion. J. Physique., 45: 395-399.

Kadanoff, L. P., 1985. Simulating hydrodynamics: a pedestrian model. J. Stat. Phys., 39(3/4): 267-283.

Kaufman, J. H., Baker, C. K., Nazzal, A. I., Flickner, M. and Melroy, O. R., 1986. Statics and dynamics of the diffusion-limited polymerization of the conducting polymer polypyrrole. Phys. Rev Lett., 56: 1932-1935.

Kiriakidis, D. G., Mitsoulis, E. and Neale, G. H., 1991. Linear displacement of a wetting fluid by an immiscible non-wetting fluid in a porous medium: a predictive algorithm. Canadian J. Chem. Eng., 69: 557-563.

Lake, L. W., 1989. Enhanced Oil Recovery. Prentice-Hall, Inc., Englewood Cliffs, NJ.

Lenormand, R., 1987. Statistical physics and immiscible displacements through porous media. AIP Conf. Proc. 154, Physics and Chemistry of Porous Media II, 98-115.

Lenormand, R., Touboul, E. and Zarcone, C., 1988. Numerical models and experiments on immiscible displacements in porous media. J. Fluid Mech., 189: 165-187.

Leverett, M. C., 1941. Capillary behavior in porous media. Trans. A. I. M. E., 142: 341-358.

Li, Y., Laidlaw, W. G. and Wardlaw, N. C., 1986. Sensitivity of drainage and imbibition to pore structures as revealed by computer simulation of displacement process. Adv. Colloid Interface Sci., 26: 1-68.

Liang, S., 1986. Random-walk simulation of flow in Hele Shaw cells. Phys. Rev. A, 33(4): 2663-2674.

Lowry, M. I. and Miller, C. T., 1995. Pore-scale modeling of non-wetting-phase residual in porous media. Water Resour. Res., 31(3): 455-473.

Maloy, K. J., Feder, J. and Jossang, T., 1985. Viscous fingering fractals in porous media. Phys. Rev. Lett., 55: 2688-2691.

Meakin, P., 1991. Fractal aggregates in geophysics. Reviews of Geophysics, 29(3): 317-354.

Meakin, P., 1988. The growth of fractal aggregates and their fractal measures. Phase Transitions and Critical Phenomena, vol. 12, edited by C. Domb and J. L. Lebowitz, Academic, San Diego, CA, 335-489.

Meakin, P., 1986. Universality, nonuniversality, and the effects of anisotropy on diffusion-limited aggregation. Phys. Rev. A, 33(5): 3371-3382.

Meakin, P. and Deutch, J. M., 1986. The formation of surfaces by diffusion limited annihilation. J. Chem. Phys., 85(4): 2320-2325.

Meakin, P., 1985. On growth and form: Fractal and non-fractal patterns in physics, edited by H. E. Stanley and N. Ostrowsky, Nijhoff, Dordrecht, 69.

Mercer, J. W. and Cohen, R. M., 1990. A review of immiscible fluids in the subsurface: Properties, models, characterization and remediation. J. Contam. Hydrol., 6: 107-163.

Morrow, N. R. and Songkran, B., 1981. Effect of viscous and buoyancy forces on non-wetting phase trapping in porous media. Surface Phenomena in Enhanced Oil Recovery, edited by D. O. Shah, Plenum Press, New York, 387-411.

Nittmann, J., Daccord, G. and Stanley, H. E., 1985. Fractal growth of viscous fingers: quantitative characterization of a fluid instability phenomenon. Nature, 314: 141-144.

Niemeyer, L., Pietronero, L. and Wiesmann, H. J., 1984. Fractal dimension of dielectric breakdown. Phys. Rev. Lett., 52: 1033-1036.

Oxaal, U., Murat, M., Boger, F., Aharony, A., Feder, J. and Jossang, T., 1987. Viscous fingering on percolation clusters. Nature, 329(3): 32-37.

Pankow, J. F., Feenstra, S., Cherry, J. A. and Ryan, M. C., 1996. Dense Chlorinated Solvents in Groundwater: Background and History of the Problem. Dense Chlorinated Solvents and other DNAPLs in Groundwater, edited by J. F. Pankow and J. A. Cherry, Waterloo Press, Portland, OR, 1-52.

Paterson, L., 1984. Diffusion-limited aggregation and two-fluid displacements in porous media. Phys. Rev. Lett., 52: 1621-1624.

Saffman, P. G. and Taylor, G. I., 1958. The penetration of a fluid into a porous medium or Hele-Shaw cell containing a more viscous liquid. Proc. Soc. London, Ser. A, 245: 312-331.

Sander, L. M., 1986. Fractal growth processes. Nature, 332(28): 789-793.

Sander, L. M., 1984. Theory of Fractal Growth Processes. Kinetics of Aggregation and Gelation, edited by F. Family and D. P. Landau, Elseview Science Publishers, B. V., 13-17.

Sherwood, J. D., 1987. Unstable fronts in a porous medium. J. Comp. Phys., 68: 485-500.

Soll, W. E. and Celia, M. A., 1993. A modified percolation approach to simulating 3-fluid capillary pressure saturation relationships. Adv. Water Resour., 16(2): 107-126.

Tsakiroglou, C. D. and Payatakes, A. C., 1990. A new simulator of mercury porosimetry for the characterization of porous materials. J. Coll. Interface Sci., 137(2): 315-339.

Wardlaw, N. C., Li, Y. and Forbes, D., 1987. Pore-throat size correlation from capillary pressure curves. Transp. Porous Media, 2: 597-614.

Wiesmann, H. J. and Zeller, H. R., 1986. A fractal model of dielectric breakdown and prebreakdown in solid dielectrics. J. Appl. Phys., 60, 1770-1773.

Wilkinson, D., 1984. Percolation model of immiscible displacement in the presence of buoyancy forces. Physical Rev. A, 30(1): 520-531.

Wilkinson, D. and Willemsen, J. F., 1983. Invasion percolation: A new form of percolation theory. J. Phys. A Math. Gen., 16(14): 3365-3376.

Witten, T. A. and Sander, L. M., 1983. Diffusion-limited aggregation. Physical Review B, 27(9): 5686-5697.

# SECTION V

# SECTION V

## SUMMARY AND CONCLUSIONS

### 1.1    INTRODUCTION

This project focused on the distribution of multiphase fluids in homogeneous and layered porous media under equilibrium and transient flow processes. A synergistic procedure was used that included pore-scale and lab-scale numerical models, and one- and two-dimensional laboratory studies.

### 1.2    CONCLUSIONS

This report is divided into several sections. Section I is the introduction. Section II reports results from the physical one-and two dimensional laboratory studies. Section III presents and verifies a one-dimensional transient model for multiphase flow through layered porous media. Finally, Section IV presents a pore-scale modified diffusion limited aggregation model. Conclusions are listed at the end of each chapter. Major conclusions are summarized here.

1)    Effects of soil layering, nonwetting phase access and differences in those effects for air and LNAPL systems were quantified in a one-dimensional, transient drainage experiment in layered soil.

2)    Perfluorocarbons have fluid properties that are similar to those of dense, chlorinated solvents but pose no health hazard and are not regulated. These non-

toxic, inert, dense nonaqueous phase liquids were identified and investigated as surrogates for laboratory and field studies of chlorinated solvents.

3) Stable mounds of DNAPL can form on heterogeneities, with lateral stability existing on flat, or even sloped, textural discontinuities.

- A predictive expression was developed for the maximum thickness of a laterally stable NAPL mound and it was found that hysteretic capillary pressure-saturation relations are needed to explain LNAPL and DNAPL mound thicknesses greater than zero.

- Models which do not include hysteresis will not result in correct distributions of free phase NAPL distribution at equilibrium.

4) A conceptual model of LNAPL infiltration and spreading at the capillary fringe was developed and verified with a series of two-dimensional flume experiments.

- The top of the lens is not necessarily at the top of the capillary fringe but its location can be calculated from the water-NAPL and NAPL-air interfacial tensions.

- Capillary pressures at each point on the water-NAPL boundary are on a different hysteresis loop of the water-NAPL capillary pressure-saturation curve.

- The top of an LNAPL lens is flat and the capillary pressure at each point is the air-entry pressure on the NAPL-air drainage curve.

- The maximum thickness of an LNAPL lens is the difference between the capillary pressure entry head on the oil-water drainage curve and the capillary pressure entry head on the oil-water imbibition curve.

5) Both a two-dimensional modified diffusion limited model and a three-dimensional invasion percolation model were developed as part of this project. Results include:

- The modified diffusion limited aggregation model appears to simulate the unstable flow of DNAPLs in saturated porous media well. We found that the model was able to simulate both DNAPL and LNAPL in two-dimensions.

- The volume of the entrapped nonwetting phase is determined mainly by the aspect ratio of the network and pore tortuosity. As the aspect ratio decreases, entrapment of the nonwetting phase and hysteresis decreases.

- The bond number was found to play a major role in determining the drainage and imbibition sequences and hence strongly influence the water retention and hydraulic conductivity curves. This study showed that, as the bond number increased, the relative hydraulic conductivity and water retention curves become scale dependent for coarse soils.

6)    A semi-analytical solution for one-dimensional, two-fluid flow in layered porous media is presented.  The modeling approach presented in this report has the following properties: a set of equations is solved explicitly and sequentially, rather than simultaneously as required by the finite difference and finite element methods, spacing between nodes is varied within and between time steps based on accuracy criteria, and the iteration process requires convergence of only one or two boundary condition values, rather than iterations on all internal nodes.

- The model was found to be unconditionally stable for one-dimensional, two-fluid transient flow in layered soil.

- The model was verified by comparing model results to an exact solution and by comparing simulations to laboratory data.

- A comparison of Richards' equation and two-fluid flow equations for drainage with limited air access showed that the hydraulics of air flow can have a significant impact on the nature of vertical water drainage.